TESIS DE LA UNIVERSIDAD DE ZARAGOZA

2016

210

David Coffey Blanco

Rare earth adatoms and nanoislands studied by scanning tunnelling microscopy

Departamento

Física de la Materia Condensada

Director/es

Ciria Remacha, Miguel Ángel

Arnaudas Pontaque, José Ignacio

ISSN 2254-7606

Prensas de la Universidad Universidad Zaragoza

ISSN 2254-7606

Universidad Zaragoza
1542

Tesis Doctoral

RARE EARTH ADATOMS AND NANOISLANDS STUDIED BY SCANNING TUNNELLING MICROSCOPY

Autor

David Coffey Blanco

Director/es

Ciria Remacha, Miguel Ángel
Arnaudas Pontaque, José Ignacio

UNIVERSIDAD DE ZARAGOZA

Física de la Materia Condensada

2016

Universidad de Zaragoza

Instituto de Ciencia de Materiales de Aragon - CSIC

Departamento de Fisica de la Materia Condensada

Rare earth adatoms and nanoislands studied by Scanning Tunnelling Microscopy

Author: **David Coffey Blanco**

Thesis advisors: Prof. J. I. Arnaudas, Dr. M. Ciria

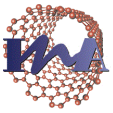

Para mi madre,

por mi padre.

Contents

Agradecimientos

Resulta complicado escribir los agradecimientos al finalizar la tesis: la inspiración hace tiempo que se mudó de país, las teclas empiezan a fallar tras tanta página y además no resulta fácil contener el impulso de darle a imprimir e ir corriendo a ver como salen las páginas de la impresora, una a una, aún calientes, dándole forma física a la versión final. O casi final, que faltan los agradecimientos.

Quiero comenzar agradeciendo a mis directores, Jose Ignacio Arnaudas y Miguel Ciria, haber hecho esta tesis posible. Son muchos años trabajando con vosotros, desde antes de terminar la carrera, y no puedo sino agradecer todo el apoyo que me habéis brindado, tanto a nivel profesional como personal. Considero que una buena comunicación es fundamental para sacar adelante un trabajo como éste, y siempre me he sentido valorado a la hora de plantear mis ideas y ayudado a la hora de resolver mis dudas. Mi más sincero agradecimiento a ambos.

Una tesis, al menos esta tesis, no sale adelante sin un trabajo de equipo detrás. He tenido suerte en coincidir durante la realización de mi tesis con otros proyectos enfocados al área de STM, que si bien suponen una lucha por horas de máquina, le ponen una cara humana a tanto acero inoxidable. Del grupo de STM quiero empezar agradeciendo a David Serrate todo el esfuerzo que ha puesto en mantener operativo el JT a pesar de todos los doctorandos que íbamos a meter nuestros muestras y nuestras zarpas, así como traer una experiencia consolidada de STM a Zaragoza, que nos ha sido de gran ayuda a todos los que hemos pasado por el laboratorio. A César de la Fuente agradecerle todo el trabajo de cálculos que lleva a cabo, que ayudan a poner en contexto los resultados experimentales. Quiero agradecer también a Jose Luis el haberme iniciado en el STM, y con la perspectiva de haber trabajado con diversas máquinas valoro aún más todo el trabajo que fuiste capaz de sacarle a ese STM infernal, el tiempo que invertí yo en él se dividía en partes iguales en frustración y en planificar un cambiazo con el microscopio en el que estaba trabajando Marten; puesto que menciono a Marten, agradecerle a él también

su interés en mi trabajo y el poder colaborar con él en la caracterización SP de redes de moléculas. La instalación de una máquina nueva trae muchas ventajas, pero tiene un coste inevitable de descubrir sus rarezas particulares, sus ruidos, sus inestabilidades, pasar sus días buenos y malos hasta conocer cómo ocurren unos y otros... Growing pains, vaya. Todos los que pasemos por el laboratorio le debemos estar agradecidos a María, que fue a la que le tocó llevarlos y, además, sacando resultados. Gracias a Jose por echarme una mano con el Cu_2N y por sus ánimos. Con Alberto he podido coincidir menos de lo que hubiera querido, pero con sólo un par de congresos ya me quedan bastantes anécdotas que llevarme (nota mental: para otra vez que llueva, primero cambiarme y luego ensayar presentación. No al revés.) A Mari Carmen también darle las gracias por su ayuda con material sobre Rashba y su apoyo desde Holanda. Cierro el sector STM dándole las gracias a Carlos, sin quien la mitad de las cosas estarían rotas, o directamente no se podrían haber construido. Trabajo de equipo, sin duda.

Los años de tesis dan para conocer a muchas personas, gente que se queda tiempo y gente que va de paso, y en ese sentido fue muy agradable el grupo de comida, siempre dispuesto a apretar una silla más para el que llegara, y a base de estar apretados, hacer irremediablemente grupo humano, nuevos y veteranos, fijos y de paso. Luego problemas logísticos fueron dificultando el comer todos juntos, pero me sirvió para concer al sector Bio del INA (un saludo a todas, no enumero que seguro que me dejo a alguien!), al sector hipertermia, etc... Al mirar para atrás siempre destacan algunos rostros, así que aunque evite listas largas no voy a terminar el párrafo sin nombrar a Alberto, Mari Carmen, Rocío.

También mencionar al grupo de compañeros del departamento de Física de la Materia Condensada, aunque cada vez quedáramos menos. Y con menos, quiero decir que os habéis ido todos. Los cafés fueron perdiendo asistentes según se fueron yendo Ana, Mariafer, Mark, Cristina... Así, hasta no haber café, ¡vaya plan!. Agradecer a Celia, Clara, Watson, Sherlock, sus perros, sus gatos, sus elefantes y toda la fauna que se les ocurra meter en casa todos las risas, los sinsentidos y también su hospitalidad - ir de sincrotrón sigue siendo duro, pero en Trieste parece que pesa menos.

Abro párrafo aparte para mi hermano Luis, por todas esas horas de hablar, horas de ver el mundo pasar desde la terraza, horas de coop, horas de planes. Y alguna que otra cicatriz. Un día de estos, lo dejamos todo y nos dedicamos a elaborar cerveza, esta vez sí que sí.

En la vida hay decisiones fáciles y decisiones difíciles, y luego hay otras que son tan evidentes que no son decisiones en absoluto. En esa última categoría está la de compartir mi vida con mi mujer, Ione, a la que no le puedo agrade-

cer lo suficiente todo su apoyo y comprensión durante los años de tesis y, en particular, durante los últimos meses. Creo que no exagero al decir que está tesis no habría sido posible sin ella, así que gracias de nuevo. Gracias también por Otto, por Moriarty y por Miso, que sin ti no habría tenido el placer de tener por casa.

Por último, quiero terminar estos agradecimientos dedicándole este trabajo y agradeciéndole el hacerlo posible a mi familia. A mi hermana Elisabeth por ser un ejemplo de capacidad de trabajo y sacrificio, por no tenerle miedo (o no hacerle caso al miedo, que al final es la verdadera valentía) a coger las maletas y cruzarse el mundo. Y por su proactividad. A mi madre, por todo su apoyo, su preocupación por mi, su ánimo, por ayudarme de infinitas maneras que voy descubriendo con el tiempo... y por último, a mi padre. Gracias por todo lo que me has dado, por ser un ejemplo de valores. Por ser una referencia. Siento que no estés aquí para verlo, pero esto es por ti.

Chapter 1

Introduction

1.1 There was plenty of room at the bottom

It seems unavoidable to start the introduction of any thesis exploring processes and phenomena at the nanoscale by quoting Feynman's memorable lecture at the 1959 Annual Meeting of the American Physical Society [1], to the point where it is actually discouraged by some journals in the name of variety [2].

The allure of Feynman's charm trascends the high walls of the ivory tower of Academia, and with his lectures and recordings at the BBC available online, his figure promises to stand the test of time and remain a cultural icon.

But what about "There is plenty of room"? Almost six decades have passed since the famous lecture, and it now reads as a recollection of milestones of the different branches of nanoscience: From methods for the preparation of nanostructures based on the use of masks [3], to direct ion milling of the surface [4], to the preparation of masks on the surface by electron beam lithography using electron sensitive resists [5]; from the call for better electronic microscopes [6] to the miniaturization of computers [7]; from the idea of mechanically arranging individual atoms [8] to the proposal of creating artificial molecules... [9, 10] The list is long, but all the checkbox have been ticked, save for the Fantastic Voyage-like cell-sized nano-surgeon, although the development of artificial molecular machines remains a very active field of research [11].

Combined with the eventual demise of Moore's law, another staple of introductions in nanoscience publications, the time is approaching where the room at the bottom is not so plentiful and scientific and technological advances have to look into new directions, as continued reduction in scale becomes no longer feasible.

Feynman proposed a $1000 prize for anyone would could store the infor-

mation on a page of a book at 1/25000 the scale, in such a way that it could be read by an electron microscope. It seems appropriate that the ultimate fulfilment of this request, using a single atom vacancy to represent a bit of information, has been realized by storing his own words at the 1959 conference [12]... although he could refuse the prize on the basis that it lies beyond the resolution capabilities of an electron microscope.

At this point, although basic research still has plenty of work to do with single atoms and nanostructures consisting in a few atoms, it is reasonable to talk about atomic engineering, where exploring new physics takes a back seat to the development of devices with technological applications. The kilobyte memory is one such example, but there are numerous other of devices built atom-by-atom to produce a prototype with technological applications in sight: Antiferromagnetic bits a few atoms in size [13], spin based logic gates with a single atom readout [14], single atom magnets [15], chemistry at the single atom/molecule level [9, 10], *etc.*

The key tool behind these devices is the scanning tunnel microscope, the development of which can be used to mark the actual birth of nanotechnology in 1981 [16, 17]. If Feynman played the visionary role of Jules Verne, Rohrer, Binnig and Gerber oversaw the Apollo Program at the IBM Zurich Research Laboratory. In what was most definitely a small hop for a Xe atom but a giant leap for science, Eigler demonstrated the capabilities of the STM to perform individual atomic manipulation in 1989, famously writing the letters IBM using 35 Xe atoms on a nickel surface [8]. Two and a half decades later, atomic manipulation has been assimilated as a fundamental part of the technique to the point where only the most spectacular examples are still able to capture the imagination of the general public, such as the awing 2013 stop-motion film "A boy and his atom" [18], where each frame is designed and captured by STM, manipulating CO molecules adsorbed on a copper surface.

1.2 Atomic engineering

Atomically engineered devices are made possible by precise knowledge and control of the interaction of the atom with its environment, and individually positioning the atoms on the surface in order to produce the desired behaviour. Changing the symmetry of the crystal environment of the atom by moving it from say and fcc to an hcp hollow position[19], putting another atom next to it forming a larger structure [13] or even slight changes in the distance between said atoms [14] can all have a very significant effect on the properties and behaviour of individual atoms and structures. In the following paragraphs, a cursory overview of the relevant interactions in these cases is provided.

1.2.1 Exchange interaction

At the scales involved in interactions between atoms, quantum considerations take precedent. In particular, the indistinguishability of particles imposes that the overall wave function describing two particles with spins $S_1 = S_2 = 1/2$ (fermions, half-integer spin) must be antisymmetric with respect to exchange of the particles, *i. e.*, it remains unchanged except for a sign inversion. The consequence of this is that the wave function must consist in the combination of a symmetric orbital part and an antisymmetric spin part (thus $S = S_1 - S_2 = 0$) or vice-versa, an antisymmetric orbital part an a symmetric spin part (and thus, $S = S_1 + S_2 = 1$). The coupling of the two spins can be described by the Heisenberg Hamiltonian

$$H = -J\mathbf{S_1} \cdot \mathbf{S_2} \tag{1.1}$$

where J is the exchange constant and S_1 and S_2 the spin operators, the linear combination of which describes the total spin operator of the system:

$$S^2 = (\mathbf{S_1} + \mathbf{S_2})^2 = S_1^2 + S_2^2 + 2(\mathbf{S_1} \cdot \mathbf{S_2}) \tag{1.2}$$

which results in a singlet state for $S = 0$ and a triplet state for $S = 1$. The ground state is governed by the value of J, which depends on the energies of the spatially symmetric and antisymmetric parts of the function, E_+ and E_- respectively, as:

$$J = \frac{1}{2}(E_+ - E_-) \tag{1.3}$$

Thus for situations where the symmetric spatial function has a lower energy than its antisymmetric counterpart, $J < 0$ and anti-parallel alignment of spins is favoured; in the opposite case, $E_+ > E_-$ results in $J > 0$ and equation 1.1 indicates a parallel alignment os spins. In the case of exchange interaction between spin moments belonging to different atoms, the system becomes a complicated many-body problem, but the same considerations are at play. Thus, the antiferromagnetic or ferromagnetic nature of the system is governed by the Pauli exclusion principle imposed by interatomic-exchange.

1.2.2 Indirect exchange interaction

The situation remains complicated even in the absence of direct overlap of wave functions with unpaired electrons, as indirect coupling mediated by the conduction electrons also leads to long range magnetic order. This indirect

exchange interaction, or RKKY for Rudderman-Kittel-Kasuya-Yosida, plays a large role in the magnetism of rare earths, as there is no overlap between the $4f$ orbitals of neighbouring atoms, but instead the coupling occurs between the $4f$ and the conduction electrons, with the particular characteristic of having a coupling constant, J_{RKKY}, with an oscillatory nature that changes in sign, determined by the Fermi wavevector, k_F, corresponding to a conduction electron at the Fermi level. RKKY is also relevant in diluted magnetic systems, such as magnetic atoms on a non-magnetic surface where ferromagnetic or antiferromagnetic coupling between atoms can be controlled by a suitable separation between atoms.

1.2.3 Magnetocrystalline anisotropy

The local environment in which the atom lies can also have a very strong effect on its behaviour, due to the magnetocrystalline anisotropy. The symmetry of the lattice produces a periodic electric potential, the crystal field, which favours the orientation of the orbitals of valence electrons along crystalline directions, thus, in the presence of the crystal field, the electron orbital angular momentum of an atom on the surface will lock onto these directions.

This anisotropy is carried over to the spin angular momentum of the atom due to the spin-orbit coupling (SOC). In a semi-classical picture, this coupling can be understood as a Zeeman-like energy: the intrinsic angular momentum of the electron (S) is in the presence of the magnetic field due to said electron's orbit around the nucleus with a given orbital angular momentum (L). More formally, the SOC term emerges naturally from the Dirac equation, or as a relativistic correction of the Schrödinger equation.

Thus, the symmetry of the system governs the magnetocrystalline anisotropy. An effective spin Hamiltonian considering only the crystal field contribution can be written as:

$$H_{CF} = D\left(S_z^2 - \frac{1}{3}S^2\right) + E\left(S_x^2 - S_y^2\right) \tag{1.4}$$

where $D = \frac{3}{2}D_{zz}$ and $E = \frac{1}{2}(D_{xx} - D_{yy})$ are constants representing the axial and transversal anisotropy, and D_ij the components of the anisotropy tensor. In a cubic system, D and E vanish as $D_{xx} = D_{yy} = D_{zz}$, resulting in an isotropic behaviour. For an axial system, $D_{xx} = D_{yy}$ resulting in E = 0 and the only contribution to the Hamiltonian is along z. If both terms are present, the axial term splits the energy levels proportional to the spin's projection along z, m_z, while the transverse term mixes the wave functions of the different eigenstates. Thus, for magnetic atoms adsorbed on a surface, the

magnetocrystalline anisotropy provides preferential spatial orientations of the magnetic moment.

1.3 Rare Earth Metals

In the pursuit of improved properties at the atomic limit, the field has recently turned to rare earth metals, lanthanides in particular, in which $4f$ orbital is only partially occupied and thus could present interesting magnetic properties. A characteristic of the $4f$ orbitals, is that despite being energetically the highest orbital it is spatially localized near the core, shielded by the energetically lower but radially more external full $5s$ and $5p$ electronic shells, as illustrated in figure 1.1. The intrinsic high anisotropy and large magnetic moment of the $4f$ shell in rare earth atoms promises a qualitative improvement in atomic magnetic anisotropy energies, while the high localization could provide for very large lifetimes of quantum states.

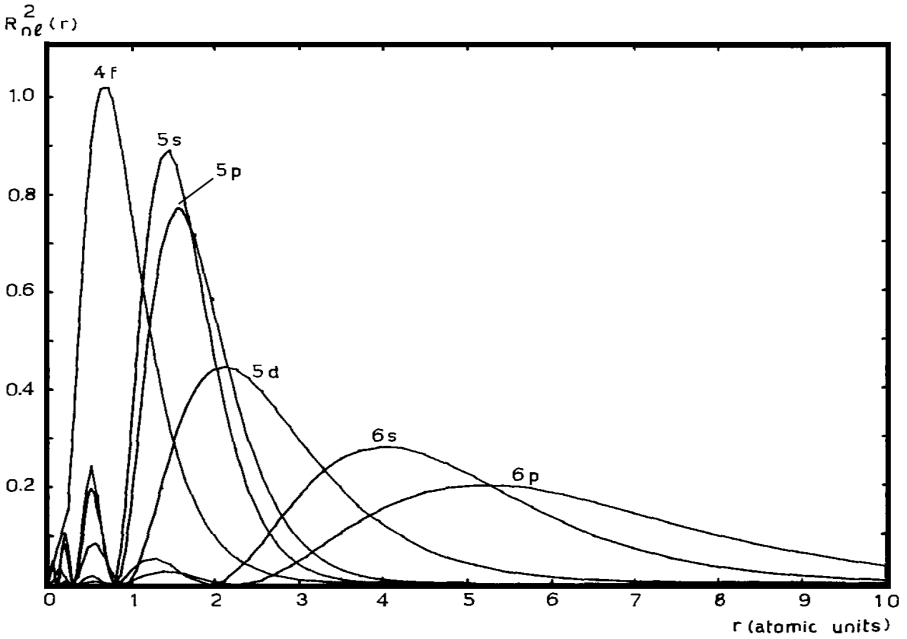

Figure 1.1: The radial components of atomic $4f$, $5s$, $5p$, $5d$, $6s$ and $6p$ wavefunctions for Ce, adapted from reference [20]. The $4f$ electrons in rare earth are thus shielded by the more external $5s$, $5p$ electrons.

Elements in this group tend to present a similar chemical behaviour, as the incomplete $4f$ shell hardly participates in chemical bonding, also due to the screening of the electrons in more external orbitals. As a consequence,

SOC plays a larger role than the crystal field in determining the magnetic properties of rare earth atoms, and even in intermetallic compounds the $4f$ levels consist in a large number of localized states. This multiplet structure of rare earth ions is well accounted for by the Russell-Saunders coupling scheme, the spin momenta s_i of the individual $4f$ electrons are coupled by the exchange interaction giving a total spin S for the incompletely filled shell, while the orbital momenta l_i combine into the total orbital momentum L due to Coulomb interaction. Applying Hund's rules leads to the ground state of the system, which from the third rule results in a state with J = |L-S| for light rare earth ($4f$ shell less than half full) and J = L + S for heavy rare earths (more than half full). The effect of crystal field can then be added as a perturbation to this state.

1.3.1 RE-TM exchange interaction

The combination of rare earths (RE) and d transition metals (TM) leads to the formation of stable intermetallic compounds, provided the latter do not belong to the first few members of the transition metal series. The bulk RE-TM alloys have been thoroughly studied in the past [21]. In the case of $3d$-type transition metals, the stable RE-TM compounds have been observed only for TM = Mn, Fe, Co or Ni. The unpaired $3d$ electrons of the transition metal component give rise to a magnetic moment in most cases. Therefore, the magnetic interactions in RE-TM compounds comprise three different types: the RE-RE interaction, the RE-TM interaction and the TM-TM interaction. The RE-RE interaction is the weakest of the three, although in rare earth compounds the RKKY coupling between the localized $4f$ moments can lead to diverse magnetic configurations, ranging from a simple ferromagnetic order to more complex situations such a sinusoidally modulated antiferromagnetic coupling between layers.

In the RE-TM interaction, the $5d$ electrons of the RE elements play an important role [22]. Through ordinary $4f$-$5d$ exchange the localized $4f$ spins produce a positive local $5d$ spin polarization. The $4f$-$3d$ coupling then arises indirectly via the interaction with the symmetry-compatible $3d^n$ electrons of the transition metal, *i.e.*, a $3d$-$5d$ interaction. Exchange between these two sets of d states is invariably antiferromagnetic with respect to the d electrons involved; the mechanism is analogous to the electron hopping mechanisms in superexchange. Because the $4f$-$5d$ exchange at the RE site is ferromagnetic, the antiferromagnetic $5d$-$3d$ interaction explains the ferromagnetic coupling of light RE to TM moments and vice versa for heavy RE species. The net result of RE-TM exchange coupling is generally larger magnetic moments for intermetallics of light RE and TM

As concerns to the exchange interactions between RE adatoms and TM surfaces, the approach in terms of electron energy bands, as in the bulk systems case, is no longer valid. In addition to their energy shifts, the adatom levels begin to broaden and, therefore, the charge transfer may be a fraction of an electron. The exact determination of the charge transfer is very difficult, since it involves the treatment of electronic interactions. This is a many-body problem for which only very approximate solutions exist.

As a first approximation, the case of adatoms on ferromagnetic metallic surfaces can be treated in a similar way as that of a single impurity atom in a ferromagnetic host. If the impurity is a much lighter 3d element than the host, like V in Ni, its d levels lie above the Fermi level in the $4s$ conduction band and acquire a width which may be $\sim$1 eV. The impurity level is then known as a virtual bound state. [23, 24] If the impurity potential is sufficiently repulsive to move also the majority-spin virtual bound state above the Fermi level, E_F, the $3d$ impurity majority electrons are emptied into the $3d$ minority-band of the host. If the host $3d$ majority-band is full, there will be a moment reduction of the impurity, in Bohr magnetons, equal to its number of $3d$ majority electrons. Additionally, the moment of one host atom is suppressed at the site of the substitution. There will unavoidably be some hybridization of the impurity and host $3d$ states, more effective for the host $3d$ minority electrons, because they lie closer to E_F. A light $3d$ impurity will then acquire a small negative moment in a heavy $3d$ host.

This is a case of the more general rule that exchange coupling between atoms with d shells that are more than half full with atoms whose d shell is less than half full is antiferromagnetic. The RE in this context should be considered as light d elements since their atomic configuration is $4f^n5d^16s^2$. There is therefore antiparallel coupling of the spin moments of the ferromagnetic 3d elements TM = Fe, Co and Ni, and the spin moment of a RE. When the $4f$ shell is half-filled, or more, this leads to antiparallel coupling of the atomic moments in RE–TM alloys with R = Gd–Yb. However, in light RE metals where the moment is mainly orbital in character, and directed opposite to the spin moment according to Hund's third rule, the RE and TM moments are parallel, although the spins are antiparallel.

1.3.2 Thulium

Most of the efforts in this thesis are devoted to the study of Thulium, Tm. At atomic number 69, Tm lies near the end of the Lanthanide group, only followed by Ytterbium (Yb) and Lutetium (Lu) with a full $4f$ shell. Tm typically presents a +3 oxidation state in solids, going from a $4f^{13}6s^2$ configuration as

a free atom to $4f^{12}(5d6s)^3$ in solids [25]. A heavy rare earth, Tm presents a $^3H_6$ ground state which leads to a large magnetic moment of 7.14 μ_B per atom in saturation [26, 27].

At room temperature Tm forms an hexagonal closed-packed (hcp) lattice with a lattice parameter in the basal plane a_{Tm} = 3.5375 Å and with c_{Tm} = 5.5546 Å between planes [25]. The magnetic behaviour of Tm represents an interesting case, since it is the only heavy RE which orders magnetically along the c axis of the bulk hcp crystal structure. Between the Néel temperature, T_N = 58 K, and 40 K, the magnetic moments are ferromagnetically ordered within the hcp basal-plane layers and have an incommensurate sinusoidal modulation along the c axis. The easy axis is parallel to the c axis, owing to strong crystal-field anisotropy. Upon decreasing the temperature, the propagation wave number along the c axis increases and, below $\sim$ 30 K, a ferrimagnetic structure with a seven-layer repeat distance develops: the magnetic moments point up along the c axis in three layers and down in the consecutive four layers [28, 29].

1.4 Structure of this Thesis

The main objective of this thesis is the study of the magnetic properties of rare earth atoms and nanostructures, in particular thulium. Chapters 2 and 3 dwell on the preparation and characterization of the Tm monolayer, while the study of Tm atoms on different substrates is present in chapters 3, 4 and 6. Spin polarized experiments are performed in chapter 3 to complement XAS/XMCD results, but it is in chapters 5 and 6 where SP-STM is used as the main tool to probe magnetic properties. A more detailed outline follows:

Chapter 2 introduces the technique of Scanning Tunnelling Microscopy (STM) and presents a theoretical description of the tunnelling process and the information that can be obtained from this kind of experiments. The different modes of operation for topography and spectroscopy are discussed, as well as the use of magnetic coated tips for spin polarized measurements. A brief overview of the main microscope used during the course of this thesis is also provided, followed by a description of the preparation process of the typical tips and samples used in this work.

Chapter 3 is dedicated to the growth of the Tm monolayer on a W(110) surface by studying *in situ* the diffusion process at high temperature. A strong correlation between Tm island size and the presence of carbon impurities on the surface is observed, thus obtaining a method for bottom-up preparation of nanometric Tm islands.

Chapter 4 expands the study of the Tm monolayer on W(110) to include the characterization of its electronic and magnetic properties. X-ray absorption (XAS) and dichroism (XMCD) experiments are compared to STM and SP-STM measurements, leading to the discussion of the magnetic configuration of the Tm monolayer and the polarization of the electrons involved in the tunnelling current. A similar experimental approach and analysis is performed for individual Tm atoms on the W(110) surface. The XAS and XMCD experiments and analysis are part of a work published in collaboration with P. Gambardella and his group [30].

Chapter 5 continues exploring the question raised in the previous chapter, regarding the possibility of exciting $4f$ states in individual rare earth atoms by inelastic tunnelling. Thulium and Lutetium adatoms are studied on a metallic substrate and on an insulating layer, exploring their spectroscopic behaviour at different energies and discussing the effect of the crystalline environment.

Chapter 6 leaves rare earth atom aside for a few pages to focus on a spin-polarized study of ferromagnetic monolayer iron islands grown on W(110). A standing wave emerging from the interference of the surface state is observed only in islands with a particular magnetic orientation respect to the tip, while a weaker pattern is present in both cases. The interference patterns are studied as a function of tip polarization, island size, and energy. The dispersion relation is obtained, allowing the identification of the feature, a surface resonance in minority electrons. The anisotropic distribution of the interference pattern, observed also on the W(110) is discussed in the context of an interaction between the Fe and W layers.

Chapter 7 returns the spotlight onto rare earth atoms, in this case a spin polarized study of Tm and Lu atoms on the ferromagnetic Fe monolayer islands presented in the previous chapter. The magnetic coupling between the Fe islands and Tm, with an incomplete $4f$ orbital, and Lu, with 14 electrons in the $4f$ orbital and thus non magnetic, is studied finding a very similar antiferromagnetic coupling. These results are complemented by first principles calculations, where the contribution of the different orbitals to the tunnelling current can be determined. These results and analysis can be found in reference [31].

A final **Summary and Conclusions** of the main experimental results obtained during this thesis is presented at the end.

Chapter 2

Materials & Methods

The purpose of this chapter is to introduce the experimental techniques relevant to this thesis. A detailed description of the Scanning Tunnelling Microscopy (STM) and its associated techniques will be provided, including a description of the actual experimental setup, as STM is the defining tool of this work.

A section of this chapter will be devoted to the tools required and preparation procedure of samples, both clean surfaces and material deposition, and STM tips with different characteristics.

2.1 Scanning Tunnel Microscopy

The theory behind the tunnel effect dates back to the 1920's [32–34] as a natural consequence of the development of Quantum Mechanics. The first experimental observation of quantum tunnelling of electrons dates corresponds to Esaki in 1958 an the introduction of the tunnel diode, where an anomalous behaviour observed in a heavily doped p-n junction is attributed to electrons tunnelling across the barrier [35]. Metal-insulator-metal junctions followed in the early 1960's [36–39], it would however take two decades until the STM saw the light of day, in 1981, at the IBM Zurich Research Laboratory [16, 17, 40]; five years later, the development of the STM led to a Nobel prize for Gerd Binning and Heinrich Rohrer, shared with Ernst Ruska for his role in the development of the electron microscope. The STM is lenseless microscope, able to bypass the diffraction limits imposed by the finite numerical aperture and wavelength, where the image is reconstructed by measuring a pointwise matrix of the interaction between the sample and a probe; their candidate for the probe consisted in a very sharp wire, which would, when brought close enough to a metallic surface, conduct via quantum tunnelling. By moving this probe

along the surface, the variation of the tunnel current provides information of the surface.

The development of the STM paved the way for a whole family of microscopies not based on lenses but on point-wise interaction with a probe, with the appropriate name of *Scanning Probe Microscopies*. The first to join the family, the Atomic Force Microscope, also developed by Binnig [41], extended the capabilities of the STM to insulating surfaces, by measuring electrostatic interatomic forces. In the following years and decades, many interactions susceptible of being measured locally have been incorporated into the SPM family, leading to a large array of tools for surface characterization [42].

Current STM systems allow for a wide range of configurations, giving rise to a broad spectrum of applications. Defining the state of the art in the field is not straight forward, as it depends strongly on the application. One of the usual strongholds of STM is single atom manipulation and spectroscopy, where ultra high vacuum and very low temperatures are required; UHV in the 10^{-11} mbar range is a standard feature for any system where UHV is required, low temperature however is usually a compromise between cost, usability and final temperature, and depending on the method the final temperature is around 4.5 K (liquid He cryostat), 1 K (low pressure liquid He) or 300 mK (low pressure liquid He^3), with temperatures down to 15 mK being possible with the use of a He^3-He^4 dilution refrigerator; even lower temperatures, around 10 mK, have been proposed using cryo-free methods. On the opposite side of the spectrum, high pressure and high temperature systems are used for catalysis studies by using a flow reactor and containing the sample in a sealed pressurized cell, reaching pressures up to 6 bar and temperatures in the 1000 K range [43]. Magnetic field up to 15 T perpendicular to the sample plane, or a full 3D vector field 9 T / 2 T / 2 T are also available in commercial systems. Low temperatures improve the spectroscopic capabilities of the STM, as the energy resolution is always going to be limited by thermal broadening; at 10 mK energy resolutions of the order of 10 μV have been obtained [44]. Time resolution is not one of the traditional strong points of STM, as data acquisition usually is done over seconds or minutes, however by use of electronic pump-probe techniques spin dynamics in the nanosecond regime have been studied in the last years [45], with the picosecond scale being pursued by optical terahertz pumping [46]. A recent promising development in the field is the use electron paramagnetic resonance (EPR) in an STM setup, allowing for greatly increased energy resolution [47].

2.1.1 The Tunnel Effect

In classical mechanics, a particle with energy E presented with a potential barrier of height V_0 and width s will only be able to overcame said potential if $E > V_0$, otherwise the particle will be reflected. This holds well into microscopic dimensions, where systems trapped in a local minima can provide interesting physics and applications (*e.g.* carbon impurities in iron impeding the movement of dislocations, granting steel its mechanical properties); when the dimensions and energies involved are further reduced, quantum phenomena come into play and a classical description is not enough. From a quantum approach, the considered particle of energy E has a finite probability of traversing the potential barrier even if $E < V_0$, as shown below in what has become a staple problem in introductory courses to Quantum Mechanics [32, 48].

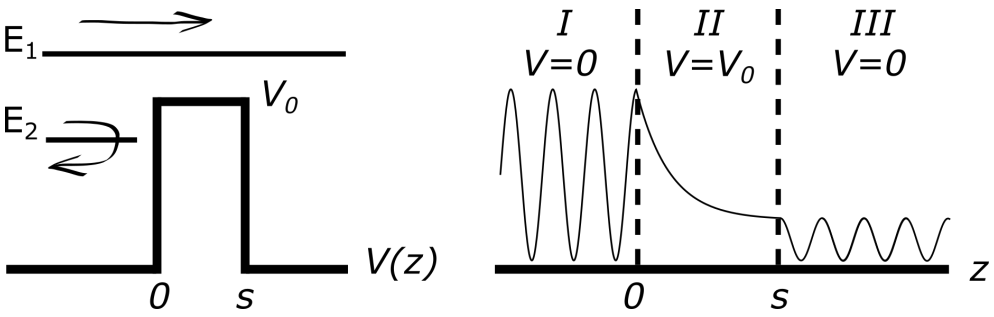

Figure 2.1: One-dimensional potential barrier problem from the point of view of Classic Mechanics (left) and Quantum Mechanics (right).

Figure 2.1 illustrates the two situations, on the left the classical approach where the particle will either overcome the barrier (E_1) or be reflected (E_2), given that $E_1 > V_0 > E_2$. Meanwhile, the situation presented on the right illustrates the phenomenon of quantum tunnelling, which requires a more detailed analysis. The problem can be divided into three regions of constant potential, noted *I*, *II* and *III* in fig. 2.1:

$$\begin{array}{lll} \textbf{Region I:} & z < 0 & V(z) = 0 \\ \textbf{Region II:} & 0 < z < s & V(z) = V_0 \\ \textbf{Region III:} & s < z & V(z) = 0 \end{array} \tag{2.1}$$

A particle of mass m and energy E can be described by its wave function, $\psi(z)$, which is a solution of the time independent Schröndinger equation:

$$\Big(-\frac{\hbar^2}{2m}\frac{d^2}{dz^2} + V(z)\Big)\psi(z) = E\psi(z) \tag{2.2}$$

where $\hbar$ is Plank's constant divided by 2π. In regions I and III, before and after the barrier, the potential is $V(z) = 0$ and the solution is that of a free particle:

$$\begin{aligned} &\textbf{Region I:} \quad z < 0 \qquad \psi_I(z) = A_1 e^{ik_a z} + A_2 e^{-ik_a z} \\ &\textbf{Region III:} \quad s < z \qquad \psi_{III}(z) = C_1 e^{ik_c z} + C_2 e^{-ik_c z} \end{aligned} \tag{2.3}$$

with $k_a = k_c = k = \sqrt{\frac{2mE}{\hbar}}$ and $A_i,\ C_i$ are arbitrary constants. In region II, where $V(z) = V_0$, the solution becomes:

$$\textbf{Region II:} \quad 0 \leq z \leq s \qquad \psi_{II}(z) = B_1 e^{ik_b z} + B_2 e^{-ik_b z} \tag{2.4}$$

where now $k_b = \sqrt{\frac{2m(E-V_0)}{\hbar}}$ gives a complex value for k, as $E < V_0$, which in the exponents $\pm\, ik_b z$ becoming real, and the solution describes waves which exponentially decay within the barrier.

The constants $A_1,\ A_2,\ B_1,\ B_2,\ C_1$ and C_2, are set by the boundary conditions. In region I, the solution is a linear combination of a wave travelling to the right and a wave, reflected at $z = 0$ by the potential barrier, travelling to the left; in contrast, in region III only a wave travelling to the right makes physical sense, as no reflection can occur, which implies $C_2 = 0$. The rest of constants can then be determined by matching the partial solutions for each region, $\psi_i(z)$, and their first derivative, $\frac{d\psi_i(z)}{dz}$, to satisfy the continuity and smoothness of the solution along z.

$$\begin{aligned} \text{at } z \ &= \ 0 \ \begin{cases} A_1 + A_2 = B_1 + B_2 \\ ik(A_1 - A_2) = ik_b(B_1 - B_2) \end{cases} \\ \text{similarly, at } z \ &= \ s \ \begin{cases} B_1 + B_2 = C_1 \\ ik_b(B_1 - B_2) = ikC_1 \end{cases} \end{aligned} \tag{2.5}$$

After some algebra [49] it can be concluded that the transmission coefficient T, defined as the ratio of the transmitted and incident probability flux, j_T and j_0 respectively, obtained from the square of the amplitude of the transmitted wave functions, results in:

$$T = \frac{j_T}{j_0} = \left[1 + \frac{(k^2 + k_b^2)^2}{4k^2 k_b^2 sinh^2(k_b s)}\right]^{-1} \tag{2.6}$$

which in the limit of $k_b s \gg 1$, a strongly attenuating barrier, can be approximated by:

$$T \simeq \left(\frac{16k^2k_b^2}{k^2+k_b^2}\right)e^{-2k_b s} \tag{2.7}$$

that is, in the regime of low transmission, T decreases exponentially with the square root of the effective potential V_0 (as $k_b = \sqrt{\frac{2m(E-V_0)}{\hbar}}$) and with the width of barrier, s. The situation $T \ll 1$ is precisely the regime of operation of the scanning tunnel microscope, and this exponential dependence is the key to the high z-resolution of this technique.

From this model some of the basic features of STM can be derived, as sample and tip, scanning a few Å from the surface, form a metal-insulator-metal system (assuming metallic tip and sample), where the tunnelling current I_t is due to the electrons that tunnel through. In this system, the width of the barrier, s, corresponds to the vacuum gap between tip and sample while the height of the potential barrier, V_0, is given by the work functions, ϕ_t and ϕ_s, of tip and sample. Although it is a parameter that depends on the material (*e.g.* $\phi_{Fe(110)} = 5.12$ eV [50], $\phi_{W(110)} = 5.47$ eV [51]), for simplicity it will be assumed that $\phi_t = \phi_s = \phi$ for this analysis.

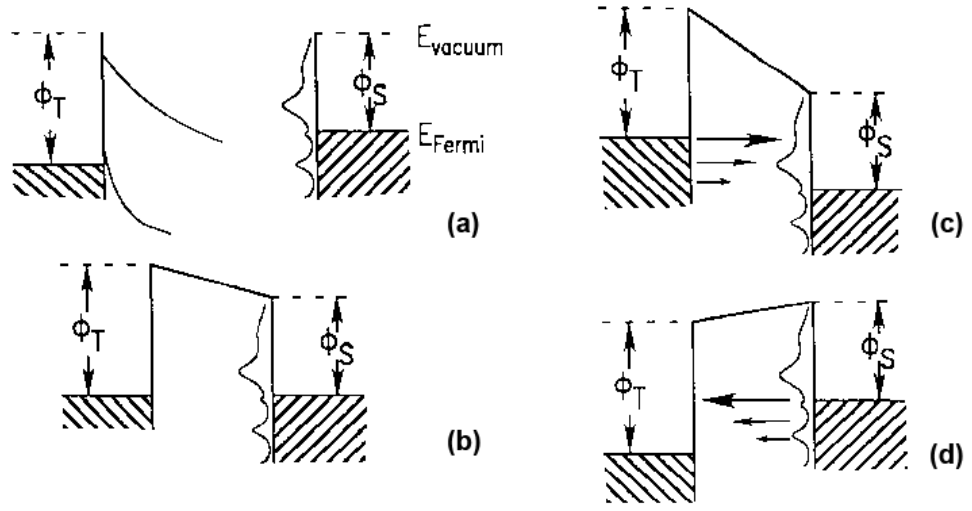

Figure 2.2: Energy level diagrams for sample and tip, as illustrated by Hamers[52]. (a) Independent sample and tip. (b) Sample and tip at equilibrium, separated by a small vacuum gap. (c) Positive sample bias: Electrons tunnel from tip to sample. (d) Negative sample bias: Electrons tunnel from sample into tip.

By applying a small bias, V_{bias}, between tip and sample the Fermi levels of the electrodes will adjust to said bias and a tunnelling current will flow between them as seen in Figure 2.2 [52]. The usual convention is that at positive sample bias electrons tunnel from occupied tip states to unoccupied

sample states, while occupied sample states tunnel to unoccupied tip states for negative bias.

Assuming a bias voltage much smaller than the work function, $eV_{bias} \ll \phi$, it can be considered that the energy of all the tunnelling electrons is approximately equal to the Fermi energy, E_F. In this limit, the wave function of an electron in the vacuum barrier can be written as:

$$\psi(z) = \psi(0)e^{-kz} \quad with \quad k = \sqrt{\frac{2m\phi}{\hbar^2}} \tag{2.8}$$

and therefore, the probability of finding an electron from the sample at the tip, on the other side of the potential barrier, is:

$$w = |\psi(z = s)|^2 = |\psi(0)|^2 e^{-2ks} \tag{2.9}$$

The tunnelling current is then the sum of all electron states available within the tunnelling energy window, given by the bias voltage, eV_0:

$$I(z = s, V_0) \propto e^{-2ks} \sum_{E_\mu = E_F - eV_0}^{E_F} |\psi_\mu(0)|^2 \tag{2.10}$$

where μ denotes occupied states of the sample. Extending this sum to a continuous number of states, equation 2.10 now becomes an integral:

$$I(z = s, V_0) \propto e^{-2ks} \int_{E_F - eV_0}^{E_F} \sum_{\mu} \delta(E_\mu - E)|\psi(0)|^2 dE \tag{2.11}$$

which can be better expressed as a function of the Local Density of States (LDOS), *n(s, E)*, defined as the number of electrons of a given energy at a given position:

$$\sum_{\mu} \delta(E_\mu - E)|\psi_\mu(0)|^2 \equiv n(z = 0, E) \tag{2.12}$$

which leads to an expression of the tunnelling current for a 1D system as:

$$I(z = s, V_0) \propto e^{-2ks} n(z = 0, E_F) eV_0 \tag{2.13}$$

Which reproduces the main characteristics of STM: an exponential dependence of the tunnelling current with the tip-sample distance and a dependence on the

LDOS, n, rather than directly with topographic features. Instead of being a setback, this apparent complication of the interpretation of the data actually provides STM with spectroscopic capabilities that will be explored in greater detail further along this chapter.

Bardeen's many-particle description of planar juntions

Up to this point, a very simplified model has been considered and the shortcomings are starting to show - the concept of "local" density of states, *n(s, E)*, is not really necessary in a 1D system, however it is an important consideration in a real STM setup, with a finite three dimensional tip, and a extensive two dimensional sample surface.

The first theoretical development towards a 3D description of tunnel junction predates the invention of the STM by two decades, exploring the problem of two planar metallic electrodes separated by a thin oxide layer [53]. In this 1961 paper, Bardeen discusses tunnelling from a many-particle point of view by applying a time dependent perturbation theory leading a tunnelling current give by:

$$I = \frac{2\pi e}{\hbar} \sum_{\mu,\nu} f(E_\mu)[1 - f(E_\nu + eV)]|M_{\mu\nu}|^2 \delta(E_\mu - E_\nu) \tag{2.14}$$

where $f_i(\epsilon)$ is the temperature dependent Fermi function for the two electrodes, noted μ and ν. M is a transition probability matrix, whose elements are given by:

$$M_{\mu\nu} = \frac{\hbar^2}{2m} \int d\vec{S} \left(\psi_\mu^* \vec{\nabla} \psi_\nu - \psi_\nu \vec{\nabla} \psi_\mu^*\right) \tag{2.15}$$

In this model the tunnelling current is then the result of electrons transferred indistinctly from the sample into empty states of the tip and vice-versa, electrons from the tip into empty states of the sample, as the two electrodes are equivalent in this analysis. In the limit of small voltage and temperature, it can be expressed as:

$$I_t = \frac{2\pi}{\hbar} e^2 V \sum_{\mu,\nu} |M_{\mu\nu}|^2 \delta(E_\nu - E_F)\delta(E_\mu - E_F) \tag{2.16}$$

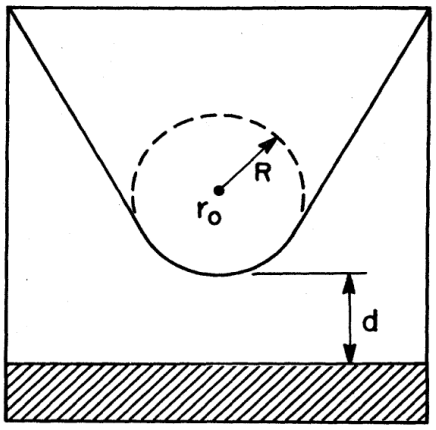

Figure 2.3: Schematic picture of tunnelling geometry, after Tersoff and Hamann [54, 55]. The tip can have an arbitrary shape but is assumed locally spherical at the apex, with a radius of curvature R centred at $\vec{r_0}$. The distance of nearest approach between tip sample surface (shaded) is noted as d.

Modelling an STM tip: Tersoff-Hamman

After the development of the STM in 1981 it was clear that a more detailed framework was required, taking into account the physicial constraints of the system. In 1985 Tersoff and Hamann [54, 55] proposed a model for a sharp tip of arbitrary shape, as only the very end of the tip would be involved in the tunnelling process. The simplest case for the potential at the apex is considered, modeled as a spherical s-like orbital with a radius of curvature R centred at $\vec{r}_0$, as shown in figure 2.3, with a distance d between tip and sample. The matrix element in 2.15 reduces to:

$$M_{ts} = -\frac{2\pi C\hbar^2}{km_e}\psi(\vec{r}) \tag{2.17}$$

where t and s denote the two electrodes, tip and sample, C is a constant, m_e is the mass of a free electron and k is given by the decay of the wave function in the tunnelling barrier, as in the situation described in eq. 2.4.

With these considerations and in the range of low transmission ($T \to 0$) and low bias ($eV_{bias} \leq \phi$), the tunnelling current in 2.16 can then be written as:

$$I_t = \frac{16\pi^3 C^2\hbar^3 e}{k^2 m_e^2} n_t \int_0^{eV_0} n_s(\vec{r}, E)dE \quad \propto \quad e^{-2ks} \tag{2.18}$$

While the Tersoff-Hamann model describes remarkably well the behaviour of the tunnelling current and is widely used in theoretical descriptions, some further tweaks are required in certain cases. The approximation of the potential at the apex as an s orbital is not always valid, and tips with different orbitals have been used to great success by picking up molecules, such as CO, where the tunnelling occurs through other orbitals (p orbitals, in the case of CO), increasing the resolution [56]. Different orbitals also decay at different rates across the vacuum gap, which can introduce further complexity in the *I(z)* dependence [57].

2.1.2 Topography

The expression for the tunnelling current obtained from the Tersoff-Hamman model (eq. 2.18) indicates that I_t is determined only by sample properties, and by regulating the tip-sample distance, d, to maintain a constant current, a contour map of LDOS can be obtained. In the simplest case, this contour follows closely the topography of the surface and sub-Å features can be observed. This is not, however, necessarily the case in a real situation where local variations of the electronic structure (due to the presence of lattice defects, adsorbates, changes in chemical species and therefore changes of the work function, etc...) can cause a variation of the LDOS that can be misinterpreted as a topographical feature of the sample.

Maintaining a constant tunnelling current requires a feedback loop sensitive enough to respond to changes in I_t in the sub-pA range and precise enough to respond by adjusting the tip-sample distance d in the sub-Å scale. This is realized by an electronic feedback loop and piezoelectric actuators, as illustrated in figure 2.4 for a typical configuration. The tunnelling current is fed to a high-gain, low-noise pre-amplifier after which a current-to-voltage converter feeds this signal to the control unit, which uses a PID feedback loop to maintain the current set-point by regulating the z position of the tip by applying a voltage on a piezoelectric actuator. These piezoelectric elements are used both for scanning (x,y) and for approaching/distancing the tip to the sample (z). Piezoelectric materials are ceramics that produce an electric charge gradient in response to an applied stress and, conversely, exhibit a change in lateral dimensions under the effect of an electric field. A typical piezo tube in an STM system can have a response of 1-10 nm/V at low temperatures (4 K), with a full range of 0.5-5 μm, although different designs might push these values into either extreme, pursuing stability by reducing the range, or range by sacrificing precision.

By recording the changes in $\Delta z(x,y)$ required to maintain a constant cur-

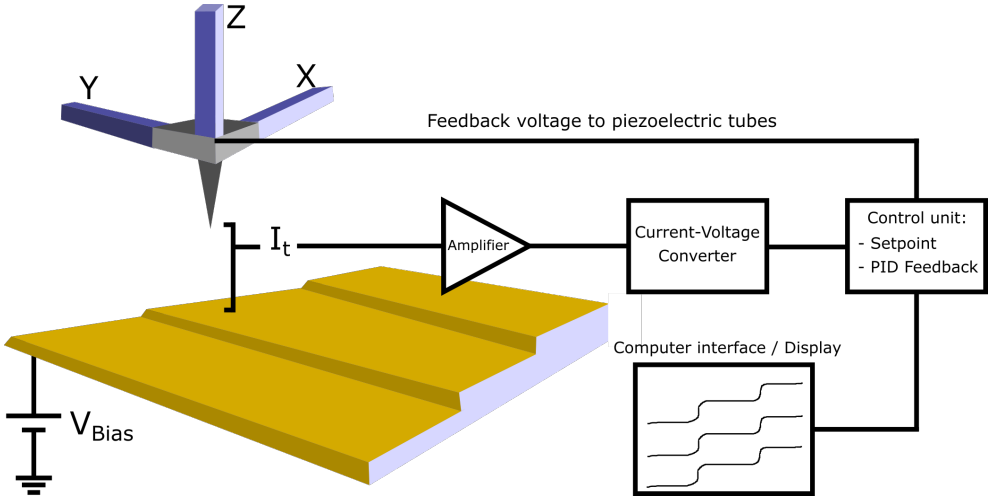

Figure 2.4: Schematic representation of an STM scanning over a sample. The tunnelling current between sample and tip is amplified and used in a feedback loop to regulate the tip-sample distance via piezoelectric actuators in order to maintain the current constant at the desired setpoint. The current and (x, y, z) position of the tip are recorded and displayed.

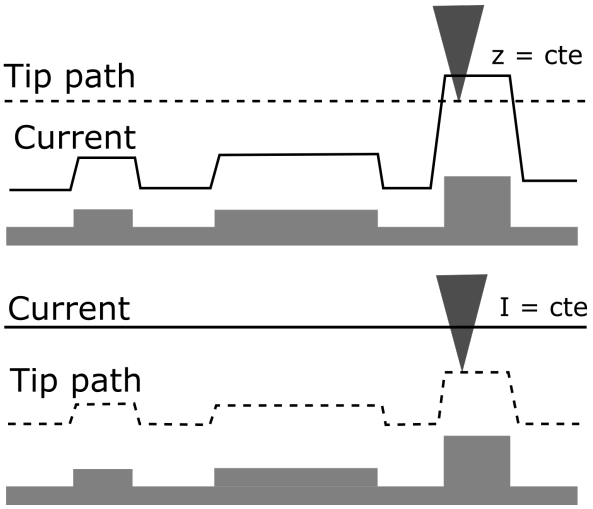

Figure 2.5: Diagram of constant height (top) and constant current (bottom) modes of STM operation.

rent I_t at a given voltage V_{bias}, a 2D map is obtained. This represents the integrated LDOS of the sample within the energy window $E_F < E < E_F + eV_{bias}$. Another mode of operation consists in scanning parallel to the surface, disregarding the feedback loop, and capturing $I_t(x, y)$ at constant z, in what

is usually called constant height mode. This method can prove useful in relatively flat samples where non-topographical effects have a strong influence on the LDOS, obscuring the interpretation of *z(x, y)*, as the tip-sample distance *d(x,y)* is not kept constant. These two modes are illustrated in figure 2.5.

2.1.3 Spectroscopy

Relaxing the requirement of $eV_0 \ll \phi$ in eq. 2.16 to just $eV_0 < \phi$ a solution to equation 2.16 can be found using the Wentzel-Kramers-Brillouin method, arriving to an expression for the tunnelling current [52]:

$$I_t(eV, r) = \int_0^{eV} n_s(r, E) n_t(r, E, eV_0) T(E, eV, r) dE \tag{2.19}$$

where n_s and n_t are the LDOS of sample and tip, respectively, and T is a transmission factor given by:

$$T(E, eV, r) = exp\left[-2d\frac{\sqrt{m}}{\hbar}\sqrt{\phi_t + (\phi_s + eV - 2E)}\right] \tag{2.20}$$

Assuming that the LDOS of the tip can be considered constant, $n_t(\epsilon) = n_t(0)$, differentiating eq. 2.19 respect to V results in:

$$\begin{aligned}\frac{dI(V)}{dV} = \; & n_s(r, eV) n_t(r, 0) T(eV, eV, r) + \\ & + \int_0^{eV} n_s(E, r) n_t(E, eV, r) \frac{dT(E, eV, r)}{dV} dE\end{aligned} \tag{2.21}$$

Assuming a smooth and monotonic increase of T with V [58], the second term contributes as a background and is often neglected; the most relevant information resides in the first term, which includes the bias dependence of the LDOS of the sample, $n_s(eV)$. The differential conductivity, dI/dV thus probes the LDOS of the sample at a given energy eV, in contrast with the tunnelling current I_t, which probes all the available LDOS from E_F to $E_F + eV$.

The differential conductivity dI/dV can be obtained by numerically differentiating $I(V)$ curves, which can be acquired by stopping the tip at a given position, disengaging the feedback loop to keep d constant and recording $I_t(V)$ while performing a V_{bias} sweep over the energy range under study. This method is, however, prone to noise issues, particularly at low bias where the current I_t

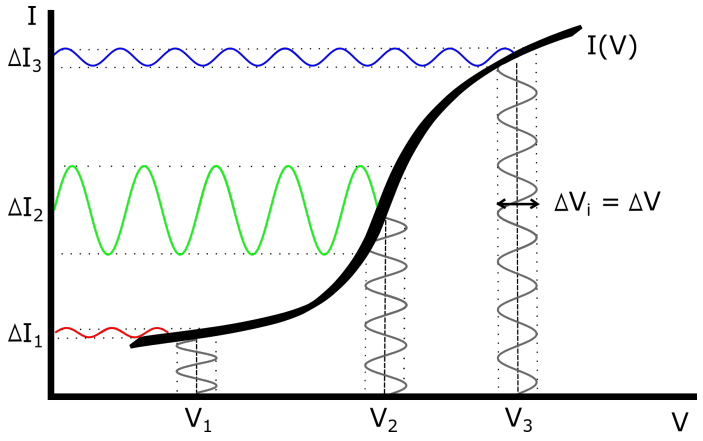

Figure 2.6: Diagram representing dI/dV acquisition by means of lock-in amplification. A ΔV modulation at different bias, V_1, V_2 and V_3 produces a current modulation ΔI_i proportional to the slope of the $I(V_i)$ curve at that energy.

will tend to zero. This problem can be avoided by using a lock-in technique to obtain dI/dV: a small sinusoidal signal (of amplitude V_{mod} and frecuency ν_{ref}) is added to the DC V_{bias} voltage which produces a periodic response (at ν_{ref}) of the tunnelling current I_t proportional to the slope of the $I_t(V)$ curve, as illustrated in figure 2.6. For small V_{mod} this is proportional to dI/dV and a factor depending on the phase between the modulation and the current response, which can be controlled to maximize the signal. This type of detection drastically improves the signal-to-noise ratio, as only the contribution of the signal responding at ν_{ref} is amplified.

Bias sweeps with a static tip provide a $\frac{dI(V)}{dV}$ signal that is related to the LDOS at the local position of the tip over the studied energy range, however the lock-in technique enables another approach to spectroscopy in STM by recording spatially resolved $\frac{dI(x,y)}{dV}$ maps at a fixed energy (eV_{bias}) by scanning over the area of interest with both the lock-in modulation and the feedback loop engaged, simultaneously recording $\Delta z(x,y)$ and $\frac{dI(x,y)}{dV}$, which allows for a correlation of variations of the LDOS at a given energy with topographic features. This situation is illustrated by figure 2.7, a study of pentacene molecules in which the molecular energy levels are found by point spectroscopy over a $\pm$3 V range and are then spatially resolved by dI/dV mapping at constant energy (from Soe *et al.* [59]).

Under certain circumstances, as mentioned for topography studies at constant current or constant height, it might be of interest to perform this kind of maps at a constant z by disengaging the feedback loop to ensure that the spectroscopic data is acquired at a constant tip-sample distance.

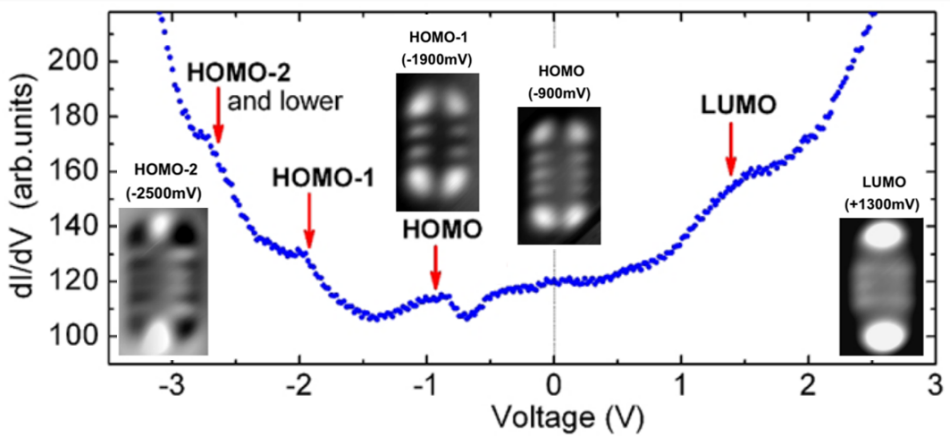

Figure 2.7: Illustration of the different information provided by energy-resolved dI/dV point-spectra and spatially-resolved dI/dV maps at a fixed energy. The energy-resolved spectra shows the energy of the successive occupied (HOMO) and unoccupied (LUMO) molecular energy levels, which can then be resolved by the spatially-resolved maps shown as insets. From Soe et al. [59]

2.1.4 Spin polarized STM

Up to this point the tunnelling problem has been considered for metallic electrodes, but the effect of different magnetic behaviours of said electrodes, ferromagnetism in particular, has not yet been explored. As in the non-magnetic case, the initial analysis for planar junctions predates the development of the STM technique. In 1975 Julliere reported [60] a dependence of the tunnelling conductance, G, between two ferromagnetic electrodes on the relative magnetic orientation between the two. A theoretical description of the problem was provided by Slonczewski in 1989 [61] by considering different density of states for spin-up and spin-down electrons (with up and down referring to parallel and antiparallel to the magnetization $\vec{M}$ of the sample, also called majority and minority electrons) for each of the electrodes, obtaining an expression for the conductance as:

$$G = G_0(1 + P_1 P_2 cos\Theta) \tag{2.22}$$

where P_1 and P_2 are the fractional spin polarizations of the density of states of each electrode, defined as:

$$P_i = \frac{n_{i,\uparrow} - n_{i,\downarrow}}{n_{i,\uparrow} + n_{i,\downarrow}} \tag{2.23}$$

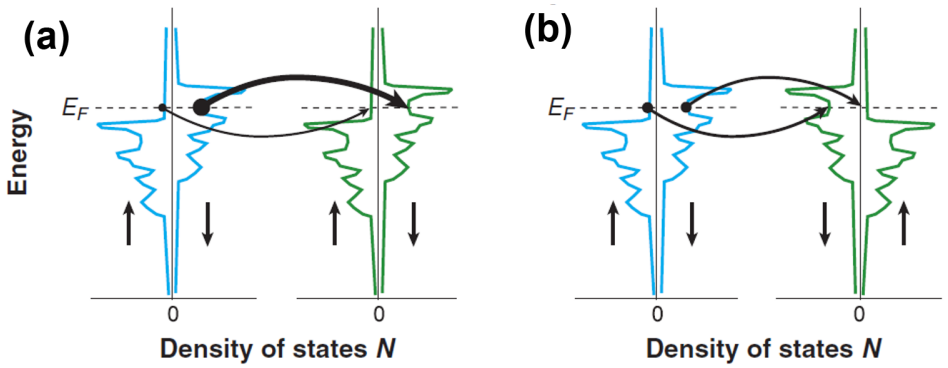

Figure 2.8: Tunnelling between two ferromagnetic electrodes that show a spin-split density of states N (↑ and ↓ indicate majority and minority states, respectively). In (a) the magnetization of the two electrodes is parallel, whereas it is antiparallel in (b). The conductivities for tunnelling from the left to the right electrode are indicated by arrows.[62]

It should be noted that the density of states is not monotonic with energy, as shown in figure 2.8. For the parallel orientation, the majority (minority) electrons of the first electrode tunnel into the majority (minority) states in the second electrode, while for an antiparallel configuration the majority (minority) electrons tunnel into minority (majority) states of the other. It can be seen, looking at fig. 2.8, that this does not necessarily imply that a parallel configuration will produce larger conductance (or differential conductance), but rather a complex, energy dependent situation occurs.

In the context of STM, Wiesendanger reported the observation of spin polarization of the tunnelling current in STM in 1990 [63], and an expansion of the Tersoff-Hamann theory to include spin considerations was provided by Wortmann in 2001 [64]. Using $n(E) = n^{\uparrow}(E) + n^{\downarrow}(E)$ to denote the local density of states at an energy E and $\tilde{n}(E) = \int_{E_F}^{E_F+E} n(E)dE$ to denote the integrated local density of states between E_F and E_F+E, and analogously $m(E) = n^{\uparrow}(E) - n^{\downarrow}(E)$ to denote the local magnetization of the LDOS at an energy E while $\tilde{m}(E) = \int_{E_F}^{E_F+E} m(E)dE$ represents the integrated local magnetization of the LDOS, from E_F to E_F+E, the tunnelling current I_t and the differential conductivity dI/dV can then be expressed as the sum of a non-spin polarized term and a spin polarized term.

$$I \propto n_t\tilde{n}_s(r,V) + m_t\tilde{m}_s(r,V)cos\Theta(r) \propto I_0(1 + P_tP_scos\Theta) \tag{2.24}$$

$$\frac{dI}{dV} \propto n_t n_s(r,V) + m_t m_s(r,V) cos\Theta(r) \propto n_t n_s(1 + P_t P_s cos\Theta) \qquad (2.25)$$

The results obtained in equations 2.24 and 2.25 closely resemble eq. 2.22, with $P_i = \frac{m_i}{n_i}$, but now the current not only depends on V but on the local position of the tip over the sample, *r(x,y)* and on the tip sample distance. In contrast with the case of planar electrodes, local changes in the polarized LDOS can be expected, and even more importantly, changes can also be expected due to variations in tip-sample distance as decay rate of the different orbitals (s, p, d) can now lead to changes of the weight of the spin polarized contribution to the total current [65].

2.2 Experimental setup

STM is strictly a surface technique, with its main strength residing in it being extremely sensitive to features at the atomic scale, which goes hand-in-hand with the weakness of being very vulnerable to contamination at the scale. To reduce the exposure of samples to unwanted molecules, experiments are usually performed in Ultra High Vacuum conditions (UHV, P $< 10^{-10}$ mbar), maintaining vacuum unbroken along the whole experimental process, from sample preparation to STM measurements. UHV is usually reached by a combination of turbomolecular and ion getter pumps, with the cryostat surrounding the sample in low temperature experiments acting as a cold trap, which enhances the vacuum in that area.

While different STM systems have been used during the course of this thesis, the vast majority of the results presented in this work were obtained using the setup shown in figure 2.9 at the Advanced Microscopies Laboratory (LMA) based in the Institute of Nanoscience of Aragon (INA) at the University of Zaragoza. This installation consists in five interconnected UHV chambers, plus an additional chamber with a load-lock system for sample transference between atmospheric and UHV conditions. The five main chambers consist in a central distribution/parking chamber, two sample preparation chambers and two dedicated STM chambers.

2.2.1 STMs

One of the STM chambers hosts a SPECS Aahurs HT-STM [66], which can operate over a wide range of temperatures, 90 K-1300 K. Low temperatures are achieved by circulating liquid nitrogen through a cooling circuit thermally connected to a large copper block that surrounds the sample, acting as both

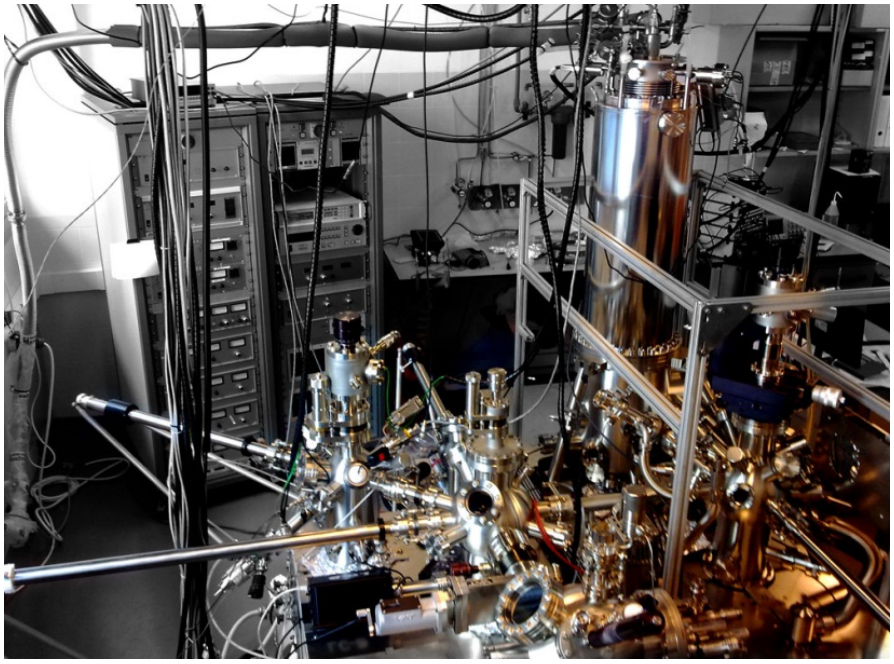

Figure 2.9: UHV multi-chamber system hosting two STMs, a low temperature SPECS JT-STM and a variable temperature SPECS Aarhus HT STM.

temperature reservoir and damping mass, to reduce vibrations. High temperatures are obtained by thermal radiation from a W filament that can be approached to the back of the sample. Temperature stability and non-measure-impeding drift can be reached in under ten minutes, even for large changes in temperature, with improving stability over time.

The other STM chamber encloses a low temperature SPECS JT-STM [67]. Low temperature is required for many STM experiments, particularly involving single atoms or artificial atomic-scale structures, as the reduced diffusion provides the necessary stability. Energy resolution is also limited by temperature T, as the thermal energy $k_B T$ will produce a broadening of all the spectroscopic features. This broadening is around 1 meV at 4.2 K, thus temperatures lower than liquid Helium (LHe) at atmospheric pressure (4.2 K) are required for sub-meV resolution. In this system low temperatures are obtained by the use of cryogenic liquids, LN_2 and LHe, in three cooling stages: an outer LN_2 cryostat (77 K, 20 l) surrounds a smaller LHe cryostat (4.2 K, 10 l), shielding it from ambient thermal radiation (300 K) improving its hold time. Operating with the sample in thermal contact to the He cryostat provides a stable base temperature of 4.3 K. Finally, a Joule-Thompson stage is used to condense He at low pressure in a third, smaller cryostat (1 K-pot), bringing the final

temperature of the system down to 1.1 K. This SPECS JT-STM also features a superconducting coil that can provide a magnetic field of up to 3 T along the sample surface normal. The hold time of the LHe cryostat is of 96 hours, although the actual uninterrupted time is limited by the LN_2, around 72 hours.

2.2.2 Preparation chambers

The two preparation chambers include the usual tools for sample preparation, totalling 3 ion guns for sputtering and 7 independent leak valves for gas dosing, 3 sample heaters by thermal radiation and electron bombardment - one of them modified to operate at T $>$ 2500 K, and several metal evaporators allowing up to 10 different materials available for deposition at a given time. A LEED/Auger system is installed for sample pre-characterization. A mass spectrometer is also available for leak detection and verifying the purity of the dosed gas, when required.

2.3 Sample and tip preparation

This thesis deals mainly with Tm evaporated onto a W(110) surface, although other materials (Lu, Fe) and substrates (Cu_2N) have also been used at particular points. As for tips, most of the experiments performed here use a polycrystalline W tip; when SP sensitivity is required, a Fe (or Cr) thin film is deposited on the W tip. In this section an overview of the typical tip and sample preparation procedures is provided.

2.3.1 Prepation of W(110)

The preparation of a clean W(110) surface is procedurally less complicated than other surfaces, but more demanding in the design of the heating stage and sample holder, as they must be able to withstand temperatures above 2300 K.

The main contaminant in a tungsten single crystal is carbon, which is dissolved in the bulk and diffuses to the surface over time. The procedure to remove said C, described in [68], consists in annealing cycles in a oxygen rich atmosphere (T $\sim$ 1500 K, $P_{0_2} \sim 5{\cdot}10^{-7}$ to $1{\cdot}10^{-8}$ mbar) which causes the C adsorbates to react with the oxygen, forming CO molecules that can desorb from the surface. The second step in the procedure is to perform a short, high temperature flash of the sample (T $>$ 2300 K) which removes atomic oxygen adsorbates and other remaining impurities from the sample. By performing

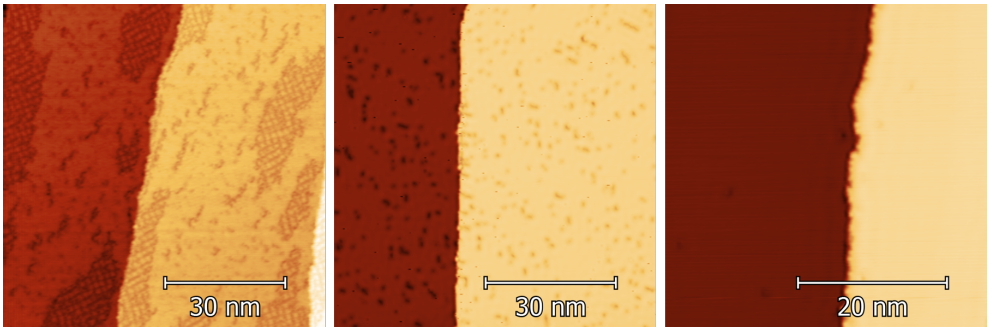

Figure 2.10: W(110) surface with different degrees of contamination. From left to right: sample with a high carbon presence on the surface, forming patches of carbon reconstruction; cleaner sample, with C in the form of individual adsorbates; pristine sample with only a few C adsorbates over the whole area.

several annealing-flash cycles until the flashes do not produce a significant pressure spike ($P_{Flash} \leq 1{\cdot}10^{-10}$ mbar) a high quality clean surface is obtained. Figure 2.10 shows the W(110) surface at different levels of contamination, ending with the clean sample shown on the right after several preparation cycles.

Reaching these temperatures (T $>$ 2300 K) is achieved by electron bombardment of the crystal: the sample is connected to a high voltage source while a filament near the back of the sample is heated by circulating a current through it, to favour thermoionic emission of electrons. These electrons are accelerated by the high voltage and impact the sample with an energy of eV_{HV}. An emission power around $W_{emi} \sim 110$ W (defined as the product of the accelerating high voltage, HV $\sim$ 900 V and the emission current, $I_{emi} \sim$ 120 mA) is enough to heat the sample, a 3 mm thick disc 1 cm in diameter, to the required temperatures.

2.3.2 Preparation of Cu_2N

Insulating thin films grown on metallic surfaces have proven to be of great interest in STM studies of single atoms and atomic-scale structures, as they reduce the coupling with the substrate [69] allowing the observation of phenomena otherwise dominated by the conduction electrons of the substrate [70]. Copper nitride Cu_2N is one such insulating thin film, consisting in nitrogen atoms adsorbed on the Cu(001) surface, which self-assemble forming small c(2x2) reconstruction islands, $\sim$ 5 nm across [71]. An example of a Cu_2N sample is shown in figure 2.11.

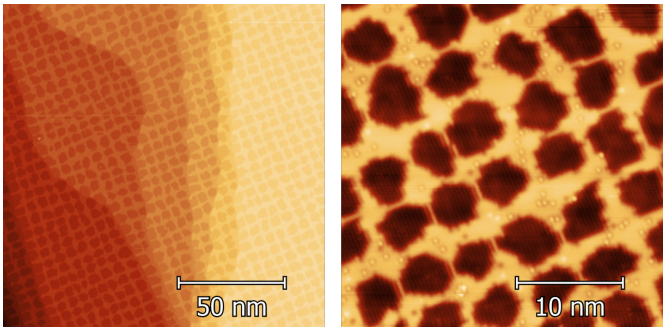

Figure 2.11: Large overview (left) and detail (right) of a Cu_2N sample. Cu_2N patches appear as depressions (darker) due to their lower conductance, not to an actual topographic height difference.

Preparing Cu_2N requires first preparing a high quality clean Cu(001) surface, which follows the typical process for noble metals. The surface is cleaned by removing the most external atomic layers by Ar^+ sputtering at 1 kV, with $P_{Ar} \sim 1{\cdot}10^{-6}$ mbar, followed by an annealing in UHV conditions at T $\sim$ 900 K. By repeated sputter-annealing cycles, a clean Cu(001) surface can be produced.

Nitrogen atoms are implanted on the Cu surface by sputtering in a N_2 atmosphere. To favour the self-assembly of regular islands, the sputtering process is followed by a gentler annealing than for the clean surface, at T $\sim$ 600 K.

2.3.3 Evaporation

Evaporation of both Transition Metals (Fe, Cr) and Rare Earths (Tm, Lu) has been performed by the same procedure, using an electron beam evaporator. In the case of Fe, the electron beam is directed onto 99.99% pure Fe rod while in the rest of the cases the beam heats a molybdenum crucible where the evaporant material is located in the form of flakes.

While the procedure is identical, evaporation parameters vary strongly between materials to achieve the same evaporation rate, depending on the particular vapour pressure curve (*e.g.* a flux producing samples with coverage around 0.1% of a monolayer per minute requires $W_{emi,\ Tm} \sim 5$ W for Tm while a similar flux for Lu requires $W_{emi,\ Lu} \sim 40$ W).

Evaporation in the range of monolayers (Tm islands, Fe islands, coating of tips with Fe or Cr) was performed at room temperature in the preparation chamber; on the other hand, evaporations in the range of single atoms were performed with the sample in the STM stage, at T $\sim$ 5 K to minimize diffusion.

2.3.4 Tip preparation

STM tips are prepared by electrochemically etching a W wire in a NaOH solution [72]. The wire is positioned through a small flat ring where a drip of the solution is placed, forming a thin layer by surface tension, minimizing the length of the wire exposed to etching which provides for a more robust tip. A voltage difference is applied between the wire and the ring, which starts the reaction. When the etching process finishes cutting through, the bottom part of the wire falls out of the solution, stopping the etching. This process is followed by rinsing in distilled water and inspection with an optical microscope. Suitable tips are mounted on a tip holder and introduced shortly after into the UHV chamber. The preparation is completed by in-situ treatment in the STM, consisting in controlled voltage pulses and crashes with a clean surface until good resolution and a stable behaviour is obtained.

Spin polarized tips are prepared by coating a W tip with magnetic material, such as Fe or Cr. Tips are flashed to remove oxides and other possible contaminants, resulting in a blunter tip apex on which a tin film of the magnetic material can be deposited. A coating of about ~ 50 atomic layers of Fe, as used in this thesis, results in a tip with in-plane magnetization [73]. Cr coating allows for in-plane and out-of-plane easy axis depending on the coating thickness [74], with the added advantage of being an antiferromagnetic coating, reducing the magnetic stray field produced by the tip.

Bulk Cr [75] tips can be etched similarly to W tips, but with the added complication that high purity Cr is usually available in the form of flakes a few millimetres in size, rather than wire. By cutting a flake with a diamond wire saw to produce a small rod and carefully etching the end of it, a tip with a sharp apex can be produced. Bulk Cr tips present an easy axis tilted respect to the tip axis, providing sensitivity to both in-plane and out-of-plane spin polarized components of the tunnelling current.

Chapter 3

Tm on W(110): A growth study

Growing of rare-earth on the (110) surface of bcc metals (Mo, W or Nb) has been widely used to obtain layers with the basal plane of the rare earth on this film plane [76–80]. Although the (110)bcc and (0001)hcp surfaces do not match with each other and therefore the concept of epitaxial growth is not applicable, it has proven to still be possible to prepare quite perfect superlatices and films. Historically, the first rare earth artificial superlattice dates from 1985 [77], a [Gd/Y] system with antiferromagnetic coupling between the ferromagntic Gd blocks through the non magnetic Y spacer[79].

Prior to nucleation of hexagonal islands, the rectangular centered mesh makes possible the existence of ordered structures with lattice parameter larger than the bulk RE values, linked to the substrate lattice. These periodicities can be recognized as multiple spots in LEED or RHEED images [81] and explained as the result of the presence of a repulsive interaction due to the negative dipolar charge appearing in the rare-earth adatoms in combination with attractive indirect electronic interactions [82]. On the other hand, heterostructures formed by magnetic layer deposited onto metal with high spin-orbit interaction is the scenario where interactions as the antisymmetric Dzyaloshinskii-Moriya exchange interaction and the Rashba effect give rise to compelling magnetic and transport phenomena.

In nanostructured systems, there exists a strong relation between the magnetic properties of the nanostructure and its crystalline configuration and size, both being controllable by the preparation procedure. In this section the preparation of islands of Tm is presented under different thermal treatments of an initial low temperature deposit. It is shown that the size of the islands can be controlled by the density of surface impurities, which diffuse to the surface over time at high temperatures.

The (110) surface of W offers the opportunity of studying the magnetic behavior of ordered RE overlayers on top of a conductive but nonmagnetic substrate. In general, the body-centered-cubic crystals of refractory metals such as W and Mo promote the two-dimensional layer growth of RE with no intermixing [83–85], with the (110) surface yielding morphologies with low corrugation.

Tm represents an interesting case since it is the only heavy RE which orders magnetically along the c axis of the bulk hcp crystal structure. Between the Néel temperature, $T_N = 58$ K, and 40 K, the magnetic moments are ferromagnetically ordered within the hcp basal-plane layers and have an incommensurate sinusoidal modulation along the c axis. The easy axis is parallel to the c axis, owing to strong crystal-field anisotropy. Upon decreasing the temperature, the propagation wave number along the c axis increases and, below $\sim$ 30 K, a ferrimagnetic structure with a seven-layer repeat distance develops: the magnetic moments point up along the c axis in three layers and down in the consecutive four layers [27, 28]. As the reduction of thickness along the c axis could drastically influence the magnetic behaviour of Tm, it is interesting to investigate the limit case of one atomic layer.

This chapter will focus on the preparation of the Tm monolayer on W(110), while the electronic and magnetic characterization will be explored in detail in the following chapter, Ch. 4.

3.1 Sample Temperature Calibration

The experiments presented in this chapter were performed using the Aarhus HT-STM described in section 2.2.1. In a typical experiment, sample temperature would be monitored by a thermocouple installed directly on the sample plate, however, due to the high temperatures required during the preparation of W(110) (see section 2.3.1) this method is not viable as the thermocouple would be destroyed during the process. Instead, an optical solution is used.

Pictured in figure 3.1, the configuration used to measure the temperature by means of a pyrometer pointed to the back of the sample presents its own set of problems, as it places the heating filament directly in the pyrometers path, which completely falsifies the instantaneous temperature readout. To account for this, a calibration of the sample's temperature at any given filament current is obtained; this is done by continuously monitoring the temperature during the cooling down process after turning off and retracting the filament, starting from different values of the heating filament current, I_f. Curves showing the cooling over time for different initial I_f can be seen in Fig. 3.2, which includes

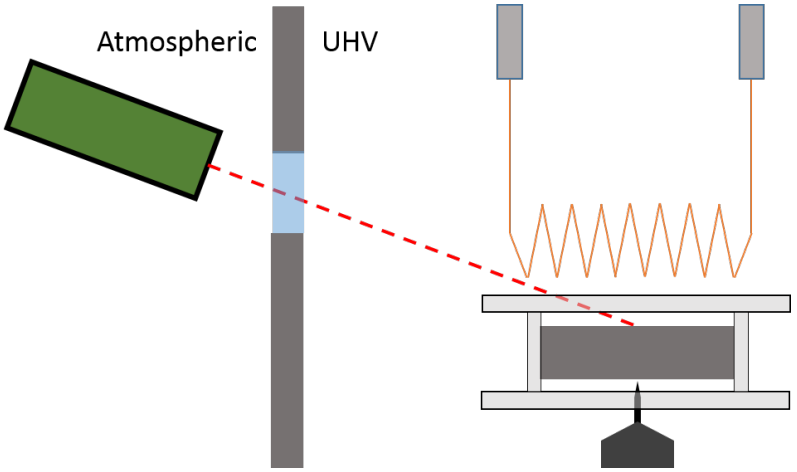

Figure 3.1: Diagram of the Aahrus VT-STM setup, using a pyrometer for temperature measurements.

fits to an exponential curve of the form:

$$T = A + Be^{-k(t-t_0)} \tag{3.1}$$

Where A is the temperature of the environment, which ideally acts as a reservoir, B is the difference between the initial temperature and the temperature reservoir, and k is the thermal conductivity; however, as experimentally the cooling is not only a thermal diffusion process (as described by the equation) but is heavily aided by radiative cooling, and also considering the non-ideallity of the whole setup, all three parameters, A, B and k are left as free parameters for the fit. To discard the points more heavily influenced by the light coming directly from the filament before it has been fully retracted out of the path of the pyrometer, t_0 is set to 5 s (1.4 s for the last three curves, corresponding to I_f = 1.35 A, 1.47 A and 1.57 A); a close up of this area can be seen in Fig 3.2.b, as well as the motivation for reducing t_0 for the lower currents, as it can be seen that, by $t = 5$ s, the temperature is already below the lower range of the pyrometer.

By extrapolating the fitted curves to $t = 0$ s, the temperature of the sample before turning off the filament can be estimated with reasonable accuracy. The resulting plot of the obtained temperature against the value of I_f used in each case presents a linear behaviour in the studied range, as shown in Fig. 3.3, which can be used to calibrate the temperature dependence with the current for this sample as:

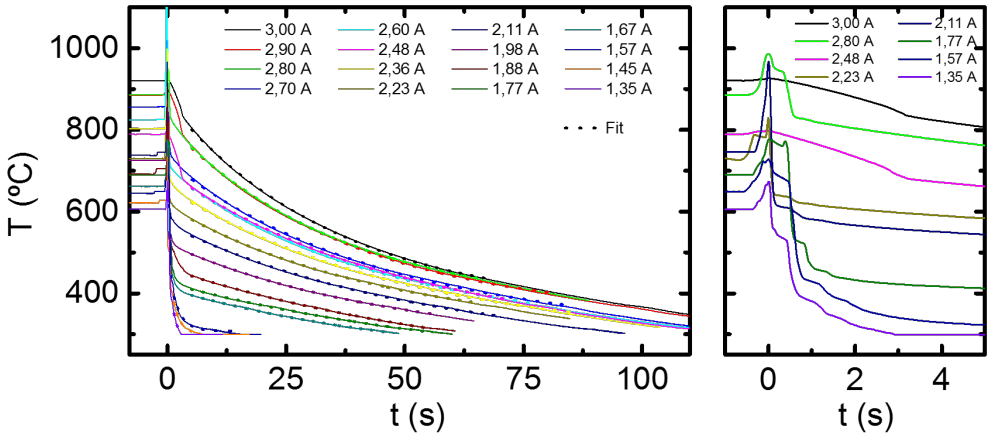

Figure 3.2: (Left) Cooling curves taken for several values of I_f, fitted to an exponential curve. (Right) Detail at low times for selected curves, highlighting the effect of the filament on the pyrometer read-out before retracting.

$$T_{Sample}(^{\circ}C) = 341 I_f - 162 \tag{3.2}$$

Although the fit to a linear dependence is good, it is obvious that it will fail for temperatures well outside the represented range. At higher temperatures, radiation cooling will be stronger and the curve used to fit the cooling process will no longer be appropriate; meanwhile, at low filament currents the T obtained from the fit would be below room temperature, which is unreasonable. Despite the good fit, deviations of near 50° C from the linear behaviour are observed, which points to the strong influence of slight differences in the sample-filament distance.

When performing experiments where T is a controlled parameter, capturing the evolution of the system during its first moments, before it has reached a stable state at the new set temperature is usually where most of the interest resides, the difficulty in this case lies in the strong drift that occurs if the whole scanning system is not at a homogeneous temperature, which impedes STM measurements. Therefore it is important that enough time has passed for the system to thermalize to avoid crashes and ensure that the sample is at the expected temperature, but not enough that the system has evolved to it's final state - this, of course, will depend on the characteristic time of the system, and will vary from experiment to experiment, however in every case it will always be advantageous to reduce the thermalization time to the minimum possible that provides a correct and reproducible behaviour. When performing small temperature variations it has proven to be possible to have no wait time at all, but rather continue measuring and retracting the tip step-wise as required; for

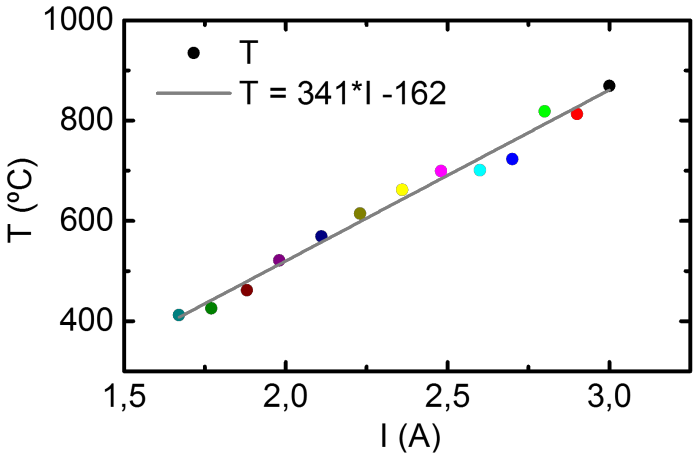

Figure 3.3: Calibration curve of $T(I_f)$ as a linear fit of the extrapolated T at t = 0 from the cooling curves.

large ΔT, low thermalization times causes a drift high enough to take the piezo out of range in a few seconds - this does not result in a tip crash, as the tip drifts away from the surface for increasing T. At 10 minutes the temperature of the sample is close to its final value, as can be observed in Fig 3.4 where cooling curves after 10 and 60 minutes at $I_f = 2.48$ A are shown, and the drift, while still enough to affect the images, is bearable.

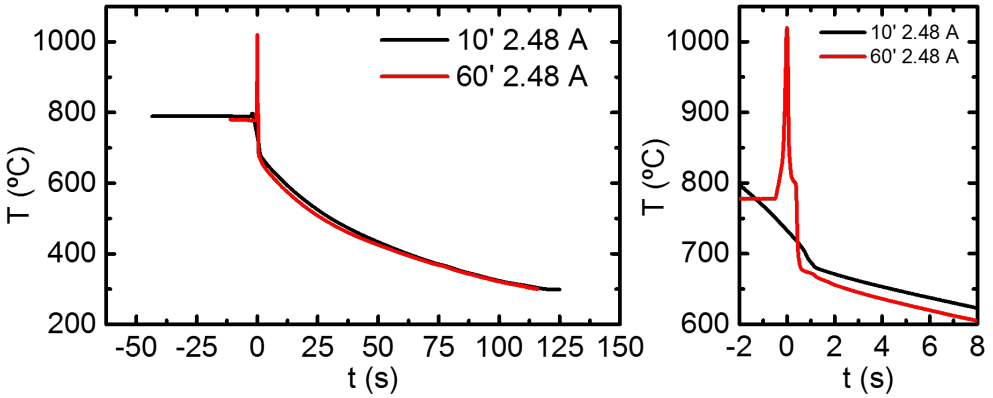

Figure 3.4: (Left) Comparison of cooling curves after heating for 10' and 60'. (Right) Detail for low time values highlighting the similarities of the curves despite the differences introduced by manually retracting and turning off the filament.

The evolution of drift overtime is shown in figure 3.5 for a sample going from room temperature to (some temperature). At t = 0 s the filament is turned on, $I_f = 1.57$ A, leading to a temperature of 370° C; the graph shows

the z position of the piezo over time while scanning over a flat atomic terrace. As shown by the stabilization of the z position, drift decreases over time. Time-sensitive measurements are thus impeded by the minimum thermalization time for fast processes, however very long processes may also be out of the reach of this system, as over time the temperature of the piezoelectric elements also increases. For temperatures near the operation upper limit, the time for the sensor at the STM tip to reach the maximum safe temperature (70° C) is just a few hours; for lower temperatures this is not an issue, as the piezo temperature stabilizes within the safe range.

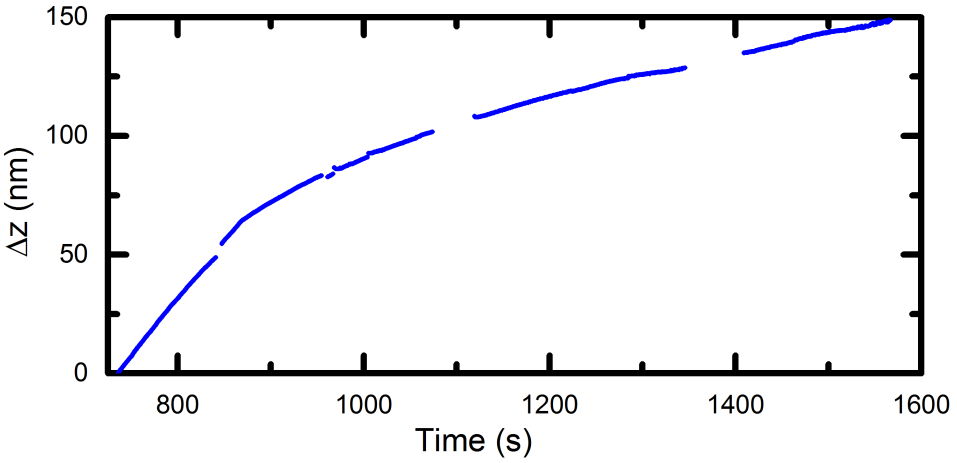

Figure 3.5: Value over time of the z position of the piezo scanner while scanning over a single atomic step at a temperature of T = 370° C.

3.2 Carbon contamination on W(110)

As mentioned in section 2.3.1, the main contaminant in tungsten crystals is carbon, which is removed from the surface by being exposed to oxygen at high temperatures during the cleaning procedure [68]. This process, however, only provides a temporary carbon-free surface, as the contamination does not come from external sources (such as placed near incandescent W filaments, or being exposed to atmospheric conditions) but rather from C atoms in the bulk of the tungsten crystal which diffuse to the surface over time [86, 87].

As with any diffusion process, the rate at which C reaches the surface is strongly related to the temperature of the crystal, which during the experiments performed in this chapter is in the 700-1200 K range for hours at a time, strongly enhancing the C segregation. This is produces a change in the quality

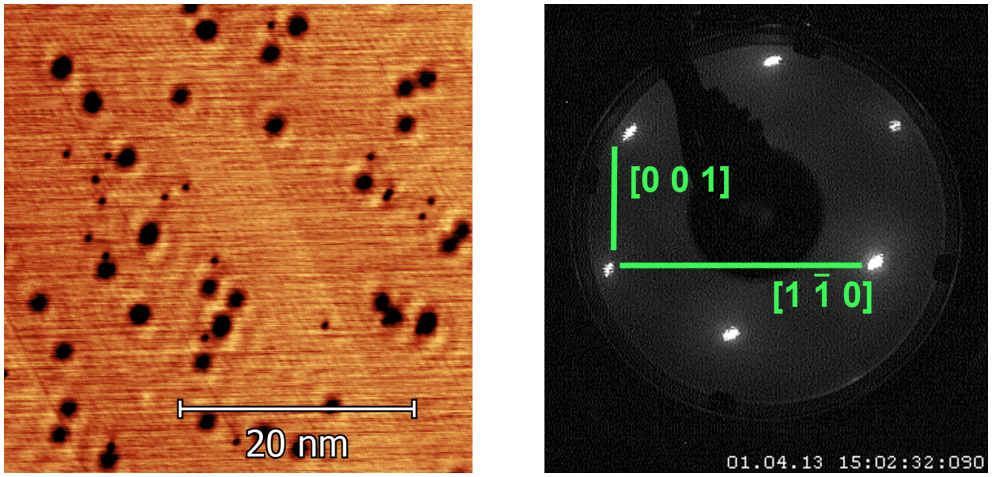

Figure 3.6: STM image of a clean W(110) surface taken at V_{Bias} = 100 mV, I_t = 1 nA. Carbon adsorbates appear as dark spots around and serve as scatter centres for the surface state, which is clearly visible around them. LEED pattern corresponding to the clean W(110) surface, with the [1$\bar{1}$0] and [001] directions indicated by green lines.

of the surface over time, affecting the growth of Tm structures. Understanding how the surface evolves as C contamination grows is therefore important for high temperature experiments.

An STM image of a clean W(110) surface is shown in figure 3.6, with only 34 adsorbates in the whole 40 x 40 nm^2 area. Carbon adsorbates appear as depressions on the surface, as the present a lower LDOS. To the right, figure 3.6.b, the LEED pattern corresponding to the clean surface is shown, where the rectangular lattice of the W(110) surface results in clear and well defined spots; the [1$\bar{1}$0] and [001] directions are indicated by lines.

At high temperatures carbon will continue to diffuse, leading to a higher adsorbate concentration at the surface. Locally, carbon reconstruction patches will start form where the adsorbate density is high enough; over time, the carbon reconstruction will cover the whole surface. An STM image of said reconstruction is shown in figure 3.7, accompanied by the corresponding LEED pattern showing the 15x3 relation [88].

While LEED measurements are able to distinguish between the two situations presented in figures 3.6 and 3.7, quantifying the non-reconstructed adsorbate density is beyond the capabilities of this and other area analysis techniques (such as Auger), and STM characterization is required to ensure an adequate surface for experiments sensitive to even low densities of impurities.

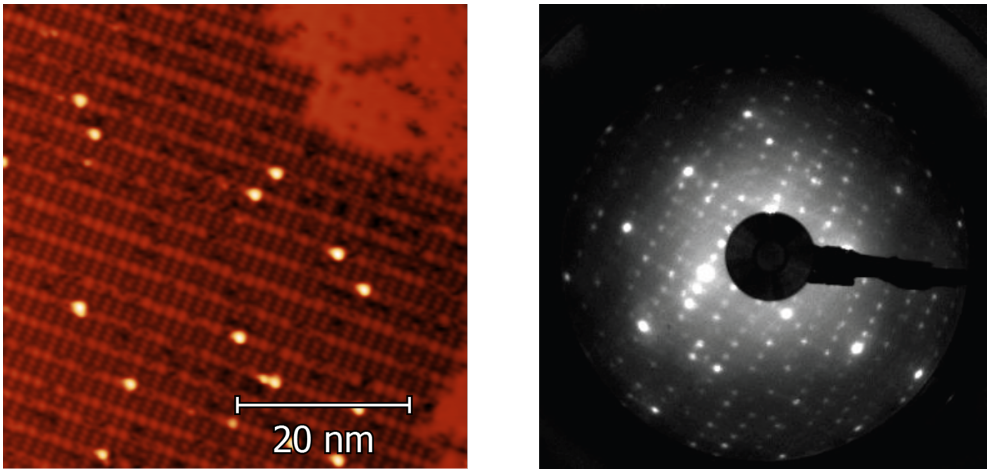

Figure 3.7: (left) STM image of the Carbon reconstruction on W(110) taken at V_{Bias} = 100 mV, I_t = 1 nA. (right) Corresponding LEED pattern illustrating the 15x3 reconstruction (courtesy of Jose Luis Diez-Ferrer)

3.3 Tm monolayer: Structural Characterization

Thulium grows heteroepitaxially on the W(110) surface, with $[10\bar{1}0]$ direction of the Tm layer along the $[1\bar{1}0]$ direction of the (110) substrate, similar to the Nishiyama-Wasserman orientation observed in other RE/W(110) systems [89, 90]. Figure 3.8 presents an STM image of the Tm ML (a) along with the corresponding LEED pattern (d), illustrating the situation. The STM image on the left (a) shows a quasi-hexagonal symmetry on the Tm layer - this is not atomic resolution, but rather a Moiré pattern caused by the overlap of the triangular Tm lattice and the rectangular W(110) surface, shown in greater detail in (b); the actual atomic resolution of the Tm layer can be seen in (c). To the right, 3.8.d shows the corresponding LEED pattern, which presents the spots due the W(110) seen in fig. 3.6 and an added quasi-hexagonal structure corresponding to the Tm layer; satellite points forming an hexagon surrounding the Tm spots are due to the Moiré pattern.

The lattice parameter measured along [001] is 4.08 Å, while for the two other sides of the isosceles triangle we obtain 3.92 Å. This means that the Tm ML displays a fairly distorted hexagonal structure, forming in fact a rhombic or isosceles triangular lattice. Thus, the lattice mismatch between Tm and W is large enough to produce in the first monolayer of thulium an asymmetric distortion of the hcp structure that, with respect to the bulk lattice parameters, is compressed along the [1-10] W by 1% and expanded along [001] W by about 15%; the W lattice parameter is slightly enlarged respect to the bulk, with a_W

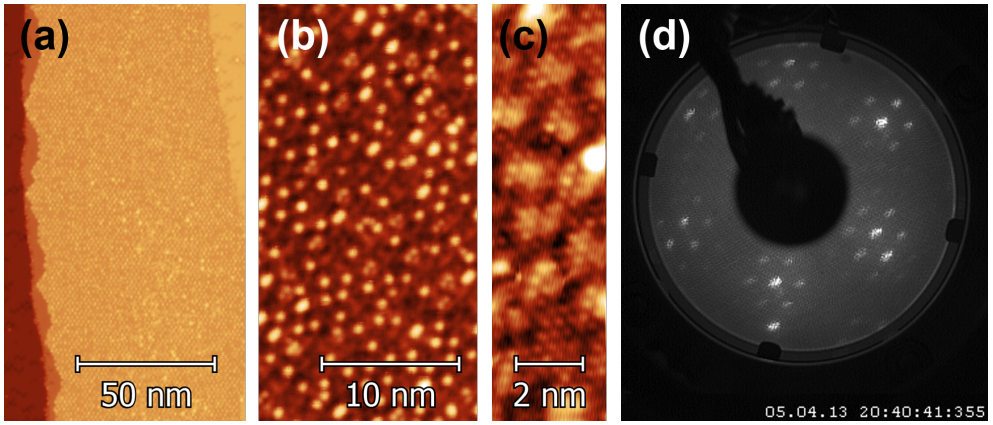

Figure 3.8: (a) STM image of a Tm/W(110) sample showing the Tm monolayer on W(110); the clean W surface can be seen to the sides of the Tm layer. (b) Detail of the Moiré pattern of the Tm monolayer and (c) detail of the underlying atomic resolution. (d) LEED pattern corresponding to the Tm monolayer on W(110) showing the spots corresponding to the crystalline structure surrounded by satellites corresponding to the Moiré pattern.

= 3.173 Å. This results in a Tm:W coincidence match of 2:3 and 7:9 along the $[1\bar{1}0]$ and [001] W directions, respectively.

3.4 In-situ preparation of submonolayer Tm on W(110)

Thulium is deposited on a clean W(110) surface using a SPECS EBE-4 system, in which a Mo crucible holding bulk Tm (purity 99.99%) is heated by electron bombardment, obtaining a rate near 1 ML/min at a flux of F_{Tm} = 450 nA. Although this flux would seem high when working with 3d metals (e.g. further along this work, in chapter 6, a coverage of the order of 0.3 ML of Fe on W(110) is obtained evaporating 20 s at F_{Fe} = 18 nA, again a rate of the order of 1 ML/min) the disparity is reproducible for all the RE (Tm, Lu) and TM (Fe, Cr) used in this work.

Tm on W(110) presents a large variety of morphologies depending on the coverage and thermal treatment after deposition, ranging from single atoms and clusters, to nanowires, to crystalline hexagonal monolayer islands for coverages below the monolayer, and a hexagonal pyramidal Stranski-Krastanov growth for a multilayer coverage, where a full monolayer is first formed, on which subsequent pyramidal multilayer islands are able to grow. The study presented here is focused on the sub-monolayer regime and its evolution with temperature treatments.

3.4.1 Low coverage: Single atoms and clusters

One of the peculiarities of this system is that for low coverages, even at room temperature, single atoms and small clusters present a very low diffusion and does not aggregate into larger objects until higher temperatures. See Fig. 3.9.a

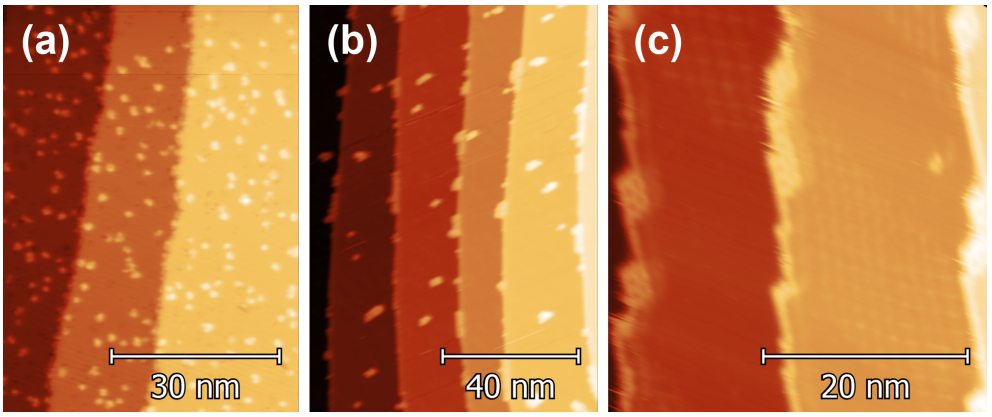

Figure 3.9: Tm/W(110) sample with a low Tm coverage (a) at RT, as deposited, (b) at 700 K after 4h in the 550-700 K range, causing a high density of C adsorbates on the tungsten surface and (c) at 900 K, after 3 additional hours in the 700-900 K range, showing the surface covered in carbon reconstruction patches.

Increasing the temperature of the sample to T = 700 K facilitates diffusion, resulting in migration of Tm to the step edges, as well as aggregation into small islands (Fig. 3.9.b). It should be noted that changes in the configuration of the sample occur in a time window smaller than the thermalization time required by the system, as no strong evolution is observed at this temperature from t_{700K} = 10' to t_{700K} = 30' where t_T is the time t the sample has been at a given temperature T. Increasing the temperature above 900 K produces a notable change in the configuration, as Tm structures acquire visible hexagonal characteristics. Fig. 3.9.c shows the resulting sample at this temperature, where all the Tm has migrated to the step edges forming a wire along the edge that expands into islands with sharp hexagonal angles.

In contrast to the previous example, a strikingly different behaviour is observed for a similar starting coverage if the heating process is altered. Figure 3.10.a shows the sample as deposited at room temperature, and while the coverage is roughly 1.5-2.0 times that of figure 3.9.a, it is still low enough for it to consist in small clusters as well as some atom-like objects.

In order to try and capture the diffusion process, longer time periods are spent measuring this sample at lower temperatures (600 K, 650 K, 700 K), without observing any significant change at any given temperature, pointing

to an equilibrium for the island size that is reached in the first few minutes after increasing the temperature, before the drift is low enough to allow STM measurements. Increasing the time spent at lower temperatures, however, does have a significant effect regarding the presence of C on the surface, which is much more evident in Fig. 3.10.b than for an equivalent temperature (730 K) reached faster, as in Fig. 3.9.b; the other difference between the two images is that in this case Tm does not migrate to the step edge or form larger islands, as the diffusion process seems to by inhibited by the presence of a large quantity of carbon adsorbates.

The difference in behaviour is stronger as the temperature is increased, as the large, regular islands with hexagonal characteristics where all the Tm accumulates, leaving free the majority of the tungsten surface, are nowhere to be seen but rather small irregular islands are distributed along the surface, with multiple carbon reconstruction patches covering the rest of the tungsten. Fig 3.9.c shows this behaviour, including double-layer islands due to the constraints imposed by the growing carbon reconstruction, even after increasing the temperature up to 1100 K.

3.4.2 Mid coverage: 0.5 monolayers

At higher coverages Tm still does not tend to aggregate into a single continuous layer, but rather tends to clusterize into small objects a few nanometers wide (Fig. 3.11.a), which when annealed at temperatures around 600 K, evolve into

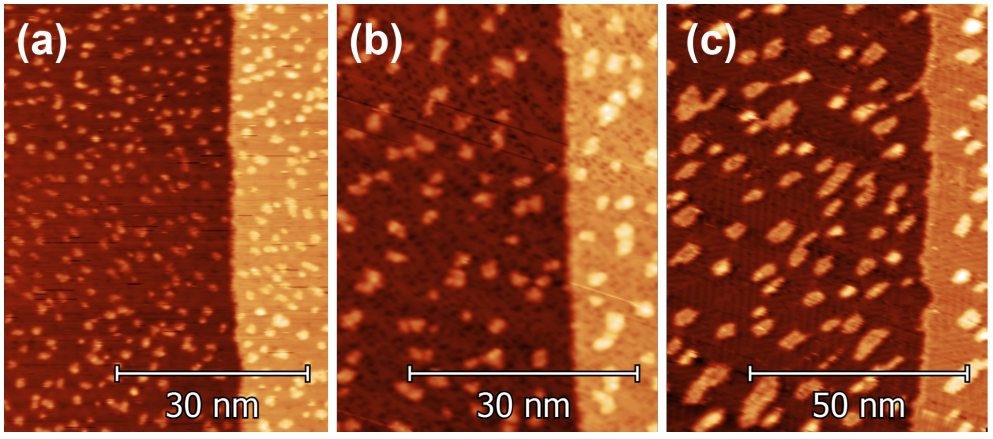

Figure 3.10: Tm/W(110) sample with a low Tm coverage (a) at RT, as deposited, (b) at 730 K after 4h in the 600-730 K range, causing a high density of C adsorbates on the tungsten surface and (c) at 1100 K, after 3h in the 750-1100 K range, showing the surface covered in carbon reconstruction patches.

small flat islands (Fig. 3.11.b). Following a slow heating process, as done for lower coverages, produces a similar behaviour: the segregation of carbon is strongly enhanced, which favours the formation of large patches of carbon reconstruction which inhibit the diffusion of Tm, limiting the size of islands; with the island size constrained by carbon, increasing the temperature up to 950 K induces a structural change where the islands become regular in shape, with hexagonal features, but without merging into a large patches, but rather staying mainly as 10-15 nm wide individual islands.

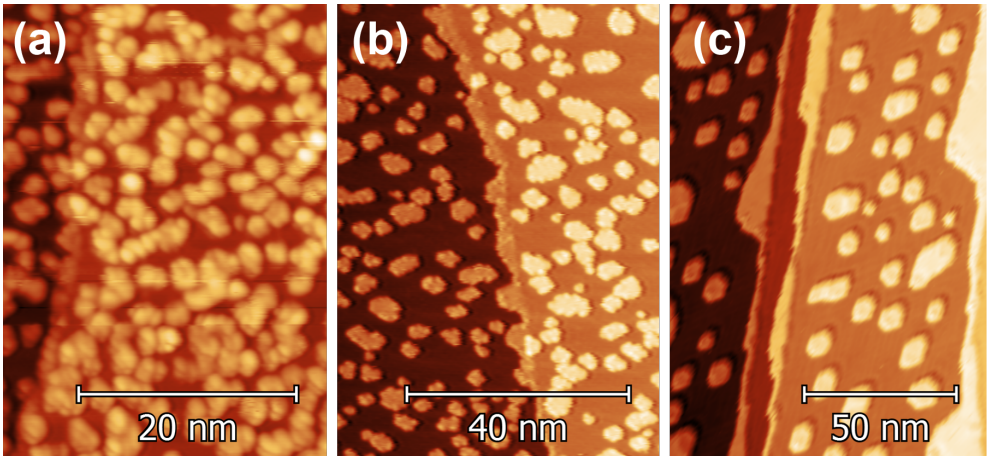

Figure 3.11: Tm/W(110) sample with coverage near 0.5 ML (a) at RT, as deposited, in the form of irregular clusterized islands (b) at 750 K showing flatter, but still irregular islands and (c) at 950 K, where the diffusion is limited by the presence of C reconstruction patches and Tm takes the form small islands with hexagonal features.

It is not until the coverage is near the full monolayer, that Tm does, in fact, aggregate rather than forming smaller individual objects. In this state, Tm presents a high corrugation and an irregular appearance, as seen in Fig. 3.12.a. Increasing the temperature to 780 K favours the mobility of Tm, allowing for the formation of a smoother but still irregular layer, with a more compact structure, as shown by the fact that the tungsten surface is clearly visible in Fig. 3.12.b and that maintaining the sample at this temperature does not increase the proportion of visible tungsten, and therefore re-evaporation of Tm can be discarded as the cause of the observed decreased coverage. As for the case of low coverage shown in Fig. 3.9, at temperatures around 950 K the Tm layer forms a hexagonal structure a single atomic layer in height, although in the form of large patches in this case (pictured in figure 3.12.c), as performing a faster annealing process conserves a surface clean enough for the Tm to diffuse all along the step edges, leaving the rest of the W step free of smaller Tm

objects.

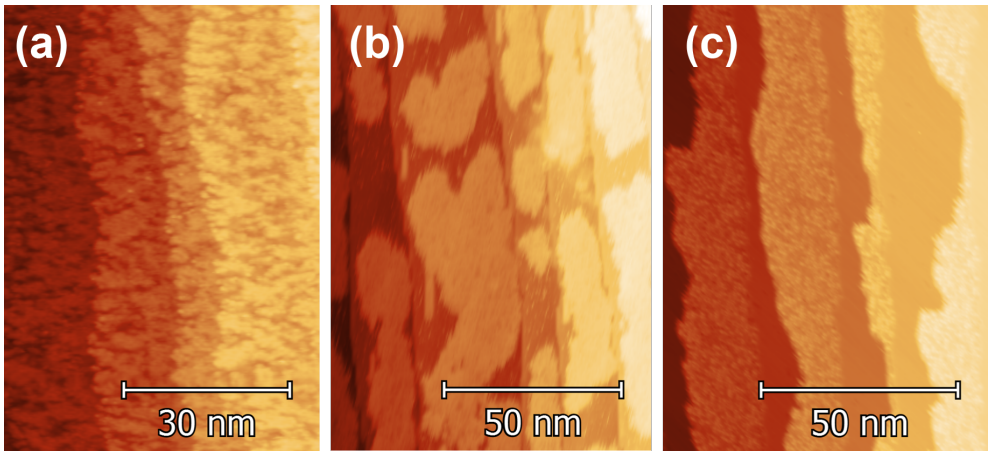

Figure 3.12: Tm/W(110) sample with a coverage around 0.5 ML coverage (a) as deposited at RT (b) at 750 K and (c) at 950 K. Islands change from irregular and rough in (b) to the crystalline with a Moiré pattern (c) for higher temperatures.

The evolution of the system as seen in 3.12 can actually be monitored by STM, as it changes in a scale of minutes. Figure 3.13 shows the same area of the course of thirty minutes at T = 780 K, showing a dynamic behaviour. The evolution pictured occurs forty minutes after setting the temperature setpoint, some self-assembled nanowires [91] can be seen in the first images although the overwhelming majority of Tm is forming irregular shaped islands. Over time the islands expand, approaching the full monolayer and covering the wire structures. As no new material is added during this time, the increase in surface covered by the Tm islands is due to the system evolving to a new, less compact, configuration. At higher temperatures this is then followed by a structural change into a more compact hexagonal lattice, as seen in the previous figure, from fig. 3.12.b to fig. 3.12.c.

3.4.3 High coverage: above 1 monolayer

For higher initial coverages, above the monolayer, the Stranski-Kastanoff growth mode is evident, with Tm forming multiple layers high hexagonal pyramids 3.14.a. Annealing this sample illustrates the origin of this growth mode: the W-Tm interface is more energy favourable than the Tm-Tm interface, therefore completion of the initial wetting layer takes priority over subsequent layers, as illustrated by the fact that said higher Tm layers are reevaporated at lower temperatures than the wetting layer. Thus, annealing at high temperature a multilayer sample, such as fig. 3.14.a leads to a similar result as for sub-

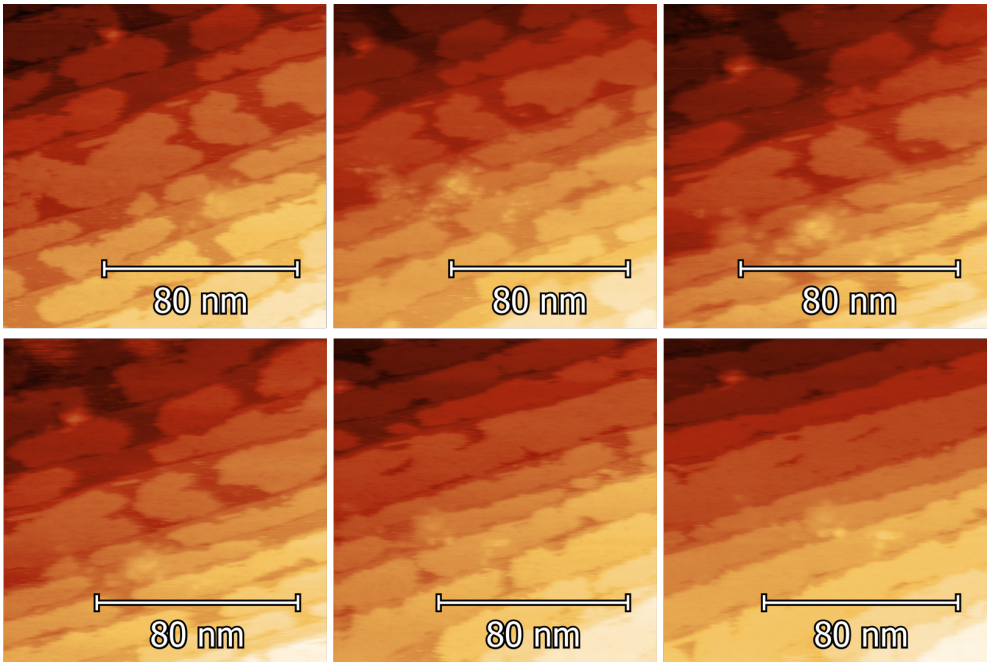

Figure 3.13: From left to right, top to bottom: Evolution over 30' of the sample at 750 K. Thulium islands expand, covering the whole surface.

monolayer samples, with the already discussed heteroepitaxial monolayer with a Moiré pattern, pictured in figure 3.14.b.

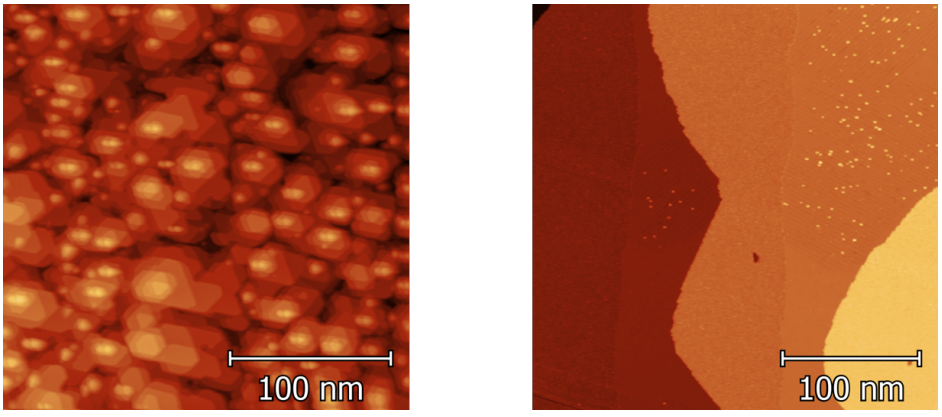

Figure 3.14: Left: Multilayer Thulium sample as deposited at room temperature showing hexagonal pyramidal islands. Right: After annealing at 1100 K, leaving only monolayer Tm islands on the W(110) surface; carbon reconstruction patches can also be seen.

At high temperatures carbon segregation to the surface is fast enough to observe its effect over consecutive scans. Figure 3.15 shows the same area of the Tm monolayer at 1000 K over the course of 5 minutes. The small dark patch in fig 3.15.a is an area with carbon reconstruction which grows over time while other small patch appears (fig 3.15.b), eventually merging with each other, forming a larger area of carbon reconstruction along the step edge. The growth of the carbon reconstruction patches displaces Tm from the layer, rather than growing below it, as it can be seen in figure 3.15.b and c: small areas on the Tm layer with a greyer colour appear to have carbon beneath, while a darker area, similar in hue to to the reconstruction along the step edge, seems to have displaced the Tm layer.

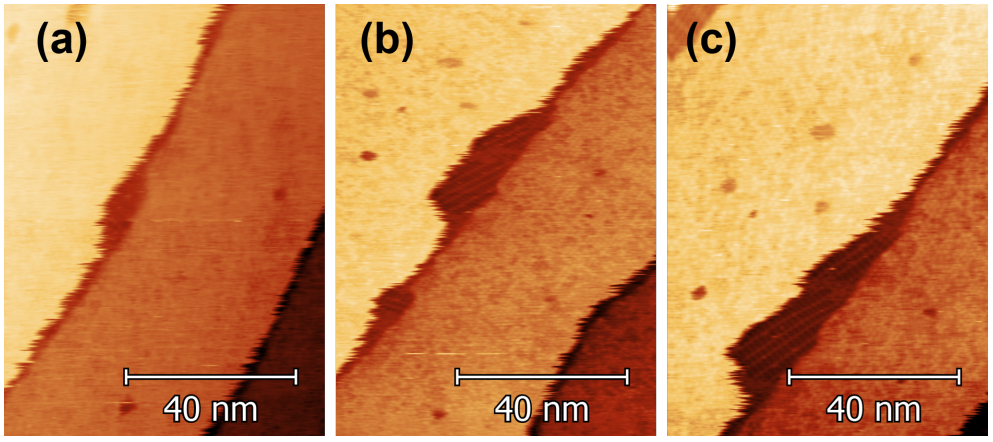

Figure 3.15: Evolution over 5' of the sample at 1000 K, showing the growth of a carbon reconstruction patch, displacing the Tm layer.

This effect is also seen on other samples, as shown in Fig. 3.16, while the time evolution is not captured it can be seen that Tm is displaced by the carbon reconstruction onto the second layer in (a), and 30' later in (b) the Tm layer is flat once again, with Tm organized along to the step edge and carbon adsorbates and reconstruction patches on the outer side of the step. As the coverage is lower than the initial, it suggests a re-evaporation at this temperature of the material that moves onto the second layer.

Figure 3.16 illustrates a similar issue. In this case, the carbon reconstruction patches within the layer have grown to the point where it is favourable for Tm to move to the second layer. Over time, this Tm is reevaporated reducing the total coverage, while the remaining material reorganizes forming a continuous layer with the carbon reconstruction patches along the step edges.

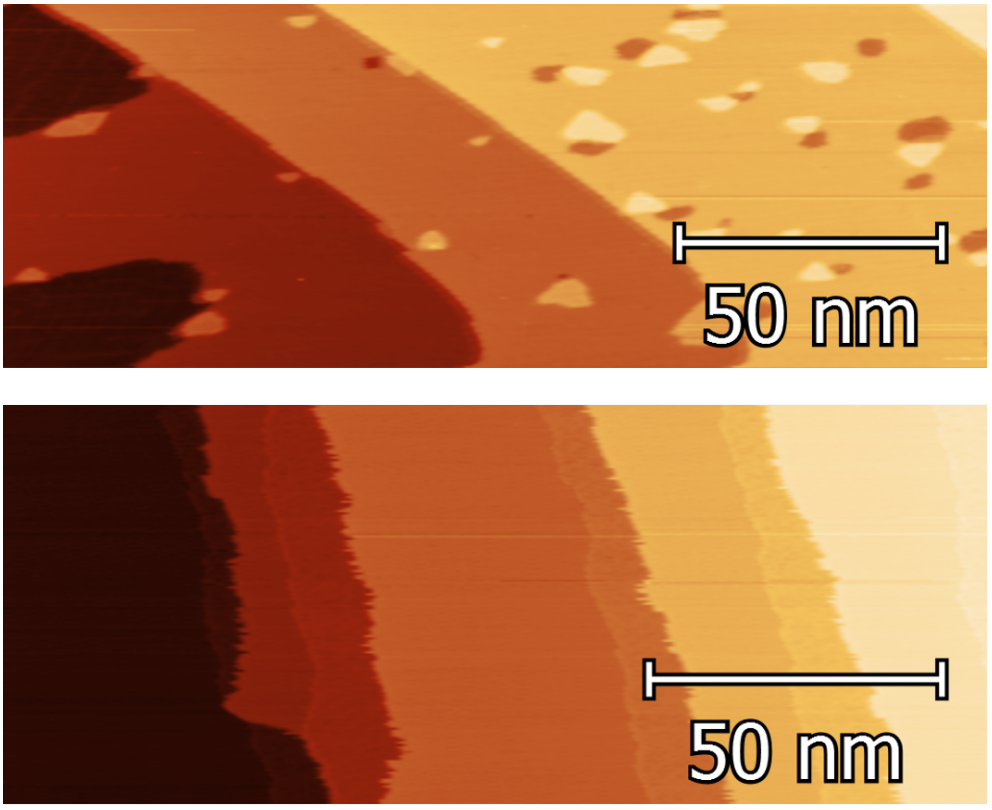

Figure 3.16: Top: Thulium being displaced by carbon reconstruction patches at 1050 K. Bottom: the same sample 30' later at while keeping the temperature at 1050 K, showing that Tm has compensated for the displaced material by migrating to the step edge

3.5 Size distribution of Tm islands

To study the effect of carbon adsorbates on the diffusion of Tm on the W(110) surface, and thus on the resulting island size, it is interesting to first introduce the basic ideas involved in the description of nucleation on ideal surfaces, omitting the effect of impurities, anisotropies, steps and other deviations from a perfect surface.

Once an atom or molecule is absorbed onto a surface, it can be reevaporated or diffuse along the surface. Adatoms diffusing on the surface can encounter each other leading to the formation of dimers, clusters and larger two-dimensional islands. These islands, as a whole, are stable and do not diffuse further; their shape and size, however, can change by dissociation and diffusion of the adatoms on the edges.

Island nucleation and growth (pro-coalescence stage) continues until islands grow to the point to merging with each other. At this point, continued growth of the layer consists in the filling of the remaining holes (post-coalescence stage). Thus, at constant temperature, the number of islands increases over time until coalescence between them begins, reducing the total number of individual islands. For the case of three dimensional islands, if no additional material deposited on top of the island, but rather there is a transference between layers, overcoming an additional energy barrier (called Ehrlich-Schwoebel [92, 93]) associated with the interlayer jumping is required.

The behaviour of single-component metallic systems is well understood, based on scaling properties of measured island densities and shapes as a function or temperature and covering. Several reviews present a thorough presentation of the state of the art [94, 95]. Usually, the diffusion process in presented in the context of a clean surface: only the adatoms and the surface are consider to obtain the relevant parameters [96]. But in same cases of practical interest the diffusion happens on surfaces partly covered by other impurities or and the diffusion is modified with respect to that observed in a clean surface. For example, adsorbed hydrogen atoms enhance the self-diffusion of Pt by two orders of magnitude [97].

3.5.1 Island density

Two factors influence the nucleation and growth of islands: deposition of atoms onto the surface with a flux F and thermally activated diffusion of adatoms along the surface with a diffusion coefficient D:

$$D = D_0 exp(-U/k_B T) \tag{3.3}$$

where U is the diffusion barrier. For atomic systems, $D_0 = \nu a^2$, where ν is an attempt frequency and a is the lattice constant of the substrate. Thus, with the definitions of F and D, the mean time for a unit cell to be hit by an atom is $1/Fa^2$, and the mean time after which the atom leaves the cell by diffusion is a^2/D. Some conclusions can be obtained observing Eq. 3.3, adatom diffusion is thermally activated, so increasing temperature produce an increment of D and adatoms can diffuse over longer distances. As a result the density N of stable islands, becomes smaller with increasing T, and the number of atoms forming the island increases.

In order to describe and quantify the structures observed by STM or AFM as function of coverage Θ or temperature, a complete set of equations has been obtained in the literature [94]. A fundamental concept is the critical island size or critical nucleus i. This variable denotes the critical cluster size, which

becomes *stable* on adding an atom. Clusters with i+1 atoms are more likely to grow than to dissociate. i depends on the substrate temperature, increasing when T increases and other factors as the crystal symmetry of the substrate and the structure of a film, either amorphous or crystalline.

Mean Field Calculation

The mean-field nucleation theory has been used to obtain a simple expression for the concentration n_x of 2-D islands of size i for the case of complete condensation [94, 95, 98]:

$$n_x \propto \left(\frac{D}{F}\right)^{-\chi} exp\left[\frac{E_i}{(i+2)k_BT}\right] \tag{3.4}$$

where $\chi = i/(i+2)$ and E_i its bending energy. Stable cluster means that grows more rapidly that the decaying, for instance by a dissociation process, in the course of deposition.

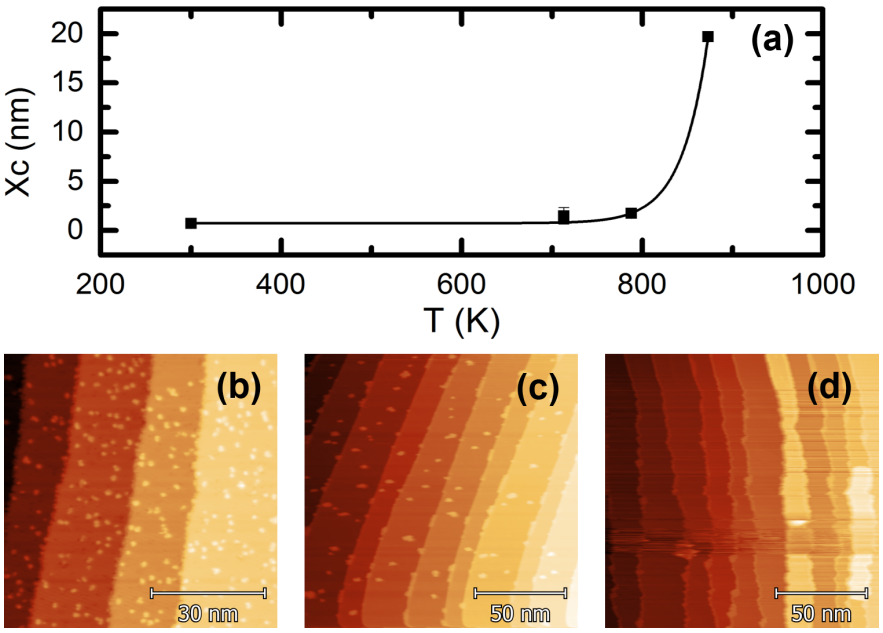

Figure 3.17: (a) Island size evolution with temperature. Below, from left to right, the evolution of the island size on the same sample at (b) room temperature, (c) 730 K and (d) 950 K. Note that the island size at high temperatures is limited by the step size.

3.5.2 Influence of C adsorbates in island size

While the discussion above pertains to the case of clusters with a small number of atoms, the dependence of the equilibrium island size with temperature is a general conclusion. Figure 3.17 shows the island size evolution with temperature of a sample where little carbon has segregated over the whole sequence, leading to a final island size that is actually limited by the step size, as seen in the lower section of the figure, illustrating the sample at different stages.

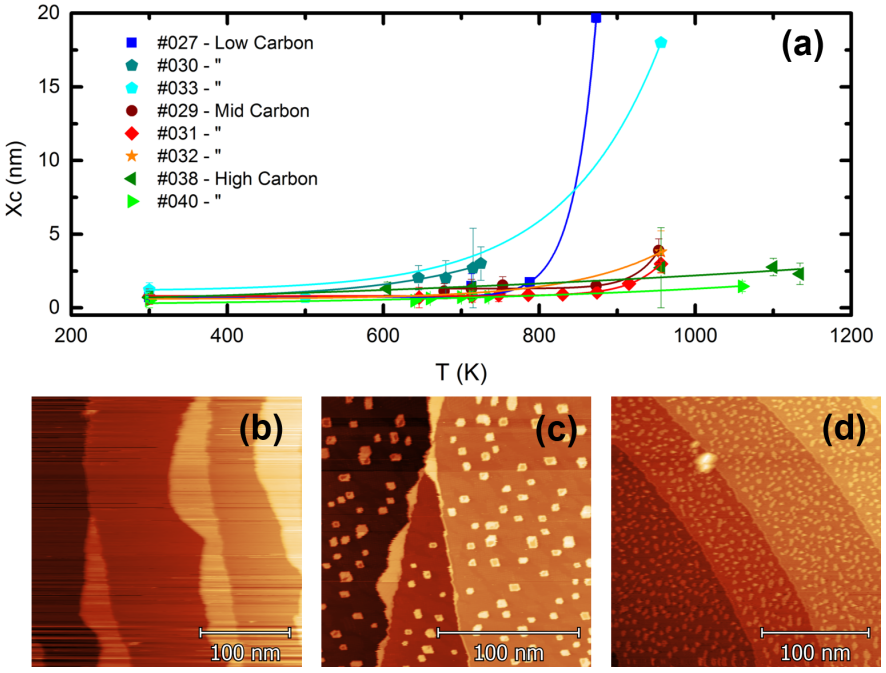

Figure 3.18: (a) Island size evolution with temperature for a set of samples. Below, representative final states for different samples, corresponding to the curves marked as (b) sample 030 at a final temperature of 950 K, with low carbon presence resulting in larga islands; (c) sample 031 at 950 K, with a strong presence of carbon reconstruction, but segregated after the islands already increased in size; and (d) sample 040 at 1050 K, where very small regular islands can be observed all over the surface, due to the inhibited diffusion due to the high density of carbon on the surface.

This is in stark contrast with the behaviour described for samples where the annealing process is performed over a longer time, allowing for a greater density of carbon adsorbates on the surface, as seen previously in figures 3.10 and 3.11. Plotting the island size as a function of temperature for several samples illustrates how different the behaviour is between a clean surface and one saturated with carbon reconstruction.

It is not trivial to quantify the number of impurities, especially with experiments at high temperature where resolution might be compromised to avoid risking tip crash, further complicated by drift issues. Figure 3.18 shows the island size evolution for several sets of samples, divided roughly in three categories depending on the carbon density on the surface: Low Carbon (blue hues in the graph), where the sample remains reasonably clean after the annealing process and island size is limited mainly by the size of the steps and the amount of Tm available; Mid Carbon, where carbon reconstruction patches and a high density of carbon adsorbates strongly limit the mean island size; High Carbon, with carbon reconstruction patches covering the whole surface.

A careful control over the carbon density on the W(110) surface can thus provide a reliable method for obtaining self-assembled islands with a definite size, ranging from being limited by the atomic step size to islands under 5 nm in diameter.

Chapter 4

Tm on W(110): Electronic and magnetic properties

Interest in low-dimensional rare-earth (RE) magnetic structures has grown steadily in recent years, focusing on single atoms as model quantum spin systems [99–103] as well as ultrathin films that display either ferromagnetic [104–107] or antiferromagnetic [108] order when grown on nonmagnetic substrates. Ultrathin RE magnetic films and multilayers have also attracted attention due to their ability to induce perpendicular magnetic anisotropy in adjacent transition-metal layers [109], control magnetic damping in spin valve devices [110, 111], as well as fabricate materials with higher magnetization compared to ransition-metal alloys [112, 113].

The interest in studying the magnetism of RE adatoms and monolayers (ML) resides in the localized character of the $4f$ states, which protects them from hybridization effects and preserves atomiclike spin and orbital magnetic moments. The extended $5d6s$ valence electron states of the RE atoms, on the other hand, couple with the partially filled $4f$ orbitals and hybridize with the surface valence electrons of the substrate. This affects the exchange interaction and, hence, the type of magnetic order and transition temperatures in ML structures [114–116]. Additionally, combined with said hybridization effects, symmetry breaking and epitaxial strain influence the magnetic anisotropy and magnetoelastic interactions [117], giving rise to a different magnetic behavior compared to that of thick films. In contrast to transition-metal adatoms, there are very few experimental studies on the magnetism of RE atoms on surfaces, limited to Ce [99, 100] and Gd impurities [101], although recent results regarding Ho adatoms has spurred a renewed interest [15, 31, 103, 118, 119]. Theoretical studies are also limited to Gd adatoms and dimers on Cu_2N/Cu substrates [102] and Ho adatoms on Pt(111) [103, 120] and MgO [15].

RE thin films deposited on crystalline magnetic and nonmagnetic transition-metal substrates have been previously studied by spin-polarized photoelectron [107, 121, 122] and Auger [123] spectroscopies, electron capture spectroscopy [104], as well as by linear and circular x-ray dichroism [124–126] and spin-polarized STM [106, 127–129]. It is worth mentioning that the decrease of the order temperature with thickness in these RE is stronger than in the case of transition-metal ferromagnets [130, 131]. Moreover, below the critical temperature, bulk RE metals display magnetically ordered phases of different complexity, depending on the element and on the temperature range [132]. These examples show that the magnetic structure of RE ultrathin films is a nontrivial issue, which, furthermore, has not been investigated in a systematic way across the lanthanide series. This chapter focuses on the study of electronic and magnetic properties of individual Tm adatoms and monolayer-thick films deposited on a W(110) surface by means of x-ray dichroism [30] and differential conductance tunnelling spectroscopy.

4.1 Experimental setup

In the previous chapter a great deal of attention has been paid to the conditions required for proper Tm/W(110) sample preparation. However, the characterization of the magnetic and electronic properties of the Tm monolayer is not enhanced, but rather hindered, by performing experiments at high temperature, which is the strong suit of the SPECS Aahrus HT STM. Instead, a thorough study of said properties has been performed by means of X-Ray Magnetic Circular and Linear Dichroism, XMCD and XMLD, respectively, complemented with STS and SP-STM experiments performed at low temperature in a SPECS JT STM.

The dichroism experiments were performed at the ID08 beamline of the European Synchrotron Radiacion Facility (ESRF). Samples were grown in-situ following the procedure described in chapter 3 and examined using a Scala RT-STM prior to being transferred, maintaining UHV conditions, into the x-ray absorption measurement chamber. The sample is exposed to a focused x-ray beam with tunable energy, 99±1 % circular and linear polarization, and a 0.1x1 mm^2 x-ray spot at full width at half maximum. The experimental setup, shown in Fig 4.1, consists in a series of connected UHV chambers: one dedicated to sample preparation, where several evaporation ports, a sputter gun and an e-beam are available; the RT-STM as well as a LEED setup for surface characterization are also in this chamber (blue square); a load-lock for sample loading for the outside (red); and the measurement chamber (green), where the sample is exposed to the x-ray beam. W(110) was cleaned by repeated

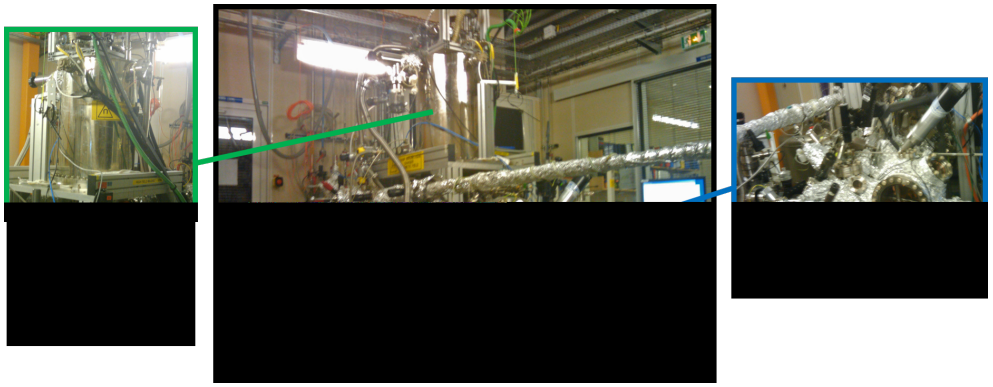

Figure 4.1: Experimental setup at beamline ID08, at ESRF. Sample preparation and STM characterization is performed in an independent UHV chamber, marked in blue. Sample loading is done via a small UHV load-lock chamber, marked in red. XMCD, XMLD and XAS experiments are perfomed in the chamber marked in green, in UHV and with controlled temperature in the 6-300 K range. Magnetic field up to 5 T can be applied along the beam direction.

oxygen annealing and flashing cycles prior to sample preparation until LEED measurements showing the reciprocal lattice of the W(110) surface with sharp spots, without trace of carbon reconstruction, were obtained. The state of the bare W surface was checked by STM to ensure a low density of C impurities and the regular, atomically flat terraces of the W(110) surface, as shown in figure 4.2.

The samples were mounted vertically on a variable-temperature (6–300 K) rotary stage holder which permitted rotation of the substrate around the vertical axis. A superconducting magnet allowed the application of magnetic fields of up to 5 T along the x-ray beam direction. X-ray absorption spectra (XAS) were measured at the $M_{4,5}$ absorption edges of Tm (corresponding to 3d to 4f core-to-valence electronic transitions) in the total electron yield mode by recording the drain current of the sample as a function of photon energy. The drain current was normalized by the photocurrent of a gold grid reference placed between the last refocusing mirror and the sample. The linearly polarized XAS were measured by aligning the electric field vector of the x rays to the vertical (I^v) and horizontal (I^h) axis, with the beam incident at an angle $\Theta = 70°$ with respect to the sample normal. The XMCD spectra were obtained by taking the XAS difference for parallel (I^+) and antiparallel (I^-) alignment of the photon helicity with the applied magnetic field. During the measurements, the pressure in the cryostat was about 2 x 10^{-10} mbar, without accounting for the decrease in pressure expected due to the cryogenic shields. No changes of the XAS line shape, due to either the x-ray beam or contamination, were

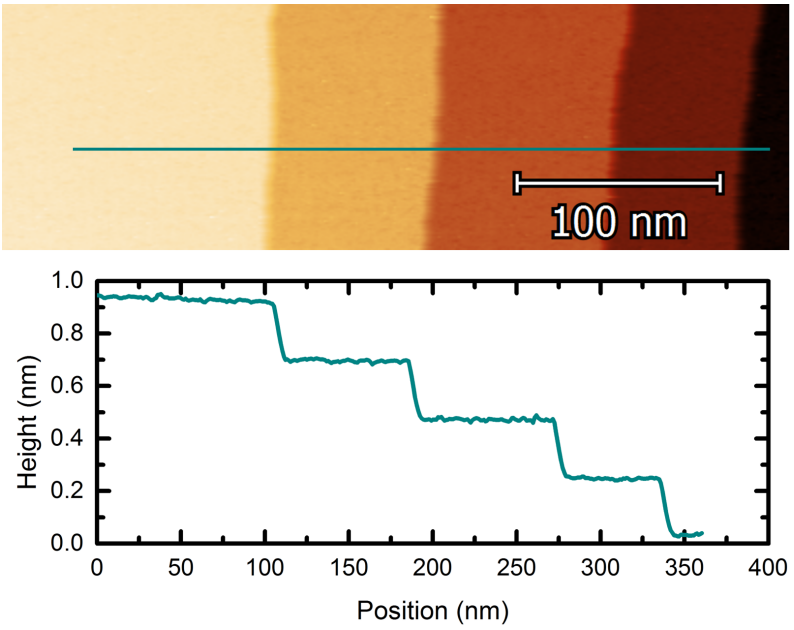

Figure 4.2: STM image of the clean W(110), as prepared prior to Tm evaporation, featuring regular clean atomic steps. (V_{Bias} = 100 mV, I_t = 1 nA)

observed within the few hours required to measure one sample, discarding any deterioration of the sample due to contamination or beam effects. The XAS data were simulated using ligand field atomic multiplet calculations [133, 134] as described in references [135, 136].

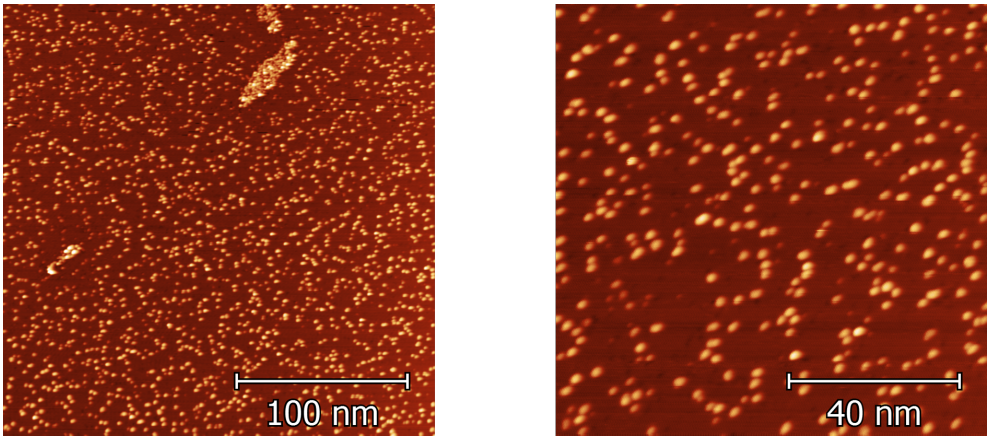

Figure 4.3: Overview and detail of samples with low coverage, featuring mainly single adatoms and trimers. Scans taken at room temperature, V_{Bias} = 2 V, I_t = 1 nA, using a Scala STM.

Two different sets of samples were studied by X-Ray Dichroism, as ilustrated in Figures 4.3 and 4.4. The case shown in Fig. 4.3 is obtained for short deposition times at low flux, leading to coverages around 2% consisting mainly in isolated Tm adatoms as well as some larger objects identified as dimers and trimers, as they split into individual adatoms at large enough tunnelling currents [91]; samples such as the one shown in Fig. 4.4 are grown at a higher flux rate followed by an annealing at temperatures around 1000 K, which leads to the formation of the one-monolayer-thick layer of Tm on W(110) with the hexagonal Moiré pattern discussed in the previous chapter.

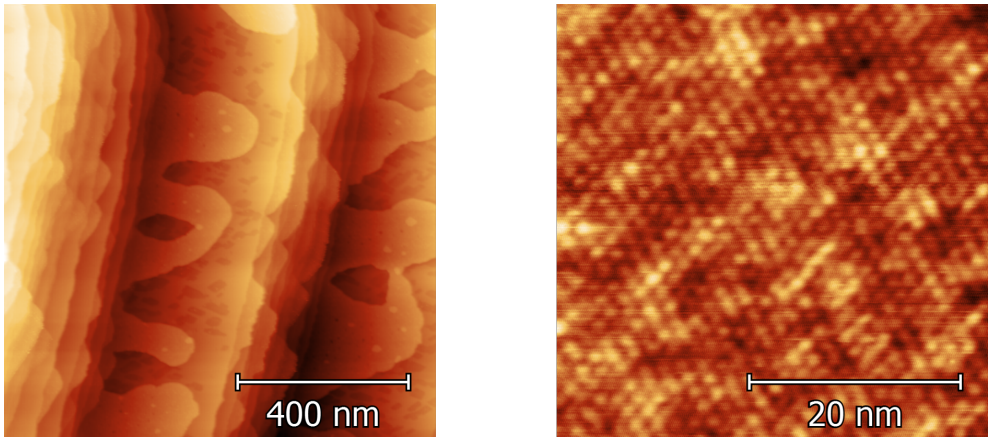

Figure 4.4: A 1x1 μm^2 overview of a sample featuring Tm monolayer islands with a coverage around 0.5 ML; on the right, detail of a 40x40 nm^2 area highlighting the Moiré pattern of the layer.

4.2 Electronic properties of Tm

X-ray absorption spectroscopy (XAS) is a technique capable of determining the electronic structure of a system. Using a crystalline monochromator, the photon energy of an x-ray beam can be tuned to induce an excitation of a core electron into an unoccupied state. The characteristics of the absorption spectrum provides information regarding the electronic transition, from which the configuration of ground state con be obtained.

4.2.1 Electronic ground state

Figure 4.5 shows the experimental and simulated x-ray absorption spectra for horizontally (h, out-of-plane) and vertically (v, in-plane) polarized light at grazing incidence ($\Theta = 70°$). The characteristic multiplet structures of

the RE $M_{4,5}$ absorption edges have been widely studied [133, 134, 137, 138] and can be used as a fingerprint for the valence state of the RE atoms in different compounds. The XAS of the isolated Tm adatoms as well as the monolayer show typical trivalent absorption features. For the $4f^{12}$ initial state configuration of Tm^{3+} the dipole selection rules allow $3d \rightarrow 4f$ transitions to $3d^9 4f^{13}$ final states with $^3H_6$, $^3H_5$, and $^3G_5$ symmetry, giving three absorption lines at the M_5 edge and a single line at the M_4 edge, as observed in Fig. 4.5. In contrast, a divalent $4f^{13}$ ground state, which is the usual case for RE atoms in gas phase with the exception of La and Gd, would give only one absorption line at the M_5 edge and none at the M_4 edge [133, 134, 137, 138]. Moreover, although most of the bulk elemental RE metals are trivalent, Tm forms divalent as well as trivalent and intermediate valence compounds. X-ray absorption and photoemission studies show that divalent Tm atoms are found not only in the gas phase [139], but also in rare gas matrices [140], endohedral fullerenes [141], and at low-coordinated surface sites of Tm films evaporated at low temperature [142].

No significant difference is observed in the XAS line shape of isolated adatoms compared to the ML sample, indicating that Tm atoms on W(110) have a stable $4f^{12}$ ground state, which can be attributed to the gain in cohesive energy of the $4f^{12}5d^16s^2$ configuration compared to the $4f^{13}5d^06s^2$ configuration [143] for Tm atoms adsorbed on a 5d metal [138]. The XAS line-shape analysis indicates a ground-state multiplet with J = 6.

To obtain more detailed information on the ground state of the Tm atoms and take into account the effect of the atomic environment, the XAS spectra in Fig. 4.5 were simulated in the presence of a crystal-field potential. The substrate was approximated by considering the two lowest-order axial crystal-field components described by the Hamiltonian $H_{CF} = B_2^0 O_2^0 + B_4^0 O_4^0$, where O_n^m are the Stevens operators. The adatom XAS in Fig. 4.5.a is well reproduced by using $B_2^0 = -637.2$ μeV and $B_4^0 = +3.5$ μeV, finding a ground state with $|J_z|$ = 5; the lowest-excited states are $|J_z| = 4$ and 6, separated by > 9 meV from the ground state. This indicates a predominant uniaxial magnetic anisotropy along the surface normal.

The relative intensity of the multiplet features in the linear-polarized XAS of the monolayer differs in comparison with that of the Tm adatoms. In particular, the peak heights of the horizontally polarized XAS are altered. This spectral line shape is neither in accordance with a $|J_z| = 6$, nor 4 or any other pure J_z ground state, and may indicate a mixed character of the ground state. Another possibility is to assume that the transversal crystal-field terms that would generate a mixing of different J_z states are negligible; in such a case the monolayer XAS can be well fitted by applying a strong out-of-plane magnetic

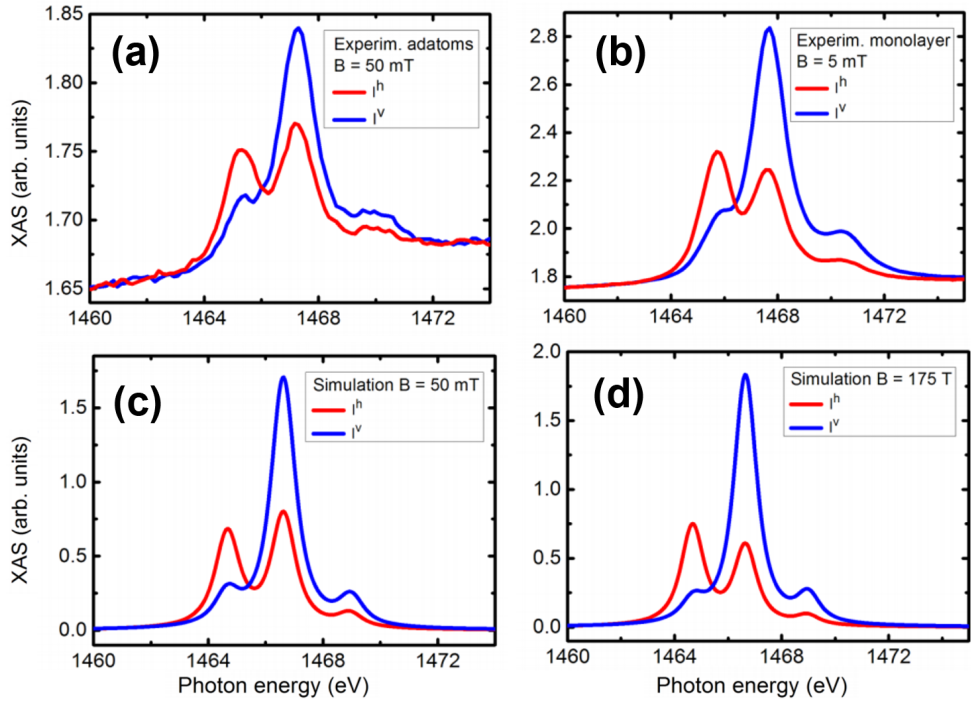

Figure 4.5: (a) Experimental linearly polarized XAS of Tm adatoms in a 50-mT field and (b) experimental linearly polarized XAS of Tm monolayer in a 5 mT field. Below, simulated linearly polarized XAS for non-interacting Tm atoms (c) in a 50 mT field applied parallel to the x-ray beam direction and (d) in a 175 T field along the surface normal. All data are measured/simulated at T = 8 K with the substrate normal tilted at 70° with respect to the x-ray beam direction.

field with B = 175 T. This strong field required for the fit could indicate a ferromagnetic or antiferromagnetic exchange coupling within the Tm monolayer, a possibility explored further in section 4.3.2. The application of a magnetic field leads to the closing of the energy gap between the J_z = -5 and -6 states with J_z = -5 still being the lowest state. Thus, the spectral weight of the J_z = -6 state increases in the absorption and modifies the XAS line shape with respect to the adatom case. This effect is strongest for the horizontal polarization while the vertically polarized XAS remains essentially the same.

4.2.2 STS on Tm adatoms

At this point it is interesting to compare this result with tunnelling spectroscopy experiments, as IETS spectra on rare earth adatoms attributed to excitations of the $4f$ states have been reported previoulsy in the literature

[101, 103], proposing as a single-atom long-lived two-state system in the case of Ho/Pt(111). The study of Tm adatoms on the W(110) surface was performed at low temperature (1 K) using a SPECS JT STM.

A ∼9 meV difference between ground and lowest excited state is of the order of the values reported for 3*d* metals on insulating surfaces (*e.g.* 4 meV for Fe adatoms on Cu_2N [70], reaching up to the 56 meV for Co on MgO, aproaching the theoretical limit for a 3*d* atom[136]) and much larger than for 3*d* metals on metallic surfaces (*e.g.* 0.75 meV and 0.19 meV for Fe on fcc and hcp sites of Pt(111), respectively [19]) suggesting that it could be possible to detect an inelastic excitation in low bias dI/dV tunnelling spectroscopy, in the form of steps at energy of the excited state.

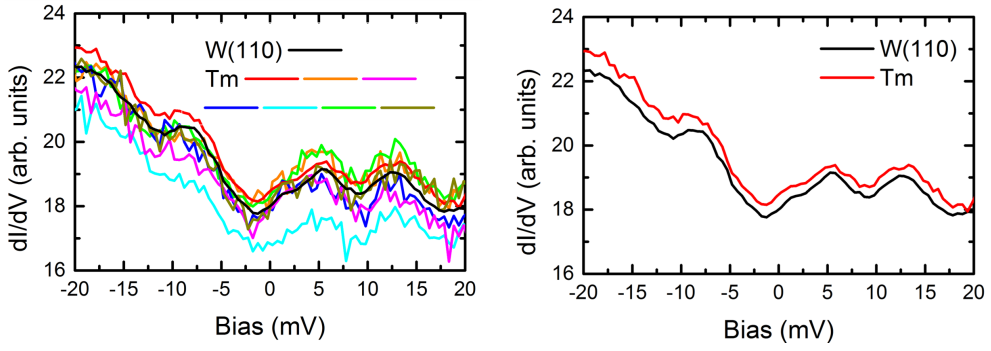

Figure 4.6: Differential conductance tunnelling spectroscopy performed on single Tm adatoms on a W(110) surface at T = 1 K. A representative set of spectra taken on Tm adatoms is shown on the left, along with the corresponding spectrum for the clean W surface for reference; to reduce clutter, a single Tm spectrum along with the reference on W, is shown on the right. No significant feature is observed for the Tm adatom, nor any evidence of inelastic excitation.

Figure 4.6 shows spectra taken on Tm adatoms on a W(110) surface over a ±20 mV range, regulating over the adatom at $I_t = 1$ nA, $V_{Bias} = 20$ mV prior to opening the feedback, and using a $V_{Mod} = 1$ mV modulation voltage; a spectrum taken on the clean W(110) surface is also included for reference. No significant feature, nor IETS signature in particular, is observed in this bias range, but rather the shape of the spectra is mainly tip-influenced, as shown in Fig. 4.6.b, where a single Tm spectrum is compared to the clean W reference showing an identical behaviour.

The absence of evidence of an inelastic excitation suggests that the tunnelling interaction between the metallic tip and the Tm adatoms is not producing an excitation of the $4f$ ground state. In chapter 7 an analysis of the SP current of magnetic and non magnetic RE adatoms on a ferromagnet shows

that, at these low bias, the tunnelling current consists predominantly of $5d$ electrons[31], leaving only the possibility of a two-electron process to mediate the inelastic excitation between the tunnelling electron and the internal, strongly shielded, $4f$ electrons, as suggested in [144]]. A recent work by [118], however, fails to observe any inelastic excitation in Ho adatoms on Pt(111) despite the electronic configuration obtained by XMCD data pointing to the existence of zero field splitting of 3.9 meV [145]. This result is in line with what is observed here for Tm adatoms on the W(110) surface, and reinforces the conclusions drawn in chapter 7, i.e., the tunnelling current at low bias is negligibly affected by the behaviour of the electrons in the $4f$ orbitals.

4.3 Magnetic properties of Tm

X-ray magnetic circular (linear) dichroism, or XMCD (XMLD), is obtained as the difference of XAS spectra taken with left and right circularly polarized light (horizontal and vertical, for XMLD). When the photon is absorbed by the electron, its angular momentum is transferred. Due to conservation of angular momentum during the interaction between photon and electron, an additional selection rule is added for the allowed transitions of the excited electron. This extra selection rule causes the photoelectrons to be ejected with a spin polarization according to the photon polarization, thus, the difference between the polarized XAS spectra (XMCD) reflects the difference in the density of empty states with different spin moment.

4.3.1 Magnetic moment and anisotropy

Fig 4.7 shows the XAS with circular polarization and corresponding XMCD spectra of the Tm adatom and monolayer samples measured at normal ($\Theta = 0°$) and grazing incidence ($\Theta = 70°$). The spectra were taken at 8 K in a 5 T magnetic field applied parallel to the x-ray beam direction. The average value of the M_5 edge jump intensity is normalized to 1 in order to compare the spectra measured on different samples. It should be noted that the Tm absorption signal is superimposed on the background intensity of the substrate due to the x-ray absorption of W in this photon energy range. The sharp multiplet features of the Tm XAS indicate that the spin and orbital magnetic moments must be close to those expected for the $4f^{12}$ ground state, namely, 2 and 5 μB/atom, respectively [146]. This is confirmed by the very large XMCD asymmetry measured at 8 K and by the orbital-to-spin moment ratio estimated from the XMCD sum rules. For the RE, this ratio is given by [147, 148]

$$\frac{\langle L_Z \rangle}{\langle 2S_Z \rangle} = \frac{X_{M_5} + X_{M_4}}{X_{M_5} - \frac{3}{2}X_{M_4}} \left(1 + 3\frac{\langle T_Z \rangle}{\langle S_Z \rangle}\right)$$

where $\langle L_Z \rangle$, $\langle S_Z \rangle$, and $\langle T_Z \rangle$ are the expectation values of the orbital, spin, and magnetic dipole moments parallel to the x-ray direction, and X_{M_4} (X_{M_5}) represent the XMCD intensity integrated over the M_4 (M_5) energy edge, respectively. Using the calculated ratio for Tm^{3+}[146], $\langle T_Z \rangle$ / $\langle S_Z \rangle$ = 0.41, the orbital-to-spin ratio obtained for both adatoms and monolayer results in $\langle L_Z \rangle / \langle S_Z \rangle = 2.5 \pm 0.1$.

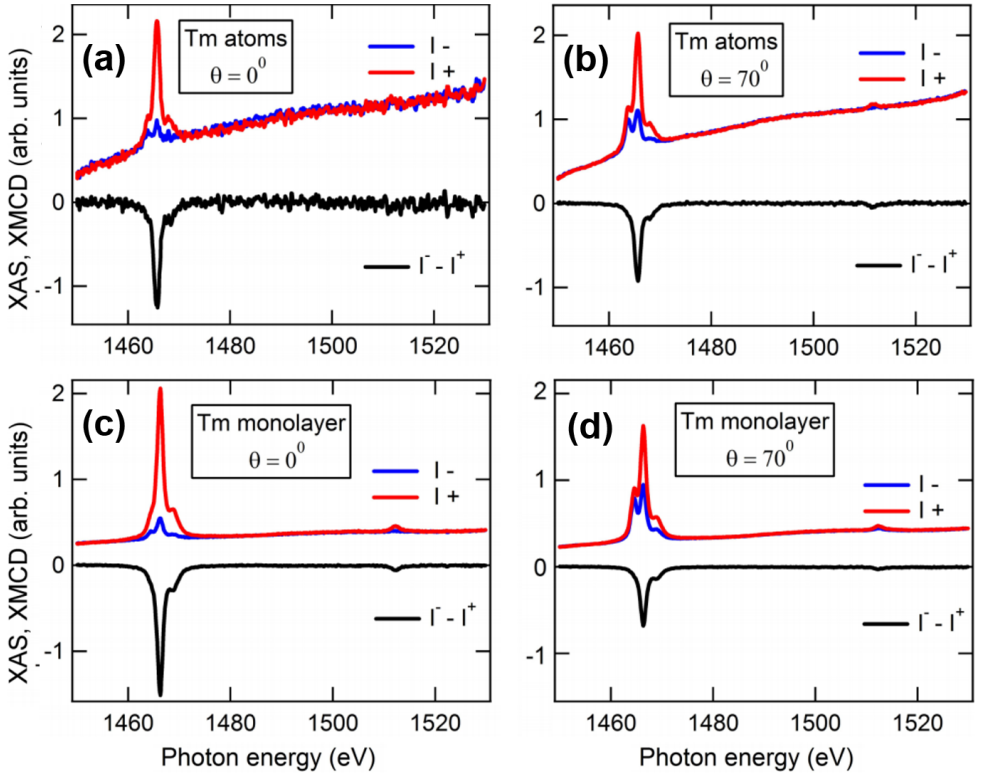

Figure 4.7: XAS and XMCD spectra of Tm adatoms on W(110) at (a) grazing and (b) normal incidence; below, the spectra for the Tm monolayer at (c) grazing and (d) normal incidence. Measurements are taken in a 5 T magnetic field applied parallel to the x-ray direction at T = 8 K. The XMCD spectra are calculated as the difference between I^- and I^+.

Figure 4.7 also shows that the XMCD amplitude is larger at normal incidence compared to grazing incidence. This implies that, for equal applied magnetic fields, the Tm magnetization is larger at normal incidence, i.e., that both the Tm adatoms and the monolayers have an out-of-plane easy axis, as expected from the results of the ligand field multiplet calculations presented

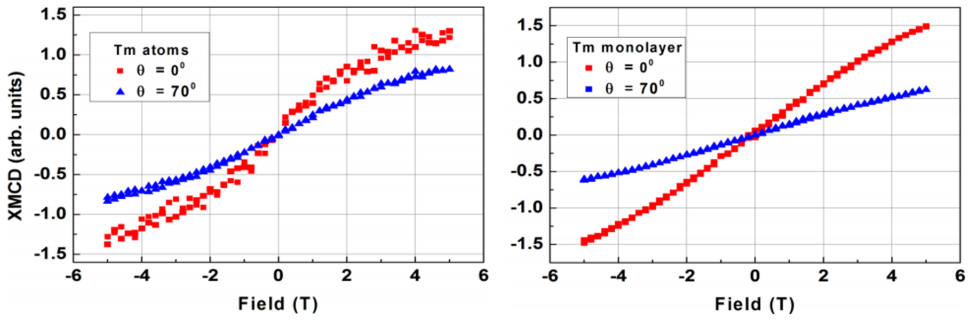

Figure 4.8: Field dependence of Tm XMCD intensity measured at the M_5 edge for the adatom (left) and the monolayer (right) samples at 8 K.

previously, in section 4.2.1. Magnetization loops were measured by recording the peak XMCD intensity at the M_5 edge at different magnetic fields. Figure 4.8 shows the field dependence of the XMCD of the Tm adatom and monolayer samples at normal and grazing incidence. The larger amplitude of the XMCD loops at normal incidence agrees with the easy magnetization axis being perpendicular to the substrate for both the Tm adatoms and the Tm monolayers. The comparison between the two curves, however, is not straightforward. According to the XMCD sum rules, the M_5 XMCD intensity is proportional to $4\langle S_\Theta\rangle + 3\langle L_\Theta\rangle + 12\langle T_\Theta\rangle$, where Θ is the direction of the x-ray beam. For a given Θ, since S, L, and T are strongly coupled together, this quantity is proportional to the Tm magnetization. Due to the strong anisotropy of L and T in the RE, the proportionality factors between the magnetization $(2\langle S_\Theta\rangle + \langle L_\Theta\rangle)$ and the M_5 XMCD intensity measured at $\Theta = 0°$ and 70° can differ significantly, which complicates a quantitative comparison between the two curves; as a consequence, it is also difficult to estimate the magnetic anisotropy energy from such curves. The interpretation can be further obscured by other effects, such as the RKKY interaction among adatoms, which cannot be quantified here, but may have an effect on the magnetization behaviour [102, 149].

4.3.2 Magnetism of monolayer films

The nonhysteretic shape of the magnetization curves in figure 4.8 indicates the absence of either ferromagnetic or ferrimagnetic ordering in both samples over this range of experimental conditions. Figure 4.8, moreover, shows that the normal incidence and grazing incidence XMCD curves of the Tm monolayer have a less pronounced S shape compared to the curves for adatoms, discarding a superparamagnetic behaviour of the monolayer. Thus, an additional anti-

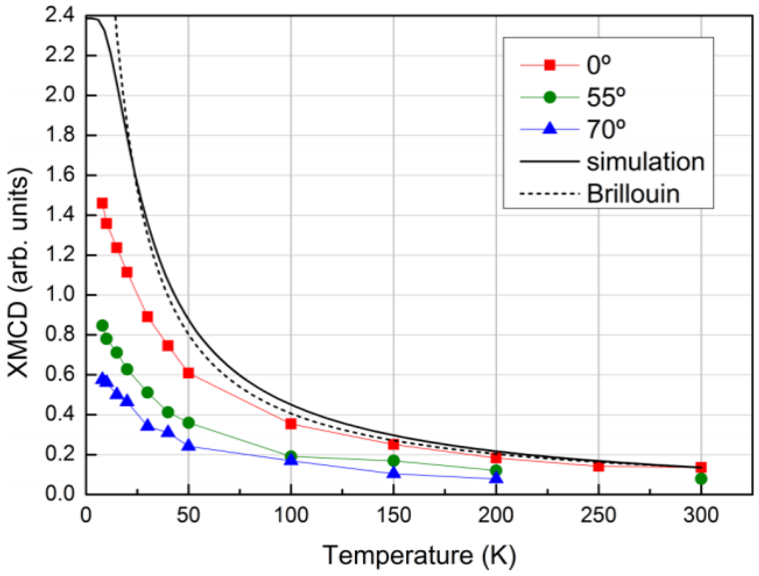

Figure 4.9: Tm monolayer XMCD as a function of temperature compared to the paramagnetic behaviour expected for noninteracting Tm atoms. Experimental data taken in a 5 T magnetic field applied parallel to the x-ray beam, at $\Theta = 0°$, 55° and 70°. Paramagnetic curves were calculated using a spin Hamiltonian model and crystal-field parameters obtained from the multiplet simulations (solid line), and by assuming a Brillouin function with the Tm^{+3} parameters J = 6 and g = 7/6 (dashed line). The calculated curves are normalized to the experimental data at 300 K.

ferromagnetic coupling in the Tm monolayer seems the most likely possibility. To further investigate the possibility of magnetic interactions in the Tm monolayer, Tm XMCD spectra while cooling down the sample in a magnetic field of 5 T are acquired, as seen in figure 4.9, where the evolution of the XMCD intensity at the M_5 edge as a function of temperature is plotted. The experimental data are compared with simulations of the Tm magnetization according to a spin Hamiltonian model taking into account the crystal-field parameters B_2^0 and B_4^0 and a Brillouin function calculated for J = 6 and a magnetic field of 5 T. In either case, a departure of the experimental magnetization from the predicted paramagnetic dependence can be noticed, particularly prominent for temperatures below 100 K, suggesting the setting in of magnetic correlations around this temperature. Since the experimental magnetization in this low-temperature range is lower than predicted by the paramagnetic simulations, it can be inferred that the Tm-Tm interactions are antiferromagnetic. Rather than XMCD, the investigation into the antiferromagnetic correlations of the Tm monolayer is better suited for x-ray magnetic linear dichroism (XMLD), which is sensitive to uniaxial magnetic ordering (in contrast with XMCD, which

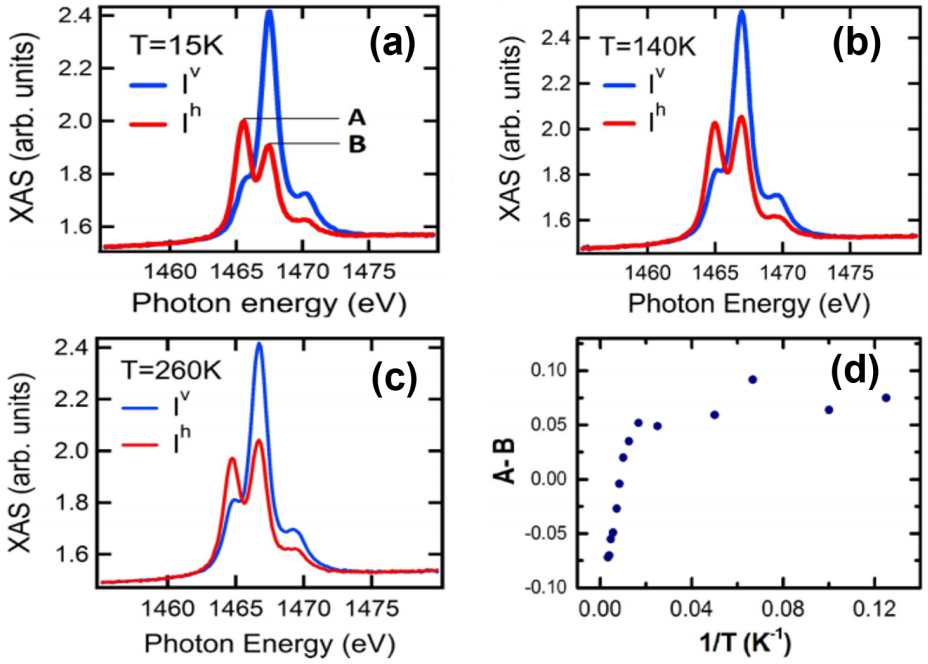

Figure 4.10: Linearly polarized XAS spectra measured on the Tm monolayer at three different temperatures: 15 K (a), 140 K (b) and 260 K (c). All spectra were taken with the substrate normal tilted at $\Theta = 70°$ with respect to the x-ray beam direction. A small (5-mT) magnetic field was applied to enhance the electron yield of the sample without significantly affecting its magnetic configuration. The first and second peaks in the h-polarized spectra are labeled A and B, respectively. (d) Temperature dependence of the difference between A and B peaks.

probes unidirectional magnetic ordering) and therefore suited to detect antiferromagnetic coupling [150]. Figures 4.10.a–4.10.c show the M_5 edge linearly polarized XAS measured at three different temperatures. For the spectra labelled I^v (vertical polarization), the photons are polarized parallel to the sample plane and therefore these spectra are sensitive to changes in the in-plane magnetic ordering of the Tm monolayer. For the spectra labelled I^h (horizontal polarization), the photons have a finite linear polarization component along the sample normal, and therefore are sensitive to changes in the out-of-plane magnetic ordering of the Tm monolayer.

Whereas the v spectra change little with temperature, there is a notable temperature dependence of the h spectra. Figure 4.10.d presents a plot of the difference between the first and the second peaks in the h spectra (marked as A and B in Fig.4.10.a) as a function of temperature. The difference between the two peak values increases with 1/T at high temperatures and reaches a

saturation value at about 50 K, suggesting that antiferromagnetic correlations are well established at this temperature. The fact that these changes occur in the h spectra suggests that the axis of antiferromagnetic ordering is parallel to the sample normal, in agreement with the easy-axis direction determined from the magnetization curves in Fig. 4.8. This conclusion is further supported by the I^h and I^v spectra simulated by considering noninteracting adatoms and an out-of-plane magnetic field of B = 175 T, which can be attributed to antiferromagnetic exchange. As shown in the bottom row of figure 4.5, the application of such a strong field reproduces the change of intensity of the A and B peaks observed upon cooling.

It is instructive to compare the magnetic behavior of Tm monolayers on W(110) with that of bulk Tm. Neutron diffraction and ac susceptibility studies [28, 29, 151] have shown that bulk Tm undergoes an antiferromagnetic transition at T = 58 K, followed by a transition to ferrimagnetic ordering at T = 33 K. These low magnetic ordering temperatures are attributed to the strong localization of the 4f electrons, which makes the exchange interaction with neighbouring atoms small. Interactions with the neighbours still occur, but indirectly via s and p electrons, which favour antiferromagnetic ordering [132]. Between 58 and 33 K, the bulk Tm moments are aligned ferromagnetically within the hcp basal planes and have a sinusoidal modulation along the c axis, such that the ordering is antiferromagnetic along the c axis. As opposed to bulk Tm crystals, the Tm monolayers studied here display antiferromagnetic coupling within the basal plane. Antiferromagnetic coupling is favoured parallel to the substrate normal by the perpendicular magnetic anisotropy generated through hybridization with the electronic states of the W(110) substrate.

The presence of antiferromagnetic coupling within the plane of the Tm monolayer is therefore intriguing and raises the question of the magnetic ground state of this system, as the Tm lattice is (nearly) hexagonal, as seen in chapter 3, and therefore geometric frustration is expected to play an important role as there is no unique ground state for a triangular arrangement of magnetic moments coupled antiferromagnetically with each other [152, 153]. Depending on the relative value of the exchange coupling, magnetic anisotropy, and external field, several configurations are possible such as, *e.g.*, one spin pointing up and two pointing down at an angle or collinear with each other, or a canted spin structure with a net perpendicular component aligned along the field direction [154]. This may explain why the magnetic response of the Tm monolayer is larger when the magnetic field is applied perpendicular to the substrate compared to grazing incidence (Figs. 4.8 and 4.9), opposite to that of an isotropic antiferromagnet for which the field-induced magnetization is larger in the direction perpendicular to the antiferromagnetic axis. Moreover, owing to the large degeneracy of the magnetic ground state, frustration in two-dimensional

systems may also lead to an intrinsically disordered ground state in the absence of an external field. This is the case for a two-dimensional triangular antiferromagnet of the Ising type [152]. Lattice distortions and defects that affect the exchange interaction between neighbouring magnetic ions lead to a partial lifting of frustration. However, even in such a case, frustration will induce a suppression of the ordering temperature below that corresponding to the energy scale of the exchange interaction, so that a correlated antiferromagnetic state persists in the absence of magnetic order. The experimentally determined near-hexagonal lattice 3, antiferromagnetic spin alignment at low temperature, uniaxial anisotropy, and lack of magnetic remanence for Tm monolayer films are consistent with this picture, although alternative explanations based on Tm domains with fully compensated staggered magnetization or noncollinear structures due to the influence of the Dzyaloshinskii-Moriya interaction at the Tm/W(110) interface[155, 156] cannot be excluded at this point.

X-Ray Dichroism, while a powerful tool for probing individual electronic levels, is not well suited for discerning the actual spatial distribution or structure of said properties, as the information provided is averaged across the whole beam spot, orders of magnitude larger than the atomic length scales here involved, which leaves the question regarding the actual magnetic structure of the Tm layer somewhat unsettled. This kind of properties are better suited for a study by means of diffraction (neutron, in the case of magnetic properties) rather than absorption or, switching to a different set of tools, locally resolved microscopies.

4.3.3 SP-STS on the Tm monolayer

In an attempt to complement the area-averaged information provided by the XMCD experiments, spatially resolved with spin sensitivity have been performed, by means of SP-STM. This spin-sensitive, spatially-resolved technique has been used in the literature to observe AF lattices with atomic resolution[157], and has been used in this thesis to study systems with subnanometric magnetic features in chapters 6 and 7.

The appropriate probe for spin-polarized STM experiments depends on the magnetic configuration of the sample under study. As the expected behaviour from the XMCD/XMLD analysis of the Tm monolayer is antiferromagnetic with an out-of-plane easy axis, although non-collinear effects cannot be discarded, a bulk Cr tip is used for the experiments in this section. This tip presents a magnetic easy axis tilted respect to the geometric tip axis, thus is sensitive to changes in both the out-of-plane and in-plane polarization of the sample. To check that this was indeed the case, the tip is first tested on

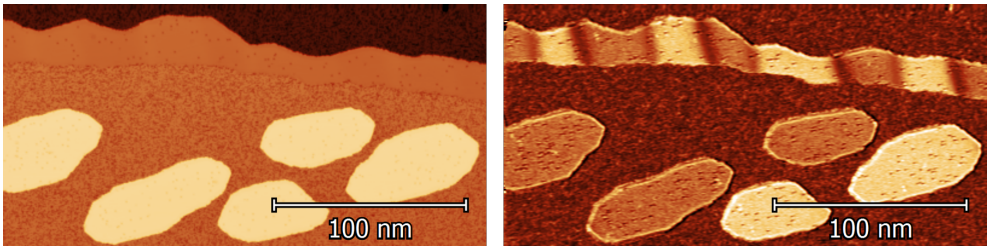

Figure 4.11: STM topography (left) and dI/dV map (right) of the Fe atomic double layer on W(110) at V_{Bias} = -80 mV, I_t = 800 pA using bulk Cr tip. Noticeable contrast is visible between out-of-plane domains (*i.e.* dark and bright islands, as well as dark and bright domains along the larger Fe wire) and in-plane areas (*i.e.* the two different dark hues marking the in-plane domain walls between out-of-plane domains).

a known system, such as the Fe double layer on W(110), which presents a spin-spiral for multidomain configurations due to Dzyaloshinskii-Moriya interaction, with out-of-plane domains separated by alternating in-plane domain walls, maintaining the sign of the helicity [74, 158, 159]; for small islands, the configuration consists in out-of-plane single domains. Figure 4.11 presents the topography and differential conductance at V_{Bias} = -80 mV of such a sample, where this configuration is readily identifiable, obtaining discernible contrast between opposite out-of-plane domains as well as for opposite in-plane domain walls.

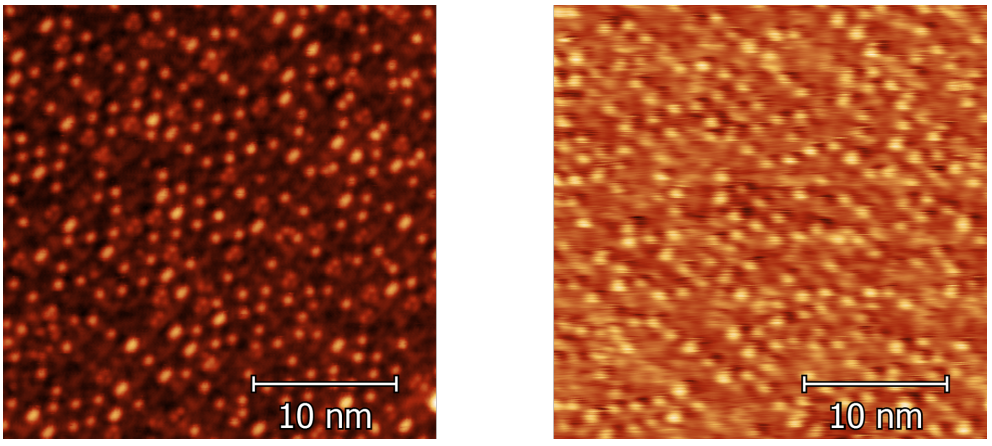

Figure 4.12: STM topography (left) and dI/dV map (right) of the Tm monolayer on W(110) at V_{Bias} = 100 mV, I_t = 200 pA.

The Tm monolayer on W(110) presents an additional complication that sets it apart from the successful examples of spin-polarized atomic resolution in the literature (*e.g.* a 15 pm corrugation of the spin averaged Cr layer in

reference [157]), and that is the high corrugation of the surface imposed by the Moire pattern, larger than that of the actual Tm lattice (around 15 pm for the atomic lattice and around 40 pm for the Moiré pattern, measured at V_{Bias} = 10 mV, I_t = 2 nA) and with a larger, but comparable, periodicity (a_{Tm} = 4.08 Å, a_{Moir} = 1.54 nm). This complicates obtaining data with atomic resolution, specially at the low scan speeds required for dI/dV maps and spectra; it also becomes a challenge in faster constant current topography images, as possible changes in z that could be attributable to a SP contribution are masked by the irregularity of the surface. Fig 4.12 shows an example of how the dI/dV signal strongly correlates with the constant current topography, complicating the extraction of any spin polarized information.

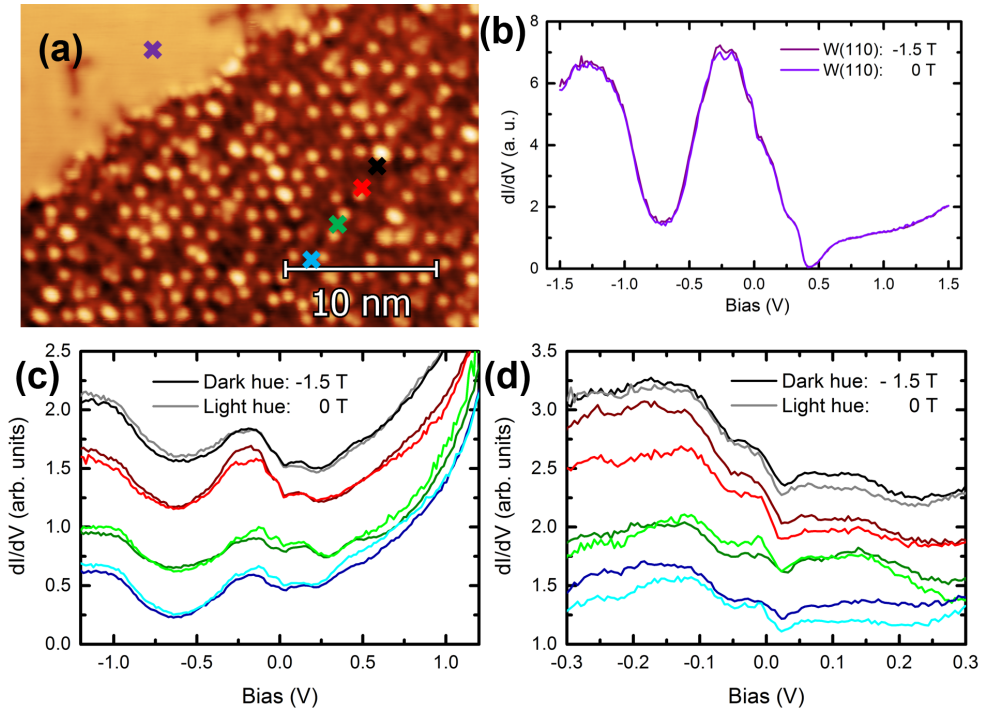

Figure 4.13: (a) STM topography image illustrating with coloured crosses the positions where spectra are taken. (b) Spectra taken on the W(110) surface at -1.5 T and 0 T. Below, spectra taken on the indicated positions on the Tm monolayer (c) over a ±1.2 V range, and (d) spectra on the same positions over a ±300 mV range. Spectra are vertically offset for clarity.

A different approach is to compare dI/dV spectra and maps taken at different fields as, while an AF lattice should remain unaffected, it could reveal the presence of domains or non-collinear orientations in the magnetic configuration that would be affected by the field. Comparing spectra at different fields requires a non-magnetic reference to ensure that any observed features

are not due to the electronic changes of the tip, but rather due to the relative polarization of tip and sample. Fig 4.13 (top left) shows the edge of the Tm monolayer, where a clean portion of the W(110) surface is also visible, which serves as reference. To the right, spectra taken at 0 T and -1.5 T on W show that no significant change in the non-magnetic behaviour of tip is observed.

The locations for the spectroscopy on the Tm layer have been repeated for different fields and bias ranges. A representative set of these spectra is shown on the bottom row of figure 4.13, over a ±1.2 V range on the left and a narrower ±300 mV range on the right. In the former, negligible differences in behaviour are observed between spectra taken at -1.5 T (shown in darker colours) and taken at 0 T (in lighter colours); in the latter, with higher energy resolution, the slight differences observed previously remain, leaving open the possibility that said features are spin polarized and thus affected by the magnetic field. However, due to the mentioned irregularity of the surface, these changes can be explained without attributing them to a magnetic response but rather a slight offset in the spectroscopy locations. To explore this possibility, dI/dV maps at multiple bias and different fields are also performed.

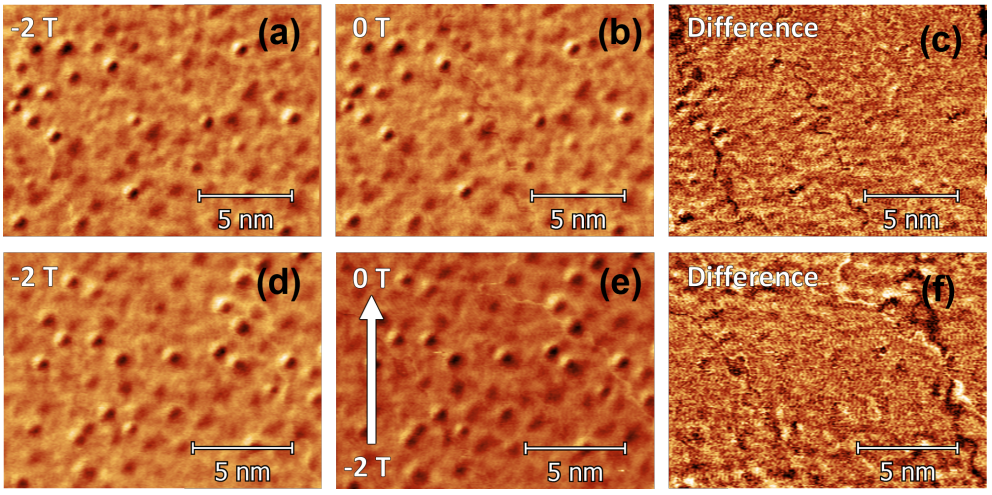

Figure 4.14: STM dI/dV maps of the Tm monolayer using a bulk Cr tip at V_{Bias} = -20 mV, I_t = 1 nA. The top row presents a comparison of the same area (a) at -2 T and (b) at 0 T; the bottom row presents a different area (d) at -2 T and while ramping from -2 T to 0 T (e). A direct subtraction of the maps corresponding to the same areas at different fields is presented on the right, (c) and (f) respectively, showing no regular feature attributable to a magnetic response.

Comparing dI/dV maps of the same area compensates for any possible drift, as the focus is on patterns in the area of interest rather than the value at a particular point. For a more direct comparison, images of the same area can

be aligned by software during data analysis, allowing for a direct subtraction of one from another.

Figure 4.14 shows this procedure performed over a small area of the Tm monolayer, in the same area as figure 4.13. In the spectra, a feature at V_{Bias} = -20 mV appears as the most significant difference between fields; differential conductance maps are therefore performed at this bias. The top row of figure 4.14 shows the same area at -2 T (a) and at 0 T (b), with the direct subtraction to the right, in (c); within the noise level, no feature is observed. Similarly, the bottom row in figure 4.14 shows a small area of the same island measured at -2 T (d) and while ramping the field from -2 T to 0 T from top to bottom (e); as before, no significant feature is observed within the noise level of the subtracted images (f).

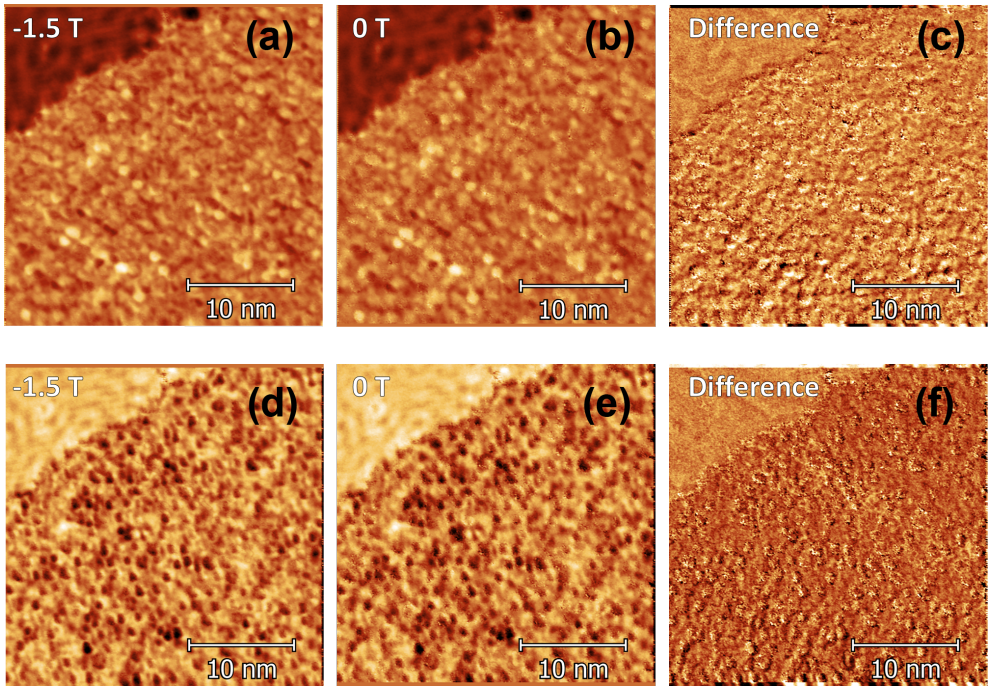

Figure 4.15: STM dI/dV maps of the Tm monolayer using a bulk Cr tip at V_{Bias} = ±150 mV, I_t = 1 nA. (a) Map taken at V_{Bias} = +150 mV and -1.5 T, reducing the field (b) to 0 T does not show significant differences, as illustrated by (c) the direct subtraction of the maps at different fields. Below, a similar process is followed at V_{Bias} = -150 mV, (d) corresponds to -1.5 T and (e) to 0 T, but no clear feature is observed (f) after subtraction.

Besides the overshadowing of possible spin polarized contributions by the high corrugation imposed by the Moiré pattern, it is also possible that the asymmetry of the spin polarization is not that significant at -20 mV, despite

what seems apparent in the spectra. Following this line of thought, maps taken at different intervals over a ±370 mV range where compared. The case for V_{Bias} = ±150 mV is presented in figure 4.15, as at this bias, particularly in the case of the red spectra, fig. 4.13 suggests that a difference could be observed. The top (bottom) row in fig. 4.15 corresponds to maps taken at V_{Bias} = +150 mV (-150 mV); as in the previous figure, the left column is measured in the presence a field of -1.5 T along the sample normal while the centre column is measured at 0 T. Similarly, the analysis of the rest of the maps in the studied bias range offers no insight into magnetic features of the Tm monolayer.

It should be expected that, if there were a field-sensitive domain configuration or non-collinear spin distribution, evidence of their response to an external field should be observed in the measurements presented above, although not having obtained the atomic resolution of the Tm lattice while maintaining spin polarized sensitivity leaves an obvious next step for further characterization. Another point that must be taken into consideration is that the XMCD/XLD measurements are performed on the $M_{4,5}$ edge, that is, probing directly the highly localized $4f$ orbitals; the case is different for STM, which interacts with electrons in the conduction band, corresponding to outer shells (s, p, d), and only indirectly through them with the $4f$. As the polarization of the LDOS is orbital dependent, no definite conclusion can be extracted regarding the magnetic ordering of the $4f$ in the Tm monolayer on W(110). While no conclusive affirmative results are obtained, the fact that no evidence for domains nor non-collinear magnetization is observed suggests that an atomic-wise antiferromagnetic lattice of the $4f$ moments is the underlying configuration, although an experimental confirmation has eluded the SP-STM experiments here performed. Spin polarized atomic resolution imaging and spectroscopy or a wholly different set of tools, such as a magnetic scattering study by neutron diffraction, could provide further insight.

Chapter 5

RE adatoms on Cu_2N

The study of free atoms is of importance from a fundamental physics point of view, however the experimental realization of such a study can be challenging. Clean metal surfaces are the most usual substrate for STM experiments, and are particularly suited for atomic manipulation and the construction of artificial structures, as the low diffusion barriers of adsorbed atoms and molecules and flat surface potential of the metal allows for reproducible lateral atomic manipulation; however, the counterpart is that metals might not be the ideal substrate for the investigation of the electronic properties of said atoms and structures, as their orbitals will strongly couple with the surface state of metals. Although an insulating substrate is not a valid sample for STM, an intermediate situation consisting in a thin insulating film grown on a conductive sample has proven to be a viable and fruitful avenue for STM experiments [160].

The role of the insulating layer is to electronically decouple adsorbed atoms and molecules from the metallic substrate by introducing a second tunnel barrier between the atoms and molecules and the metal, represented schematically in figure 5.1[161]. This opens several interesting avenues for research, as, to name a few, in the new situation molecular bonds that were previously hybridized will retain its discrete energy levels and allow its orbitals to be imaged by STM [69], lifetimes of quantum states can improve significantly due to the closing of decay paths involving scattering with substrate electrons [162], or the charge state of a single atom can be controlled, charging and discharging a single electron [163]. This chapter is most interested, however, in the use of thin insulating layers to enhance single-atom spin flip spectroscopy, as has been done to great effect for $3d$ atoms[164, 165].

The electronic structure of rare earths differs from that of transition metals in the $4f$ electron shell, incomplete in the case of rare earths, while for transition metals it is either empty, as in lighter $3d$ and $4d$ elements, or complete for

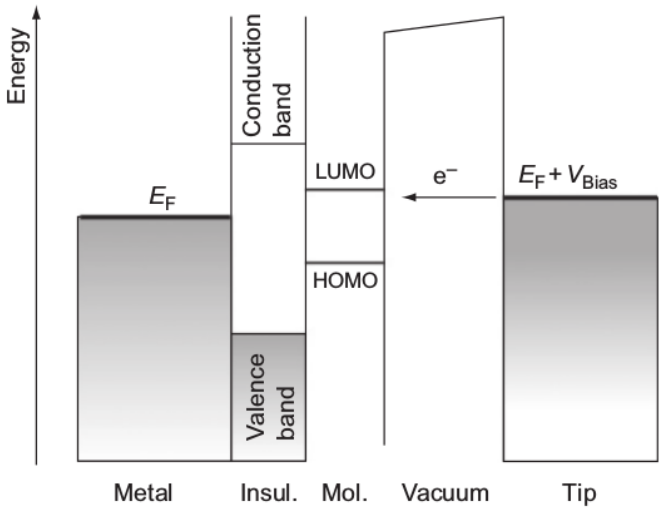

Figure 5.1: Diagram of the tunnelling process for a molecule on a thin insulating layer. Due to the separation imposed by the insulating layer, only a weak electronic coupling of adsorbates to an underlying conducting substrate occurs. [161]

the case heavier $5d$ metals. Accessing these states is an area of open research in single atoms [118, 144, 166–168] and molecules with RE centres [169–172], as they have great interest for technological applications as single-atom[15] or single-molecule magnets[173]. Apart from STM, other approaches have been used in the literature, particularly XMCD[15, 119, 145] to explore the magnetic properties of single rare earth adatoms on different surfaces.

In this chapter two different rare earth species, Tm and Lu, are studied as single atoms on a metallic Cu(100) surface and on an insulating Cu_2N layer grown on it. By performing differential conductance spectroscopy over different energy ranges, a mapping of the LDOS of the RE adatoms is obtained. The origin of the electronic features can be further explored by first principles calculations, determining their orbital character. In single RE atoms, the presence of an inelastic excitation at low bias would indicate a spin excitation of the $4f$ orbital is produced by the tunnelling current, opening a pathway for probing and switching the magnetic state of the atom.

5.1 Tm on Cu_2N

The decoupling insulating layer used in this chapter consists in a single atomic layer of Cu_2N [174–176], prepared by implanting N atoms on a clean Cu(100) surface (see chapter 2.3.2). Before dosing rare earth atoms on the sample it

is convenient to characterize the surface, as prepared. As much of the effort is going to be invested into dI/dV spectroscopy over a wide energy range, it is important to perform a prior characterization of both Cu(100) and Cu_2N. Fig.5.2.a shows an STM image of a typical Cu_2N sample, and the dI/dV spectra taken over ±3 V on (b) Cu(100), and (c) Cu_2N the feature at 2 V being due to the end of the insulating gap[175].

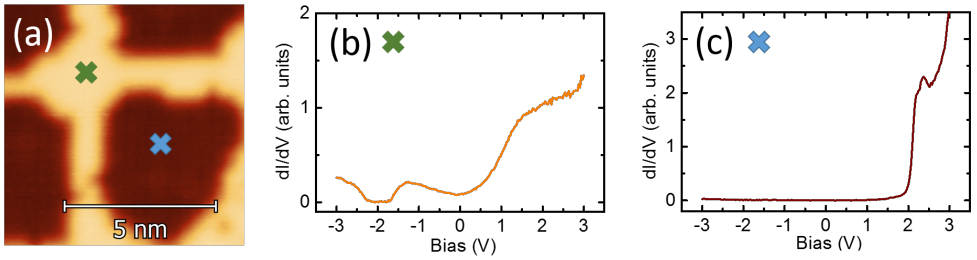

Figure 5.2: (a) Detail of a STM image of Cu_2N islands on Cu(100) and dI/dV spectroscopy on the two areas, (b) the remaining clean Cu(100) surface and (c) a Cu_2N island.

The study of Tm adatoms presented in this section was done in collaboration with the group of Dynamics of Nanoelectronic Systems at the Center for Free-Elecetron Laser Science (CFEL) in Hamburg, under the leadership of Dr. Sebastian Loth. The experimental system, a ^{3}He LT Unisoku STM, differs from the other setups used in this thesis in that the sample is loaded vertically into the STM stage, which is enclosed in a large Helium cryostat housing a set of superconducting coils allowing for 2 T / 2 T magnetic field in plane, and up to 9 T perpendicular to the sample. As a trade-off, the configuration does not allow for evaporation ports with direct access to the STM stage. Thulium atoms were evaporated by e-beam heating a Mo crucible with bulk Tm (99.99% purity) onto a pre-cooled Cu_2N surface to minimize diffusion and cluster formation. The evaporation was performed in the preparation chamber after pre-cooling the sample to 4 K in the STM stage for three and a half hours; in order to minimize heat transfer to the sample, the transfer rod was also pre-cooled by remaining in contact with the 4 K thermal shield of the cryostat.

The same preparation process was repeated using a Cernox temperature sensor instead of the Cu_2N sample, including a mock Tm evaporation, in order to determine the temperature that the sample reaches during preparation. As temperature read out is only possible when the sample is fully inserted into the STM stage, a process that can take up to a minute, some cooling will have occurred prior to read out, and thus this temperature serves as a lower limit. The recorded temperature evolution is presented in figure 5.3.

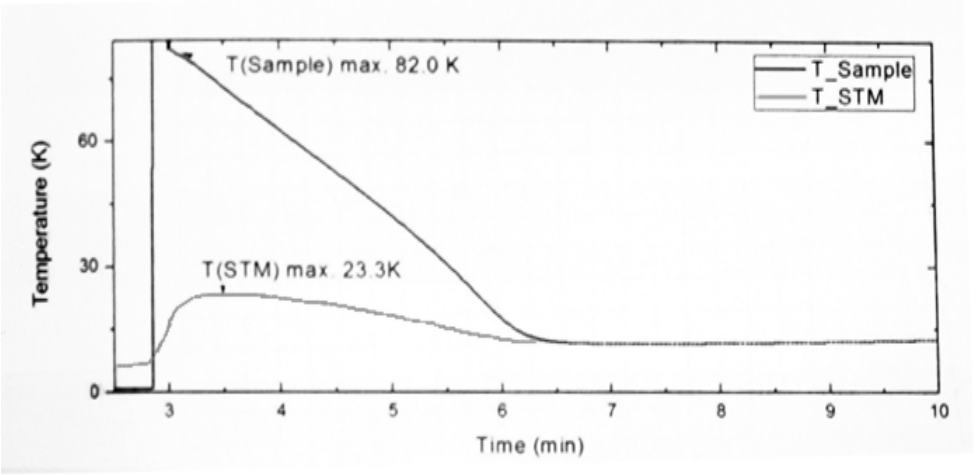

Figure 5.3: Temperature evolution of a Cernox sensor used to simulate the evaporation process. The sample was precooled to 4 K in the STM stage, extracted into the preparation chamber and exposed to the Tm flux, and returned to the STM stage. The initial temperature, 82 K, is recorded when the sample is fully inserted.

Despite reaching a temperature a little above 80 K during the evaporation process a clean sample with individual Tm adatoms is produced, although there is evidence evidence of a non-negligible diffusion, as can be seen in Fig.5.4.a: While adatoms on Cu_2N appear evenly distributed, adatoms on the Cu(100) surface accumulate near the Cu-Cu_2N borders, indicating that this frontier acts as a pinning center, and also that diffusion is higher on Cu than on Cu_2N. Profiles taken on Tm adatoms at 150 mV show a height of 260 pm for adatoms on Cu, and 240 pm for adatoms on Cu_2N (Fig.5.4.b, c), while the Cu_2N patches appear as a 100 pm dip, represented by a darker color in the topography image.

5.1.1 Spectroscopy on Tm/Cu_2N

Identification of the adatoms is done by performing dI/dV spectroscopy on different objects over a wide energy range (±3.5 V), both for objects on the Cu(100) surface and for objects on the Cu_2N patches. Representative spectra of each case are shown in figure 5.5. Two different behaviours are observed, depending on the substrate: Objects on Cu(100) all present a similar spectra (Fig. 5.5.a), indicating that they are all the same species, consistent with the objects being single Tm atoms; objects on Cu_2N also present a coherent spectra (Fig. 5.5.b), although different than that observed in the previous case. On Cu(100), the spectra of Tm adatoms somewhat resembles the spectra of bare Cu (Fig. 5.2.b); on the other hand, the features are sharper for Tm adatoms

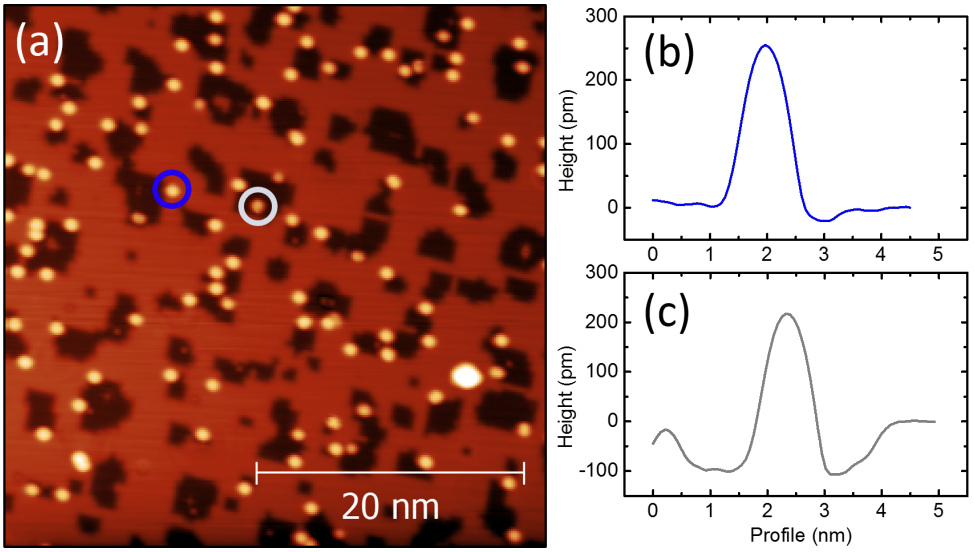

Figure 5.4: (a) Topography of a Cu_2N sample with Tm adatoms, taken at V_{Bias} = 150 mV, I_t = 1 nA. Profiles over the indicated Tm adatoms: (b) on Cu(100), indicated in blue; and (c) on Cu_2N, indicated in grey.

on Cu_2N, presenting a larger peak at 2.1 V an additional smaller feature at 0.8 V.

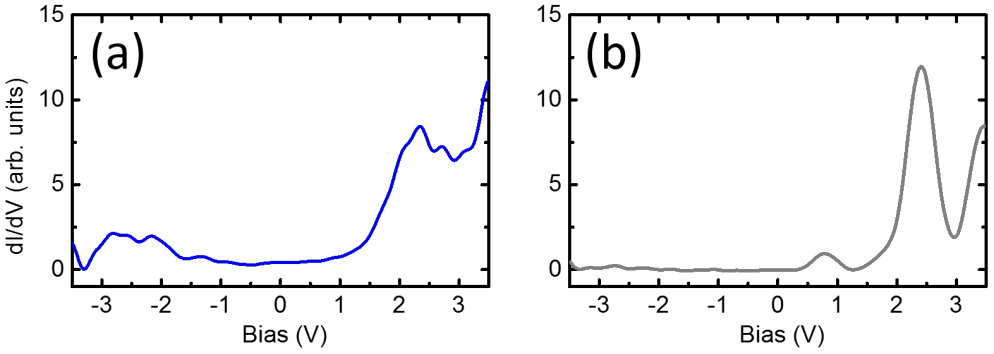

Figure 5.5: Spectra taken on Tm adatoms on (a) Cu(100) and (b) Cu_2N.

To ensure that this behaviour is not atom dependent, and that objects on Cu(100) and on Cu_2N are not, in fact, two different species, Tm adatoms on Cu(100) are vertically manipulated onto Cu_2N patches. Vertical manipulation requires moving the atom onto the tip, and then dropping it back to the surface in a controlled fashion. While lateral atomic manipulation is the usual approach in metals, it does not work well on insulating layers[161, 165], additionally, as the adatom is moved onto a different substrate, if the manipulation

parameters are not changed accordingly while crossing the border, successful manipulation would be unlikely. With vertical manipulation these problems are not an issue. A single Tm adatom on the Cu(100) surface can be reliably picked up onto the tip by regulating over it at $V_{Bias} = 10$ mV, $I_t = 1$ nA, disengaging the feedback loop, lowering the tip 300 pm towards the atom and applying a 1 V pulse; conversely, after picking up the Tm atom it can be dropped onto a Cu_2N patch by regulating over ir at $V_{Bias} = 10$ mV, $I_t = 1$ nA, lowering the tip 200 pm towards the surface and applying a -1 V pulse. Figure 5.6 shows the topography of a 15x15 nm area before and after vertically manipulating several Tm atoms on Cu (indicated by blue circles) onto Cu_2N patches (atoms at new positions are indicated by white circles).

Prior to manipulation, all the atoms presented the same spectra as shown on Fig.5.5.a, corresponding to a Tm adatom on Cu(100); however, as shown in Fig.5.7, after manipulation onto Cu_2N two different spectra can be observed, in one case the same as the spectra corresponding to Tm on Cu_2N seen in figure 5.5.b, with a large peak at 2.1 V and a smaller feature at 0.8 V, while other adatoms present a similar spectra shifted to higher energies: The large peak occurs at 2.6 V, while the smaller feature is shifted above 1.5 V.

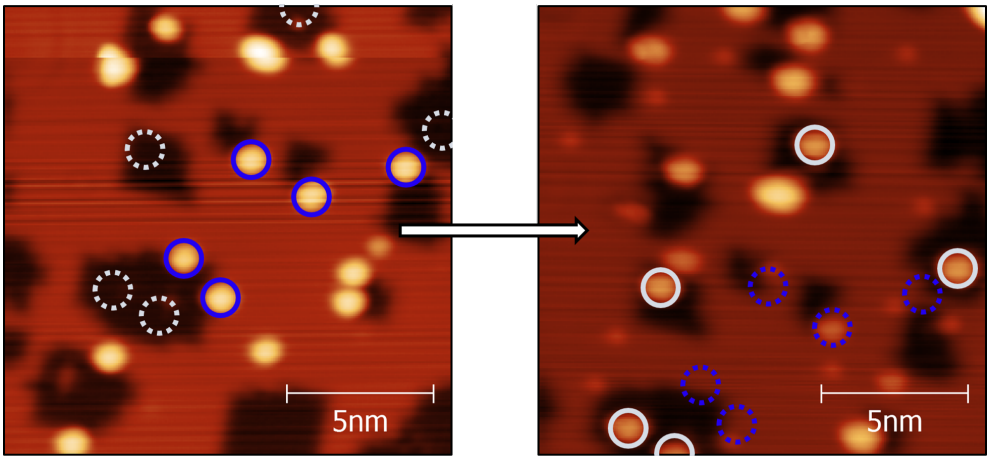

Figure 5.6: Atomic manipulation of Tm adatoms. Atoms were picked up onto the STM tip from the Cu(100) surface, marked in blue, and dropped onto Cu_2N islands at the positions marked in grey. The image shows the the sample prior to starting and after several successful manpiulations.

This shift in energy could be caused by different sources, the two most obvious being a contamination during manipulation or differences in the local environment. Hydrogen contamination, which can be an issue in longer experiments as H adsorbed on the chamber walls desorbs over time, would be expected to produce a difference in the constant current topography of the

adatom, as well as a large change in the differential conductance spectroscopy [177, 178], which does not seem to be the case. Instead, the most likely origin of the shift is due to the adatom being in a different position on the Cu_2N lattice and thus in the presence of a different crystal field. Figure 5.8 shows a diagram of the lattice and indicates the three possible adsorption binding sites: On a Cu position, on a N position or on a hollow position. Adsorption on different binding sites has been shown to have a very strong effect on the electronic properties of 3d metals[176]. In the case of Rare Earths, the $4f$ electrons are highly shielded and thus a feature of $4f$ origin would be less affected by changes in the local crystal field. The fact that this situation only occurs for adatoms that have been vertically manipulated and not on the adatoms as-deposited can be easily explained: During evaporation at 80 K, Tm adatoms are able to diffuse slightly over the Cu_2N surface and reach the binding site of minimum energy; on the other hand, atomic manipulation is performed at 1 K and diffusion is strongly inhibited, and adatoms are more likely to stay in a local minimum of the surface energy potential.

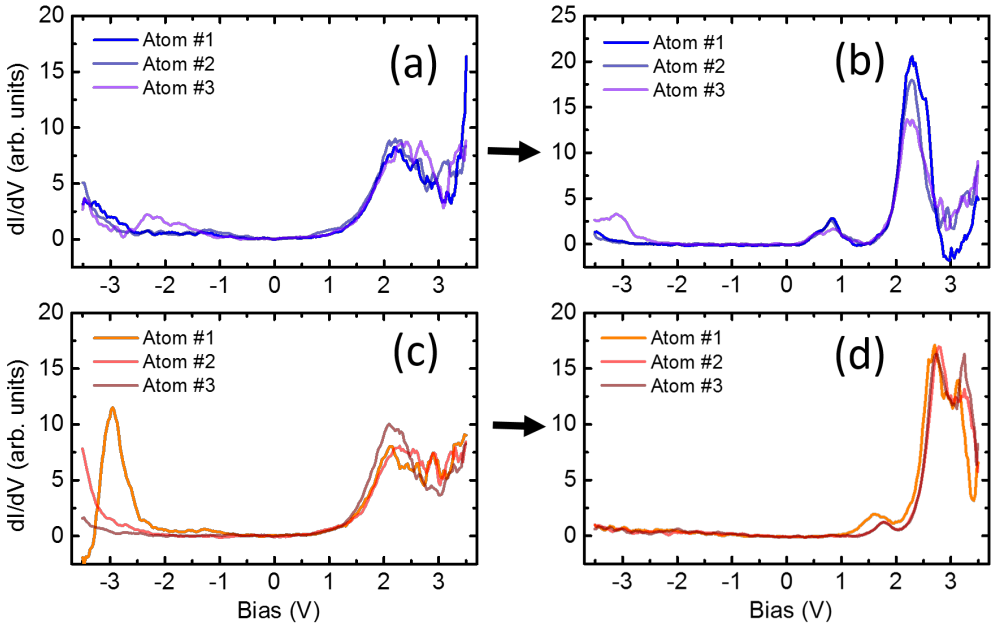

Figure 5.7: Spectra taken on Tm adatoms on Cu(100) (a) prior to manipulation, showing the same behaviour for Tm/Cu(100) as seen in Fig. 5.5.a and (b) after vertical manipulation onto Cu_2N, showing the same behaviour as seen for Tm/Cu_2N in Fig. 5.5.b; on the other hand, the set of Tm adatoms presented in (c), which also conform to Tm/Cu(100), present a shifted spectra when manipulated onto Cu_2N (d).

The fact that this feature at 0.8 V only appears on Cu_2N and not on the

Cu(100) surface could indicate that in the latter case it hybridizes with the metallic surface, and thus it could be expected for it to be due to external orbitals rather than to the core $4f$ orbitals.

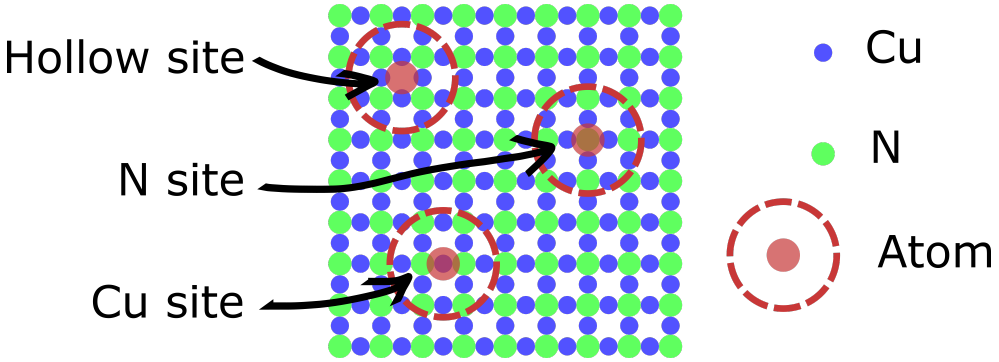

Figure 5.8: Diagram of the Cu_2N surface, indicating the possible binding sites.

5.2 Lu on Cu_2N

To further investigate the nature of the observed feature at 0.8 V, the experiment is repeated using Lutetium. Lu presents a similar electronic configuration as Tm, but with the significant difference of having a full $4f$ shell. Due to the shell being complete, $4f$ electrons will not be able contribute to the LDOS, either while lying on Cu(100) or on Cu_2N.

Sample preparation follows a similar process as for the case of Tm, but in this case the experiment was performed in a SPECS JT system, which allows to evaporate directly onto the sample in the STM stage, keeping the sample at 5 K. Lu is evaporated, as in the case of Tm, from a Mo crucible heated by electron beam bombardment, although Lu requires a higher temperature than Tm for a given evaporation rate, as its vapour pressure is much lower at the same temperature.

The difference in sample temperature during evaporation is quite noticeable when comparing Fig.5.9, which shows the Lu sample after evaporating at 5 K, with the Tm sample prepared at 80 K shown in Fig. 5.4. In the case of Lu, the adatoms are randomly distributed over both Cu and Cu_2N, in contrast to the distribution observed for Tm, where they preferentially lied in the Cu-Cu_2N border. Taking profiles over adatoms give a similar height for Lu as for Tm, with Lu on Cu(100) showing a profile of 220 pm and 240 pm on Cu_2N, with the Cu_2N patch appearing as a 110 pm dip at 100 mV.

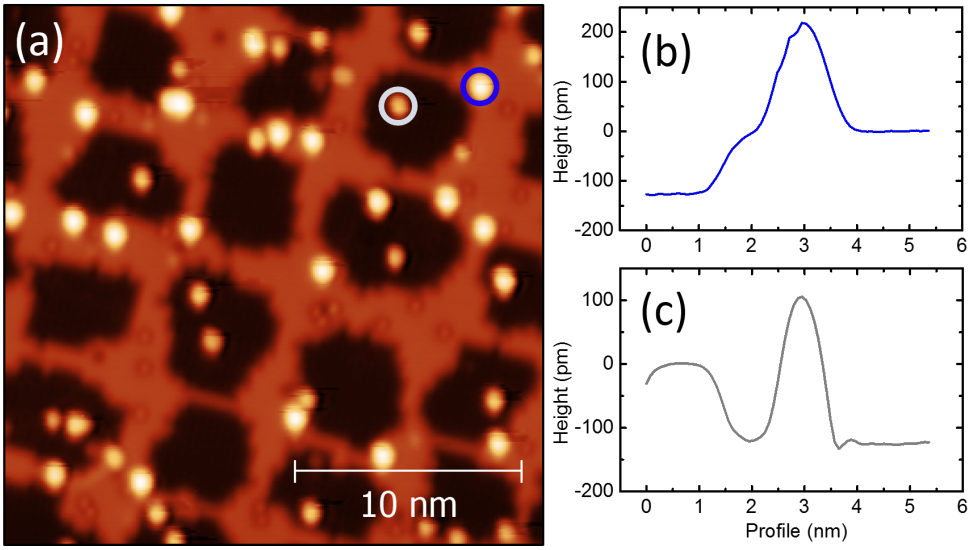

Figure 5.9: (a) STM image of Lu adatoms on a Cu_2N sample (V_{Bias} = 100 mV, I_t = 1 nA). At the right, profiles for (b) the circled Lu adatom on Cu(100) an for (c) the circled Lu adatom on Cu_2N.

5.2.1 Spectroscopy on Lu/Cu_2N

Figure 5.10 shows representative spectra taken on Lu adatoms on both Cu(100) (a) and Cu_2N (b) from 0.5 V to 3.5 V. In this case both species present a very similar behaviour, a single large broad feature centred around 2.6 V, and no other features at lower bias.

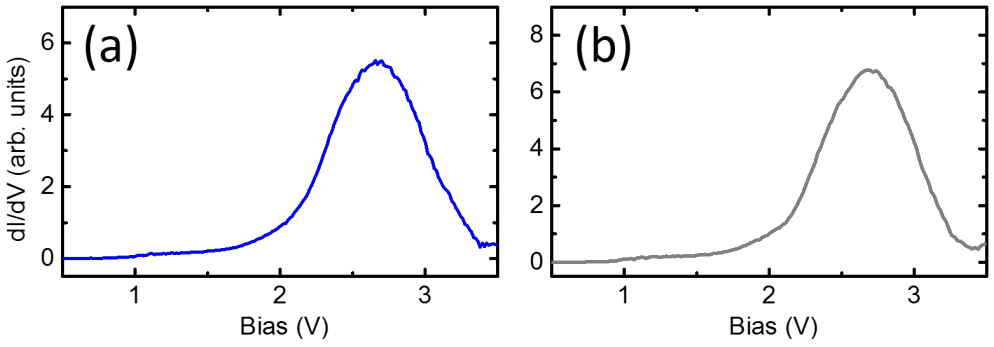

Figure 5.10: dI/dV spectra from 0.5 V to 3.5 V on (a) a Lu adatom on the Cu(100) surface, and (b) a Lu adatom on the Cu_2N surface.

Such a strikingly similar behaviour for Lu adatoms in a metallic environ-

ment and for adatoms on the insulating layer is surprising, as the substrate had a very noticeable effect for Tm adatoms. This might suggest that there might be an effect on the $4f$ orbital for Tm, as this orbital being complete in Lu but incomplete in Tm is the main electronic difference between the two.

5.3 DFT Calculations: Tm on Cu_2N

In order to discern the nature of the feature observed at 0.8 V, the density of states of a Tm adatom on a Cu(100) and a Cu_2N surface is calculated using DFT-based first-principles calculations. The system is described using the generalized gradient approximation (GGA) for correlation and exchange in the local density approximation (LDA) [179] with a correction for the treatment of strongly correlated systems, LSDA+U [180]. The plane basis is set on a projector augmented wave (PAW) pseudopotential for describing the core electrons [181] as implemented in Vienna ab initio simulation package (VASP) [182].

The Cu_2N/Cu system is represented by a (4 x 4 x 5) supercell containing 1 layer of pseudomorphic Cu_2N (32 Cu atoms and 16 N atoms forming the Cu_2N monolayer) over 5 Cu layers (32 atoms/layer) oriented along the [001] direction, with a vacuum thickness of 40 Å.

A fully 3D ionic relaxation calculation is done for the Cu_2N ML plus the first two Cu layers, keeping fixed the central layer of the Cu substrate. This optimization finds the interlayer distances along the [001] direction: d(Cu_2N-Cu1) = 2.080 Å, d(Cu2-Cu1) = 1.835 Å and d(Cu3-Cu2) = 1.805 Å. Adding the Tm adatom under the above conditions, a fully 3D ionic relaxation calculation is done for the Tm atom, the Cu_2N monolayer and the first 2 Cu layers, keeping fixed the central layer of Cu substrate, as in the previous case.

The optimization indicates that Tm adsorbs on a hollow site of Cu_2N-layer, although slightly shifted (by 0.18 Å) respects to the theoretical hollow centre. This could be an indication of the limitations of a (4 x 4 x 1) supercell, but the higher computational cost of larger cells made them inaccessible for the time. The hollow binding site for Tm is in contrast with the results reported for Co atoms on Cu_2N, where the metal atom adsorbs preferentially on a Cu position [176].

From the calculated projected density of states (PDOS) over the Tm adatom the orbital character of the observed features can be determined. Figure 5.11 shows the calculated $5d$ PDOS of the Tm adatom, in good agreement with the experimental results presented in figure 5.5 for both substrates. The relevant features are reproduced in both cases, with a clear peak at 0.8 V present

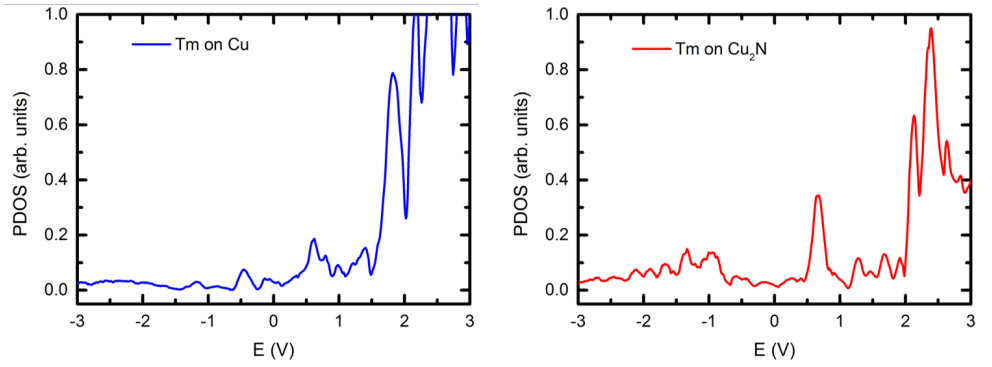

Figure 5.11: Calculated LDOS of a Tm adatom on (left, blue) the Cu(100) surface and (right, red) the Cu_2N surface. Both cases are in good agreement with the experimental results observed in fig. 5.5.

for the Tm adatom on Cu_2N that is absent for the case of the adatom on Cu(100). This indicates that this feature has actually a $5d$ character, and no $4f$ significant contributions are observed in the presented bias range.

With the adsorption site and orbital character of the features in mind, the discussion in 5.1.1 can be approached again: As seen in figure 5.8, the are three available positions on Cu_2N, but actually only two different symmetries: Hollow and N sites present a four-fold symmetric environment, surrounded by four Cu atoms; meanwhile, Cu sites present an uniaxial anisotropy, hollow positions surround the Cu site in one direction, and N atoms surround it along the other [176]. As the $5d$ orbitals find the same symmetry for hollow and N sites, it could be expected that they produce a similar spectra; the anisotropic environment in Cu positions, however, can modify the orientation of the $5f$ orbitals of the Tm adatom, thus causing the shift to a higher energy of the $5d$ feature at 0.8 V, as seen experimentally in figure 5.7.

5.4 Probing for Inelastic Excitations

In recent years, the issue of inelastic spin-flip excitation on rare earth atoms and clusters has seen conflicting results, in some cases positive results have been reported [144, 166, 167] while in others the absence of any excitation has been explicitly noted [118, 168]. The IETS is a very powerful, as it allows not only probing the magnetic state of an atom, but actually controlling it spin state[183]. A long lived state could be probed unperturbed by tunnelling at energies lower than the excitation threshold, and switched by going over it. Rare Earths, due to their strongly localized $4f$ states, are candidates for

long lived atomic magnetic states, aided by their large spin (S) and orbital (L) momenta, leading to a large magnetic anisotropy energy.

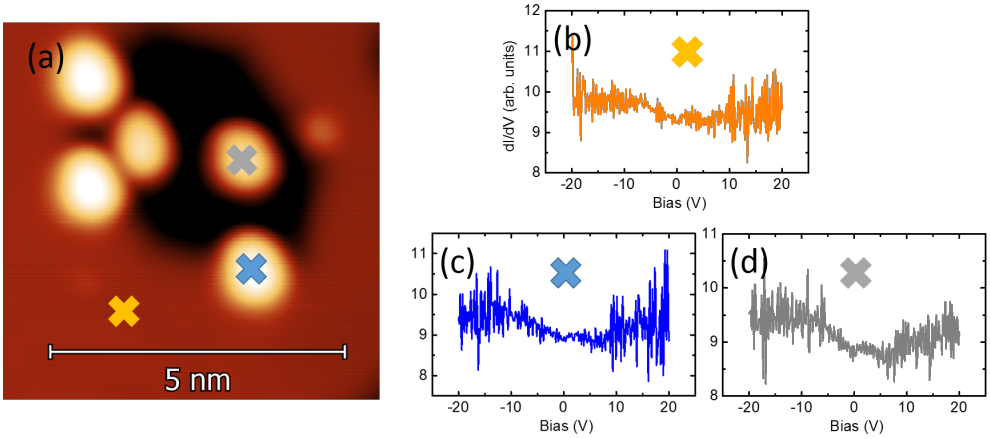

Figure 5.12: (a) STM image showing a 6x6 nm^2 area with Tm adatoms lying on both the Cu(100) and Cu_2N surfaces. Differential conductance spectra taken over ±20 mV dI/dV on (b) the Cu(100) surface, (c) a Tm adatom on Cu(100), and (d) on a Tm adatom on Cu_2N.

5.4.1 Spectroscopy near E_F

The spectroscopic behaviour near E_F of Tm and Lu adatoms on Cu_2N and Cu(100) is presented in the following figures, Tm in 5.12 and Lu in 5.13. Even though the electronic configuration of Tm could allow for spin excitations, spectra taken on single Tm adatoms on the Cu(100) surface present no evidence of an IETS signature (Fig. 5.12.b), or any other distinct feature, nor do the spectra taken on Tm adatoms on Cu_2N (Fig. 5.12.c)]. While the spectra are not flat in the explored range, both are hardly distinguishable from spectra taken on the Cu(100) surface (Fig 5.12.a), indicating that the shape of the spectra is tip-related, rather than due to the Tm adatoms.

Similarly, the study of the LDOS near E_F of Lu adatoms, presents no feature that would suggest a spin excitation, although it is expected in this case due to the $4f$ orbital being complete for Lu. Spectra in the ±50 mV range are presented in Fig.5.13.

The study of the electronic properties of Tm and Lu adatoms on a metallic and on an insulating substrate indicates that there is no access to $4f$ electrons, or at least none capable of producing a measurable contribution to the LDOS. This result, in the context of the controversy regarding the possibility of tunnelling into $4f$ electrons, suggests that this is not, in general, the case. This

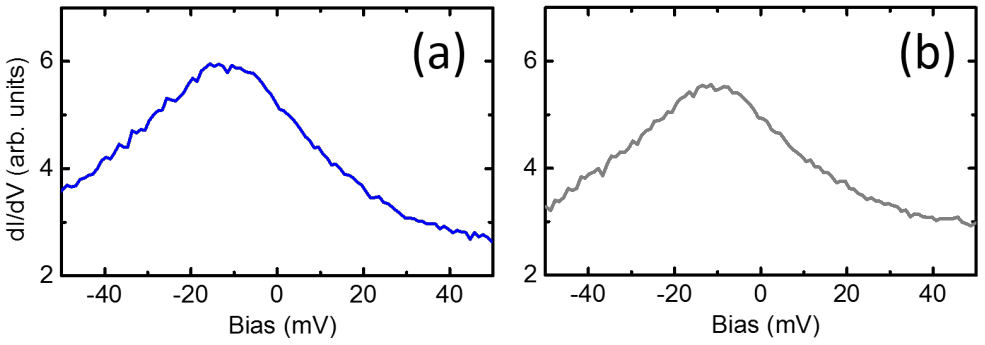

Figure 5.13: Differential conductance spectra taken over a ±50 mV range of Lu adatoms on (a) the Cu(100) surface and (b) the Cu_2N surface.

conclusion will be expanded further in chapter 7, after a spin polarized analysis of the tunnelling current of RE adatoms. Despite this apparently discouraging setback for the use of RE adatoms, recent advances in combining STM with electron paramagnetic resonance [47] which allow for a very precise excitation energy determination have enabled the use of the Zeeman splitting of a single Fe atom on MgO to detect the dipolar field of a magnetically stable Ho atom (in the order of seconds at T = 1.2 K), proving even able to distinguish between the four possible configurations of two adjacent Ho atoms[168]; as direct tunnelling onto the Ho atom does not produce any inelastic excitation, magnetic switching is instead managed by spin-polarized current pulses. These recent developments keep the door open for to further studies of rare earth atoms on surfaces of varied properties.

Chapter 6

Spin polarized Quasiparticle Interference in Fe/W(110)

Standing wave patterns are the result of coherent scattering of surface electronic states (SS) off defects like terrace edges, impurities or adsorbates. This phenomenon has been observed by means of scanning tunnelling microscopy (STM) [184–192] and represents a direct evidence of quantum interference of quasiparticles. Continued attention has been devoted to the study of surface states since their first observation in noble metal surfaces [184], as fundamental information of the SS such as their energy dependence [193] or their spin character [194] can be determined experimentally [188–190]. The development of topological insulators in the last decade [195] has also put the spotlight on surface states [191], as in these systems conducting surface states are topologically protected.

In this chapter, the focus will be set on the Fe monolayer on W(110) and, more particularly, on the standing wave pattern observed near the Fermi level on said monolayer and its spin polarized character. With this in mind, an introductory discussion regarding the origin and characteristics of theses patterns and the basic magnetism of the Fe(110)/W(110) system is in order.

6.1 Surface states, and other states at the surface

In an infinite periodic potential, the eigenstates of the Schrödinger equation for a single electron are given by Bloch waves of the form $\Psi_{nk} = e^{ikr}u_{nk}(r)$, where $u_{nk}(r)$ is the periodic potential and k is the wave number. The allowed k must satisfy the Born-von Karman periodic boundary conditions. Deviations

from the perfect potential, such as those introduced by lattice defects or impurities, give rise to the formation of localized energy states [196] that would be forbidden in the perfect crystal.

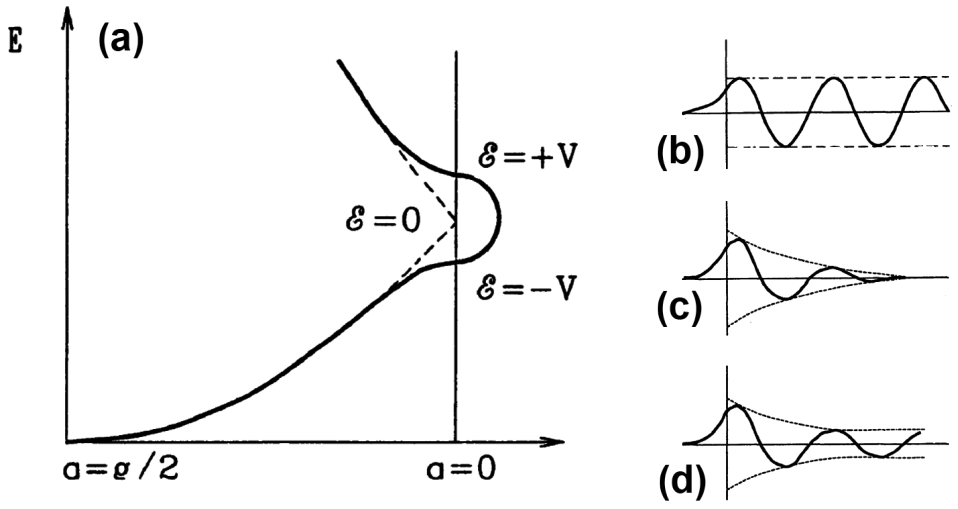

Figure 6.1: (a) Dispersion relation for a nearly free electron system. The periodic potential induces the folding of the bands at the zone edge, creating a gap where surface states can exist. (b) Stationary bulk state, (c) true surface state decaying exponentially into the bulk, and (d) surface resonance. Adapted from [197]

One particular instance of lattice defect is the actual surface of the crystal, which breaks the translational symmetry. In a one-dimensional model, the periodic potential causes the opening of a gap at the Brillouin zone edges where the solutions to the Schrödinger equation take imaginary wavevectors (see figure 6.1.a) which are not valid solutions in the bulk, as they would diverge; at the surface, however, these solutions are valid as they may be bounded to the surface, decaying exponentially into the bulk, and thus are aptly named surface states [198]. In a three dimensional case, the treatment is formally more complicated, but the main features remain: a surface state may only exist in a forbidden gap of the bulk band structure; however, this gap might be present in all directions of k-space and thus a "true surface state" can be present, confined to the surface, as pictured in figure 6.1.c; or the gap might exist in one direction of k-space with bulk states allowed in other directions, and thus the surface state can propagate further into the bulk by connecting to bulk states, giving rise to what is called a surface resonance (pictured in figure 6.1.d. This localization of electrons in states at the surface gives rise to a quasiparticle interference phenomenon, where the 2D free-electron-like gas forms a standing wave pattern near scattering centres, such as step edges or

impurities [185, 199], or due to lateral confinement [184, 200].

Quantum interference is established between coherent quasiparticles, described as plane waves with a crystal moment $\mathbf{k}_b$ and $\mathbf{k}_i$, with b and i standing for the back-scattered and incident states, with wave function Ψ_b and Ψ_i, that includes spatial ($|\psi_i(r)\rangle$ and $|\psi_b(r)\rangle$) and the spin components ($|S(k_i)\rangle$ and $|S(k_b)\rangle$). The scattering process conserves the energy, $E(k_i) = E(k_b) = E_q$, while for interference wavevector $\mathbf{q}$, states with crystal moment with the condition $\mathbf{q} = \mathbf{k}_b - \mathbf{k}_i$ have to exist at E_q. The amplitude of the resulting standing wave is modulated by a factor $cos^2(\mathbf{q} \cdot \mathbf{r}/2 - \phi/2)$, where ϕ is a phase. There is a spin-dependent contribution to the scattering given by $T(q, k_i) = |\langle S(k_i)| |S(k_b)\rangle|^2$ [201]. As a result, incident and back-scattered states with $\mathbf{k}_b = -\mathbf{k}_i$ but non-degenerate with respect to the spin states modifies the landscape of the interference pattern as observed in Bi(110) [192] or $Bi_{1-x}Sb_x$[201].

Overall, the resulting spatial distribution of a single standing wave can be described as:

$$|\Psi|^2 \propto cos^2\left(\frac{\mathbf{q}\cdot\mathbf{r}}{2} + \frac{\phi}{2}\right) T(q, k_i) \propto cos\left(\mathbf{q}\cdot\mathbf{r} + \phi\right) T(q, k_i) \tag{6.1}$$

Therefore for a symmetric band dispersion with $\mathbf{k}_b = -\mathbf{k}_i = \mathbf{k}$, $|q| = 2k$ and the experimental wavelength λ along some crystal direction corresponds to π/k. Thus the angular distribution of k at fixed energy as well as the energy dependence can be determined by a set of measurements of the standing waves at different value of bias voltage in large and plane islands, as illustrated in figure 6.4 [202].

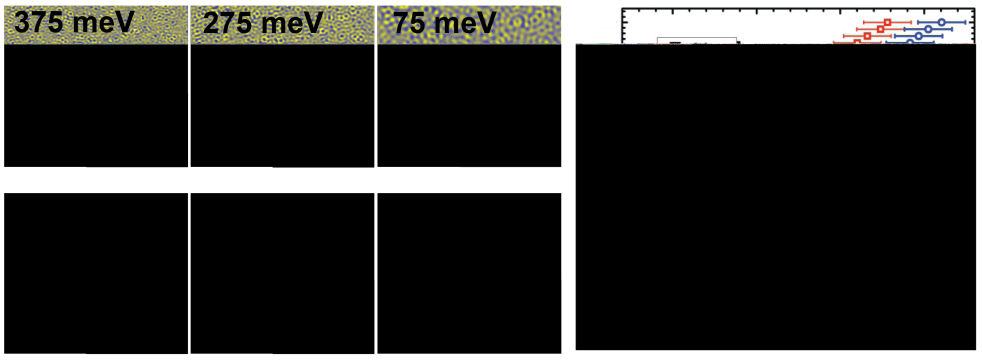

Figure 6.2: Experimental determination of the surface state dispersion relation by QPI mapping by taking Fourier Transforms of dI/dV maps at different bias. Adapted from [202].

In magnetic metals the spin-up and spin-down bands undergo a shift in

energy due to the internal exchange interaction and, as a result, the density of states can be strongly asymmetric with respect to the spin component. This result is observed in SP-STM experiments, and standing waves with a defined polarization have been detected in Co(111) islands [189, 190], or the highly anisotropic spatial oscillations in the local density of states around adsorbates in the double layer of Fe on W(110) [188] These works have demonstrated not only that $\mathbf{q}$ can take different values as function of the energy but also that the detection of $\mathbf{q}$ requires electrons in the surface state with a spin component parallel to that of the magnetic tip.

6.1.1 Surface resonance in Fe(110)

The existence of spin polarized states on the Fe(110) surface has been determined by spin and angle-resolved photoemission (PE) spectroscopy [203, 204] and inverse photoemission (IPE) [205]. The analysis of the data and their interpretation in terms of either surface or surface resonance states is a complex issue that is aided by the calculation of the band dispersion E($\mathbf{q}$) of surface states and the projected bulk band structure on the (110) surface. Further, a realistic description of the surface barrier is fundamental to represent the electronic structure underlying the relativistic one-step calculations of the PE and IPE experiments performed in magnetic closed-packed surfaces [205–207]. The one-step model of photoemission, was originally proposed by Pendry and co-workers [208] and is the most successful theoretical approach to describe PE experiments. The main idea of the one-step model is to describe the actual excitation process, the transport of the photoelectron to the crystal surface as well as the escape into the vacuum as a single quantum-mechanically coherent process including all multiple-scattering events. The result of the I(PE) spectral densities [205–207] along the $\overline{\Gamma}$ $\overline{N}$ line is shown in Fig. 6.3 for both the majority and minority spin components. The projected bulk band structures (shaded areas) resulting from potentials calculated by use of the self-consistent tight-binding linear muffin tin (TB-LMTO) method [209] is shown in Fig. 6.3 for both the majority and minority spin components. This model explains the inverse photoemission experiments [205, 206] in Fe(110)/W films.

6.2 Fe on W(110)

The preparation and magnetic properties of thin iron films have been studied in metallic, semiconductors and insulator crystalline substrates. In the case of Fe grown on W, the orientation of the substrate plays a large role. Due

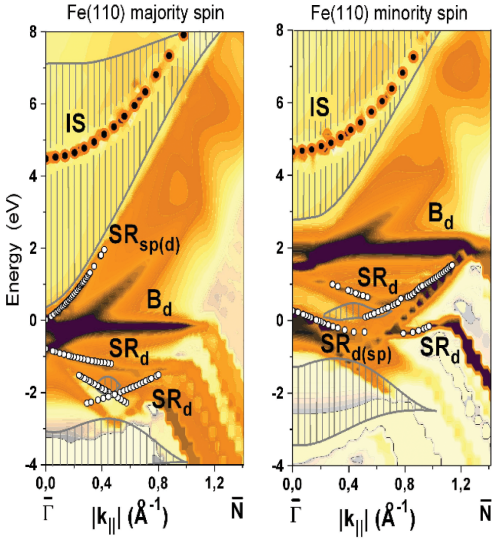

Figure 6.3: Calculated contour plots for majority (left panel) and minority (right panel) (I)PE spectral densities of Fe(110) along $\overline{\Gamma N}$. Values of high spectral density are shown by dark regions. Shaded areas represent gaps in the projected bulk band structure. IS stands for the the n = 1 image-potential state. Features denoted by SR and B_d are identified as surface resonances and d-like bulk emissions, respectively. The subscript in SR indicates the orbital character of the involved electrons. The open circles represent resonance surface states. Adapted from [206].

to the high surface energy of W $\gamma_W = 2.9 J/m^2$[210]) compared to that of Fe ($\gamma_W = 2.0 J/m^2$), a Fe wetting of the W surface occurs for the first layer.

This results in the preparation of smooth epitaxial Fe films, despite the large misfit strain between W and Fe: $(a_{Fe} - a_W)/a_W = 9.4\%$ with $a_{Fe} = 2.866$ Å and $a_W = 3.165$ Å. Pseudomorphic growth is observed up to 1ML for the (110) surface [2, 211] and up to 3ML for Fe/W(100) [212, 213]. The effect of this large strain is fundamental to understand the magnetoelastic [213] and electrical [214] properties of the system and, in combination with the surface contribution, the reduction of the Curie temperature [215] or the reorientation of the magnetization, from <100> directions for bulk and thick films to the in-plane [1$\bar{1}$0] axis in the monomolayer range [216].

On W(110), the first Fe atomic layer grows pseudomorphically forming islands and stripes along the step edges. The size and shape of the islands is influenced by coverage and substrate temperature, with higher temperatures producing larger, more regular islands; at coverages above 0.5 ML the layers starts to coalesce and the islands lose their regularity. After a full wetting layer is completed, subsequent layers can grow prior to completion of previous

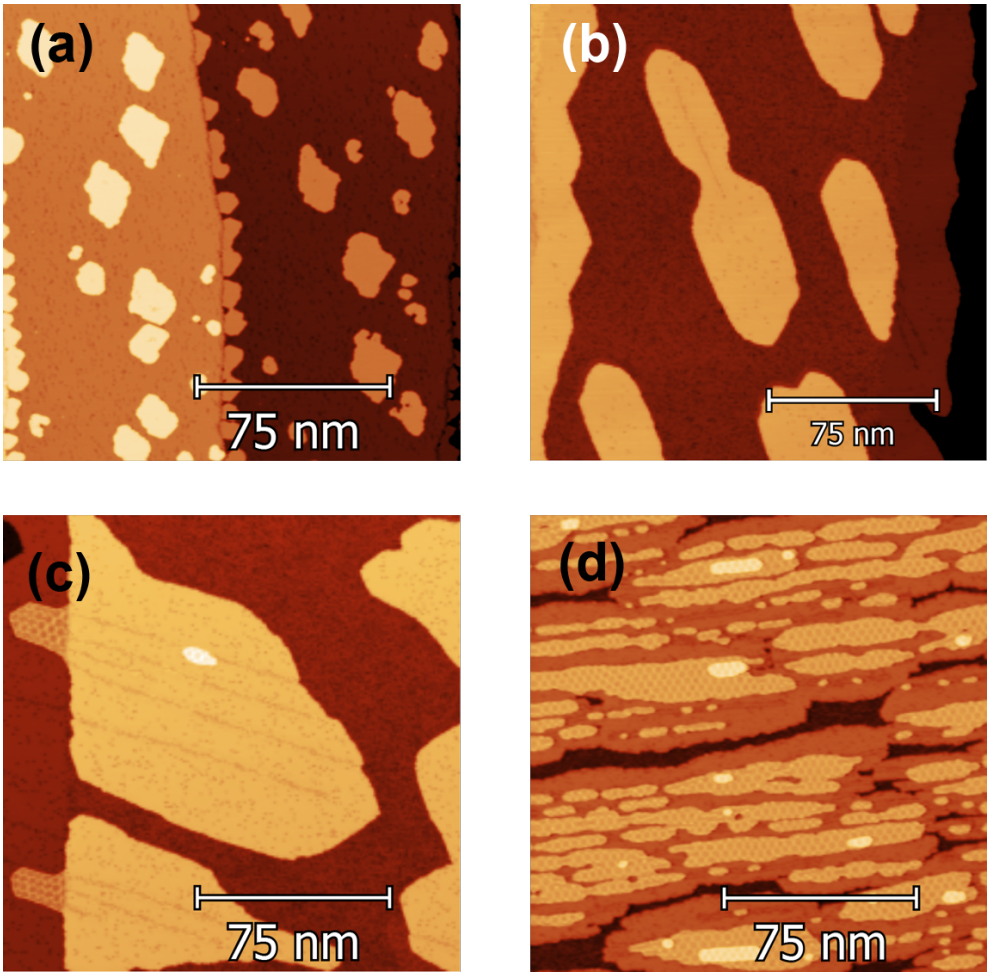

Figure 6.4: Topography images at $V_{bias} = 100$ mV, $I_t = 1$ nA of a 175 nm side square area of Fe/W(110) samples for different Fe coverages, showing how the first, second and third monolayers grow. (a) $\Theta_{Fe} = 0.3$ with smooth Fe monolayer islands; (b) $\Theta_{Fe} = 1.5$ with smooth second layer islands on a rough first Fe wetting layer; (c) $\Theta_{Fe} < 2$, where small third layer patches are able to grow before completing the second layer; and (d) $\Theta_{Fe} > 2$ third and fourth layer patches over a still incomplete second layer.

layers, in what is known as a Stranski-Krastanov growth mode, as now the surface energies are similar for either layer [217]. The strong coupling between W and the first Fe layer is also reflected in the fact that the first layer is dislocation free, while dislocations along the [001] direction are common in the second layer, and ubiquitous, along [001] and [1$\bar{1}$0] directions in the third [218]. Figure 6.4 presents STM topography images of these first few layers of Fe on W(110).

6.2.1 Magnetic properties of Fe on W(110)

The magnetic properties of Fe thin films on W(110) have been studied by diverse methods, with much of the characterization performed by U. Gradmann and H.J. Elmers and their respective groups. The first monolayer has been shown to be ferromagnetic [219] with an in-plane uniaxial anisotropy oriented along $[1\bar{1}0]$ [220, 221]. The second layer presents an out of plane easy axis [222], and has been thoroughly studied by STM [74, 223]. Above 4 ML, the strained Fe film starts to relax and is magnetized in plane, eventually reaching the bulk magnetization value at a thickness of 6 nm [224], and the easy axis rotates to the easy bulk direction [001] at a critical thickness around 10 nm [225].

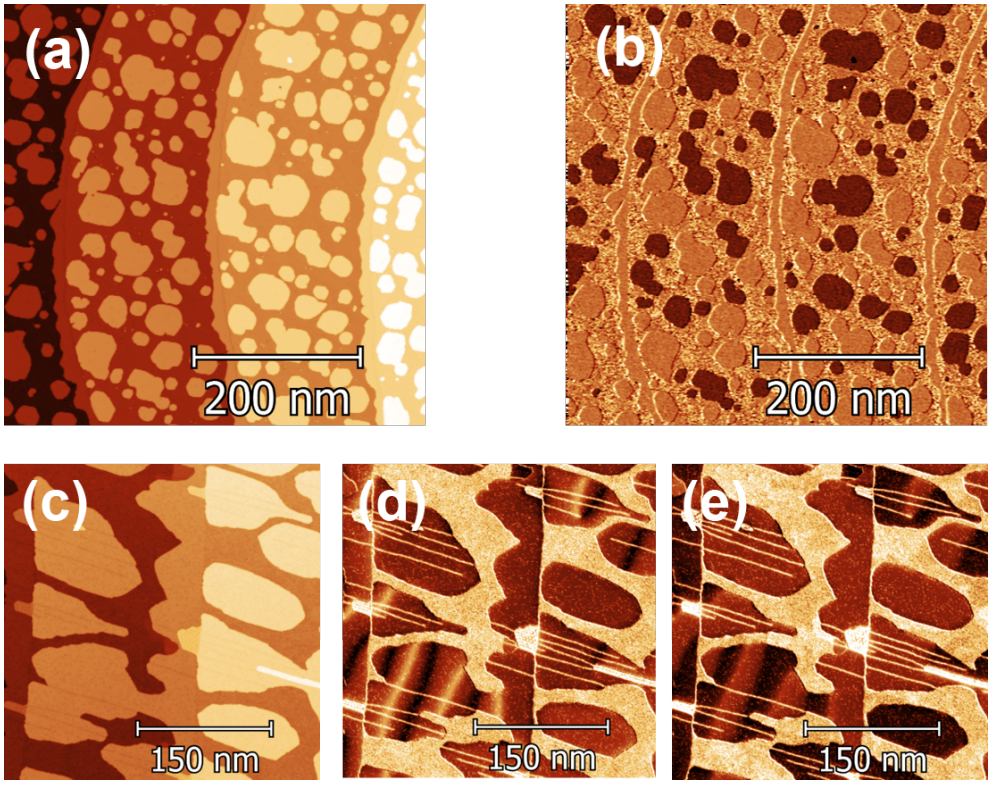

Figure 6.5: (a) Topography and (b) differential conductance map of monolayer Fe islands on W(110) taken at V_{bias} = -200mV, I_t = 1 nA with a Fe coated W tip, with in-plane magnetization. (c) Topography and differential conductance map of the second Fe atomic layer taken with a Cr coated W tip with (d) in-plane magnetization and (e) out-of-plane magnetization.

STM can explore these different magnetic configurations by means of spin-polarized STM. A Fe coated W tip, sensitive to the in-plane polarization of the

sample is used to study Fe samples below the monolayer, while a Cr coated tip is used for coverages above the monolayer, as it is sensitive to out-of-plane polarization, although with some in-situ tip treatment in-plane sensitivity can also be achieved.

The spin polarization of the density of states is particularly noticeable during dI/dV measurements, as it only probes sates at energies at $eV_{bias} \pm V_{mod}$, in contrast with the tunnelling current which integrates all the states between eV_{bias} and E_F (see chapter 2.1.4). Figure 6.5 illustrates the Fe/W(110) system studied with Fe and Cr coated tips. The left side shows topography images, while dI/dV maps taken at V_{bias} = -200 mV, I_t = 1 nA are shown on the right. Figure 6.5.a shows the topography of a sample with monolayer Fe islands, with the corresponding dI/dV map in Fig.6.5.b, presenting a monodomain configuration with two clearly differentiated dI/dV signals corresponding to islands with polarization parallel and antiparallel respect to the tip. The second layer (Fig.6.5.c) presents a more complicated magnetic structure, as shown in the adjacent dI/dV maps taken with a Cr coated tip, Figures 6.5.d and 6.5.e (out-of-plane), revealing the (001) easy axis along with the alternating domain walls that conform the spin spiral present in the double Fe layer system due to the Dzyaloshinskii-Moriya interaction [74, 223, 226, 227].

6.3 Fe monolayer islands on W(110)

The samples studied in this chapter are in the submonolayer regime, with a coverage around $\Theta \sim 0.2$. As stated above, the first Fe monolayer grows forming smooth regular islands, free of structural defects although some adsorbates may by present despite thorough degassing. This smooth surface hold up to a coverage around $\Theta \sim 0.5$, above which the islands start to coalesce and present a more irregular appearance; in fact, at $\Theta \leq 0.6$ the coalescence of the islands enables percolation of the magnetic domains, resulting in a ferromagnetic configuration up to T_C = 190 K [220]. The full monolayer, as a wetting layer on top of which the second layer grows, presents a much rougher surface than the nanometric individual islands.

6.3.1 Sample preparation

The preparation of the Fe islands here presented consists in evaporation of the material by EBE, directly heating a 99.99% pure Fe rod onto a clean W(110) surface. The sample is flashed at 2300 K prior to evaporation to ensure that the surface is as free of contaminants as possible. Figure 6.6 illustrates several preparations of Fe islands with a coverage between $\Theta \sim 0.2$ and $\Theta \sim 0.5$.

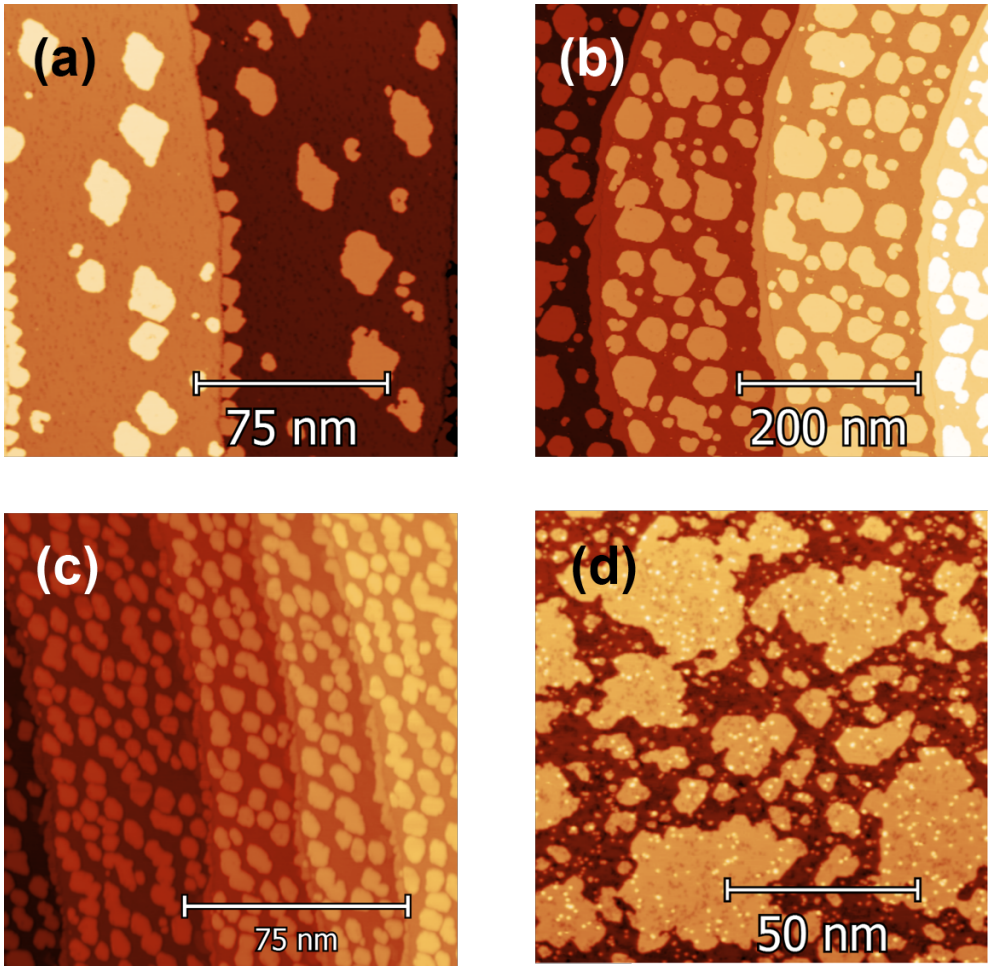

Figure 6.6: Topography images at V_{bias} = 100 mV, I_t = 1 nA of four Fe/W(110) samples with increasing coverage. (a) For $\Theta_{Fe} \sim 0.2$ Fe grows forming clean flat islands and decorating the step edges; (b) at a higher coverage of $\Theta_{Fe} \sim 0.4$ the islands grow in size and a full stripe is formed along the step edge; (c) similar coverage but with smaller islands; and (d) at coverages above $\Theta_{Fe} \sim 0.5$, Fe islands start to coalesce and lose their smoothness, leading to the rough wetting layer shown in the previous figure.

As discussed in chapter 3, the use of a thermocouple to monitor the sample temperature during evaporation is precluded by the high temperatures required for the preparation of a clean the W(110) surface; the pyrometer which is used instead has a lower temperature limit of 300° C, well above the substrate temperature during the typical evaporation in this chapter. This is unfortunate, as the temperature of the W substrate during Fe evaporation plays a significant role in island size and regularity, as illustrated by figure 6.7, where samples

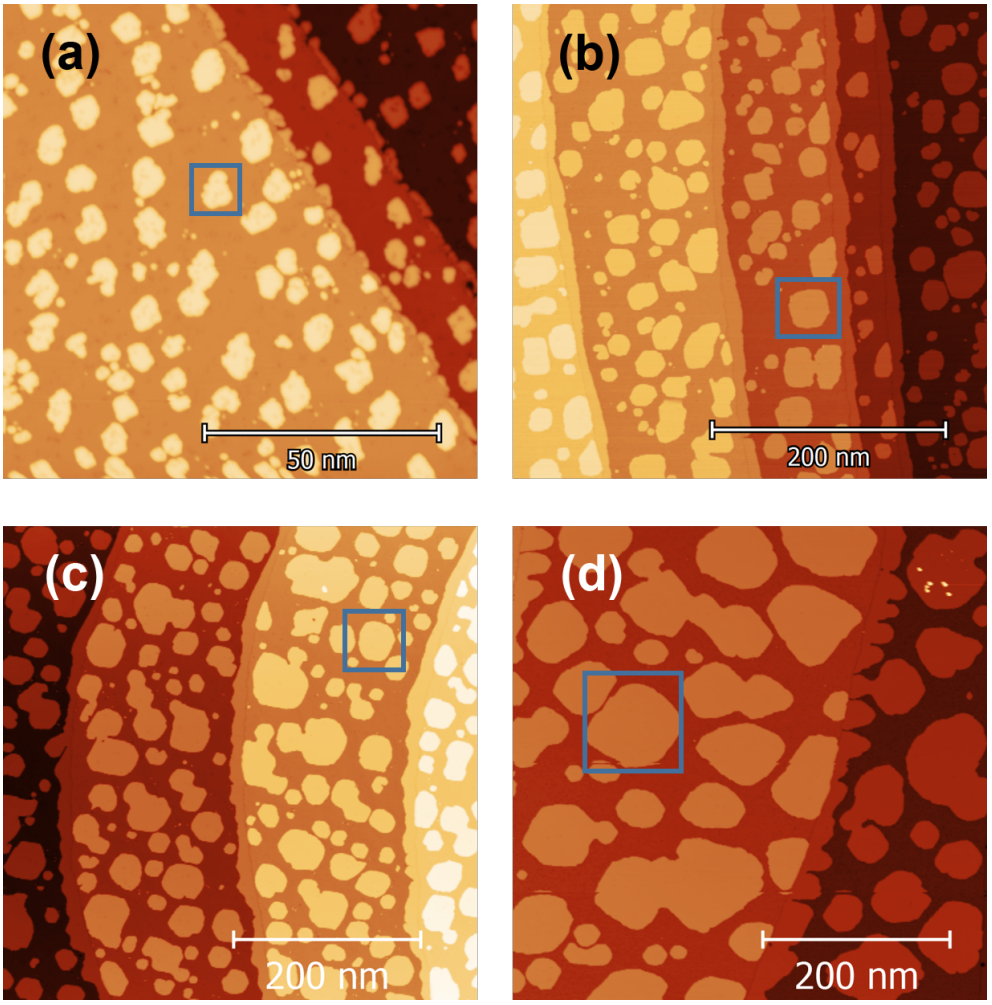

Figure 6.7: Topography images at V_{bias} = 100mV, I_t = 1 nA of four Fe/W(110) samples with similar coverage grown at different substrate temperature. (a) A sample grown at room temperature at T, with a mean island size of 1.4 nm; a representative island is marked in blue, 5 nm across; (b) for a substrate temperature of $\sim$ 85° C during evaporation, mean island size increases to 7 nm; and islands as the one marked in blue, 13 nm across, are easy to find; (c) substrate at T $\sim$ 105° C, mean island size of 21 nm, with multiple 40 nm diameter islands (as shown squared in blue). Finally, for T $\sim$ 125° C mean island is up to 40 nm, and islands with lateral sizes up to 200 nm are present, although islands 100 nm across are more prevalent (squared in blue).

with a similar coverage present wildly different island size, the main difference between them being the time elapsed between flashing the W crystal and starting the Fe evaporation, which leads to different substrate temperature.

Estimating T(t) from the fit in figure 3.3 in in section 3.1 and using Fig.6.7.a

as a reference of a preparation near room temperature, an almost two orders of magnitude increase in island size is observed with increased substrate temperature. The room temperature reference in Fig.6.7.a, presents a large number of islands in a 50 x 50 nm^2 area with a mean island size of $\sim$ 1.4 nm; fig.6.7.b, shows a 200 x 200 nm^2 area of a sample evaporated 10' after flashing the crystal which leads to a temperature of T(10') $\sim$ 85° C already presents a much larger island size, with a mean of $\sim$ 7 nm; figures 6.7.c and Fig.6.7.d show a 500x500 nm^2 area, prepared respectively at T(9') $\sim$ 105° C with a mean island size $\sim$ 21 nm and at T(8') $\sim$ 125° C with a mean island size $\sim$ 40 nm.

6.3.2 SP-STM on Fe monolayer islands

Although the monodomain, in-plane Fe islands have already been presented superficially in figure 6.5.b, it is of interest to dwell on them a bit longer and describe their behaviour in greater detail, as they are the basis of the experimental system in this chapter and the next, in which their interaction with rare earth adatoms will be explored.

When considering SP-STM experiments, it is important to note that a larger dI/dV signal for a given orientation does not imply a parallel tip-sample configuration, as STM involves tunnelling electrons and not net magnetization. Figure 6.8.a provides a more detailed picture of the topography of a 50x50 nm^2 area measured at I_t = 1 nA and V_{bias} = -400 mV, where the smooth surface of the islands can be better appreciated, as can the carbon adsorbates (black spots) on the W(110) surface (brown background); the bright dots on the islands and on the tungsten are rare earth adatoms, which will be discussed in the next chapter. The dI/dV map of the same area (figure 6.8.b) shows islands with brighter and darker hue representing higher and lower differential conductance, respectively; the dark shadow to the left of the islands and the bright shadow to the right are due to feedback effects, and would be avoided with a slower scan of the image or a lower integration time in the lock-in. The profiles below provide a more quantitative point-of-view, relating the colour scale to actual values. Both Fe islands have a similar height of 210 pm, despite a small difference due to the SP contribution; meanwhile, the dI/dV signal on the two islands presents a strong difference, nearly 10% of the total signal, the darker island (right) is at 16.8 nA/V while the brighter one (left) is at 18.7 nA/V; meanwhile the signal on the bare tungsten is just below 20 nA/V (note that these are arbitrary units, and not strictly nA/V).

A clear visualization of how parallel/antiparallel cannot be inferred from high/low differential conductivity is presented in Fig.6.10, showing dI/dV maps of the same area described in the previous paragraph and figure, measured

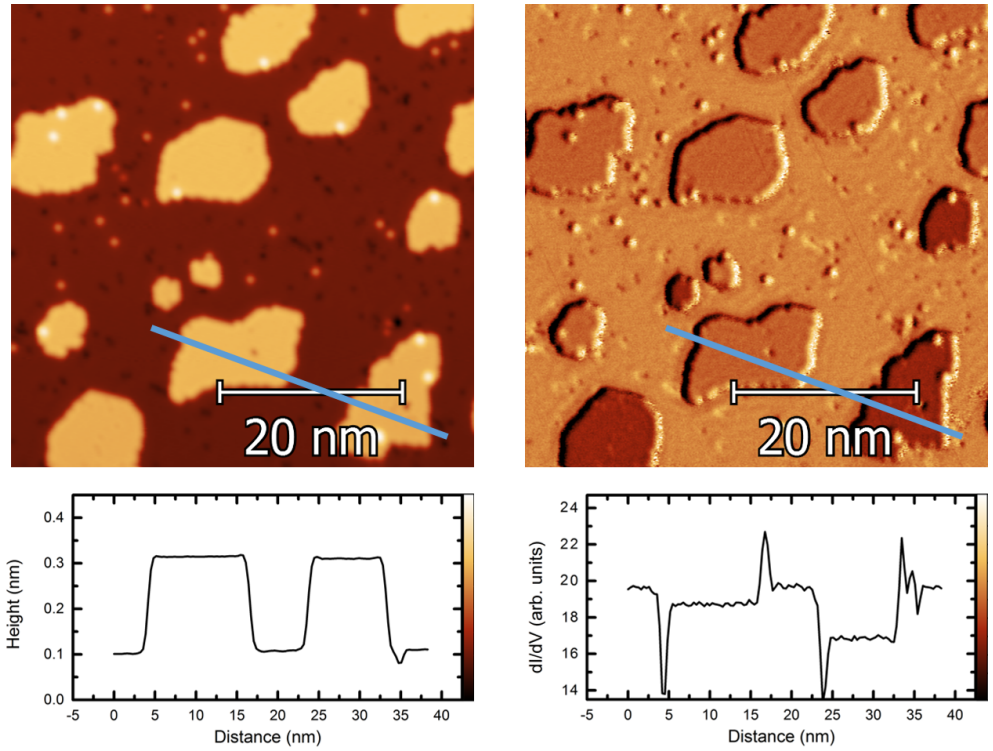

Figure 6.8: (a) Topography and (b) dI/dV map taken at V_{bias} = -400 mV, I_t = 1 nA showing the spin polarized contrast of Fe islands with opposite polarization when measured with a Fe coated tip. Below, profiles taken over the blue present more quantitative data of the (c) topography and (d) dI/dV signal.

at different bias, ranging from -1.9 V to +30 mV. It can be seen how the contrast not only increases and decreases for different biases, but actually inverts at several points (-1.9 V to -1.2 V and -800 mV to -400 mV). This is due to the non-monotonic LDOS profile for both majority and minority carriers independently. This means that a shift in energy can either increase or decrease the contribution to the tunnelling current of either, which will be reflected in dI/dV measurements.

It is useful to define a parameter that represents the dI/dV contrast between opposite polarizations to better describe the behaviour of the SP tunnel junction formed by tip and sample. Figure 6.9 shows dI/dV spectra taken on dark (blue) and bright (red) islands over a ±1 V bias range ("dark" and "bright" are assigned respect to their behaviour at -200 mV, for reference), below, following Oka et al. [189] shows such a parameter, typically called asymmetry, defined as the difference between the signals on islands of opposite orientations divided by the sum of the signals. The asymmetry over the ± 1 V

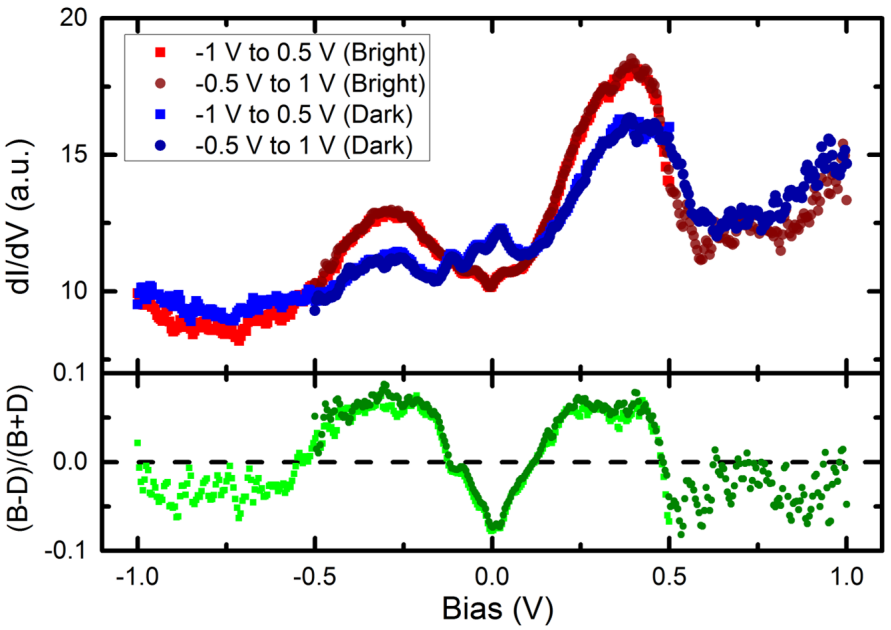

Figure 6.9: Differential conductivity spectra over a ±1 V range taken on Fe monolayer islands with opposite polarization using a Fe coated W tip. Below, asymmetry of the junction calculated as the difference between the dI/dV signals divided by the sum.

range shows the two contrast inversions mentioned for the previous figure as well as two additional crosses at similar energies, but positive bias, ± 500 mV, ± 50 mV. It should be noted that slight differences can be expected between dI/dV maps taken at constant current at dI/dV spectra taken with an open feedback loop, at constant height, as the tip-sample distance may vary during constant-current maps - an issue that will be discussed in greater detail in chapter 7.

Generally, determining which contrast to majority and which to minority is not necessary to study magnetic features, as parallel/antiparallel is a somewhat arbitrary concept as it depends on the tip orientation and a contrast inversion due to tip an opposite reorientation would not change spatial features. If a definite experimental confirmation of the relative orientation is required, an external magnetic field strong enough to saturate both tip and sample is required, in order to provide a clear reference of the dI/dV signal that corresponds to the parallel situation.

Another way of determining majority and minority states is comparing the observed behaviour with calculated band structures or spin-polarized ARPES experiments, where separate bands for majority and minority electrons can be obtained. In the particular case of Fe islands on W(110), an SP feature

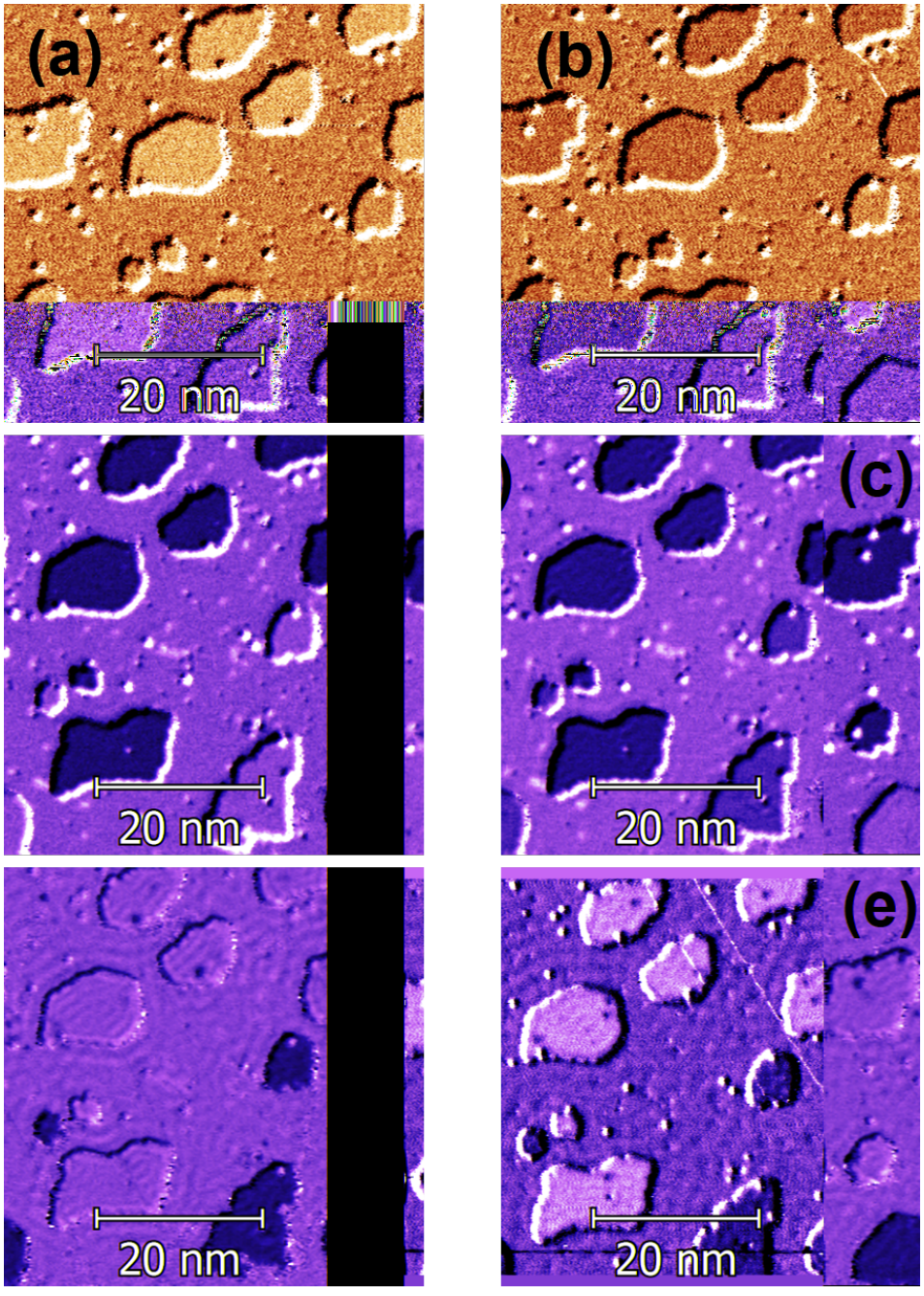

Figure 6.10: Differential conductivity maps taken over the same 50 x 50 nm^2 area of a monolayer Fe/W(110) sample at different bias. (a) -1.9 V, (b) -1.2 V, (c) -800 mV, -575 mV, -200 mV and +30 mV. Tunnelling current is set at $I_t = 1$ nA in all cases.

stands out over the simple bright/dark contrast, providing some insight into the properties of the electrons at the surface.

6.4 Quasiparticle interference in Fe islands

In the case of the Fe islands studied in this chapter, there are more differences in SP-STM experiments between islands of opposite polarization than just the total dI/dV signal, although a more subtle analysis is required to highlight them: Fig6.11 shows three differential conductivity maps of Fe islands on W(110) taken with a Fe coated W tip at I_t = 1 nA. The top image, acquired at V_{bias} = -300 mV, presents a smooth homogeneous signal on both islands of dark and bright hue; meanwhile, the same area measured at a different bias as shown on the bottom left (V_{bias} = -150 mV) presents a significantly different behaviour: while bright islands remain mostly smooth and homogeneous, dark islands show a strong interference pattern; finally, the map on the bottom right shows islands, both dark and bright, with a strong interference pattern - while being acquired at the same bias as the previous image, V_{bias} = -150 mV.

This behaviour can be easily explained as follows: The standing wave pattern corresponds to a spin polarized surface state, present in either the majority or the minority band, but absent in the other. The pattern is not observed at -300 mV on islands of either orientation in Fig6.11 because the onset of the surface state lies below this energy, at around -250 mV, and therefore a flat, homogeneous behaviour is observed in the dI/dV signal; the difference between the bottom two could be pointed out without even considering the behaviour of the surface state: the diminished contrast between the islands on the image on the right respect to the island of the left points to a tip not fully aligned with the magnetization of the islands, providing a lower asymmetry of the junction, as electrons from the minority (majority) band of the sample have a non-zero probability to tunnel into the minority (majority) band of the tip, as they are not orthogonal states; on the other hand, when the tips polarization is aligned with the magnetization axis of the islands, electrons are forbidden to tunnel into a band with an opposite spin, and therefore the pattern appears in only the islands in which there is allowed tunnelling from the surface state to the tip, which produces the image on the bottom left.

In this section, the effect of the polarization of the tip is explored by applying an external magnetic field. Islands of different size are investigated to determine the influence of size on the QPI pattern. Finally, the dispersion relation of the surface state is obtained by mapping the pattern at multiple bias.

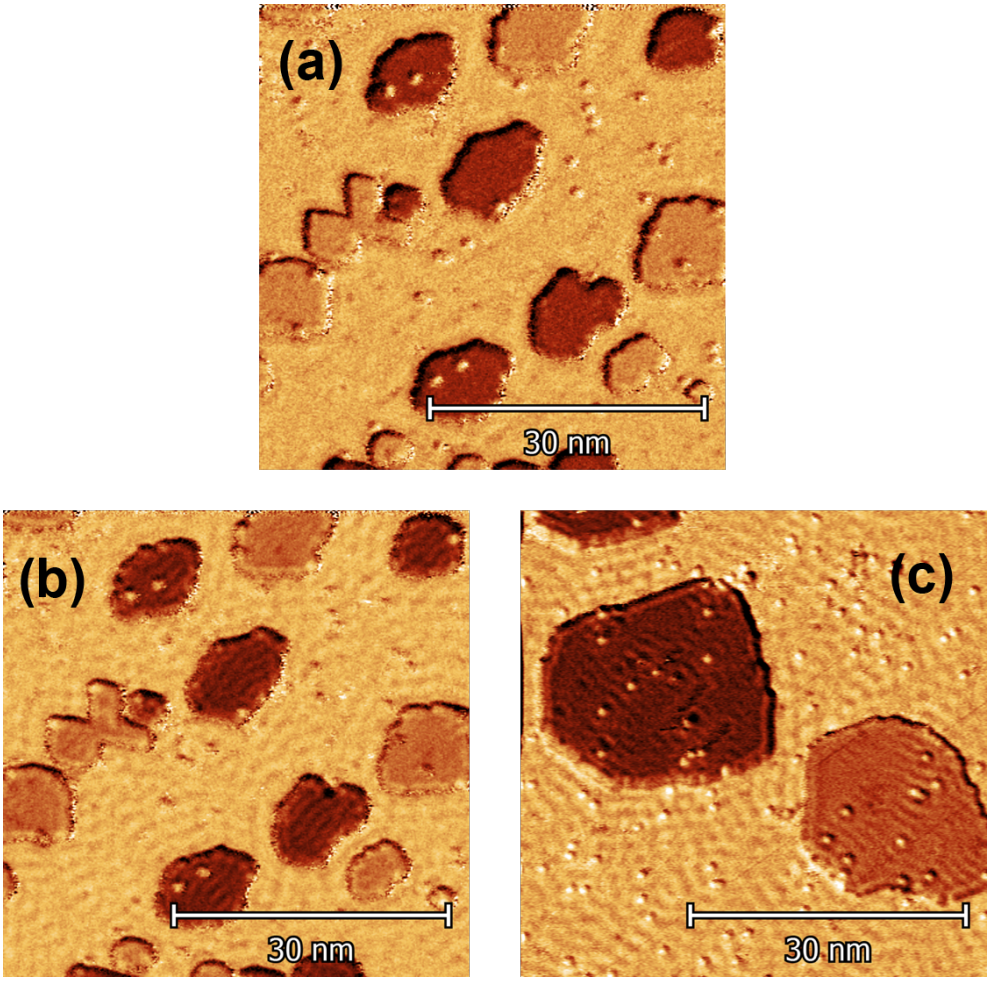

Figure 6.11: Differential conductivity maps taken at I_t = 1 nA and (a) V_{bias} = -300 mV and (b, c) V_{bias} = -150 mV. The map in (a) shows no interference pattern, (b) shows a clear pattern exclusively on dark islands and (c) said the same interference pattern on islands of either polarization.

6.4.1 Tip polarization dependence

A very striking example of how this feature is intrinsic to the spin of the electrons involved in the tunnelling current and not to particular islands is shown in Fig.6.12, where a dI/dV map of two Fe islands of opposite polarization is shown. What makes this figure stand out from the previous, similar examples is that, during the course of data acquisition, two spontaneous tip reorientations occur. Starting from the top, the first fifth of the image shows a moderate contrast between islands and the oscillation pattern, while visible with a narrower colour scale, is not readily apparent; at this point, the polarization of the

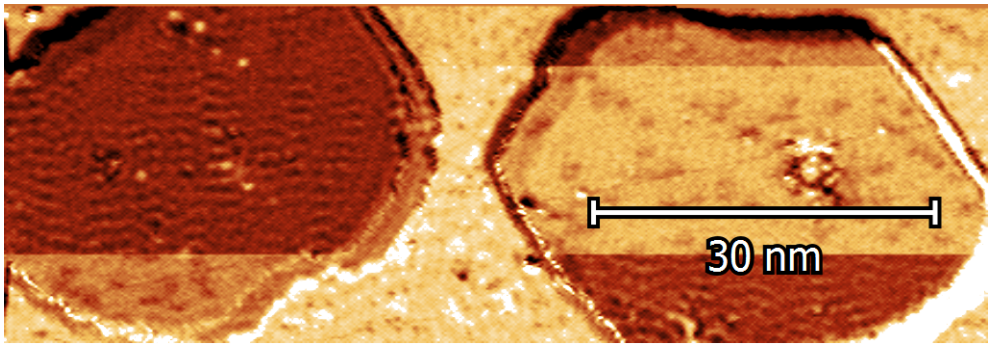

Figure 6.12: Differential conductivity map of two Fe islands with opposite polarization at I_t = 1 nA, V_{bias} = -150 mV using a Fe coated W tip. Two spontaneous changes in the tip behaviour occur, one near the top where the contrast is enhanced and after which a clear interference pattern can be see on the dark island, on the right; another change, a magnetization flip of the tip, occurs near the bottom of the map, exchanging the contrast between the islands.

tip shifts closer to the islands' easy axis, increasing the contrast and revealing a very clear interference pattern on the dark island while the bright island remains relatively homogeneous. Three quarters through the map acquisition, another tip reorientation occurs, this time a full magnetization reversal leading to an inversion of the contrast between the islands, which also carries with it the interference pattern, which is now clearly visible on the island of the right, previously bright and now dark, while absent on the left (now bright).

A closer examination of the oscillation pattern is required to extract further information, such as its symmetry and dispersion relation, E(k). To better explore these properties a Fourier Transform of the area of interest can be performed using the Fast Fourier Transform (FFT) algorithm, which highlights the periodicities present in the original image. Figure 6.13 shows a differential conductivity map of a 120 x 70 nm^2 area featuring three islands: a large dark island and two smaller islands, one bright and one dark. Taking a Fourier Transform of the area corresponding to the large dark island (bottom left in Fig.6.13) reveals that the interference pattern is actually formed by two distinct, although close, periodicities. Surprisingly, a Fourier Transform of the area corresponding to the much smaller bright island (bottom right in 6.13) shows a faint feature with the same symmetry as observed for the island of opposite polarization. As the bright island is much smaller, the quality of the Fourier Transform suffers and it is not immediately obvious if it is a single or double feature, as in the other case.

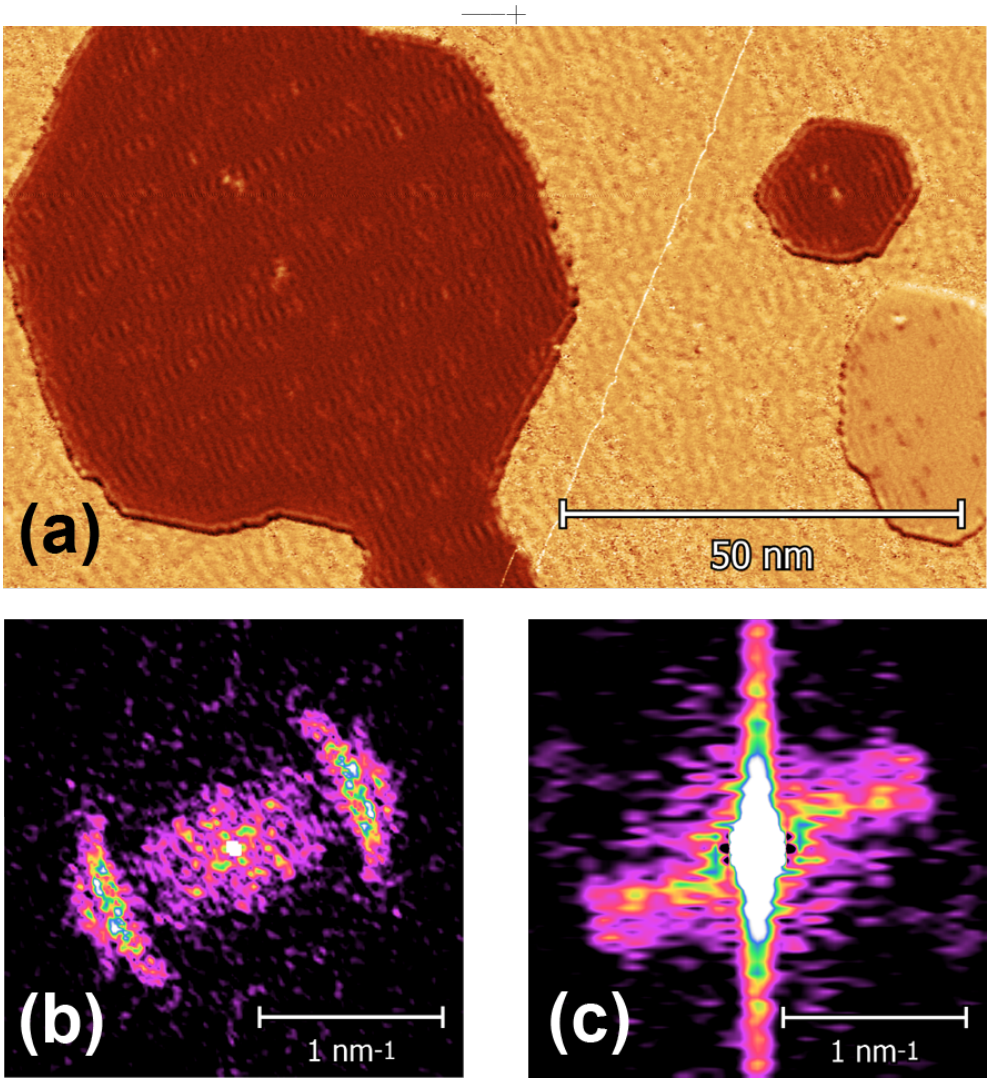

Figure 6.13: (a) Differential conductivity map of a 120 x 70 nm^2 area taken at I_t = 1 nA, V_{bias} = -100 mV, showing two dark islands with a clearly visible interference pattern and a bright island, in which the pattern is only slightly visible towards the island edge. Below, (b) Fourier Transform of the area corresponding to the large dark island on the left, showing two distinct features; and (c), Fourier Transform of the area corresponding to the bright island on the right, with some sort of feature although with a much worse signal-to-noise relation, due to the weaker oscillation.

Controlling the polarization with an external magnetic field

Monitoring the evolution of the contrast under applied out-of-plane magnetic field allows further investigation of this issue. An external field is able to

tilt the tip's magnetization continuosly out of plane, reducing the in-plane polarization of the tip. This produces a diminished contrast between islands (which are barely affected by the applied field as their easy axis lies strongly in-plane [2]) as it gradually opens a tunnelling channel between sample majority (minority) and tip minority (majority) states, which leads to the apparition of a clear interference pattern on bright islands. Figure 6.14 reproduces this situation, showing a zoom into the two islands discussed in Fig.6.13 at 0.0 T (top), 0.3 T (centre) and 1.0 T (bottom) applied perpendicular to the sample plane.

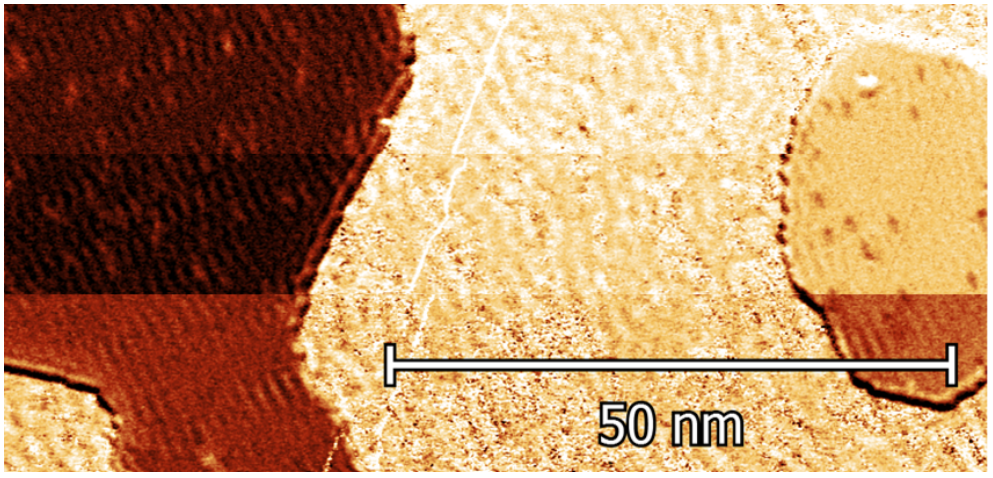

Figure 6.14: Differential conductivity map under different applied external fields, which changes the orientation of the tip. Top third taken at 0.0 T, middle third at 0.3 T and bottom third 1.0 T. Note how the interference pattern on the bright island on the right is most noticeable on the bottom third of the image, where the polarization of the tip is the most out-of-plane.

Fourier Transform analysis

Figure 6.15 provides a more detailed look into the behaviour presented in Fig.6.14. Fourier Transforms of both islands are taken at the three different applied fields (shown at 0.0 T in the figure, bottom left and bottom right for dark and bright islands, respectively) and, after masking for clarity the strong contribution at low k-values, which are due to noise and artefacts and not related to the oscillation, a profile across the direction of maximum symmetry is taken (top left, dark island; top right, bright island) to compare the evolution of each feature. The masked area is marked with a grey square on the profiles and by a smooth pink area in the Fourier Transforms. The module of $\mathbf{q}$ is obtained from the distance between the two peaks corresponding to the same

feature; due to how the FT is represented, $|\mathbf{q}|$ is equal to an eighth of the peak-to-peak distance.

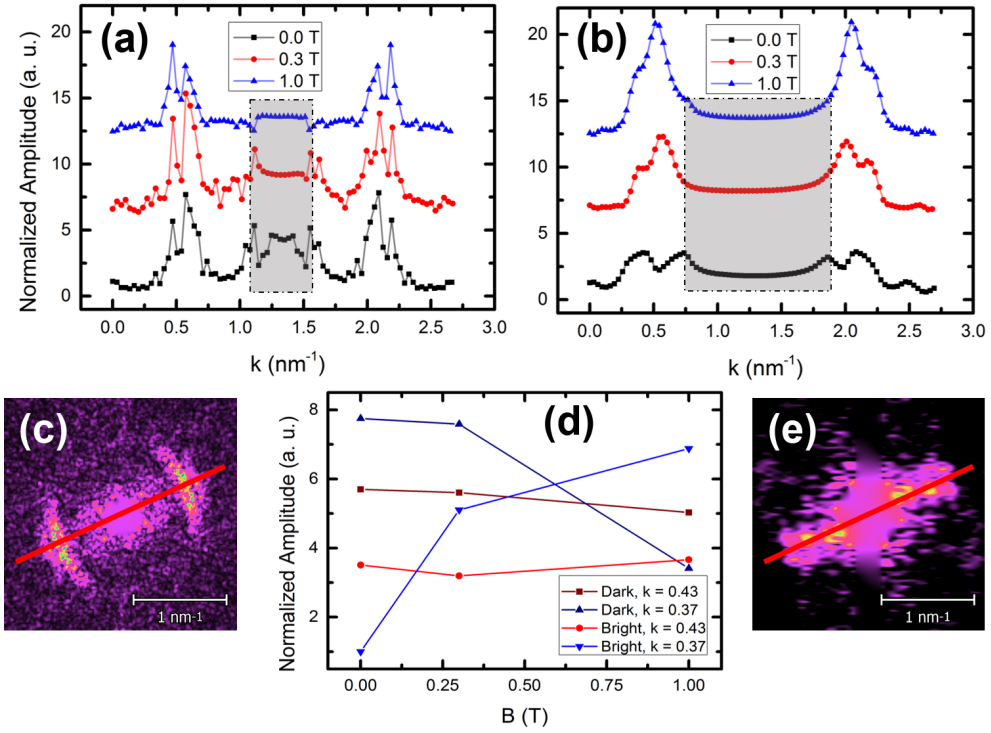

Figure 6.15: Analysis at different fields (0.0 T, 0.3 T and 1.0 T) of the interference pattern. (a) and (b) show the profiles taken across the Fourier Transforms below, in (c) and (e), respectively on the dark and bright islands on the previous figure (fig.6.13). The centre area of the FT, marked as a shaded area in the profiles, has been masked to allow for better visualization. (d) Background-normalized (divided by median) amplitudes of the two features in the FT, the more external feature, with q = 0.27 Å^{-1}, is unaffected by the change in tip polarization; meanwhile, the inner feature with q = 0.23 Å^{-1} is inhibited in the dark island and enhanced in the bright island as field is increased.

The profiles in Fig.6.15 quantitatively illustrate the issue introduced with Fig.6.11 and expanded with Fig.6.14 - *i.e.* that a strong oscillation appears on island of either polarization for a SP tip not aligned with the island's easy axis. To better compare the observed features, the FTs are normalized by their median value prior to measuring the profiles. The evolution of the features is readily observable for both islands: at 0.0 T the tip is strongly aligned in-plane and pointing along the easy axis of the islands, the two distinct features in the dark island result in two clear peaks (left) at q = 0.27 Å^{-1} and q = 0.23 Å^{-1}; meanwhile, a single broad and faint feature is observed for the bright island

(right) at q = 0.27 $Å^{-1}$. Increasing the field to 0.3 T takes the tip slightly out-of-plane, but this effect is not very noticeable for the dark island, where only a slight change in peak amplitudes is observed; on the other hand, a significant change takes place for the bright island as the previously absent feature at q = 0.23 $Å^{-1}$ appears clearly and the feature at q = 0.27 $Å^{-1}$ is just a shoulder on the dominant new peak. At this point it should be noted that the broadening and general poor quality of the FT on the bright island is due to the much smaller size of the studied island (less than a tenth of the total surface of the dark island) and not an intrinsic property of the features on bright islands; figure 6.17 shows the FT of a large bright island, resulting in a FT quality comparable to that of dark islands. Finally, at 1.0 T the tip is considerably out of plane and the change in amplitudes is more noticeable on the dark island, although both features remain distinctly visible; on the bright island the evolution observed for lower field is continued, with the feature at q = 0.23 $Å^{-1}$ growing further. To summarize the evolution of the amplitude of the peaks in the profiles, it is better to visualize them together as plotted at the bottom centre of Fig.6.15: Two clearly distinct behaviours are observed depending on the feature, rather than the island - the feature at q = 0.27 $Å^{-1}$, marked in red hues, dark squares for the dark island and bright circles for the bright island, presents a seemingly constant amplitude, independent of the applied field; in contrast, the feature at q = 0.23 $Å^{-1}$ is strongly field dependent, decreasing on dark islands and increasing (being initially absent) on bright islands with increasing applied out-of-plane magnetic field. This indicates that the feature at q = 0.23 $Å^{-1}$ is spin polarized while the feature at q = 0.27 $Å^{-1}$ is not, as it is present equally in both islands.

6.4.2 Island size dependence

To study the influence of island size on the oscillation pattern, a set of four islands of different sizes is examined for both configurations, parallel and antiparallel to the tip. This is achieved by field cycling the tip until an in-plane magnetization reversal is observed at 0.0 T. Figure 6.16 shows a similar analysis to the one performed for field dependence, but for island size. To the left, the unmasked FT are shown: bright islands on the left column, dark islands on the right, with increasing island size from top to bottom. The actual islands here analysed can be seen in Fig.6.17, with the largest island (noted XL) being 60 nm in diameter, down to 20 x 10 nm^2 for the next largest island (L), 8 nm in diameter (M) and finally, the smallest is around 5 nm across (S). As expected, the quality of the features worsens with decreased size, leading to broad peaks and poor signal-to-noise ratio for smaller islands. Despite this, the general properties of the oscillation seem to remain unchanged, the SP feature

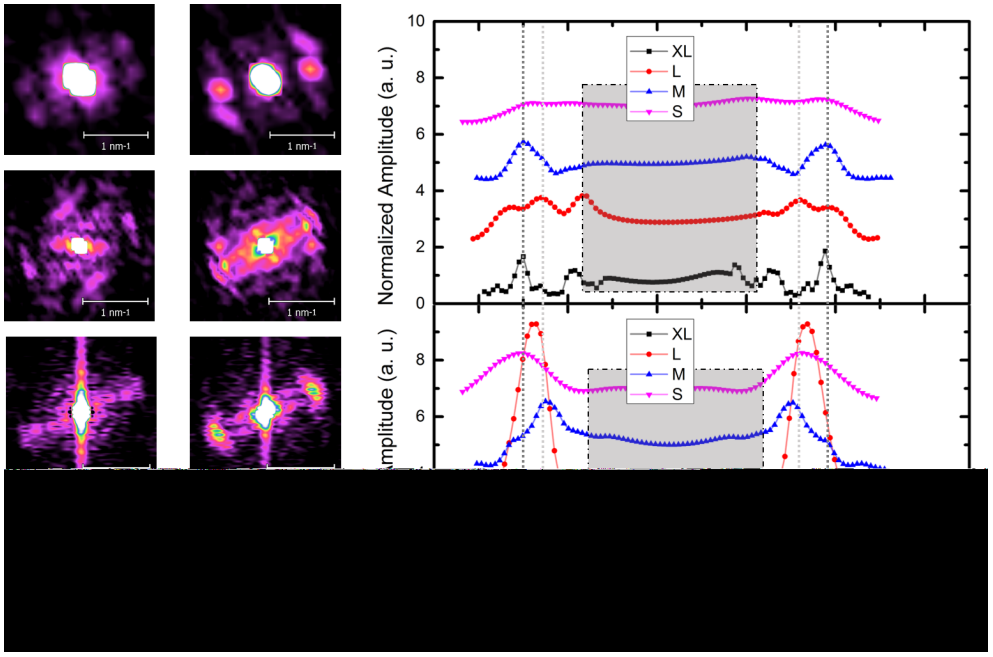

Figure 6.16: Left: Fourier transforms of dIdV maps for islands of different site, before and after inverting tip orientation, taken at I_t = 1nA, V_{bias} = -100 mV. Left column shows FT for bright islands, right column FT for dark islands. The island size increases from top to bottom. The actual dI/dV maps are shown in Fig.6.17. To the right: Profiles taken on the corresponding FT, top for bright islands and bottom for dark, show no evidence of size effects on the k of the dispersion, but rather only in the quality of the FT.

being only present on dark islands, while the other, smaller, exterior feature is present in all cases.

To discern whether the feature present in all islands is a non-spin-polarized contribution or actually two independent spin-polarized states with similar k, a detailed comparison of the same island when parallel and antiparallel to the tip can be performed. Figure 6.17 shows this situation, with maps taken on the largest of the islands discussed previously, before and after inducing the tip magnetization reversal; to the left, the corresponding FT of said island. The two images are aligned and a new image is formed by subtracting one image from the other (bright island minus dark island). The resulting image shows a clear interference pattern, and taking the FT reveals that only one the SP component remains, while the non-SP has practically vanished. This indicates that k is not similar for both polarizations, but rather the same; the amplitude and phase are also identical, as otherwise the oscillation would still be noticeable in the FT.

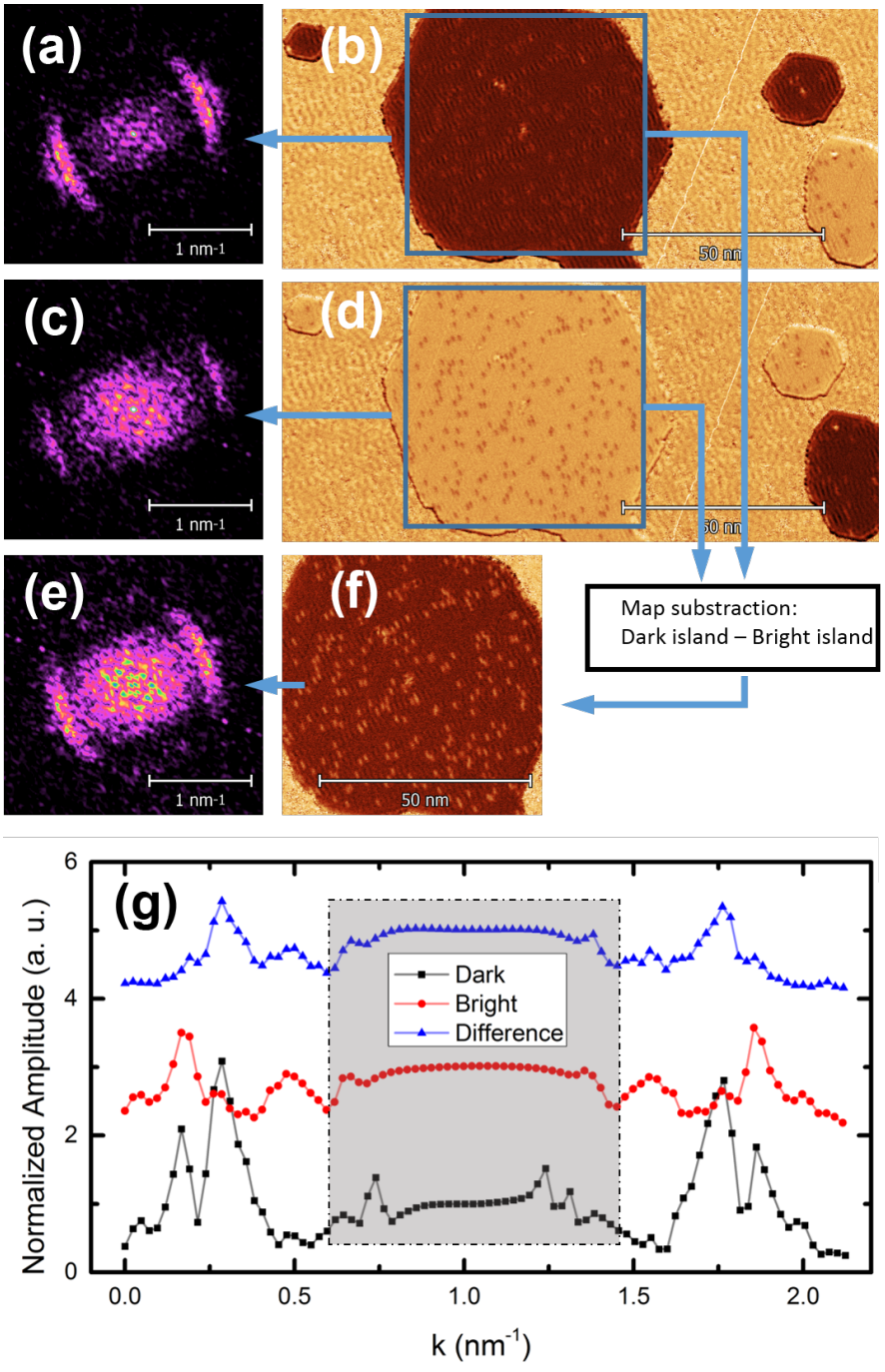

Figure 6.17: Fourier Transforms (a), (b) of differential conductance maps taken at I_t = 1nA, V_{bias} = -100 mV before (b) and after (d) inducing a tip-flip by field cycling. Below, an aligned, direct subtraction of the area corresponding to the (f) large island and (e) its FT. (g) Profiles taken across the FT, showing the disappearance of the weaker feature in the FT of the subtracted map.

6.4.3 Dispersion relation

The dispersion relation of each state, E(k), can be obtained by taking dI/dV maps at different bias voltages over the relevant energy range and measuring the evolution of the position of the peaks in the FT. The dispersion relation can then be compared to band calculations to identify the particular features observed in the experiment, which can provide further insight into the nature of the electrons involved, as well as a reference point for the expected behaviour in an ideal system.

It is interesting to perform this analysis of the bias dependence on islands of both orientations respect to the tip, as it has already been shown that the FT is capable of discerning details not evident in real space.

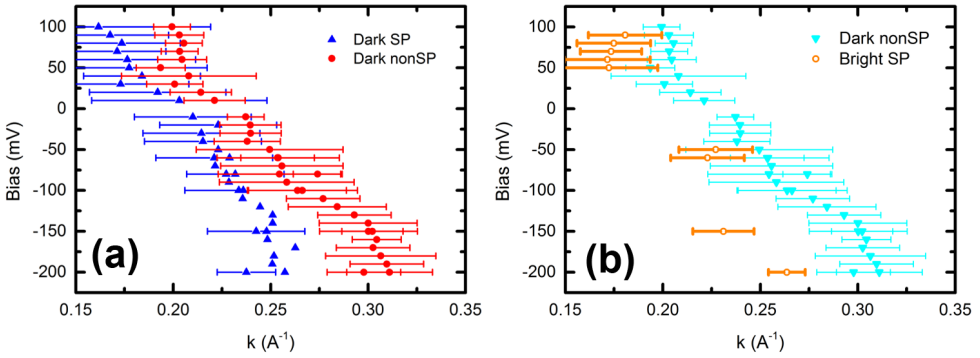

Figure 6.18: Dispersion relation E(k) of the two features observed in the FT (a) of dark islands in Fig.6.17, with the error bars calculated from the FWHM of the peaks in the profile. (b) Shows the same analysis for the bright islands, where the non-SP feature is observed and, except in some cases where the tip polarization was not optimal and both features can be discerned.

Figure 6.18.a shows the dispersion relation measured on a large dark island from -200 mV to +100 mV, showing the evolution of the two features described in the previous section. Both present a negative dispersion ($dE/dk < 0$) with a similar slope, although the values near the Fermi level for one and another feature become close enough to consider the possibility of a crossover of the two dispersions instead of the approximately parallel situation suggested by the colour selection in the plot, which would result in a stronger slope for the spin polarized feature and a flatter non-spin polarized dispersion.

Comparing with a similar analysis for a bright island clarifies the situation (see Figure 6.18.b), as the feature that is visible in all cases corresponds with the outer feature of the dark islands over the whole bias range. As the data acquisition was performed in several steps, some of them after the field de-

pendent experiments, at some biases both features can be detected, although faintly, due to a tip not fully aligned with the easy axis of the islands. In any case, this is useful as it allows for a comparison of both features as observed on the dark island. In figures 6.18.a and 6.18.b the error bars are obtained from the full width at half maximum of the peaks observed in the profiles; the uncertainty could be improved by measuring larger islands at a higher resolution, increasing both the number of oscillations per island and the number of data points per oscillation that would be used for the Fourier Transform - this would be particularly beneficial for the study of bright islands, as in this experimental run they have been studied in relatively small islands which leads to poorly defined features.

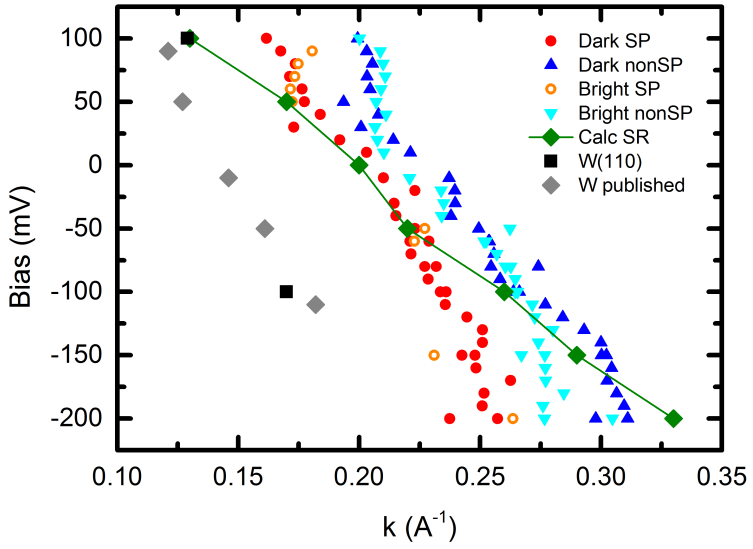

Figure 6.19: Dispersion relations E(k) measured on islands of both orientations, without error bars to avoid clutter. The $SR_{d(sp)}$ present for minority electrons in figure 6.2 is plotted in green. Black squares indicate the measured k for the interference pattern on the W(110) surface, compared to values reported in the literature marked in gray [228].

Comparing with figure 6.3, it can be seen that there exists a feature for minority electrons, a surface resonance of mixed character *d-sp*, that presents a comparable behaviour and is absent for majority electrons. Including this surface resonance in a plot with the experimental dispersion relation shows a good agreement in both position and dispersion, as can be seen in figure 6.19, this time without error bars to reduce clutter. Thus, it is reasonable to conclude that the spin polarized feature observed on dark islands corresponds

to a surface resonance of minority electrons (and, therefore, the dark hue at V_{Bias} = -200 mV corresponds to an antiparallel configuration between tip and island). On the other hand, the non-spin polarized feature present on all islands, at a k slightly larger than the surface resonance feature, remains unaccounted for.

Similar results with two close dispersions, although not spin polarized, have been reported for noble metal (111) surfaces (Au, Ag, Cu), one corresponding to a surface state and the other being attributed to either bulk states [229, 230] or, more recently, to an acoustic surface plasmon [231]. Two close spin polarized dispersions, one for majority and one for minority, have been observed on the Ni(111) surface [202]. The present case is set apart from these by the fact the Fe islands are ferromagnetic, and thus a spin polarized difference would also be reasonably expected for bulk contributions. Exploring the robustness of the feature against contamination (such as hydrogenation or oxidation), or studying its evolution with film thickness could serve to discard some possibilities and suggests others. If the origin is related to the Fe-W(110) interface, a thicker film should see this contribution diminished and the feature disappear while a pure Fe-surface feature would remain; on the other hand, surface states related to dangling bonds can be quenched by passivation, but a feature due to the interaction with the W layer would be expected to survive.

6.5 QPI anisotropy

A characteristic feature observed in the QPI pattern and, more clearly, in the FT, is the preferential orientation of the patterns along a fixed crystallographic direction of the islands, resulting in a **q** vector parallel to the $[1\bar{1}0]$ direction (*e.g.* see figure 6.17). It is remarkable that the orientation ot this quantum interference is only weakly affected by the island edges, hardly completing a period of the oscillation parallel to the border in the dI/dV maps; the oscillation along the $[1\bar{1}0]$ direction, however, is equally visible across the whole island, even in the largest of them. More surprisingly, a similar issue is observed for the W(110) surface state when Fe is present.

6.5.1 QPI on W(110)

The fact that the W(110) surface presents a similar behaviour, suggests that the origin of this anisotropic **q** lies in the interaction between W(110) states and Fe states. Figure 6.20 shows a series of dI/dV maps and their corresponding FT focusing only on the W(110) contribution, where different cases can be described:

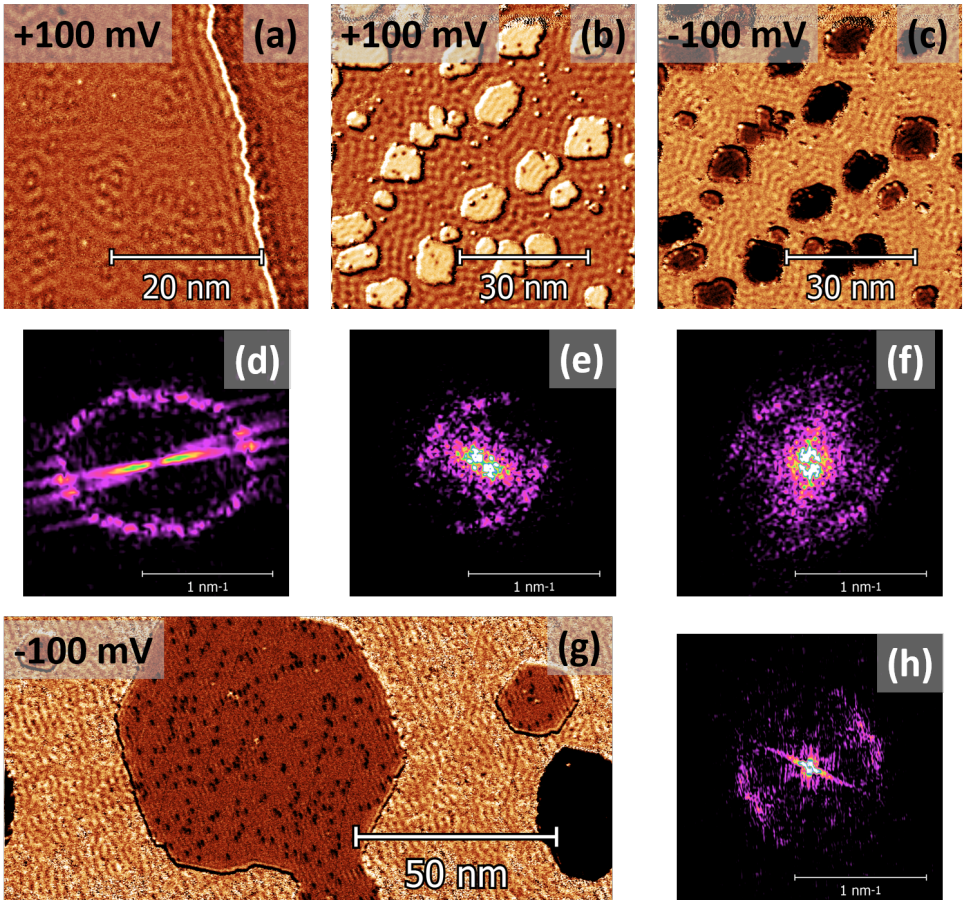

Figure 6.20: Evolution of the W(110) surface state in the presence of Fe. (a) Shows a dI/dV map at V_{Bias} = +100 mV of the pristine W(110) surface, which produces an interference pattern with componentes in all directions, as illustrated by the FT in (d). The presence of Fe islands introduces an anisotropic distribution of amplitude, as seen at +100 mV (b, e) and -100 mV (c, f). In the presence of larger Fe islands, the interference pattern in W(110) is fully directional along the $[1\bar{1}0]$ direction, parallel to the interference pattern on the islands.

- In clean W(110) samples where Fe is not present, the surface state disperses in all directions as seen in figure 6.20.a at V = +100 mV, and performing a FT results the expected ellipsoidal shape [228], the long and short axis corresponding to the [001] and $[1\bar{1}0]$ directions, respectively (see fig. 6.20.d).

- When Fe islands are grown on the surface, the interference pattern on W(110) appears to favour the $[1\bar{1}0]$ direction, as on the islands. This is shown in figures 6.20.b and 6.20.c for +100 mV and -100 mV, respec-

tively, and emphasized by the FT below, figures 6.20.e and 6.20.f, where the long axis of the ellipse is inhibited. This effect could be attributed to the geometry of the sample, as the Fe islands form two parallel lines enhancing the standing wave along the $[1\bar{1}0]$ direction, but a closer inspection of the dI/dV maps reveals that, although the wave pattern does somewhat follow the island edges, it doesn't propagate far along the [100] direction.

- For larger Fe deposits, as shown in 6.20.g, the interference pattern appears oblivious to the presence of the island borders, and the **q** vector in the W(110) surface is aligned parallel to the **q** in the Fe layer, along the $[1\bar{1}0]$ direction.

Similar anisotropic patterns have been reported in the literature, for example in the case of the (110) surface of the NiAl alloy [232]. The NiAl alloy crystallizes forming the B2 bcc structure, with Al in the center of the cube surrounded by Ni atoms. STM measurements show an interference pattern where the signal along the [100] direction is much stronger than along the $[1\bar{1}0]$. This fact is explained as the result of the strongly directional nature of the *d* states due to the Ni atoms. In the case of a single element material the closer atomic distances in the plane are along $<1\bar{1}1>$ directions, which could introduce anisotropy along these directions. However, if this were the case for W, it would be expected that this anisotropic amplitude distribution would also be observed on the pristine W(110) surface, something that has been shown to not be the case in figure 6.20.d, where the amplitude is quite constant independently of the orientation of **q**.

6.5.2 Phenomenological Model

A different approach to understanding the problem can be found by considering equation 6.1: the lack of an oscillation along the [100] direction in the Fe island could be explained by making the factor T = 0 for values of k_i and k_b perpendicular to **M**, *i.e.*, by introducing a relation between spin and moment, not unlike the spin-moment locking present in Rashba systems [233–235]. Asymmetric bands have been reported for Rashba systems grown on ferromagnetic films [236]; conversely, a coupling between the Fe surface resonances with the underlying W(110) surface state, which presents a Dirac-cone-like behaviour and a strong Rashba spin-orbit coupling that induces a spin texture [237–244], can be used to build a phenomenological model that accounts for this asymmetry.

In hybrid structures with a topological material and a the non-topological layer, the existence of perfectly conducting channels in the material without

topological protection (a metal) by the proximity of a 2D TI material has been reported [245]. The resulting band structure in the metallic layer incorporates a band with a spin state non degenerate for k and -k at fixed values of E.

In the Fe/W(110) system it is reasonable to consider the proximity effect of the W layer, as the surface resonance in Fe incorporates electronic densities coming also from the second atomic layer[203], and thus interaction between electrons from the Fe and W layers can be expected.

Fe *sp* mobile electrons, which have a defined spin orientation due the exchange field in the islands, couple with *d* electrons of the W interface layer, which have a spin-texture similar to spin-locked surface states in topological insulators [246]; thus, the density of states of minority and majority spins is modified in their k-dependence by the spin-texture of the W layer, as states in Fe and W with orthogonal spins will not able to produce a resonance. As a result, the number of states in the surface resonance is maximized for the k values where the spin component in the Fe and W layers is parallel. A simple diagram of the situation is shown in figure 6.21.

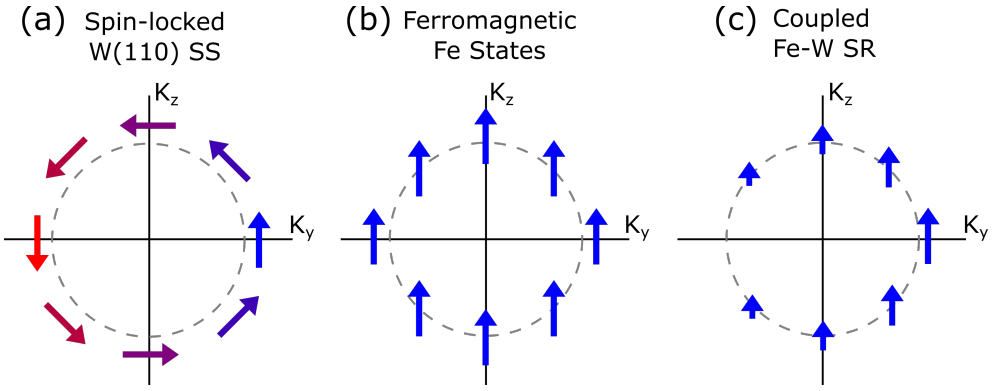

Figure 6.21: Simple diagram depicting the relevant ingredients of the model. (a) The Surface State in W(110) presents a Rashba-like spin-moment locking due to the strong spin-orbit coupling, with the spins aligned perpendicular to the k momentum. (b) The Fe layer presents states with spin along the magnetization direction, z, for all k. (c) The Fe Surface Resonance couples the two previous cases, leading to an unequal distribution of k momenta but with spins still aligned along z.

Using the language of the quantum mechanics, the majority and minority iron spin states are quantized along the z $\parallel [1\bar{1}0]$ direction, thus the majority and minority spin band can be represented as $|S_z;+\rangle$ and $|S_z;-\rangle$, respectively. For the W(110) surface, the spin operator is defined along the vector $\hat{\mathrm{n}}$ perpendicular to the k vector with a defined eigenvalue for every θ that form $\bar{\mathrm{n}}$ and $\bar{\mathrm{z}}$, denoted as $|S_n(\theta);+\rangle$. The spin component of the surface resonance in the Fe/W system, $|S_z(\theta);+/-\rangle$, can then be expressed as the result of a projection

of the spin state of the W layer with the quantification axis n̂ perpendicular to the $\hat{\mathbf{k}}$ vector over $|S_z;+\rangle$ or $|S_z;-\rangle$. For spin minority electrons the projection operator is $|S_z;-\rangle\langle S_z;-|$ and:

$$|S_z(\theta);-\rangle = |S_z;-\rangle\langle S_z;-|\,|n;+\rangle \tag{6.2}$$

On the W(110) surface the spins are confined to the yz plane (with x normal to the plane), so with $n = (n_x, n_y, n_z) = (sin\theta cos\phi, sin\theta sin\phi, cos\theta)$ and $\phi = \pi/2$, this can be expressed as:

$$|S_n(\theta);+\rangle = cos(\theta/2)\,|S_z;+\rangle + isin(\theta/2)\,|S_z;-\rangle \tag{6.3}$$

and eq. 6.2 becomes:

$$|S_z(\theta);-\rangle = isin(\theta/2)\,|S_z;-\rangle \tag{6.4}$$

Analogously, for majority spin states:

$$|S_z(\theta);+\rangle = cos(\theta/2)\,|S_z;+\rangle \tag{6.5}$$

The angular distribution of $\langle S_z(\theta);-/+|\,|S_z(\theta);-/+\rangle$, represented in figure 6.21.c, indicates that the density of states is k-dependent; according to this model, the distribution becomes anisotropic and has a maximum for the value of θ at which the spin in the W(110) layer is parallel to the spin in the Fe(110) layer, while states at the opposite k are forbidden. As the spin-orbit coupling locks spin and momentum perpendicular to each other, the maximum is obtained for k perpendicular to the magnetization direction, *i.e.* k_y.

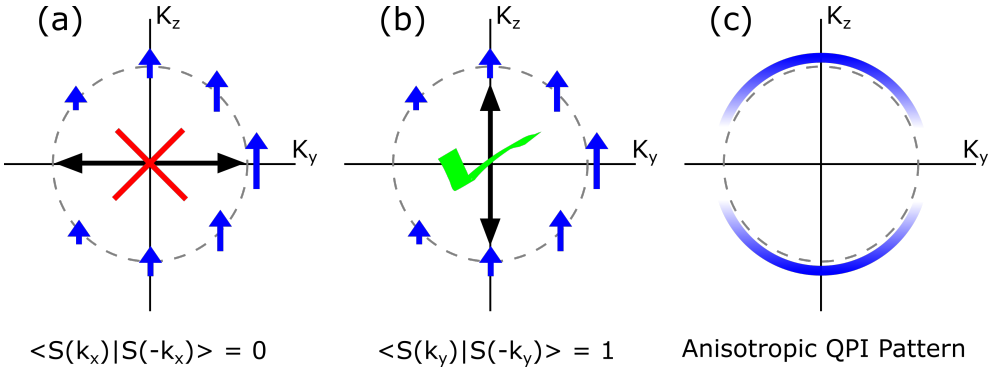

Figure 6.22: (a) Interference between states with $\pm k_y$ is not possible, as no $-k_y$ states exist. (b) Other interferences are allowed, with a maximum amplitude at $\pm k_z$. (c) This results in an anisotropic QPI pattern, modulated as $\sin^2\Theta$, where $\Theta = 0$ indicates pointing along $+k_y$.

Experimentally, the maximum amplitude of the observed pattern corresponds to k-states along the magnetization direction, *i.e.* k_z. This is readily

explained in this model by noting that there are no states with -k_y, and thus despite the maximum density of states at k_y, interference is not possible. Figure 6.22 presents a simple diagram of the situation. Calculating the scattering probability, includes a spin-dependent scattering matrix element T(q,k) [201], given by T(q,k)= $|\langle S(k)|\,|S(k+q)\rangle|^2$, leads to the same results. Using the expressions obtained for $|S_z(\theta);-\rangle$, T(q,k) becomes proportional to $sin^2\theta$, Thus T(q,k) has the minimum for $\pm k_y$, perpendicular to M_z, as T(q,k) = 0 for θ=π and θ=0; conversely, the maximum value of T(q,k) is observed at θ=$\pm\pi/2$, *i.e.* k parallel to M.

The fact that the behaviour is also reproduced on the W(110) surface can be understood in the context of this model by an induced magnetization of the W(110) surface, similar to what has been reported for the Pt(111) surface in Pt/Co systems [247, 248].

Chapter 7

RE adatoms on Fe/W(110): The role of d and f electrons

The study of single magnetic atoms adsorbed on solid surfaces of different elements has been a subject of steady interest during the past two decades, mainly as concerns to adatoms of transition metals (TM). Adatoms of different 3d magnetic TM deposited on various kinds of substrates have been fairly well studied by scanning tunneling spectroscopy (STS), spin-polarized scanning tunneling microscopy (SP-STM), and inelastic scanning tunneling spectroscopy (IETS) [13, 183, 199, 249–262]. The capability of SP-STM to reveal the spin state down to the single-atom level has led to experimental findings which encouraged further research work for a better understanding of the magnetic interactions of individual adatoms and larger nanostructures on surfaces [13, 253, 263]. Furthermore, looking for larger magnetic moments and magnetic anisotropy, two quantities to keep as large as possible in nanomagnetic materials designed for ultra-high density magnetic storage media and advanced spintronic devices, Rare Earth (RE) elements have to be considered. This is what has fostered the research in single ion RE molecular magnets over the last years [264].

Regarding RE adatoms on surfaces, Ce attracted some early interest associated with Kondo effect [265–267], but much of the later work has focused on their magnetic properties, studied by means of STM and XMCD: Ho [15, 166–168, 268], Gd [269], Er [119, 268] and Tm [31, 270]. Nevertheless, the role of $4f$ electrons in the tunnelling process, as well as the accessibility of these inner electrons, recently addressed in RE molecular magnets [170], remains an open issue for the case of RE adatoms on metals [31, 166, 269].

In RE metals the $4f$ electrons are the main responsible for the magnetic moment of the atom and the external $5d$ and $6s$ electrons make only a discreet

contribution to it. Nevertheless, their role cannot be disregarded, since these outer electrons mediate the magnetic interactions among different atoms and greatly determine the magnetic properties of the element or compound [271, 272]. In particular, the RE-transition metal compounds have been thoroughly studied [273], and the magnetic coupling between the RE and TM sublattices explained through the model proposed by Campbell [274], in which the RE-5d/TM-3d bands hybridization results in an antiparallel spin coupling, while the RE-4f and 5d spins are ferromagnetically exchange coupled [272, 275, 276].

This chapter explores the spin polarization state of single RE adatoms, Tm and Lu, on a ferromagnetic substrate, consisting of Fe monolayer nanoisland grown on a W(110) surface. The SP-STM measurements demonstrate a conduction mechanism for 4f metals involving 5d electrons and prove that these 5d-states have a net spin moment, which couples antiferromagnetically (AFM) to the overall 3d-spin moment of the Fe island, for both types of RE adatoms, independently of the existence or not of a 4f magnetic moment.

7.1 Sample preparation

In the previous chapter, Ch. 6, the procedure for preparing suitable samples consisting in Fe ML islands on W(110) has been discussed in detail. In this chapter the focus shifts to the magnetic coupling of RE adatoms evaporated onto said islands.

As in chapter 5, RE are evaporated onto a pre-cooled sample to minimize diffusion (5 K) from a Mo crucible filled with 99.99% pure Tm (Lu), which is heated by electron bombardment. The evaporator used is a SPECS EBE-1 pointed to the sample in the STM-stage, which can be exposed by opening a small window through the thermal shields.

7.1.1 Rare Earth Dosing

Optimizing the coverage for this experiment means fulfilling a series of requisites, *i.e.*: isolated, individual adatoms; several adatoms per island; large, clean Fe islands. Figure 7.1 shows the coverage obtained for different flux rates / times, ranging from a low coverage around 0.05% of a ML in (a) to a denser deposit, which is starting to clusterize, around 1.9% of a ML in (d). Fig 7.1.c shows a compromise of the isolated-adatoms and multiple-adatoms-per-island requirements, which will be the kind of samples that will be used in this chapter, at 0.3% of a ML.

Ideally, comparing the behaviour of Tm and Lu adatoms should be done

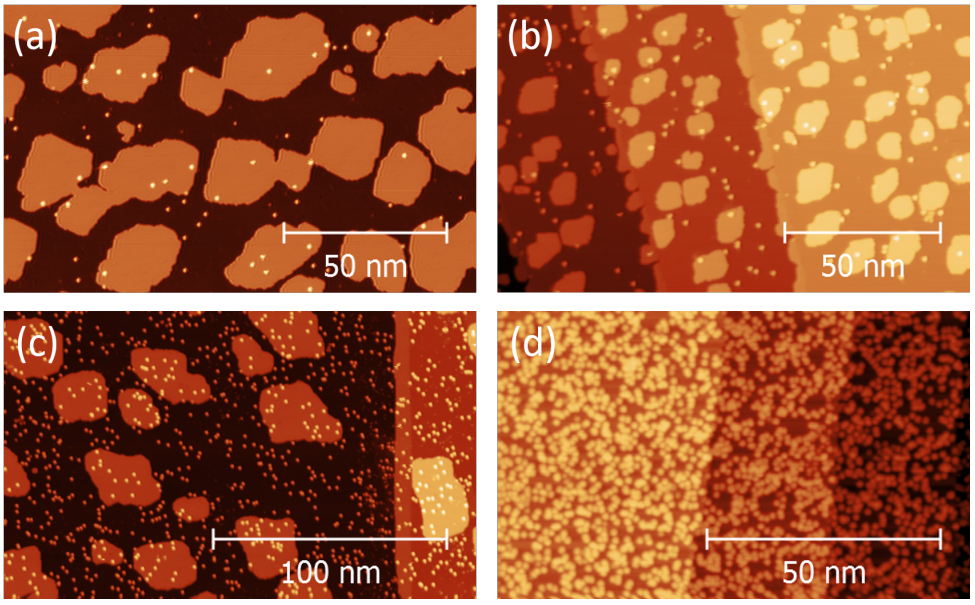

Figure 7.1: STM constant current topography of Fe islands on W(110) after dosing with RE adatoms. From (a) to (d) increasing coverage. An ideal coverage is shown in (c), around 0.3% of a ML. The coverage in (d), around 1.9% of a ML, already leads to clusterization.

simultaneously, on the sample and with the same tip. This requires being able to identify each species, which due to their similar atomic radius and electronic behaviour is not a trivial issue. The easiest way to tell different species apart in an STM experiment is by their apparent height, however, as shown in figure 7.2, profiles taken at different bias on Tm and Lu adatoms are not enough to identify each species, as they present a similar height (∼110 pm at low bias) and behaviour (increasing to ∼320 pm at higher bias).

7.1.2 Sequential Evaporation

Another approach is to evaporate the different species sequentially, mapping the area of interest in some detail prior to the second evaporation (as illustrated in fig.7.3.a, 7.3.c-g), identifying all the observed adatoms as belonging to the first species. Returning to the same area (shown in fig.7.3.b) after evaporating a second time highlights the stability of the system, as the process includes exchanging the evaporator, performing a bake-out for ∼12 hours and a thorough degass prior to opening the valve to the STM chamber, which results in at least 24 hours between images 7.3.a and b, on top of which the STM tip is retracted ∼10 mm to avoid blocking the evaporation flux onto the area under

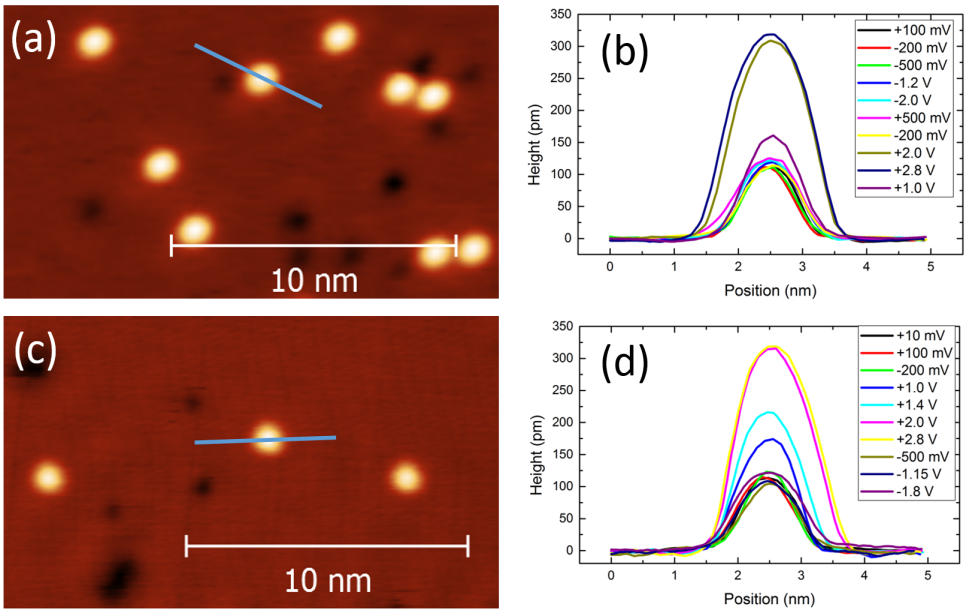

Figure 7.2: (a) STM topography of Tm adatoms on W(110) and (b) profiles taken at different sample bias. Below, (c) and (d) show the same situation for Lu adatoms.

study; despite this gruelling procedure, approaching back to the sample finds a displacement of the tip of only ∼150 nm between the two images.

Figure 7.4 shows a detailed scan of the same area before 7.4.a and after 7.4.b the second evaporation. Tm adatoms from the first evaporation are highlighted in green, allowing for an easier visualization of the effect of the evaporation of Lu adatoms: while Tm adatoms on W(110) fall perfectly within the mask, those on Fe islands are more susceptible to have been displaced. This further complicates identifying the two species, and thus sequential evaporation does not produce good enough samples to justify such a long process. Taking spectra on the adatoms on the W(110) surface reveals that dI/dV signatures do not serve as identifying characteristic either, as illustrated by figure 7.4.c, showing spectra for a Tm adatom (red), Lu adatom (blue) and the W(110) surface (green), where both adatoms present the same features.

The difficulty in identifying reliably each species, compounded by the risk of not finding the same area which was previously characterized in detail if it falls beyond the scan range, added to the fact that the preparation process consists in a long series of time consuming steps with a considerable probability of not obtaining a good enough sample make sequential evaporation a less than ideal procedure.

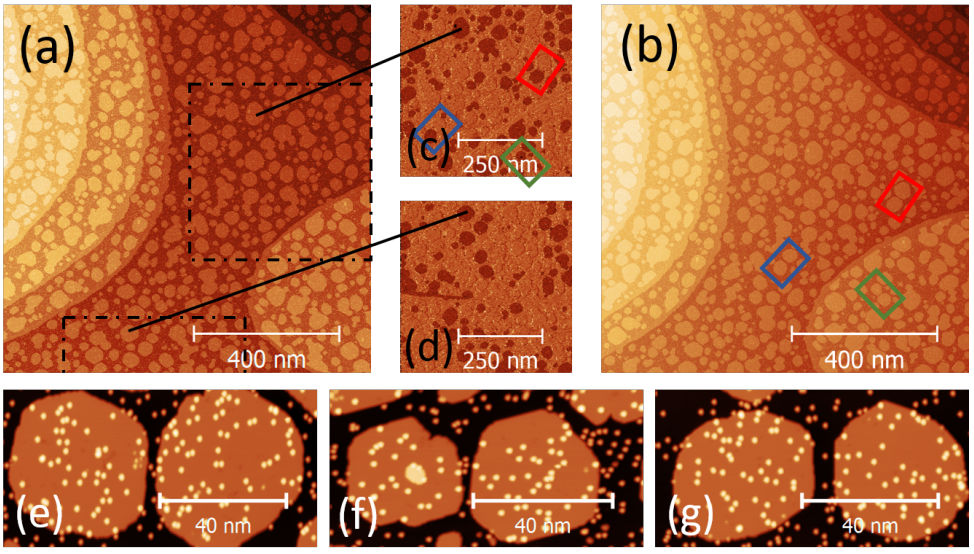

Figure 7.3: 1x1 μm^2 STM overview of an area (a) before and (b) after evaporating atoms of a second RE species. (c, d) show dI/dV maps with spin sensitivity. (e) through (f) show pairs of neighbouring islands with opposite polarization.

7.2 SP-STM: RE adatoms on Fe monolayer islands on W(110)

As identifying the two species, Tm and Lu, is not as straight forward and reliable as it would be desired, the SP-STM experiments in this section are performed on samples with a single species, Tm or Lu on Fe/W(110) samples.

7.2.1 Tm on Fe/W(110)

Figure 7.5.a shows a constant current topography image of a 50x50 nm^2 area showing Fe islands on W(110) onto which Tm adatoms have been evaporated; while the adatom density is lower than would be ideal, only around 1 adatom per 7x7 nm^2 island, the observed behaviour is reproducible across the different islands: Figure 7.5.b shows a dI/dV map of the same area taken at V_{Bias} = -200 mV, I_t = 1 nA using a Fe coated W STM tip, which presents an in-plane magnetization and, therefore, is sensitive to the in-plane component of the polarization of the sample. A strong contrast observed for Fe islands with opposite polarization and, in what is the focus of this chapter, the contrast observed between the Tm adatoms on islands of opposite polarization, as adatoms on dark islands present a larger signal than those on light islands.

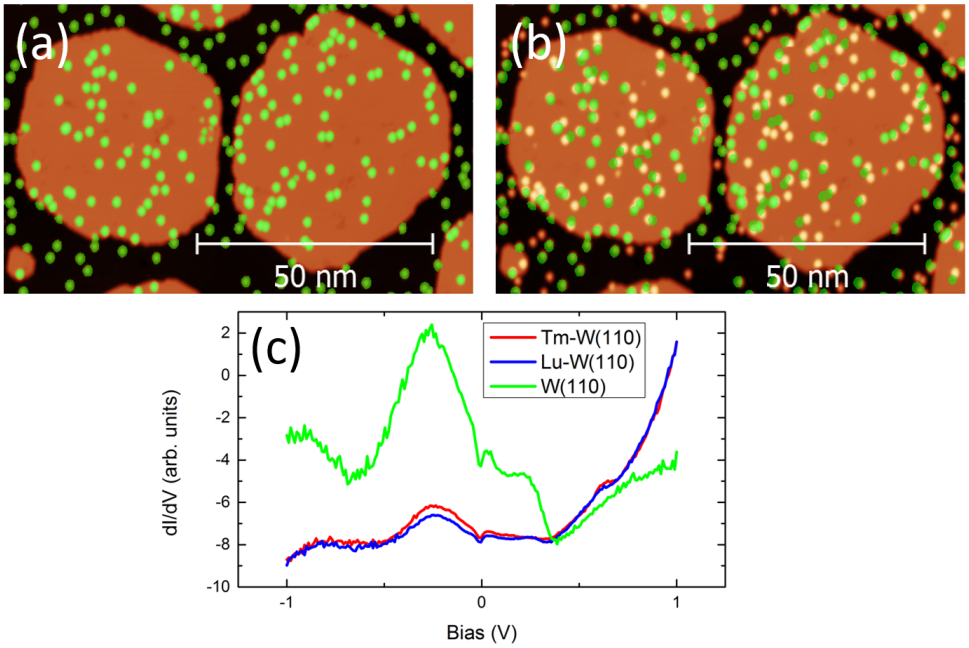

Figure 7.4: Detailed STM topography of figure 7.3.e. In (a) only Tm adatoms have been evaporated; (b) shows the situation after evaporating Lu adatoms. Below, (c) shows the dI/dV spectra for Tm and Lu adatoms and the W(110) surface.

Figures 7.5.c and 7.5.d expand on this observation, showing spectra over a +100 mV to -900 mV range taken 7.5.c on Fe islands and 7.5.d on the Tm adatoms lying on them. The spectra in fig.7.5.c show the expected behaviour for Fe ML islands on W(110), as detailed in the previous chapter (Ch.6), presenting a larger LDOS for majority electrons around the ($\sim$ -500 mV, $\sim$ -50 mV) range, with an inversion of the observed contrast above $\sim$ -50 mV and below $\sim$ -500 mV; on fig.7.5.d a very similar behaviour is observed for spectra taken on Tm adatoms, presenting said inversion of the spin contrast at the same energies, but with the order in which they appear inverted respect to the islands: a larger LDOS is observed on adatoms on islands with a dark color respect to adatoms on islands with a light color, which suggests an antiferromagnetic coupling between islands and Tm adatoms.

This behaviour is well reproduced when taking dI/dV maps at different bias, as shown in figure 7.6. However, it might be premature to explain this as an antiferromagnetic coupling between Tm adatoms and Fe islands, as in reference [259] Néel *et al.* discuss a similar situation for Co and Cr adatoms on double layer Fe islands on W(110) (with an out-of-plane magnetization) and conclude that spin polarized dI/dV spectra might not be enough to unambigu-

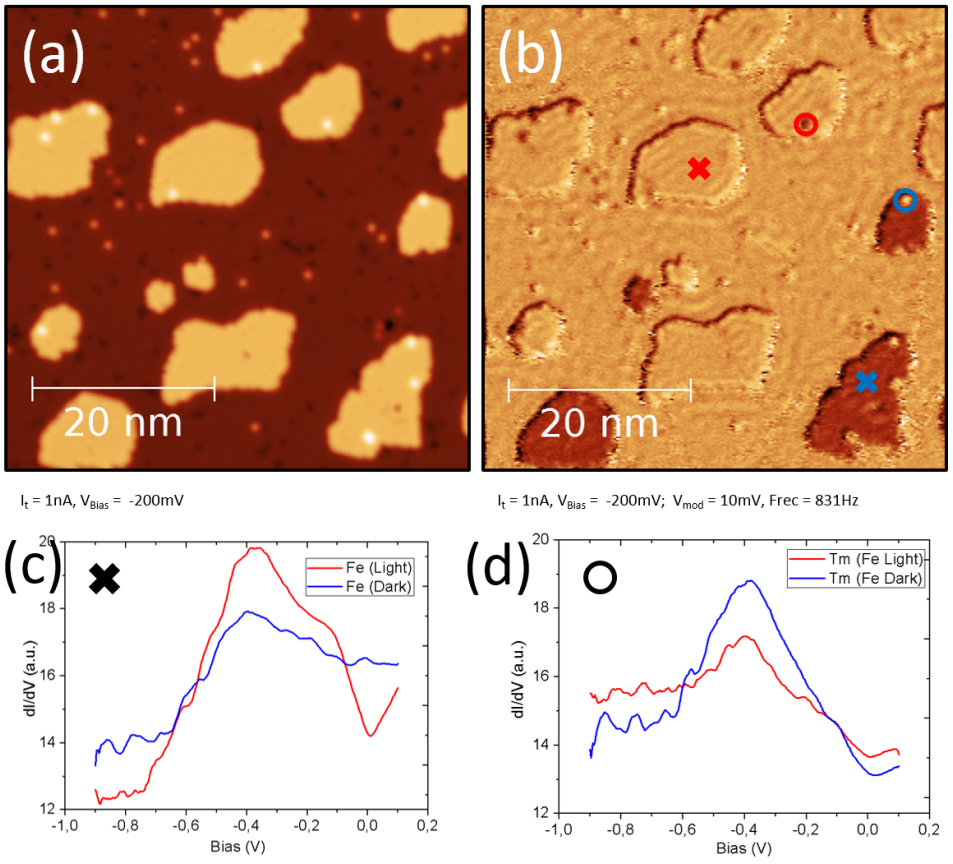

Figure 7.5: (a) STM topography and (b) spin polarized dI/dV map of a Tm/Fe/W(110) sample, at V_{Bias} = -200 mV, I_t = 1 nA. Below, dI/dV spectra on (c) Fe islands of opposite polarization, marked with **X** in (b); and (d) spectra on Tm adatoms on either island, marked with **O** in (b).

ously determine the magnetic coupling between adatoms and islands. Their study discusses the effect of the different orbital character of majority and minority states and their different spatial decays into the vacuum, producing an apparent discrepancy in the LDOS observed for the adatoms and their known magnetic coupling with the substrate.

To investigate this situation in greater detail dI/dV maps are performed with an open feedback in section 7.3 to avoid probing the adatoms at different distances; first-principles calculations are performed in section 7.4 to explore the orbital composition of the polarization and the LDOS. Before tackling those issues, however, it is of interest to compare the spectroscopic study presented in this section to the behaviour of a non-magnetic RE, Lu, to discern the role played by the 4f electrons in this situation.

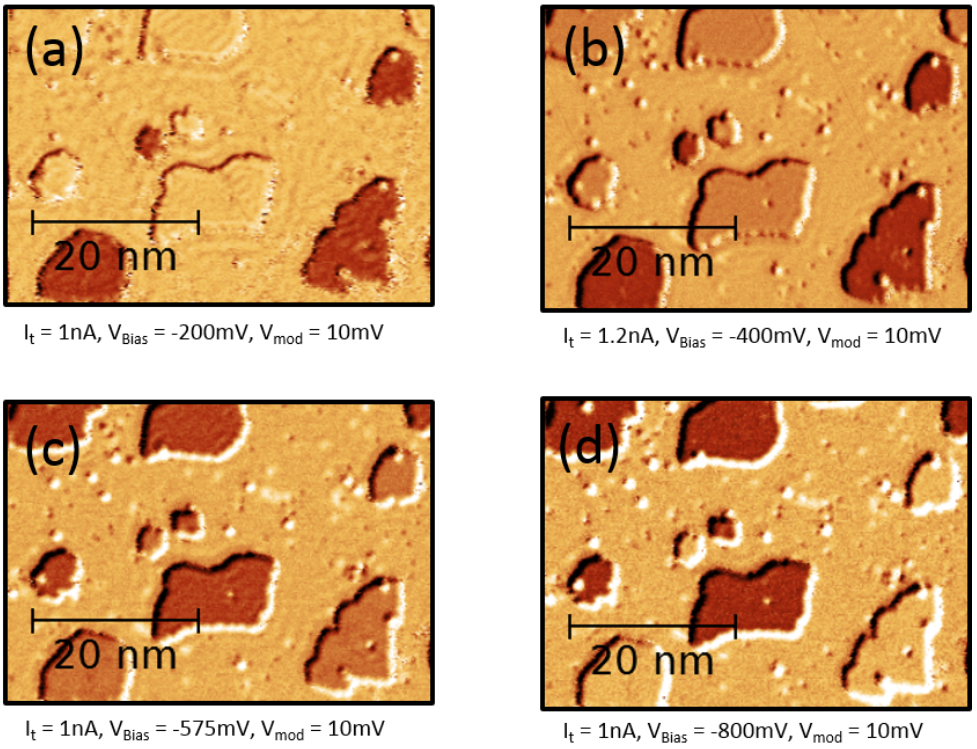

Figure 7.6: Maps of the same area as Fig.7.5.b at different bias: (a) V_{Bias} = -200 mV, (b) V_{Bias} = -400 mV, (c) V_{Bias} = -575 mV and (d) V_{Bias} = -800 mV. A contrast inversion is observed between islands (b) and (c) accompanied by a contrast inversion of the Tm adatoms.

7.2.2 Lu on Fe/W(110)

In a similar fashion as for the Tm samples of the previous section, Lu adatoms are evaporated onto monolayer Fe islands and investigated via SP-STM using a Fe coated W tip.

Figure 7.7.a shows a constant current topography image taken at V_{Bias} = -100 mV, I_t = 1 nA, depicting two Fe islands onto which Lu adatoms have been evaporated and (b) the simultaneously acquired dI/dV map, showing a strong contrast between the islands, indicating their opposite polarization; Lu adatoms on either island also present a strong contrast, with the adatoms on the dark island having a larger differential conductance than those on the light island.

Figures 7.7.c and 7.7.d show, respectively, dI/dV spectroscopy for Fe islands and for Lu adatoms, over a bias range of -300 mV to +200 mV (+100 mV for

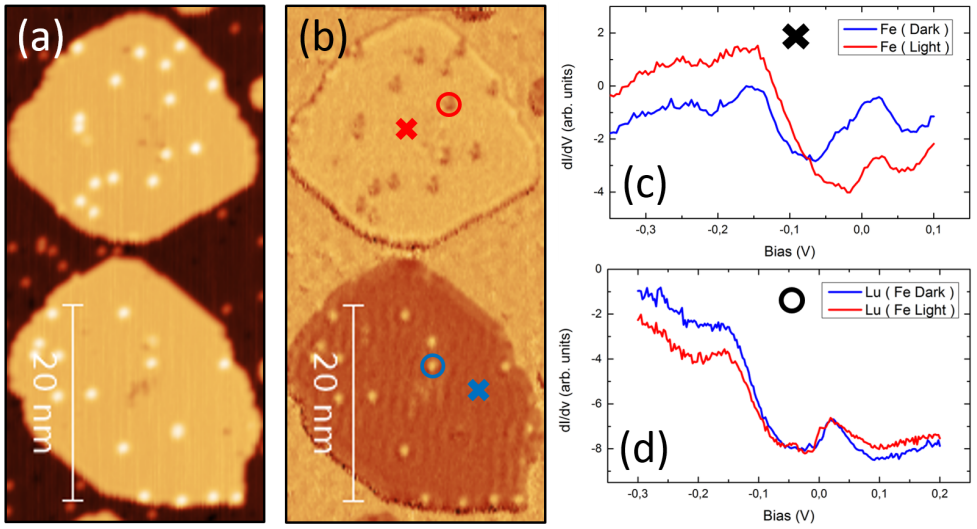

Figure 7.7: (a) Topography and (b) dI/dV map with spin polarization of a Lu/Fe/W(110) sample at V_{Bias} = -200 mV, I_t = 1 nA. To the right, dI/dV spectra on (c) Fe islands of opposite polarization and (d) Lu adatoms on said islands.

Fe islands), presenting a similar behaviour as observed for Tm in figure 7.5, that is, the asymmetry for the adatoms is inverted respect to that of islands, but closely follows its behaviour, switching in order at the same energy, around -50 mV. As for Tm, this behaviour is reproduced when taking dI/dV maps at different bias, shown in figure 7.8.

The observed behaviour is very similar between Lu and Tm adatoms, a somewhat unexpected result due to stark difference in their magnetic nature: Lu has a full $4f$ shell, and thus no $4f$ magnetic moment; meanwhile Tm has 12 $4f$ electrons, leaving two electrons unpaired in the shell, which grants it a strong magnetic character.

7.3 Constant Height dI/dV Maps

A problem that arises when performing SP-STM experiments, relevant for the questions rised in 7.2.1 regarding the information provided by dI/dV spectroscopy in a SP system, is that measurements at constant current are taken at different tip-sample distances for equivalent areas with different polarization.

This effect is illustrated in figure 7.9.a, showing a constant current topography image of three Fe islands on W(110) which have an identical height, *i.e.*, one Fe monolayer, that nonetheless appear different when taking a profile

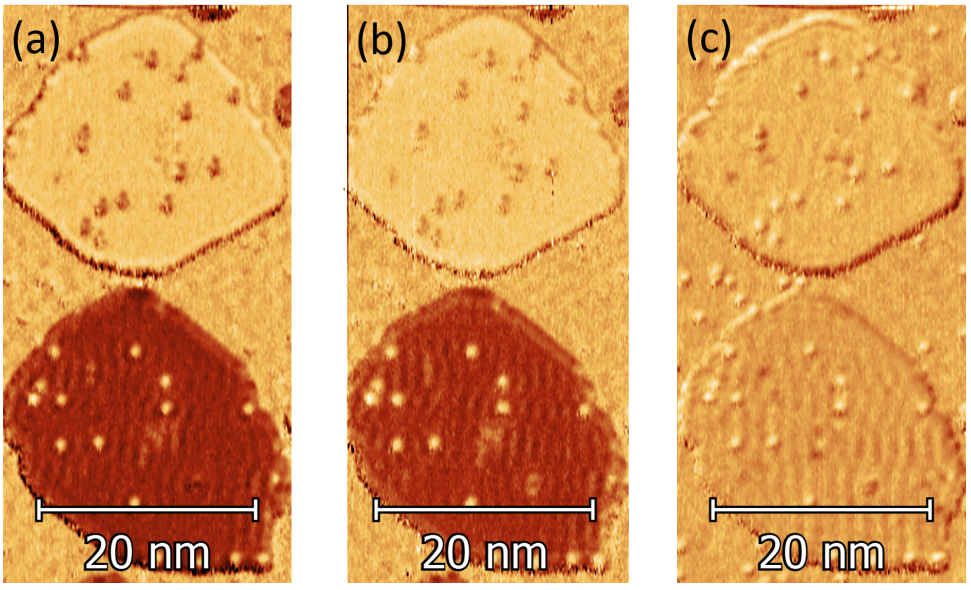

Figure 7.8: Same area as Fig.7.7 mapped at different bias, (a) V_{Bias} = -150 mV, (b) V_{Bias} = -100 mV, (c) V_{Bias} = +20 mV, showing varying spin polarized contrast on both islands and adatoms.

across the image (Fig. 7.9.b), as it has been recorded using a spin polarized tip, with the island on the right appearing 18 pm higher than the other two, as the tip was farther from the sample for said island in order to maintain the current constant.

While 18 pm is much smaller than the island height (210 pm) it can actually make a very large difference in the dI/dV signal, as illustrated in figures 7.9.c and 7.9.d. In fig.7.9.c, a dI/dV map taken at -25 mV, 300 pA shows two islands with a light colour and an island on the right with a darker hue, indicating a lower LDOS for the latter; however, as pointed out in fig.7.9.b, the tip is actually 18 pm farther away from the island on the right, which, when accounted for, completely changes the picture: in figure 7.9.d a dI/dV map of the same three islands is shown, taken immediately after fig.7.9.c, at the same bias of -25 mV, using the same modulation voltage and with no changes in polarization of the Fe coated STM tip; in this case it is the island on the right the one with the lighter hue, indicating a larger LDOS. The difference with fig.7.9.c is that, in this case, instead of using a current setpoint to regulate the tip-sample distance, the feedback is left open (after ensuring that the scanning plane is completely parallel to the sample surface) so the distance remains the same between the tip and the Fe islands, regardless of their polarization.

Due to the exponential dependence between the tunnelling current and

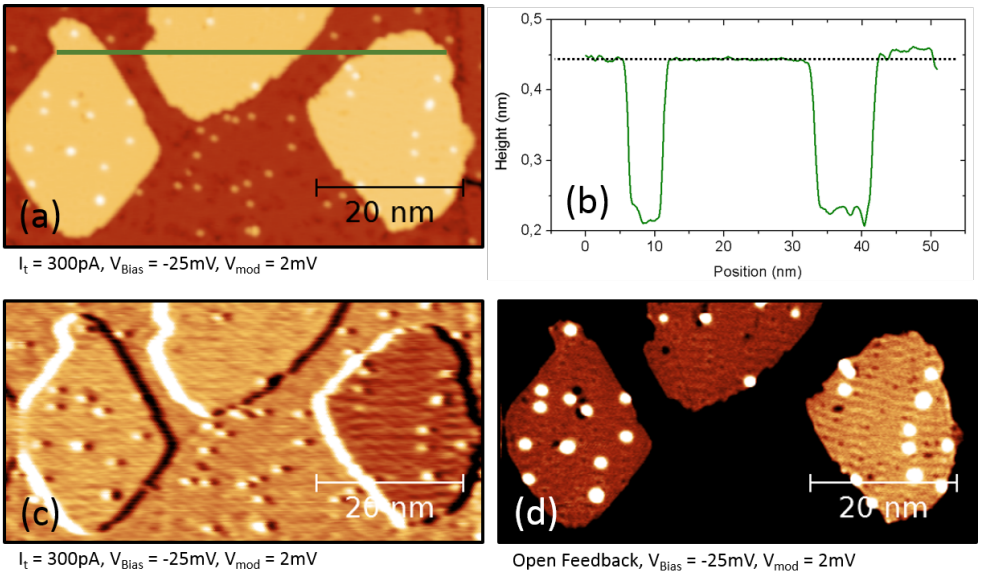

Figure 7.9: (a) STM constant current topography with a spin polarized sensitivity and (b) profile taken along the green line. Below, dI/dV maps at the same bias voltage and modulation (V_{Bias} = -25 mV, V_{mod} = 2 mV) at (c) constant current and (d) constant height, illustrating the influence of spin-polarization in the tip-sample distance and thus on the dI/dV signal.

the tip-sample distance given by eq. 2.18 in chapter 2.1.1, open feedback measurements present a very large current difference between the tungsten surface, the Fe islands, and the adatoms on top of them; in fact this variation is also very noticeable across the width of a single adatom, which gives rise to a non-flat dI/dV signal for said adatoms.

This considerations make it desirable to confirm the previous results for Tm and Lu with constant height measurements, as compounding the effects due to the feedback plus the differences in the tip-sample distances, it is plausible that the observed behaviour is actually an artefact. In order to clarify this issue, open feedback measurements are performed for both the Tm/Fe/W(110) and Lu/Fe/W(110) systems.

7.3.1 Tm on Fe/W(110)

Figure 7.10 shows how the dI/dV maps look at different bias using a linear colour scale, where only slight, if any, contrast is distinguisable. These maps are recorded after at least 24 hours of scanning the area of interest to minimize the drift after opening the feedback. The scanning plane is adjusted to compensate

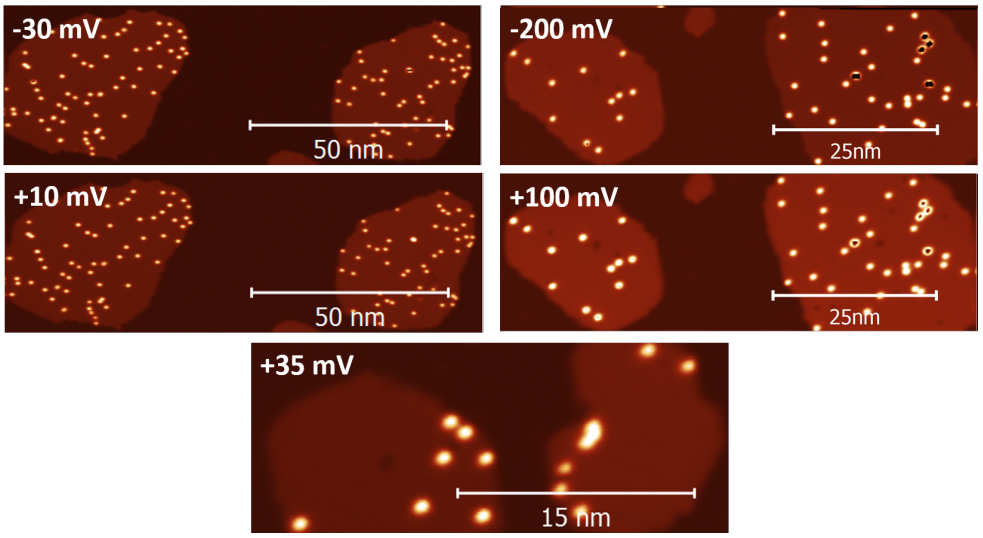

Figure 7.10: Constant height dI/dV maps of Tm/Fe/W(110) samples taken at different bias, indicated over each map. Contrast is not easily noticeable using a linear colour scale, as dI/dV for the Fe islands is grouped around a lower signal, while dI/dV for the Tm adatoms is grouped around a larger signal, due to the large differences in current between islands and adatoms.

for any sample tilt so the tip runs parallel to the surface across the whole area. To avoid saturating the lock-in used to record the dI/dV signal the tip is situated over an adatom, a suitable current setpoint is selected and, finally, the feedback is turned off.

A strongly non-linear colour scale is able to highlight said contrast, as shown in figure 7.11.a, but also highlights how susceptible to pixel-hunting the apex value is when taking profiles on adatoms in these dI/dV maps. To avoid this issue a different approach is used to analyse these maps: rather than taking profiles, all the data in a given area is represented as a histogram. This is illustrated in figures 7.11.b and 7.11.c, showing in the former the profiles indicated by lines in fig. 7.11.a, aligned with the histograms shown in the latter of the areas indicated by rectangular boxes.

A weakness of this histogram representation, where the peak in count number is very dominant and is associated to the flat dI/dV signal for the Fe island while the maximum dI/dV value, associated to the adatom apex, has the smallest sample size, is that it is susceptible to noise, where artifacts could be mistaken as actual valid data points due to the low count number at maximum dI/dV values. To address this point the inset in 7.11.c shows a more detailed view of the tail-end of the histograms, corresponding to the apex of

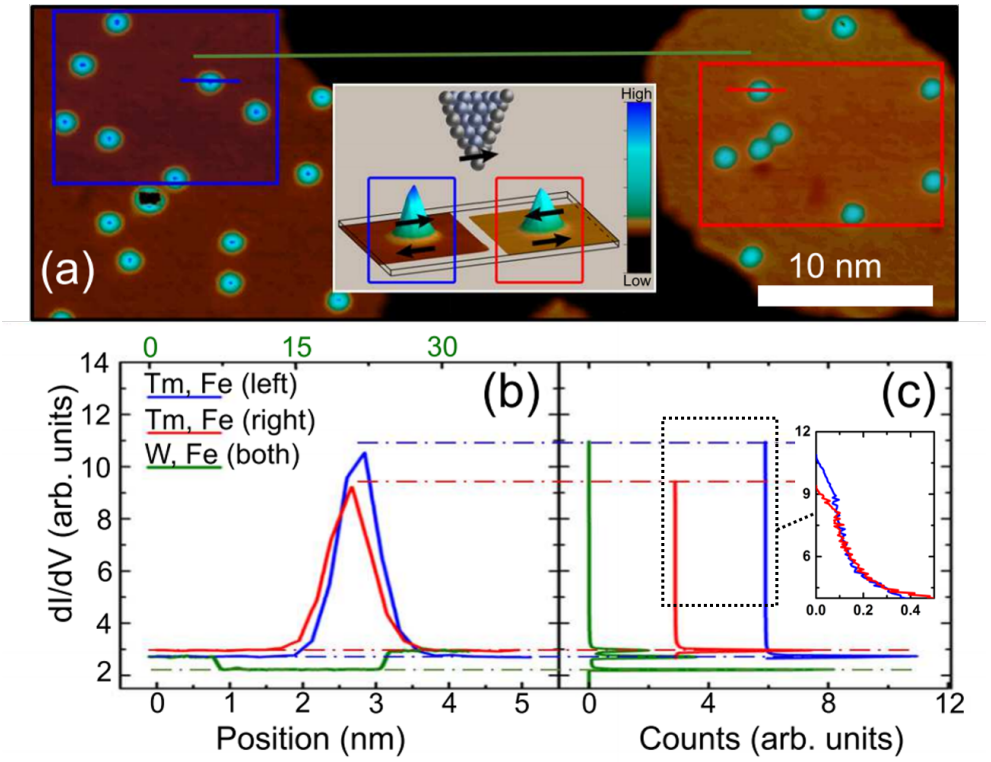

Figure 7.11: (a) Constant height dI/dV map of a Tm/Fe/W(110) sample at V_{Bias} = -200 mV, using a highly non-linear *ad hoc* colour scale to highlight the contrast between islands and between Tm adatoms. Inset in (a) shows the colour scale and a diagram of the proposed situation. (b) Profiles of the dI/dV signal taken over the indicated lines in (a), over an atom on each island (blue, red) and across the two islands (green). (d) Histograms of the the indicated areas: blue for the left island, red for the right island and green for the whole image, shifted horizontally for clarity. The inset in (d) shows a detail of the contribution of the adatom apex to the histograms; values with zero counts are not plotted.

the adatoms, where the count number strongly decreases but showing a smooth behaviour and therefore discarding noise-dominated effects. Values with zero count are not plotted.

To better compare the relevant information extracted from each map, i. e., the dI/dV signal corresponding to the Fe islands and the dI/dV corresponding to the apex of the adatoms, figure 7.12 shows a pair of histograms for each map in figure 7.10, centred around the dI/dV signal for the island on the left and horizontally shifted for easier visualization.

As in the case for constant current measurements, an opposite contrast is observed between Fe islands and Tm adatoms for all the studied bias. It

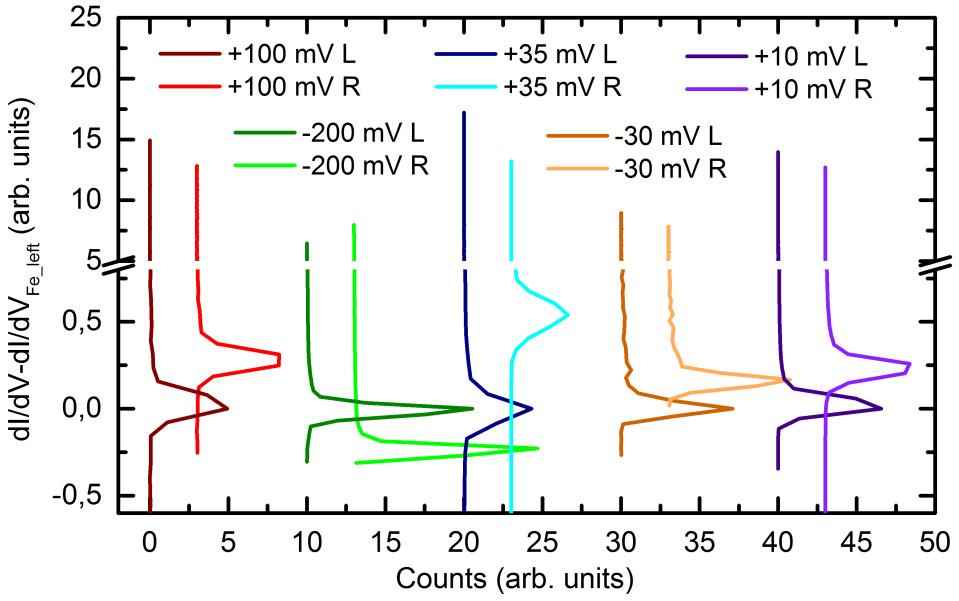

Figure 7.12: Histograms taken from dI/dV maps in figure 7.10, horizontally shifted for clarity, and zeroed at the dI/dV signal of the island on the left of each map, for easier comparison. Adatoms and islands present an opposite contrast at all bias.

should be noted that the histograms for +100 mV and -200 mV correspond to the same pair of islands, as do the histograms for +10 mv and -30 mV; a contrast inversion is observed for the former pair, but not for the latter, which is in agreement with the expected behaviour, as the bias at which the contrast inverts is around -50 mV. These results support an antiferromagnetic coupling between the Tm adatoms and the Fe islands.

7.3.2 Lu on Fe/W(110)

As for Tm, Lu adatoms on Fe/W(110) are studied by performing open feedback dI/dV maps. The tip is placed over a Lu adatom prior to turning off the feedback, after thoroughly correcting the sample tilt and ensuring that no drift is observed in the time required to record a map.

Figure 7.13 shows the dI/dV maps acquired in this way, again with very little discernible contrast without using a strongly non-linear, *ad hoc*, colour scale; (a), (b) and (c) show the same two islands measured at -200 mV, -100 mV and +20 mV respectively. A histogram analysis can be seen in figure 7.14.

These results reproduce what was observed for constant current maps, that is, an opposite contrast between Lu adatoms and Fe islands, including an

inversion for +20 mV respect to -100 mV and -200 mV. This sugests that Lu, a non magnetic rare earth, is antiferromagnetically coupled to the ferromagnetic island. This result is in line with the behaviour observed in chapter 5, where the $4f$ does not play a critical role in the tunnelling current in single adatoms.

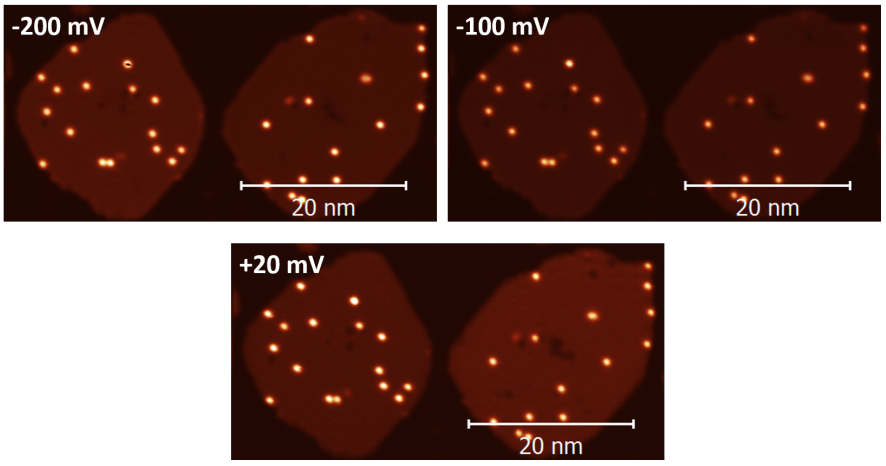

Figure 7.13: Constant height dI/dV maps taken over the same pair of islands on a Lu/Fe/W(110) sample, at the bias indicated on the figure.

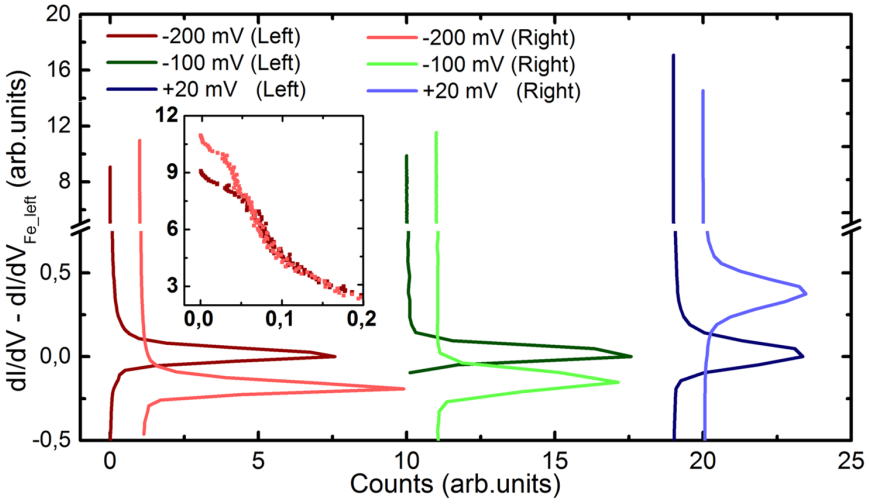

Figure 7.14: Histograms taken from the constant height dI/dV maps in Fig.7.13. Inset shows the contribution to the dI/dV signal near the apex for V_{Bias} = -200 mV, presenting a smooth behaviour.

7.4 DFT calculations: RE on Fe/W(110)

To support the proposed antiferromagnetic coupling, density functional theory (DFT) based first-principles calculations have been performed using the Vienna ab-initio simulation package (VASP) [182] using the generalized gradient aproximation (GGA) for correlation and the local spin density aproximation (LSDA) for exchange [179], with the plane basis set on a projector augmented wave (PAW) pseudopotential to describe the core electrons [181]. When considering rare earths, LSDA often fails to correctly describe the system due to the strongly correlated d and f electrons, a problem that is overcome by introducing a strong intra-atomic interaction in a screened Hartree-Fock manner as an on-site replacement of the LSDA, in what is known as the LSDA+U method [180]. Without this correction the 4f orbitals show a maximum of their projected density of states, PDOS, at the Fermi level, suggesting that the Tm adatom should behave as a Kondo impurity, which is not observed experimentally highlighting the need for the corrected aproximation.

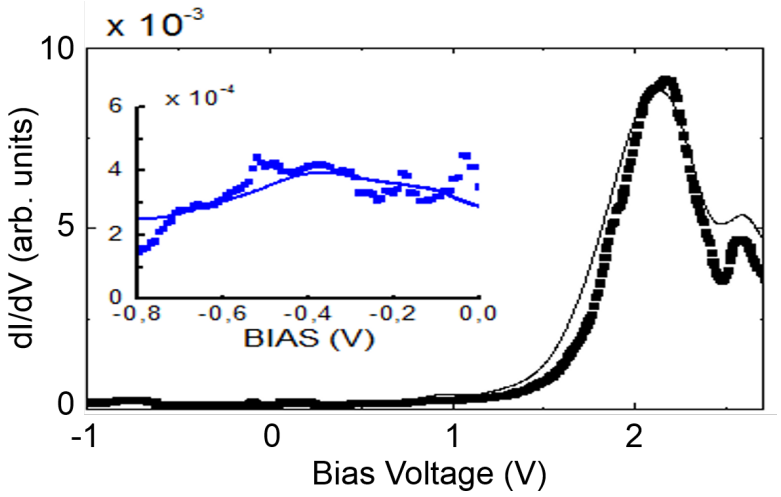

Figure 7.15: Calculated spin averaged differential conductance (squares) compared to experimental results (line). Inset shows a more detailed comparison of the behaviour at lower bias.

A non-collinear spin polarized electronic relaxation is thus performed, including the spin-orbit coupling (SOC) and LSDA+U using U = 0.8 eV for 3d Fe states and U 5.0 eV for the $4f$-adatom states [276]. Calculating the spin-average differential conductance over a -1 V to 2.7 V bias range shows good agreement with experimental results for Tm adatoms on Fe/W(110), as shown in figure 7.15. An analysis of the contribution to the PDOS shows that the cal-

culated 4f to 5d DOS ratio between -1 eV and 140 meV is $\sim$ 8x10^{-4}, and barely $\sim$ 7x10^{-3} at higher energies, up to 2.7 eV. Therefore, at the energies involved in the SP-STM measurements, the main contribution to the tunnelling current when the tip is over Tm or Lu adatoms comes from the RE 5d-electrons.

Tm/Fe/W(110)	s	p	d	f	Total
Tm	-0.02	0.00	-0.13	-0.92	-1.07
Fe	0.01	-0.01	2.45	-	2.45

Lu/Fe/W(110)	s	p	d	f	Total
Lu	-0.02	0.00	-0.17	0.02	-0.17
Fe	0.02	-0.01	2.34	-	2.36

Table 7.1: Orbital decomposition of the spin moment at Fe, Tm and Lu sites for the two situations, a Tm adatom or a Lu adatom on a Fe monolayer on W(110).

Full electronic relaxation was carried out for each case, with a lanthanide adatom (Tm, Lu) placed over a ferromagnetic monolayer of Fe over a 5 monolayers thick W(110) slab, using (3x3x1) supercells and a Γ-centered 3x3x1 k-mesh. Table 7.1 summarizes the most relevant data for this discussion, *i.e.*, the orbital decomposition of the spin moment at the Fe, Tm and Lu sites along the [1$\bar{1}$0] direction, the magnetic easy direction for the Fe monolayer. The spin moments are practically aligned along said direction, with negligible components along other directions, except for a small $4f$ spin moment (+0.14 μB) obtained for Tm along the [110] direction. The $5d$ electrons for both lanthanide adatoms, Tm and Lu, display a net spin moment and that said spin moment has the opposite direction to the $3d$ spin moment of Fe. The obtained $4f$ spin moment is FM coupled with the $5d$ spin moment, resulting in a total spin moment for Tm that is AFM coupled to the Fe monolayer; for Lu, as expected, the $4f$ contribution is negligible and the spin moment is due to the contribution of the $5d$ electrons, resulting again in an AFM coupling between the RE adatom, Lu in this case, and the Fe island.

This behaviour is explained when considering the adsorption of the RE adatom on the transition metal in the Campbell model [274], which by hybridization with the $3d$ bands allows the $5d$ orbitals of the Tm adatom to be populated (as a free Tm atom has no $5d$ electrons), and increase their occupancy in the case of a Lu adatom (which has a $5d^1$ configuration as a free atom). As these $5d$ orbitals are polarized due to their hybridization with the $3d$ orbitals of the Fe island, a net $5d$ spin moment is observed in both cases and, as these orbitals propagate further into the vacuum that the more inter-

nal $4f$, the resulting tunnelling current becomes spin-polarized and, being the coupling between the 5d and 3d electrons spin moments antiferromagnetic, the resulting spin polarization of the current over the atom is opposite to that of the Fe island monolayer on which the adatom is adsorbed, as illustrated in figure 7.16.

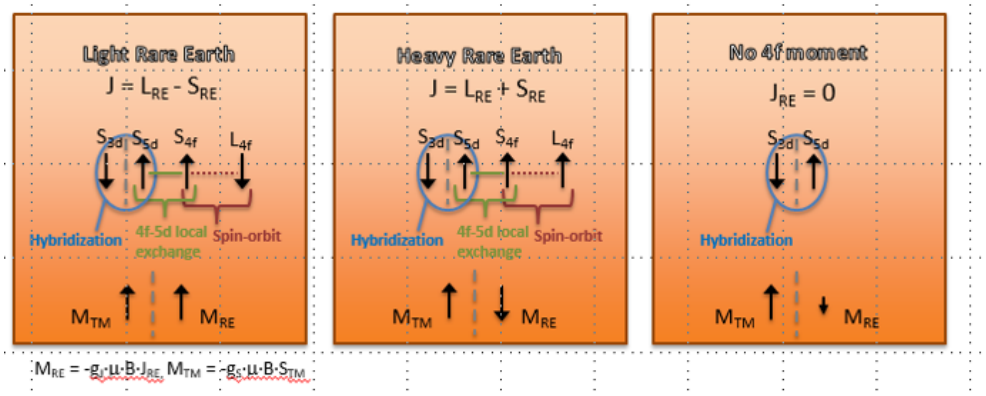

Figure 7.16: Schematic representation of the coupling between the Rare Earth atom and the Transition Metal host in the Campbell model. An antiferromagnetic coupling between the $3d$ of the TM and the $4f$ of the RE is always present, although the total magnetic moments may be parallel (light RE) or antiparallel (heavy RE, as the case of Tm).

Experimentally, this difference in the orbital contribution to the tunnelling current can be seen in the dI/dV signal. As the polarization of the $4f$ orbital for Tm is much stronger (see table 7.1) than that of the $5d$ for either Tm or Lu, it should be expected that Tm gave rise to a larger spin contrast. While a direct comparison using the same SP tip has not been possible to obtain due to the difficulties involved in coevaporation detailed in section 7.1.2, an indirect comparison can be performed by using the contrast observed between the Fe islands as a reference. Comparing the maps taken at -200 mV for Tm (fig.7.10) and Lu (fig.7.13) by taking the ratio between the difference in signal between adatoms on either islands and the difference between said islands, and using the FWHM of the peak corresponding to the Fe contribution to estimate the uncertainty, a very similar behavior between Tm and Lu is observed:

$$\Delta Lu_{Norm} = \frac{\Delta Lu}{\Delta Fe} = 8.4 \pm 2.3 \qquad \Delta Tm_{Norm} = \frac{\Delta Tm}{\Delta Fe} = 6.8 \pm 1.7 \qquad (7.1)$$

The ratio between these is much closer to a direct comparison between the polarization of the $5d$ orbitals than to a comparison of the total spin moment that includes the $4f$ orbitals, from the data from table 7.1:

$$\frac{\Delta Lu_{Norm}}{\Delta Tm_{Norm}} = 1.24 \qquad \frac{Lu_{5d}}{Tm_{5d}} = 1.31 \qquad \frac{Lu_{tot}}{Tm_{tot}} = 0.16 \tag{7.2}$$

Thus, by using spin-polarized scanning tunneling microscopy and spectroscopy in combination with first-principles calculations, the magnetic coupling existing between Tm and Lu adatoms and Fe monolayer islands with in-plane magnetization can be determined: the RE $5d$ moments lie in plane and couple antiferromagnetically with the underlying Fe islands. This case represents an extreme manifestation of the Campbell mechanism [274], used in higher dimensionality structures and bulk RE-TM alloys, and now tested in the limit of single atoms. Furthermore, by comparing the behaviour of Tm and Lu adatoms, it can be seen that the RE-TM interaction proceeds via the $3d$–$5d$ direct antiferromagnetic interaction, and that it is these $5d$ electrons that grant the spin-polarized character to the tunnelling current on the RE adatoms, while the RE $4f$ electrons have a negligible contribution to said tunnelling current.

Summary and Conclusions

This thesis has devoted its attention to the study and characterization of electronic and magnetic properties of Thulium at the atomic scale. The interest in studying the magnetism of rare earth adatoms and monolayers resides in the localized character of the $4f$ states, which protects them from hybridization effects and preserves atomic-like spin and orbital magnetic moments; at the same time, the role of $4f$ states in conduction and tunnelling is not always obvious.

Interest in low-dimensional rare earth magnetic structures, beyond ferromagnetic or antiferromagnetic thin films, has its place in the form of inducing perpendicular magnetic anisotropy in adjacent TM layers, enhancing of magnetic moment in RE-TM multilayers, or improving the characteristics of spin valves; producing nanostructured systems introduces geometry as another variable, as there exists a strong relation between crystal structure, size and magnetic properties. Chapters 3 and 4 deal with the preparation and characterization of the Tm monolayer and monolayer nanoislands.

Reducing dimensions further leads to the single atom. A magnetic single atom on a surface is the smallest conceivable system for storing information, be it as a typical base 2 bit represented by spin-up (1) and spin-down (0) states of an atom with an effective spin 1/2, or even more complex, multi-state bits, if such control of the spin state is achieved. The study of the magnetism of single atoms has grown steadily over the last two decades, accompanied by the development of powerful tools for this purpose. For spatially resolved experiments, spin polarized STM and inelastic excitation tunnelling spectroscopy have proven invaluable in the study of the magnetic properties of individual atoms and have been used to extensively characterize Transition Metal atoms and structures on different substrates.

In the pursuit of improved properties at the atomic limit, the study of rare earth atoms on metallic and insulating surfaces has become a hot topic during the course of this thesis and, with the recent publication of several studies in high impact journals, promises to stay relevant in the foreseeable future. In

this context, the experiments and findings here reported have contributed to the discussion of STM experiments on RE, in particular regarding the orbital composition of the tunnelling current and how it limits the access to $4f$ electrons. Chapters 4, 5 and 7 study individual Tm and Lu atoms on different substrates, while chapter 6 is devoted to the ferromagnetic Fe islands that serve as a substrate for the atoms in chapter 7.

The following paragraphs present a more detailed summary as well as the main conclusions of each chapter:

In **chapter 3** the preparation of single atomic layer Tm films on a W(110) substrate is explored. Sub-monoloyer Tm deposits can present a varied morphology depending on initial coverage, substrate temperature and adsorbate density. The key to achieving high quality pseudomorphic Tm films resides in an annealing process after evaporation, which motivates the study presented here, where STM experiments are performed at high temperature to observe *in situ* the evolution of the Tm film. Measurements over time evidence the diffusion of carbon adsorbates from the bulk of the W crystal onto the surface. The effect of carbon impurity density on the diffusion process of Tm atoms is studied by observing the evolution of multiple samples at different initial coverages following different thermal processes, with longer times leading to a higher adsorbate density. It is observed that the presence of carbon strongly limits the diffusion of Tm , thus leading to the formation of pseudomorphic nanometric islands instead of the full monolayer; with careful control of the impurity density, mean island size can be controlled, with the experiments showing samples with islands down to 5 nm in diameter.

Chapter 4 focuses on the study of the electronic and magnetic properties of the Tm monolayer on W(110), characterized by X-ray absorption (XAS) and dichroism (XMCD) experiments [30]. Tm is found to be in a 3+ state, indicating a $4f^{12}$ ground state. The magnetic configuration is studied by both circular and linear dichroism, suggesting an antiferromagnetic configuration of the monolayer, with an onset around 50 K. Due to the near hexagonal Tm lattice could lead to a frustrated state, a possibility that is explored by spin polarized STM measurements, although no spin polarized contrast is observed over the explored energy range and applied fields. This could indicate an atom-wise antiferromagnetic coupling, which is difficult to resolve in this system as atomic resolution of the Tm layer is obscured by the strong Moiré pattern emerging from the overlap of the hexagonal Tm lattice over the W rectangular lattice. Tm adatoms are also studied by XAS and XMCD, finding a uniaxial magnetic anisotropy along the surface normal, although with no remanence. STM measurements are performed on Tm adatoms on W(110) exploring the possibility of a spin-flip inelastic excitation, but no evidence of such is observed

in the spectroscopy.

A decoupling insulating layer has been shown to play a role in enabling spin-flip excitations. This is explored for Thulium and Lutetium atoms in **chapter 5**, using a insulating Cu_2N monolayer as a decoupling layer from the Cu substrate. No such effect is observed in either atom, expected for Lu as it has a full $4f$ shell, but it in the case of Tm it suggests that the tunnelling current is unable to produce an excitation of the $4f$ electrons. The spectroscopic differences between Tm and Lu on Cu and Cu_2N substrates is compared, finding a feature in Tm absent in Lu, which only is significant when the Tm atom is on the Cu_2N surface. First principle calculations show that this feature is $5d$ in nature.

Chapter 6 presents a detailed study of ferromagnetic Fe monolayer islands grown on W(110). A spin polarized study is presented, focusing on the behaviour at different bias. A standing pattern is observed in islands of a given polarization, but not on those of the opposite. The characterization of this interference pattern, obtaining its dispersion relation by analysing differential conductance maps at different bias, allows for the identification of this feature as a surface resonance of Fe minority electrons. Dependence on island size and tip polarization is also studied to discard possible artefacts. The interference pattern presents a strongly anisotropic behaviour which also carries onto the interference pattern on the W(110) surface. This anisotropy is explained as a coupling between the surface resonance of the ferromagnetic Fe island and the Rashba-like spin-moment locked surface state in W.

In **chapter 7** Tm and Lu adatoms are evaporated onto monolayer Fe islands. A spin polarized STM study of this atoms indicates that they couple antiferromagneticaly with the Fe islands in both cases [31]. A very similar behaviour is observed for Tm and Lu adatoms, which is significant as Tm is a magnetic rare earth, as it has an incomplete $4f$ shell, while it is complete for the case of Lu, rendering it non-magnetic. First principle calculations are used to complement this observations confirming the antiferromagnetic configuration. The coupling occurs between the $5d$ electrons of the rare earth atoms and the $3d$ electrons of the Fe layer. The magnetic moment is obviously higher for Tm, due to the $4f$ contribution, however the spin polarized contrast is similar, or even a bit larger, for Lu, very similar to the relation between $5d$ moments of the two species. This indicates that the tunnelling current consists mainly in $5d$ electrons while the $4f$ contribution is negligible. This is coherent with the absence of inelastic excitations observed in the previous chapters.

Outlook

While many significant advances have been made in the last decade in the field of single atoms and atomic structures, obtaining bistable magnetic single atoms [15] or the automatic repositioning of thousands of individual atoms [12], effort should be made to avoid falling in the trap of declaring "The End of History", as basic research is alive and well at the single atom limit. The recent development of combined ESR-STM [47] by Baumann *et al.* opens new possibilities for probing the atom, as they have illustrated by locally determining and switching the orientation of single atom magnets [168]. Efforts in improving the time-resolution capabilities of STM setups also offer a very promising avenue for probing new interactions [46]. The interplay of systems with different properties also opens an almost infinite of configurations where new physics can be explored, as illustrated by the emergence of Majorana fermions in ferromagnetic atomic Fe chains on a superconducting Pb surface [277].

The obvious short term future of rare earth atoms is exploring the behaviour of different species on a varied array of substrates, to determine the optimal configuration for single atom magnets. Exploring the implications and possibilities of this situation should lead to an interesting analysis of the competition of different interactions and if direct tunnelling to the $4f$ states is possible in some particular situation, which would grant better control over the magnetic properties of the atom. Even if this is not the case, RE single atom magnets present a very interesting possibility in the form of introducing a local magnetic bias on nearby structures, reducing the nanometric islands used in reference [14] to single atoms; another use of local magnetic bias is producing pinning points for domain walls, or, in the same spirit but reducing the scale, an asymmetric potential for the propagation of spin waves on an atomic chain.

While the need for UHV and cryogenic conditions will limit the technological application of single atoms in the short term, the a-decade-away from being a-decade-way promise of quantum computing promises a qualitative leap that would justify the cost for specific applications, should the right system be found. The high localization of the $4f$ orbitals are at the same time the strong point of rare earth and its main drawback, as them interacting weakly with the environment is what grants them the high lifetimes that have been observed, but also makes it difficult to interact with them intentionally.

Resumen y Conclusiones

El trabajo de esta tesis se ha centrado en el estudio y caracterización de las propiedades electrónicas y magnéticas del Tulio (Tm) a escala atómica. El interés del magnetismo de atómos y estructuras de tierras raras reside en la capa incompleta $4f$, altamente localizada, lo cual reduce los efectos de hibridación, dando lugar a un comportamiento de los momentos de spin y orbitales más parecidos a la situación del átomo libre; como contraprestación, la localización de los estados $4f$ hace que su papel en la conducción y transmisión por túnel no sea siempre evidente.

El interés en estructuras de tierras raras (RE) de bajas dimensiones, más allá de la producción de capas delgadas ferromagnéticas o antiferromagnéticas, encuentra su justificación en la mejora de propiedades de interés tecnológico: formación de dominios magnéticos perpendiculares en capas adyacentes de metales de transición (TM), aumentar el momento magnético de multicapas RE-TM, mejorar las características de válvulas de spin, etc... Un sistema nanoestructurado introduce su geometría como una variable adicional, puesto que existe una fuerte relación entre el tamaño de la estructura, su estructura cristalina y sus propiedades magnéticas. En los capítulos 3 y 4 se estudia la preparación y caracterización de capas de Tulio con una monocapa atómica de espesor, así como de islas nanométricas monocapa.

Reducir más las dimensiones lleva al límite del átomo individual. Un átomo magnético en una superficie es el sistema de almacenamiento de información que se puede concebir, a día de hoy, ya sea almacenando un bit en base 2 mediante un átomo con espín efectivo 1/2, o incluso bits más complejos, con un mayor número de estados, si se tuviera suficiente control sobre el estado de espín del átomo. El estudio del magnetismo de átomos individuales ha crecido mucho en las dos últimas décadas, impulsado por el desarrollo de técnicas experimentales que han hecho posible su investigación. Para experimentos locales, con resolución espacial de átomos individuales, la microscopía de efecto túnel (STM) y, en particular, su versión polarizada en espín, así como la espectroscopía túnel de excitación inelástica, han mostrado ser fundamentales

en el estudio de las propiedades magnéticas de átomos individuales, y han sido utilizadas extensamente para la caracterización de átomos de metales de transición sobre distintos sustratos.

Con el objetivo de mejorar las propiedades pero manteniéndose en la escala de átomos individuales, esta línea de investigación ha dirigido su atención hacia el estudio de tierras raras, convertiéndose en un tema candente durante el transcurso de esta tesis. La reciente publicación de varios trabajos en revistas de alto impacto, así como la realización límite de un átomo magnético individual con un comportamiento biestable, indican que el estudio de tierras raras a esta escala mantendrá su relevancia en el futuro próximo. En este contexto, los experimentos y conclusiones obtenidos en esta tesis han contribuido a la discusión del uso de STM en la caracterización de átomos de tierras raras, en concreto ayudando a dilucidar la composición de la corriente túnel y cómo ello afecta a la posibilidad de interactuar con los estados $4f$. En los capítulos 4, 5 y 7 se presenta el estudio de átomos de Tulio y Lutecio sobre distintos sustratos, metálico, aislante y ferromagnético; por su parte, el capítulo 6 presenta una caracterización exhaustiva de las islas de hierro utilizadas en el capítulo 7.

Los siguientes párrafos presentan un resumen más detallado de cada capítulo, así como las principales conclusiones que se pueden extraer:

En el capítulo 3 se estudia la preparación de capas monoatómicas de Tulio sobre un sustrato de Tungsteno, W(110). La preparación de Tm sobre W(110) con depósitos por debajo de la monocapa presenta una morfología muy variada en función del depósito inicial, la temperatura del sustrato y la presencia de impurezas en la superfice. Para obtener películas pseudomórficas de Tm de alta calidad es clave la realización de un recocido de la muestras tras la evaporación, por ello en este capítulo se estudia el proceso de recocido *in situ*, utilizando para ello un STM de alta temperatura, capturando la evolución de la monocapa a distintas temperaturas. La realización de tratamientos térmicos de larga duración produce un aumento de la difusión de impurezas de carbono en el cristal de tungsteno, desde el masivo hasta la superficie. El efecto de la densidad de impurezas sobre la difusión del Tm es estudiado caracterizando la evolución de muestras con diversos recubrimientos ante diferentes tratamientos térmicos; en los procesos en que se mantiene una temperatura elevada durante intervalos más largos produce una mayor densidad de adsorbatos en la superfice. Se observa que la presencia de carbono inihibe fuertemente la difusión del Tm, de forma que se favorece la formación de islas de tamaño nanométrico en lugar de una monocapa extensa. Con un control preciso de la densidad de impurezas se puede, por tanto, determinar el tamaño de las islas resultantes.

El capítulo 4 se centra en el estudio de las propiedades electrónicas y magnéticas de la monocapa de Tm sobre W(110), characterizada por espectroscopía

de absorción de rayos X (XAS) y medidas de dicroísmo magnético (XMCD, XMLD) [30]. El estado de valencia del Tm en la monocapa es 3+, indicando un estado fundamental $4f^{12}$. La configuración magnética obtenida por medidas de dicroísmo circular y lineal es un acoplamiento antiferromagnético en la capa, presente por debajo de 50 K. Puesto que la red del Tm sobre W(110) es casi hexagonal, esto podría dar lugar a un estado magnético frustrado, una posibilidad que es explorada mediante experimentos de STM polarizado en espín. En este caso no se observa ningún contraste debido a la polarización de espín en el rango de energías estudiado y con los campos magnéticos aplicados, lo cual podría indicar que el acoplamiento antiferromagnético sucede a escala atómica, puesto que a ésta resulta difícil de acceder en este sistema dado que la superposición de la estructura hexagonal de la red del Tm sobre la estructura rectangular de la red del W(110) da lugar a un patrón de Moiré cuya corrugación es superior a las diferencias que se pudieran esperar por diferencias de polarización. En este capítulo también se presenta el estudio de átomos individuales de Tm sobre la superficie de W(110), caracterizados mediante XAS y XMCD, determinando una anisotropía magnética uniaxial, perpendicular a la superficie, aunque sin remanencia alguna; dichos átomos son estudiados también mediante STM, para comprobar si es posible producir una excitación inelástica de espín mediante corriente túnel, con resultado negativo.

El uso de capas aislantes es habitual para favorecer las excitaciones de spin por corriente túnel, una situación que es explorada en el capítulo 5 para átomos de Tm y Lu sobre un sustrato de nitruro de cobre, Cu_2N, una monocapa aislante sobre un sustrato de cobre. No se observa ninguna señal en la espectroscopía que indique una excitación inelástica para ninguna de las especies, algo esperable en el caso del Lu debido a que su capa $4f$ está completa; en el caso del Tm, nuevamente indica que la corriente túnel es incapaz de producir una excitación de espín en este átomo. Al comparar las espectroscopías tomadas en átomos de Tm y Lu sobre sustratos de Cu y Cu_2N se observa la presencia de un pico para el átomo de Tm cobre Cu_2N que está ausente cuando el átomo está sobre Cu, y que está ausente en ambos casos para átomos de Lu. El estudio del sistema Tm/Cu_2N desde primeros principios permite determinar que este pico proviene de los electrones $5d$.

El capítulo 6 presenta un estudio detallado de islas ferromagnéticas de Fe sobre W(110), basado en medidas de STM polarizado en espín a differentes energías. Se observa la presencia de un patrón de interferencia en islas de una determinada polarización respecto de la punta, pero ausente en islas de polarización opuesta. La caracterización de este patrón se realiza mediante el estudio de mapas de conductancia diferencial a distintas energías, dando lugar a la obtención de la relación de dispersión del estado que da origen al patrón de interferencia, identificado como una resonancia de superfice presente

para elctrones minoritarios del hierro. Para descartar contribuciones espúreas, se estudia la dependencia del patrón con el tamaño de las islas así como con la polarización de la punta. Una característica singular del patrón es su alta anisotropía, propagándose únicamente en una dirección, comportamiento que también se ve reflejado en el estado de superfice del W(110). Esta anisotropía se explica a partir de un acoplamiento entre la resonancia de superfice del Fe ferromagnético y el estado de superficie del W(110), que presenta una relación entre el espín y el momento de sus electrones, similar a sistemas Rashba.

En el capítulo 7 se investiga el comportamiento electrónico y magnético de átomos de Tm y Lu sobre islas ferromagnéticas de Fe. Un estudio de STM polarizado en espín muestra que los átomos se acoplan antiferromagneticamente con la isla de Fe en ambos casos [31]. Se observa una espectroscopía similar para átomos de Tm y de Lu, lo cual es significativo debido a que Tm es una tierra rara magnética, teniendo la capa $4f$ incompleta, mientras que dicha capa está llena en el caso del Lu y, por tanto, es no magnética. La realización de cálculos desde primeros principios permite profundizar en las observaciones experimentales, confirmando el acoplamiento antiferromagnético. Dicho acoplamiento ocurre entre electrones $5d$ de los átomos de tierra rara y electrones $3d$ de la capa de Fe. El momento magnético obtenido es mayor para el caso del Tm, debido a la contribución $4f$ ausente para Lu, sin embargo el contraste observado en medidas polarizadas en espín es similiar en ambos casos, incluso ligeramente mayor en el caso del Lu, presentando una relación muy similar a la relación entre momentos $5d$ obtenida a partir del cálculo. Esto indica que la parte polarizada de la corriente túnel consiste principalmente en electrones $5d$, mientras que la contribución $4f$ es despreciable, un resultado que explica la ausencia de excitaciones inelásticas descrita en capítulos anteriores.

Perspectivas

Aunque ha habido grandes avances en el campo de átomos individuales y estructuras a escala atómica, como la obtención de átomos indivdiuales magnéticamente estables [15] o la automatización de la manipulación atómica incluyendo miles de átomos [12] es importante no ser prematuros en declarar "El Fin de la Historia", puesto que queda mucho trabajo de ciencia básica en el límite del átomo individual, y cada avance no hace sino abrir nuevos caminos. El desarrollo reciente de STM combinado con resonancia paramagnética electrónica, ESR-STM [47], supone una herramienta nueva para interactuar con el átomo cuyas aplicaciones no se han hecho esperar, como muestra el mismo grupo identificando y manipulando el estado magnético de átomos individuales de tierras raras [168]. Los esfuerzos en la mejora de la resolución temporal alcanzable en experimentos de STM prometen abrir toda una nueva dimensión,

explorando la dinámica de los sistemas en la escala del picosegundo [46]. Por otra parte, la interacción entre diferentes sistemas ofrece un abanico casi infinito donde explorar nueva física, ejemplificado por la obtención de fermiones de Majorana en cadenas atómicas ferromagnéticas de Fe sobre una superficie superconductora de Pb [277].

El futuro inmediato de los átomos de tierras raras está sin duda en la caracterización de los distintos elementos del grupo sobre sustratos con distintas propiedades y simetrías, para optimizar la configuración necesaria para obtener átomos magnéticos individuales. El estudio de la competición entre diferentes interacciones así como si existe una configuración adecuada que permita el túnel a estados $4f$, lo cual daría un mayor control sobre su estado magnético, prometen ser temas de interés a corto y medio plazo. Incluso sin esta posibilidad, el uso de átomos magnéticos estables es muy interesante a la hora de introducir un campo magnético local, afectando a las estructuras cercanas, eliminando la necesidad de nanoislas ferromagnéticas en el sistema de puertas lógicas atómicas presentado en la referencia [14]; otra aplicación inmediata es su uso como centros de anclaje de paredes de dominio o, con el mismo concepto pero reduciendo la escala hasta nivel atómico, para producir un potencial asimétrico que afecte a la propagación de ondas de espín en cadenas atómicas.

Aunque la necesidad de temperaturas criogénicas y condiciones de ultra alto vacío limitan la aplicación tecnológica de átomos individuales a corto plazo, la presencia en el horizonte de la computación cuántica y su promesa de un salto cualitativo, más allá de un simple escalado del número de transistores en un ordenador convencional, justificaría el coste para determinadas aplicaciones en caso de diseñarse un sistema adecuado. La alta localización de los orbitales $4f$ es al mismo tiempo el punto fuerte de las tierras raras y su mayor dificultad, puesto que la misma baja interacción con el entorno que permite las largas vidas de estados cuánticos observadas también dificulta la interacción intencionada con dichos electrones.

Bibliography

1. Feynman, R. P. *There is plenty of room at the bottom* in *Annual Meeting of the American Physical Society* (1959).
2. Editorial. 'Plenty of room' revisited. *Nat Nano* **4,** 781–781 (2009).
3. Agnihotri, R. *et al.* Structure and Behaviour of Cyclized Rubber Photoresist. *Photographic Science and Engineering* **16,** 443+ (1972).
4. Melngailis, J. Focused ion beam technology and applications. *Journal of Vacuum Science & Technology B* **5,** 469–495 (1987).
5. Vettiger, P. *et al.* Nanotechnology Electron beam lithography-Resolution limits. *Microelectronic Engineering* **32,** 131–142 (1996).
6. Pennycook, S. J. Fulfilling Feynman's dream: "Make the electron microscope 100 times better" - Are we there yet? *MRS Bulletin* **40,** 71–78 (2015).
7. Lee, H. *et al. Sub-5nm All-Around Gate FinFET for Ultimate Scaling* in *Symposium on VLSI Technology* (2006), 58–59.
8. Eigler, D. M. & Schweizer, E. K. Positioning single atoms with a scanning tunnelling microscope. *Nature* **344,** 524–526 (1990).
9. Yamachika, R., Grobis, M., Wachowiak, A. & Crommie, M. F. Controlled Atomic Doping of a Single C60 Molecule. *Science* **304,** 281–284 (2004).
10. Zhao, A. *et al.* Controlling the Kondo Effect of an Adsorbed Magnetic Ion Through Its Chemical Bonding. *Science* **309,** 1542–1544 (2005).
11. Erbas-Cakmak, S., Leigh, D. A., McTernan, C. T. & Nussbaumer, A. L. Artificial Molecular Machines. *Chemical Reviews* **115,** 10081–10206 (2015).
12. Kalff, F. *et al.* A kilobyte rewritable atomic memory. *Nature Nanotechnology* (2016).
13. Loth, S., Baumann, S., Lutz, C. P., Eigler, D. M. & Heinrich, A. J. Bistability in atomic-scale antiferromagnets. *Science* **335,** 196–9 (2012).

14. Khajetoorians, A. A., Wiebe, J., Chilian, B. & Wiesendanger, R. Realizing All-Spin-Based Logic Operations Atom by Atom. *Science* **332,** 1062–1064 (2011).

15. Donati, F. *et al.* Magnetic remanence in single atoms. *Science* **352,** 318–321 (2016).

16. Binnig, G., Rohrer, H., Gerber, C. & Weibel, E. Surface Studies by Scanning Tunneling Microscopy. *Phys. Rev. Lett.* **49,** 57–61 (1982).

17. Binnig, G. & Rohrer, H. Scanning Tunneling Microscopy. *Helvetica Physica Acta* **55,** 726–735 (1982).

18. Casavecchia, N. *A Boy and his Atom* IBM Research. 2013.

19. Khajetoorians, A. A. *et al.* Spin Excitations of Individual Fe Atoms on Pt(111): Impact of the Site-Dependent Giant Substrate Polarization. *Phys. Rev. Lett.* **111,** 157204 (2013).

20. Goldschmidt, Z. B. in *Handbook on the Physics and Chemistry of Rare Earths* 1–171 (Elsevier, 1978).

21. Buschow, K. Chapter 4 Rare earth compounds. *Handbook of Ferromagnetic Materials* **1,** 297–414 (1980).

22. Campbell, I. A. Indirect exchange for rare earths in metals. *Journal of Physics F: Metal Physics* **2,** L47 (1972).

23. Friedel, J. Metallic alloys. *Il Nuovo Cimento (1955-1965)* **7,** 287–311 (1958).

24. O'Handley, R. C. *Modern Magnetic Materials: Principles and Applications* (Wiley and Sons, 1999).

25. Barret, S. & Dhesi, S. *The Structure of Rare-Earth Metal Surfaces* (Imperial College Press, 2001).

26. Davis, D. D. & Bozorth, R. M. Magnetic Properties of Thulium Metal. *Phys. Rev.* **118,** 1543–1545 (1960).

27. Richards, D. B. & Legvold, S. High-Field Magnetization of Thulium Single Crystals. *Phys. Rev.* **186,** 508–514 (1969).

28. Koehler, W. C., Cable, J. W., Wollan, E. O. & Wilkinson, M. K. Magnetic Structures of Thulium. *Phys. Rev.* **126,** 1672–1678 (1962).

29. Brun, T. O. *et al.* Temperature Dependence of the Periodicity of the Magnetic Structure of Thulium Metal. *Phys. Rev. B* **1,** 1251–1253 (1970).

30. Nistor, C. *et al.* Structure and magnetism of Tm atoms and monolayers on W(110). *Phys. Rev. B* **90,** 064423 (2014).

31. Coffey, D. *et al.* Antiferromagnetic Spin Coupling between Rare Earth Adatoms and Iron Islands Probed by Spin-Polarized Tunneling. *Scientific Reports* **5,** 13709 (2015).

32. Nordheim, L. Zur Theorie der thermischen Emission und der Reflexion von Elektronen an Metallen. *Zeitschrift für Physik* **46,** 833–855 (1928).

33. Hund, F. Zur Deutung der Molekelspektren. I. *Zeitschrift für Physik* **40,** 742–764 (1927).

34. Hund, F. Zur Deutung der Molekelspektren. III. *Zeitschrift für Physik* **43,** 805–826 (1927).

35. Esaki, L. New Phenomenon in Narrow Germanium $p - n$ Junctions. *Phys. Rev.* **109,** 603–604 (1958).

36. Giaever, I. Energy Gap in Superconductors Measured by Electron Tunneling. *Phys. Rev. Lett.* **5,** 147–148 (1960).

37. Giaever, I. Electron Tunneling Between Two Superconductors. *Phys. Rev. Lett.* **5,** 464–466 (1960).

38. Nicol, J., Shapiro, S. & Smith, P. H. Direct Measurement of the Superconducting Energy Gap. *Phys. Rev. Lett.* **5,** 461–464 (1960).

39. Fisher, J. C. & Giaever, I. Tunneling Through Thin Insulating Layers. *Journal of Applied Physics* **32,** 172–177 (1961).

40. Binnig, G., Rohrer, H., Gerber, C. & Weibel, E. Tunneling through a controllable vacuum gap. *Appl. Phys. Lett.* **40,** 178–180 (1982).

41. Binnig, G., Quate, C. F. & Gerber, C. Atomic Force Microscope. *Phys. Rev. Lett.* **56,** 930–933 (1986).

42. Lawrence A. Bottomley, P. N. F. Joseph E. Coury. Scanning Probe Microscopy. *Analytical Chemistry* **68,** 185–230 (1996).

43. Herbschleb, C. T. *et al.* The ReactorSTM: Atomically resolved scanning tunneling microscopy under high-pressure, high-temperature catalytic reaction conditions. *Review of Scientific Instruments* **85** (2014).

44. Assig, M. *et al.* A 10 mK scanning tunneling microscope operating in ultra high vacuum and high magnetic fields. *Review of Scientific Instruments* **84** (2013).

45. Loth, S., Etzkorn, M., Lutz, C. P., Eigler, D. M. & Heinrich, A. J. Measurement of Fast Electron Spin Relaxation Times with Atomic Resolution. *Science* **329,** 1628–1630 (2010).

46. Cocker, T. L. *et al.* An ultrafast terahertz scanning tunnelling microscope. *Nat Photon* **7,** 620–625 (2013).

47. Baumann, S. *et al.* Electron paramagnetic resonance of individual atoms on a surface. *Science* **350,** 417–420 (2015).

48. Cohen-Tannoudji, C., Diu, B., Laloe, F. & Dui, B. *Quantum Mechanics (2 vol. set)* (Wiley-Interscience, 2006).

49. Levi, A. F. J. *Applied Quantum Mechanics* (Cambridge University Press, 2006).

50. Fischer, R., Fischer, N., Schuppler, S., Fauster, T. & Himpsel, F. J. Image states on Co(0001) and Fe(110) probed by two-photon photoemission. *Phys. Rev. B* **46,** 9691–9693 (1992).

51. Polizzotti, R. & Erhlich, G. The work function of perfect W(110) planes: Fowler-Nordheim studies. *Surf. Sci.* **91,** 24–36 (1980).

52. Hamers, R. J. Atomic-Resolution Surface Spectroscopy with the Scanning Tunneling Microscope. *Annual Review of Physical Chemistry* **40,** 531–559 (1989).

53. Bardeen, J. Tunnelling from a Many-Particle Point of View. *Phys. Rev. Lett.* **6,** 57–59 (1961).

54. Tersoff, J. & Hamann, D. R. Theory and Application for the Scanning Tunneling Microscope. *Phys. Rev. Lett.* **50,** 1998–2001 (1983).

55. Tersoff, J. & Hamann, D. R. Theory of the scanning tunneling microscope. *Phys. Rev. B* **31,** 805–813 (1985).

56. Gross, L. *et al.* High-Resolution Molecular Orbital Imaging Using a *p*-Wave STM Tip. *Phys. Rev. Lett.* **107,** 086101 (2011).

57. Heinze, S., Blügel, S., Pascal, R., Bode, M. & Wiesendanger, R. Prediction of bias-voltage-dependent corrugation reversal for STM images of bcc (110) surfaces: W(110), Ta(110), and Fe(110). *Phys. Rev. B* **58,** 16432–16445 (1998).

58. Li, J., Schneider, W.-D. & Berndt, R. Local density of states from spectroscopic scanning-tunneling-microscope images: Ag(111). *Phys. Rev. B* **56,** 7656–7659 (1997).

59. Soe, W.-H., Manzano, C., De Sarkar, A., Chandrasekhar, N. & Joachim, C. Direct Observation of Molecular Orbitals of Pentacene Physisorbed on Au(111) by Scanning Tunneling Microscope. *Phys. Rev. Lett.* **102,** 176102 (2009).

60. Julliere, M. Tunneling between ferromagnetic films. *Phys. Lett. A* **54,** 225–226 (1975).

61. Slonczewski, J. C. Conductance and exchange coupling of two ferromagnets separated by a tunneling barrier. *Phys. Rev. B* **39,** 6995–7002 (1989).

62. Wulfhekel, W. & Kirschner, J. Spin-Polarized Scanning Tunneling Microscopy of Magnetic Structures and Antiferromagnetic Thin Films. *Annual Review of Materials Research* **37,** 69–91 (2007).

63. Wiesendanger, R., Guntherodt, H.-J., Guntherodt, G., Gambino, R. J. & Ruf, R. Observation of vacuum tunneling of spin-polarized electrons with the scanning tunneling microscope. *Phys. Rev. Lett.* **65,** 247–250 (1990).

64. Wortmann, D., Heinze, S., Kurz, P., Bihlmayer, G. & Blügel, S. Resolving Complex Atomic-Scale Spin Structures by Spin-Polarized Scanning Tunneling Microscopy. *Phys. Rev. Lett.* **86,** 4132–4135 (2001).

65. Néel, N. *et al.* Energy-resolved spin-polarized tunneling and exchange coupling of Co and Cr atoms on Fe islands on W(110). *Phys. Rev. B* **85,** 155406 (2012).

66. Laegsgaard, E. *et al.* A high-pressure scanning tunneling microscope. *Review of Scientific Instruments* **72,** 3537–3542 (2001).

67. Zhang, L., Miyamachi, T., Tomanic, T., Dehm, R. & Wulfhekel, W. A compact sub-Kelvin ultrahigh vacuum scanning tunneling microscope with high energy resolution and high stability. *Review of Scientific Instruments* **82** (2011).

68. Bode, M., Krause, S., Berbil-Bautista, L., Heinze, S. & Wiesendanger, R. On the preparation and electronic properties of clean W(1 1 0) surfaces. *Surface Science* **601,** 3308–3314 (2007).

69. Repp, J., Meyer, G., Stojkovi ć, S. M., Gourdon, A. & Joachim, C. Molecules on Insulating Films: Scanning-Tunneling Microscopy Imaging of Individual Molecular Orbitals. *Phys. Rev. Lett.* **94,** 026803 (2005).

70. Loth, S., Lutz, C. P. & Heinrich, A. J. Spin-polarized spin excitation spectroscopy. *New Journal of Physics* **12,** 125021 (2010).

71. Leibsle, F. M., Flipse, C. F. J. & Robinson, A. W. Structure of the Cu100- *c* (2x2)N surface: A scanning-tunneling-microscopy study. *Phys. Rev. B* **47,** 15865–15868 (1993).

72. Bryant, P. J., Kim, H. S., Zheng, Y. C. & Yang, R. Technique for shaping scanning tunneling microscope tips. *Review of Scientific Instruments* **58,** 1115–1115 (1987).

73. Bode, M., Getzlaff, M. & Wiesendanger, R. Spin-Polarized Vacuum Tunneling into the Exchange-Split Surface State of Gd(0001). *Phys. Rev. Lett.* **81,** 4256–4259 (1998).

74. Kubetzka, A., Bode, M., Pietzsch, O. & Wiesendanger, R. Spin-Polarized Scanning Tunneling Microscopy with Antiferromagnetic Probe Tips. *Phys. Rev. Lett.* **88,** 057201 (2002).

75. Schlenhoff, A., Krause, S., Herzog, G. & Wiesendanger, R. Bulk Cr tips with full spatial magnetic sensitivity for spin-polarized scanning tunneling microscopy. *Applied Physics Letters* **97** (2010).

76. Weller, D., Alvarado, S. F., Gudat, W., Schroder, K. & Campagna, M. Observation of Surface-Enhanced Magnetic Order and Magnetic Surface Reconstruction on Gd(0001). *Phys. Rev. Lett.* **54,** 1555–1558 (1985).

77. Kwo, J. *et al.* Magnetic and Structural Properties of Single-Crystal Rare-Earth Gd-Y Superlattices. *Phys. Rev. Lett.* **55,** 1402–1405 (1985).

78. Salamon, M. B. *et al.* Long-range incommensurate magnetic order in a Dy-Y multilayer. *Phys. Rev. Lett.* **56,** 259–262 (1986).

79. Majkrzak, C. F. *et al.* Observation of a Magnetic Antiphase Domain Structure with Long-Range Order in a Synthetic Gd-Y Superlattice. *Phys. Rev. Lett.* **56,** 2700–2703 (1986).

80. Kwo, J., M., H. & NakaharaS. Growth of rare-earth single crystals by molecular beam epitaxy: The epitaxial relationship between hcp rare earth and bcc niobium. *Appl. Phys. Lett.* **49,** 319–321 (1986).

81. Stenborg, A. & Bauer, E. Two-dimensional Yb on a Mo(110) surface. *Phys. Rev. B* **36,** 5840–5847 (1987).

82. Kolaczkiewicz, J. & Bauer, E. The adsorption of Eu, Gd and Tb on the W(110) surface. *Surf. Sci.* **175,** 487–507 (1986).

83. Kolaczkiewicz, J. & Bauer, E. The adsorption of Eu, Gd and Tb on the W(110) surface. *Surface Science* **175,** 487–507 (1986).

84. Nicklin, C., Binns, C., Norris, C., McCluskey, P. & Barthes-Labrousse, M.-G. Structural study of Tm on Mo(110). *Surface Science* **269,** 700–706 (1992).

85. Bodenbach, M., Hohr, A., Laubschat, C., Kaindl, G. & Methfessel, M. Surface electronic structure of Tm(0001) and Yb(111). *Phys. Rev. B* **50,** 14446–14451 (1994).

86. Bachmann, M., Gabl, M., Deisl, C., Memmel, N. & Bertel, E. Quasi-one-dimensional self-assembly of metal nanoclusters on C/W(110). *Phys. Rev. B* **78,** 235410 (2008).

87. Zakeri, K., Peixoto, T., Zhang, Y., Prokop, J. & Kirschner, J. On the preparation of clean tungsten single crystals. *Surface Science* **604,** L1–L3 (2010).

88. Bode, M., Pascal, R. & Wiesendanger, R. STM study of carbon-induced reconstructions on W(110): strong evidence for a surface lattice deformation. *Surface Science* **344,** 185–191 (1995).

89. Li, H. *et al.* Structural and electronic properties of ultrathin films of Gd, Tb, Dy, Ho, and Er. *Phys. Rev. B* **45,** 3853–3856 (1992).

90. Tober, E. D., Ynzunza, R. X., Westphal, C. & Fadley, C. S. Relationship between morphology and magnetic behavior for Gd thin films on W(110). *Phys. Rev. B* **53,** 5444–5448 (1996).

91. Diez-Ferrer, J. L. *Propiedades magnéticas y electrónicas de materiales nanoestructurados determinadas mediante técnicas de microscopia de sonda local* PhD thesis (Universidad de Zaragoza, 2010).

92. Schwoebel, R. L. Step Motion on Crystal Surfaces. II. *Journal of Applied Physics* **40,** 614–618 (1969).

93. Schwoebel, R. L. & Shipsey, E. J. Step Motion on Crystal Surfaces. *Journal of Applied Physics* **37,** 3682–3686 (1966).

94. Brune, H. Microscopic view of epitaxial metal growth: nucleation and aggregation. *Surf. Sci. Rep.* **31,** 121–229 (1998).

95. Einax, M., Dieterich, W. & Maass, P. *Colloquium* : Cluster growth on surfaces: Densities, size distributions, and morphologies. *Rev. Mod. Phys.* **85,** 921–939 (2013).

96. Brune, H., Bales, G. S., Jacobsen, J., Boragno, C. & Kern, K. Measuring surface diffusion from nucleation island densities. *Phys. Rev. B* **60,** 5991–6006 (1999).

97. Horch, S. & Lorensen, H. T. Enhancement of surface self-diffusion of platinum atoms by adsorbed hydrogen. *Nature* **398,** 134 (1999).

98. Venables, J. A. Nucleation calculations in a pair-binding model. *Phys. Rev. B* **36,** 4153–4162 (1987).

99. Li, J., Schneider, W.-D., Berndt, R. & Delley, B. Kondo Scattering Observed at a Single Magnetic Impurity. *Phys. Rev. Lett.* **80,** 2893–2896 (1998).

100. Gardonio, S. *et al.* Spectral Functions of Isolated Ce Adatoms on Paramagnetic Surfaces. *Phys. Rev. Lett.* **107,** 026801 (2011).

101. Schuh, T. *et al.* Magnetic Excitations of Rare Earth Atoms and Clusters on Metallic Surfaces. *Nano Letters* **12,** 4805–4809 (2012).

102. Lin, C.-Y., Li, J.-L., Hsieh, Y.-H., Ou, K.-L. & Jones, B. A. Magnetic Interaction between Surface-Engineered Rare-Earth Atomic Spins. *Phys. Rev. X* **2,** 021012 (2012).

103. Miyamachi, T., Schuh, T., Markl, T. & Bresch, C. Stabilizing the magnetic moment of single holmium atoms by symmetry. *Nature* **503,** 242–6 (2013).

104. Rau, C., Jin, C. & Robert, M. Novel magnetic surface anisotropies and critical behavior of Tb(0001)/W(110) films. *Physics Letters A* **138,** 334–338 (1989).

105. Farle, M., Baberschke, K., Stetter, U., Aspelmeier, A. & Gerhardter, F. Thickness-dependent Curie temperature of Gd(0001)/W(110) and its dependence on the growth conditions. *Phys. Rev. B* **47,** 11571–11574 (1993).

106. Berbil-Bautista, L., Krause, S., Bode, M. & Wiesendanger, R. Spin-polarized scanning tunneling microscopy and spectroscopy of ferromagnetic Dy(0001)/W(110) films. *Phys. Rev. B* **76,** 064411 (2007).

107. Getzlaff, M. Surface Magnetism. *Springer Tracts in Modern Physics* **240,** 21 (2010).

108. Weschke, E. *et al.* Finite-Size Effect on Magnetic Ordering Temperatures in Long-Period Antiferromagnets: Holmium Thin Films. *Phys. Rev. Lett.* **93,** 157204 (2004).

109. Sato, N. Magnetic properties of amorphous Tb Fe thin films with an artificially layered structure. *Journal of Applied Physics* **59,** 2514–2520 (1986).

110. Maat, S., Smith, N., Carey, M. J. & Childress, J. R. Suppression of spin torque noise in current perpendicular to the plane spin-valves by addition of Dy cap layers. *Applied Physics Letters* **93** (2008).

111. Marcham, M. K. *et al.* Influence of a Dy overlayer on the precessional dynamics of a ferromagnetic thin film. *Applied Physics Letters* **102** (2013).

112. Sanyal, B. *et al.* Forcing Ferromagnetic Coupling Between Rare-Earth-Metal and 3d Ferromagnetic Films. *Phys. Rev. Lett.* **104,** 156402 (2010).

113. Ward, C. *et al.* Realizing a high magnetic moment in Gd/Cr/FeCo: The role of the rare earth. *Applied Physics Letters* **102** (2013).

114. Rhyne, J. J. *et al.* Occurrence of long range helical spin ordering in Dy Y multilayers (invited). *Journal of Applied Physics* **61,** 4043–4048 (1987).

115. Borchers, J. *et al.* Magnetic and structural characterization of Dy Y superlattices. *Journal of Applied Physics* **61,** 4049–4051 (1987).

116. Dowben, P., McIlroy, D. & Li, D. in, 1–46 (Elsevier, 1997).

117. Benito, L. *et al.* Magnetocrystalline and magnetoelastic basal plane anisotropies in Ho Lu superlattices. *Phys. Rev. B* **70,** 052403 (2004).

118. Steinbrecher, M. *et al.* Absence of a spin-signature from a single Ho adatom as probed by spin-sensitive tunneling. *Nat Commun* **7** (2016).

119. Singha, A. *et al.* Magnetic Hysteresis in Er Trimers on Cu(111). *Nano Letters* **16,** 3475–3481 (2016).

120. Karbowiak, M. & Rudowicz, C. Ground state of Ho atoms on Pt(111) metal surfaces: Implications for magnetism. *Phys. Rev. B* **93,** 184415 (2016).

121. Carbone, C. *et al.* Electronic and magnetic coupling between rare-earth adatoms and the Fe(001) surface. *Phys. Rev. B* **41,** 3866–3869 (1990).

122. Hubinger, F. *et al.* Temperature-dependent study of the partially filled surface state on Tb(0001). *Journal of Electron Spectroscopy and Related Phenomena* **76,** 535–539 (1995).

123. Paul, O., Toscano, S., Hursch, W. & Landolt, M. Magnetic behaviour of Gd and Tb adlayers on Fe and Ni surfaces studied by spin polarized auger spectroscopy. *Journal of Magnetism and Magnetic Materials* **84,** L7–L11 (1990).

124. Kappert, R., Sacchi, M., Goedkoop, J., Grioni, M. & Fuggle, J. X-ray dichroism of Dy overlayers on Ni(110). *Surface Science* **248,** L245–L249 (1991).

125. Kappert, R. J. H., Vogel, J., Sacchi, M. & Fuggle, J. C. Linear-dichroism studies of thin Dy overlayers on Ni(110) and Cu(110) substrates. *Phys. Rev. B* **48,** 2711–2720 (1993).

126. Vogel, J. & Sacchi, M. An X-ray dichroism study of magnetic and crystal field effects in thin rare earth overlayers. *Surface Science* **365,** 831–839 (1996).

127. Getzlaff, M., Bode, M., Heinze, S., Pascal, R. & Wiesendanger, R. Temperature-dependent exchange splitting of the magnetic Gd(0 0 0 1) surface state. *Journal of Magnetism and Magnetic Materials* **184,** 155–165 (1998).

128. Getzlaff, M., Bode, M., Heinze, S. & Wiesendanger, R. New insight into the surface magnetic properties of Gd(0001). *Applied Surface Science* **142,** 558–563 (1999).

129. Bode, M. *et al.* Temperature-Dependent Exchange Splitting of a Surface State on a Local-Moment Magnet: Tb(0001). *Phys. Rev. Lett.* **83,** 3017–3020 (1999).

130. Vaz, C. A. F., Bland, J. A. C. & Lauhoff, G. Magnetism in ultrathin film structures. *Reports on Progress in Physics* **71,** 056501 (2008).

131. Gradmann, K. H. J. U. edited by Buschow. Handbook of Magnetic Materials. **7,** 1 (1993).

132. Jensen, J. & Mackintosh, M. Rare Earth Magnetism: Structures and Excitations (1991).

133. Thole, B. T. *et al. 3d* x-ray-absorption lines and the $3d^9 4f^{n+1}$ multiplets of the lanthanides. *Phys. Rev. B* **32,** 5107–5118 (1985).

134. Goedkoop, J. B. *et al.* Calculations of magnetic x-ray dichroism in the 3 *d* absorption spectra of rare-earth compounds. *Phys. Rev. B* **37,** 2086–2093 (1988).

135. Stepanow, S. *et al.* Giant spin and orbital moment anisotropies of a Cu-phthalocyanine monolayer. *Phys. Rev. B* **82,** 014405 (2010).

136. Rau, I. G. *et al.* Reaching the magnetic anisotropy limit of a 3d metal atom. *Science* **344,** 988–992 (2014).

137. Sugar, J. Interpretation of Photoabsorption in the Vicinity of the 3*d* Edges in La, Er, and Tm. *Phys. Rev. A* **6,** 1764–1767 (1972).

138. Kaindl, G., Kalkowski, G., Brewer, W. D., Perscheid, B. & Holtzberg, F. M edge X ray absorption spectroscopy of 4f instabilities in rare earth systems (invited). *Journal of Applied Physics* **55,** 1910–1915 (1984).

139. Sarpal, B. K. *et al.* The 3d core spectra of Sm and Tm vapours. *Journal of Physics B: Atomic, Molecular and Optical Physics* **24,** 1593 (1991).

140. Blancard, C., Esteva, J. M., Connerade, J. P., Kuetgens, U. & Hormes, J. The 3d X-ray absorption spectra of matrix-isolated Tm atoms and clusters. *Journal of Physics B: Atomic, Molecular and Optical Physics* **22,** L575 (1989).

141. Pichler, T. *et al.* Monometallofullerene $Tm@C_{82}$: Proof of an Encapsulated Divalent Tm Ion by High-Energy Spectroscopy. *Phys. Rev. Lett.* **79,** 3026–3029 (1997).

142. Domke, M. *et al.* Experimental Proof for Coordination-Dependent Valence of Tm Metal. *Phys. Rev. Lett.* **56,** 1287–1290 (1986).

143. Johansson, B. Valence state at the surface of rare-earth metals. *Phys. Rev. B* **19,** 6615–6619 (1979).

144. Schuh, T. *et al.* Magnetic Excitations of Rare Earth Atoms and Clusters on Metallic Surfaces. *Nano Letters* **12,** 4805–4809 (2012).

145. Donati, F. *et al.* Magnetism of Ho and Er Atoms on Close-Packed Metal Surfaces. *Phys. Rev. Lett.* **113,** 237201 (2014).

146. Teramura, Y., Tanaka, A., Thole, B. T. & Jo, T. Effect of Coulomb Interaction on the X-Ray Magnetic Circular Dichroism Spin Sum Rule in Rare Earths. *Journal of the Physical Society of Japan* **65,** 3056–3059 (1996).

147. Thole, B. T., Carra, P., Sette, F. & van der Laan, G. X-ray circular dichroism as a probe of orbital magnetization. *Phys. Rev. Lett.* **68,** 1943–1946 (1992).

148. Carra, P., Thole, B. T., Altarelli, M. & Wang, X. X-ray circular dichroism and local magnetic fields. *Phys. Rev. Lett.* **70,** 694–697 (1993).

149. Zhou, L. *et al.* Strength and directionality of surface Ruderman-Kittel-Kasuya-Yosida interaction mapped on the atomic scale. *Nat Phys* **6,** 187–191 (2010).

150. Thole, B. T., van der Laan, G. & Sawatzky, G. A. Strong Magnetic Dichroism Predicted in the $M_{4,5}$ X-Ray Absorption Spectra of Magnetic Rare-Earth Materials. *Phys. Rev. Lett.* **55,** 2086–2088 (1985).

151. Astrom, H. U., Nogues, J., Nicolaides, G. K., Rao, K. V. & Benediktsson, G. Magnetic transitions in single-crystal thulium. *Journal of Physics: Condensed Matter* **3,** 7395 (1991).

152. Wannier, G. H. Antiferromagnetism. The Triangular Ising Net. *Phys. Rev.* **79,** 357–364 (1950).

153. Fazekas, P. & Anderson, P. W. On the ground state properties of the anisotropic triangular antiferromagnet. *Philosophical Magazine* **30,** 423–440 (1974).

154. Collins, M. F. & Petrenko, O. A. Review/Synthese: Triangular antiferromagnets. *Canadian Journal of Physics* **75,** 605–655 (1997).

155. Bode, M. *et al.* Chiral magnetic order at surfaces driven by inversion asymmetry. *Nature* **447,** 190–193 (2007).

156. Grigoriev, S. V., Chetverikov, Y. O., Lott, D. & Schreyer, A. Field Induced Chirality in the Helix Structure of Dy/Y Multilayer Films and Experimental Evidence for Dzyaloshinskii-Moriya Interaction on the Interfaces. *Phys. Rev. Lett.* **100,** 197203 (2008).

157. Heinze, S. *et al.* Real-Space Imaging of Two-Dimensional Antiferromagnetism on the Atomic Scale. *Science* **288,** 1805–1808 (2000).

158. Kubetzka, A., Pietzsch, O., Bode, M. & Wiesendanger, R. Spin-polarized scanning tunneling microscopy study of 360° walls in an external magnetic field. *Phys. Rev. B* **67,** 020401 (2003).

159. Meckler, S. *et al.* Real-Space Observation of a Right-Rotating Inhomogeneous Cycloidal Spin Spiral by Spin-Polarized Scanning Tunneling Microscopy in a Triple Axes Vector Magnet. *Phys. Rev. Lett.* **103,** 157201 (2009).

160. Schintke, S. & Schneider, W.-D. Insulators at the ultrathin limit: electronic structure studied by scanning tunnelling microscopy and scanning tunnelling spectroscopy. *Journal of Physics: Condensed Matter* **16,** R49 (2004).

161. Repp, J. & Meyer, G. in *Atomic and Molecular Manipulation* (eds Mayne, A. J. & Dujardin, G.) 17–49 (Elsevier, 2011).

162. Rau, I. G. *et al.* Reaching the magnetic anisotropy limit of a 3d metal atom. *Science* **344,** 988–992 (2014).

163. Repp, J., Meyer, G., Olsson, F. E. & Persson, M. Controlling the Charge State of Individual Gold Adatoms. *Science* **305,** 493–495 (2004).

164. Heinrich, A. J., Gupta, J. A., Lutz, C. P. & Eigler, D. M. Single-Atom Spin-Flip Spectroscopy. *Science* **306,** 466–469 (2004).

165. Hirjibehedin, C. F., Lutz, C. P. & Heinrich, A. J. Spin Coupling in Engineered Atomic Structures. *Science* **312,** 1021–1024 (2006).

166. Miyamachi, T. *et al.* Stabilizing the magnetic moment of single holmium atoms by symmetry. *Nature* **503,** 242–246 (2013).

167. Balashov, T. *et al.* Dynamic magnetic excitations in 3d and 4f atoms and clusters. *Surface Science* **630,** 331–336 (2014).

168. Natterer, F. *et al.* Reading and Writing Single-Atom Magnets. *ArXiv e-prints* (2016).

169. Zhang, Y. *et al.* Low-temperature scanning tunneling microscopy study on the electronic properties of a double-decker DyPc2 molecule at the surface. *Phys. Chem. Chem. Phys.* **17,** 27019–27026 (2015).

170. Fahrendorf, S. *et al.* Accessing 4f-states in single-molecule spintronics. *Nat Commun* **4** (2013).

171. Schwöbel, J. *et al.* Real-space observation of spin-split molecular orbitals of adsorbed single-molecule magnets. *Nat Commun* **3,** 953 (2012).

172. Komeda, T. *et al.* Observation and electric current control of a local spin in a single-molecule magnet. *Nat Commun* **2,** 217 (2011).

173. Rinehart, J. D., Fang, M., Evans, W. J. & Long, J. R. A N23– Radical-Bridged Terbium Complex Exhibiting Magnetic Hysteresis at 14 K. *Journal of the American Chemical Society* **133,** 14236–14239 (2011).

174. Leibsle, F., Dhesi, S., Barrett, S. & Robinson, A. STM observations of Cu(100)-c(2x2)N surfaces: evidence for attractive interactions and an incommensurate c(2x2) structure. *Surface Science* **317,** 309–320 (1994).

175. Ruggiero, C. D., Choi, T. & Gupta, J. A. Tunneling spectroscopy of ultrathin insulating films: CuN on Cu(100). *Applied Physics Letters* **91** (2007).

176. Choi, T., Ruggiero, C. D. & Gupta, J. A. Tunneling spectroscopy of ultrathin insulating Cu2N films, and single Co adatoms. *Journal of Vacuum Science & Technology B* **27,** 887–890 (2009).

177. Serrate, D., Moro-Lagares, M., Piantek, M., Pascual, J. I. & Ibarra, M. R. Enhanced Hydrogen Dissociation by Individual Co Atoms Supported on Ag(111). *The Journal of Physical Chemistry C* **118,** 5827–5832 (2014).

178. Pivetta, M., Ternes, M., Patthey, F. & Schneider, W. Diatomic Molecular Switches to Enable the Observation of Very-Low-Energy Vibrations. *Phys. Rev. Lett.* **99,** 126104 (2007).

179. Perdew, J. P. & Zunger, A. Self-interaction correction to density-functional approximations for many-electron systems. *Phys. Rev. B* **23,** 5048–5079 (1981).

180. Hobbs, D., Kresse, G. & Hafner, J. Fully unconstrained noncollinear magnetism within the projector augmented-wave method. *Phys. Rev. B* **62,** 11556–11570 (2000).

181. Blöchl, P. E. Projector augmented-wave method. *Phys. Rev. B* **50,** 17953–17979 (1994).

182. Kresse, G. & Furthmüller, J. Efficiency of ab-initio total energy calculations for metals and semiconductors using a plane-wave basis set. *Computational Materials Science* **6,** 15–50 (1996).

183. Loth, S. *et al.* Controlling the state of quantum spins with electric currents. *Nat Phys* **6,** 340–344 (2010).

184. Crommie, M. F., Lutz, C. P. & Eigler, D. M. *Science* **262,** 218 (1993).

185. Hasegawa, Y. & Avouris, P. Direct observation of standing wave formation at surface steps using scanning tunneling spectroscopy. *Phys. Rev. Lett.* **71,** 1071–1074 (1993).

186. Li, J., Schneider, W.-D., Berndt, R. & Crampin, S. Electron Confinement to Nanoscale Ag Islands on Ag(111): A Quantitative Study. *Phys. Rev. Lett.* **80,** 3332–3335 (1998).

187. Diekhöner, L. *et al.* Surface States of Cobalt Nanoislands on Cu(111). *Phys. Rev. Lett.* **90,** 236801 (2003).

188. Von Bergmann, K. *et al.* Spin-Polarized Electron Scattering at Single Oxygen Adsorbates on a Magnetic Surface. *Phys. Rev. Lett.* **92,** 046801 (2004).

189. Oka, H. *et al.* Spin-Dependent Quantum Interference Within a Single Magnetic Nanostructure. *Science* **327,** 843 (2010).

190. Pietzsch, O. *et al.* Spin-Resolved Electronic Structure of Nanoscale Cobalt Islands on Cu(111). *Phys. Rev. Lett.* **96,** 237203 (2006).

191. Zhang, T. *et al.* Experimental Demonstration of Topological Surface States Protected by Time-Reversal Symmetry. *Phys. Rev. Lett.* **103,** 266803 (2009).

192. Pascual, J. I. *et al.* Role of Spin in Quasiparticle Interference. *Phys. Rev. Lett.* **93,** 196802 (2004).

193. Simon, L., Bena, C., Vonau, F., Cranney, M. & Aubel, D. Fourier-transform scanning tunnelling spectroscopy: the possibility to obtain constant-energy maps and band dispersion using a local measurement. *J. Phys. D: Appl. Phys.* **44,** 464010 (2011).

194. Oka, H. *et al.* Spin-polarized quantum confinement in nanostructures: Scanning tunneling microscopy. *Rev. Mod. Phys.* **86,** 1127–1168 (2014).

195. Hsieh, D. *et al.* A topological Dirac insulator in a quantum spin Hall phase. *Nature* **452,** 970–974 (2008).

196. Tamm, I. Über eine mögliche Art der Elektronenbindung an Kristalloberflächen. *Zeitschrift für Physik* **76,** 849–850 (1932).

197. Michel Lannoo, P. F. *Atomic and Electronic Structure of Surfaces - Theoretical Foundations* (Springer-Verlag Berlin Heidelberg, 1991).

198. Shockley, W. On the Surface States Associated with a Periodic Potential. *Phys. Rev.* **56,** 317–323 (1939).

199. Crommie, M. F., Lutz, C. P. & Eigler, D. M. Imaging standing waves in a two-dimensional electron gas. *Nature* **363,** 524–527 (1993).

200. Avouris, P., Lyo, I., Walkup, R. E. & Hasegawa, Y. Real space imaging of electron scattering phenomena at metal surfaces. *Journal of Vacuum Science & Technology B* **12,** 1447–1455 (1994).

201. Roushan, P. *et al.* Topological surface states protected from backscattering by chiral spin texture. *Nature* **460,** 1106 (2009).

202. Krönlein, A., Kemmer, J., Hsu, P.-J. & Bode, M. Quasiparticle interference scattering of spin-polarized Shockley-like surface state electrons: Ni(111). *Phys. Rev. B* **89,** 155413 (2014).

203. Kim, H.-J., Vescovo, E., Heinze, S. & Blügel, S. Surface electronic structure of Fe(110): the importance of surface resonances. *Surf. Sci.* **478,** 193–202 (2001).

204. Sanchez-Barriga, J. *et al.* Strength of Correlation Effects in the Electronic Structure of Iron. *Phys. Rev. Lett.* **103,** 267203 (2009).

205. Braun, J., Math, C., Postnikov, A. & Donath, M. Surface resonances versus surface states on Fe(110). *Phys. Rev. B* **65,** 184412 (2002).

206. Braun, J. & Donath, M. Contest between surface resonances and surface states at 3 d ferromagnets. *Europhys. Lett.* **59,** 592 (2002).

207. Braun, J. & Donath, M. Theory of photoemission from surfaces. *J. Phys.: Condens. Matter* **16,** S2539 (2004).

208. Pendry, J. Theory of Photoemission. *Surf. Sci.* **57,** 679–705 (1976).

209. Andersen, O. K. *Phys. Rev. B* **12,** 3060 (1975).

210. Przybylski, M. & Gradmann, U. *J. Phys. (Paris) C* **33,** 1705 (1988).

211. Przybylski, M., Kaufmann, I. & Gradmann, U. Mossbauer analysis of ultrathin ferromagnetic Fe(110) films on W(110) coated by Ag. *Phys. Rev. B* **40,** 8631–8640 (1989).

212. Chen, J. & Erskine, J. L. Surface-step-induced magnetic anisotropy in thin epitaxial Fe films on W(001). *Phys. Rev. Lett.* **68,** 1212–1215 (1992).

213. Sander, D. The correlation between mechanical stress and magnetic anisotropy in ultrathin films. *Reports on Progress in Physics* **62,** 809 (1999).

214. Bode, M., Pascal, R., Dreyer, M. & Wiesendanger, R. Nanostructural and local electronic properties of Fe/W(110) correlated by scanning tunneling spectroscopy. *Phys. Rev. B* **54,** R8385–R8388 (1996).

215. Gradmann, U., Przybylski, M., Elmers, H. J. & Liu, G. Ferromagnetism in the thermodynamically stable monolayer Fe(110) on W(110), coated by Ag. *Appl. Phys. A* **49,** 563–571 (1989).

216. Gradmann, U., Korecki, J. & Przybylski, M. In-Plane Magnetic Surface Anisotropies in Fe(110). *Appl. Phys. A* **39,** 101–108 (1986).

217. Sander, D., Enders, A., Schmidthals, C., Reuter, D. & Kirschner, J. International Conference on Magnetism (Part II) Stranski-Krastanov layers of Fe on W(1 1 0): A combined MOKE, LEED, SAM and stress measurement investigation. *Journal of Magnetism and Magnetic Materials* **177,** 1299–1300 (1998).

218. Jensen, C., Reshöft, K. & Köhler, U. Direct observation of strain relaxation in iron layers on W(110) by time-resolved STM. *Applied Physics A* **62,** 217–221 (1996).

219. Przybylski, M. & Gradmann, U. Ferromagnetic order in a Fe(110) monolayer on W(110) by Mössbauer spectroscopy. *Phys. Rev. Lett.* **59,** 1152–1155 (1987).

220. Elmers, H. J. *et al.* Submonolayer Magnetism of Fe(110) on W(110): Finite Width Scaling of Stripes and Percolation between Islands. *Phys. Rev. Lett.* **73,** 898–901 (1994).

221. Elmers, H.-J., Hauschild, J. & Gradmann, U. Critical behavior of the uniaxial ferromagnetic monolayer Fe(110) on W(110). *Phys. Rev. B* **54,** 15224–15233 (1996).

222. Hauschild, J., Gradmann, U. & Elmers, H. J. Perpendicular magnetization and dipolar antiferromagnetism in double layer nanostripe arrays of Fe(110) on W(110). *Applied Physics Letters* **72,** 3211–3213 (1998).

223. Bode, M. *et al.* Magnetization-Direction-Dependent Local Electronic Structure Probed by Scanning Tunneling Spectroscopy. *Phys. Rev. Lett.* **89,** 237205 (2002).

224. Stünkel, D. Die Magnetisierung sehr dünner Eisenschichten. *Zeitschrift für Physik* **176,** 207–220 (1963).

225. Elmers, H. J., Furubayashi, T., Albrecht, M. & Gradmann, U. Analysis of magnetic anisotropies in ultrathin films by magnetometry insitu in UHV (invited). *Journal of Applied Physics* **70,** 5764–5768 (1991).

226. Heide, M., Bihlmayer, G. & Blügel, S. Dzyaloshinskii-Moriya interaction accounting for the orientation of magnetic domains in ultrathin films: Fe/W(110). *Phys. Rev. B* **78,** 140403 (2008).

227. Zakeri, K. *et al.* Asymmetric Spin-Wave Dispersion on Fe(110): Direct Evidence of the Dzyaloshinskii-Moriya Interaction. *Phys. Rev. Lett.* **104,** 137203 (2010).

228. Bode, M., Krause, S., Berbil-Bautista, L., Heinze, S. & Wiesendanger, R. On the preparation and electronic properties of clean W(110) surfaces. *Surf. Sci.* **601,** 3308 (2007).

229. Schouteden, K., Lievens, P. & Van Haesendonck, C. Fourier-transform scanning tunneling microscopy investigation of the energy versus wave vector dispersion of electrons at the Au(111) surface. *Phys. Rev. B* **79,** 195409 (2009).

230. Petersen, L., Laitenberger, P., Laegsgaard, E. & Besenbacher, F. Screening waves from steps and defects on Cu(111) and Au(111) imaged with STM: Contribution from bulk electrons. *Phys. Rev. B* **58,** 7361–7366 (1998).

231. Sessi, P. *et al.* Direct observation of many-body charge density oscillations in a two-dimensional electron gas. *Nat Commun* **6** (2015).

232. Song, Z., Pascual, J. I., Conrad, H., Horn, K. & Rust, H. .-.-P. d States. *Surf. Sci.* **491,** 39–47 (2001).

233. LaShell, S., McDougall, B. A. & Jensen, E. Spin Splitting of an Au(111) Surface State Band Observed with Angle Resolved Photoelectron Spectroscopy. *Phys. Rev. Lett.* **77,** 3419–3422 (1996).

234. Manchon, A., Koo, H. C., Nitta, J., Frolov, S. M. & Duine, R. A. New perspectives for Rashba spin-orbit coupling. *Nat Mater* **14,** 871–882 (2015).

235. Bihlmayer, G., Rader, O. & Winkler, R. Focus on the Rashba effect. *New Journal of Physics* **17,** 050202 (2015).

236. Carbone, C. *et al.* Asymmetric band gaps in a Rashba film system. *Phys. Rev. B* **93,** 125409 (2016).

237. Hochstrasser, M., Tobin, J. G., Rotenberg, E. & Kevan, S. D. Spin-Resolved Photoemission of Surface States of W(110)-1x1H. *Phys. Rev. Lett.* **89,** 216802 (2002).

238. Rotenberg, E. & Kevan, S. D. Evolution of Fermi Level Crossings versus H Coverage on $W(110)$. *Phys. Rev. Lett.* **80,** 2905–2908 (1998).

239. Miyamoto, K. *et al.* Spin-Polarized Dirac-Cone-Like Surface State with d Character at W(110). *Phys. Rev. Lett.* **108,** 066808 (2012).

240. Shikin, A. M. *et al.* Origin of Spin-Orbit Splitting for Monolayers of Au and Ag on W(110) and Mo(110). *Phys. Rev. Lett.* **100,** 057601 (2008).

241. Honma, K. *et al.* Switching of Dirac-Fermion Mass at the Interface of Ultrathin Ferromagnet and Rashba Metal. *Phys. Rev. Lett.* **115,** 266401 (2015).

242. Mirhosseini, H., Flieger, M. & Henk, J. Dirac-cone-like surface state in W(110): dispersion, spin texture and photoemission from first principles. *New Journal of Physics* **15,** 033019 (2013).

243. Miyamoto, K. *et al.* Massless or heavy due to two-fold symmetry: Surface-state electrons at W(110). *Phys. Rev. B* **86,** 161411 (2012).

244. Shikin, A. M. *et al.* Induced Rashba splitting of electronic states in monolayers of Au, Cu on a W(110) substrate. *New Journal of Physics* **15,** 095005 (2013).

245. Essert, S., Krueckl, V. & Richter, K. Using topological insulator proximity to generate perfectly conducting channels in materials without topological protection. *New J. Phys* **16,** 113058 (2014).

246. Kutnyakhov, D. *et al.* Spin texture of time-reversal symmetry invariant surface states on W(110). *Scientific Reports* **6,** 29394 (2016).

247. Meier, F. *et al.* Spin polarization of platinum (111) induced by the proximity to cobalt nanostripes. *Phys. Rev. B* **83,** 075407 (2011).

248. Alvarez, J. *et al.* Magnetization of Pt in the Co/Pt(110) system investigated with surface x-ray magnetic diffraction: Evidence for in-plane magnetic anisotropy. *Phys. Rev. B* **60,** 10193–10198 (1999).

249. Bryant, B., Spinelli, A., Wagenaar, J. J. T., Gerrits, M. & Otte, A. F. Local control of single atom magnetocrystalline anisotropy. *Phys. Rev. Lett.* **111,** 127203 (2013).

250. Hirjibehedin, C. F. Large magnetic anisotropy of a single atomic spin embedded in a surface molecular network. *Science* **317,** 1199–203 (2007).

251. Khajetoorians, A. A. Current-driven spin dynamics of artificially constructed quantum magnets. *Science* **339,** 55–59 (2013).

252. Khajetoorians, A. A. Spin excitations of individual Fe atoms on Pt(111): Impact of the site-dependent giant substrate polarization. *Phys. Rev. Lett.* **111,** 157204 (2013).

253. Khajetoorians, A. A. Atom-by-atom engineering and magnetometry of tailored nanomagnets. *Nature Phys.* **8,** 497–503 (2012).

254. Khajetoorians, A. A., Wiebe, J., Chilian, B. & Wiesendanger, R. Realizing all-spin-based logic operations atom by atom. *Science* **332,** 1062–1064 (2011).

255. Knorr, N., Schneider, M., Diekhöner, L., Wahl, P. & Kern, K. Kondo effect of single Co adatoms on Cu surfaces. *Phys. Rev. Lett.* **88,** 096804 (2002).

256. Madhavan, V., Chen, W., Jamneala, T., Crommie, M. F. & Wingreen, N. S. Tunneling into a single magnetic atom: Spectroscopic evidence of the Kondo resonance. *Science* **280,** 567–569 (1998).

257. Manoharan, H., Lutz, C. & Eigler, D. Quantum mirages formed by coherent projection of electronic structure. *Nature* **403,** 512–5 (2000).

258. Meier, F., Zhou, L., Wiebe, J. & Wiesendanger, R. Revealing magnetic interactions from single-atom magnetization curves. *Science* **320,** 82–6 (2008).

259. Néel, N. Energy-resolved spin-polarized tunneling and exchange coupling of Co and Cr atoms on Fe islands on W(110). *Phys. Rev. B* **85,** 155406 (2012).

260. Otte, A. Spin excitations of a Kondo-screened atom coupled to a second magnetic atom. *Phys. Rev. Lett.* **103,** 1–4 (2009).

261. Otte, A. F. *et al.* The role of magnetic anisotropy in the Kondo effect. *Nat Phys* **4,** 847–850 (2008).

262. Yayon, Y., Brar, V., Senapati, L., Erwin, S. & Crommie, M. Observing spin polarization of individual magnetic adatoms. *Phys. Rev. Lett.* **99,** 8–11 (2007).

263. Krause, S., Berbil-Bautista, L., Herzog, G., Bode, M. & Wiesendanger, R. Current-induced magnetization switching with a spin-polarized scanning tunneling microscope. *Science* **317,** 1537–1540 (2007).

264. Sorace, L., Benelli, C. & Gatteschi, D. Lanthanides in molecular magnetism: old tools in a new field. *Chem. Soc. Rev.* **40,** 3092–3104 (2011).

265. Li, J., Schneider, W.-D., Berndt, R. & Delley, B. Kondo scattering observed at a single magnetic impurity. *Phys. Rev. Lett.* **80,** 2893–2896 (1998).

266. Silly, F. Creation of an atomic superlattice by immersing metallic adatoms in a two-dimensional electron sea. *Phys. Rev. Lett.* **92,** 1–4 (2004).

267. Ternes, M. Scanning-tunneling spectroscopy of surface-state electrons scattered by a slightly disordered two-dimensional dilute solid: Ce on Ag(111). *Phys. Rev. Lett.* **93,** 146805 (2004).

268. Donati, F. Magnetism of Ho and Er atoms on the close-packed surfaces of Pt and Cu. *Phys. Rev. Lett.* **113,** 237201 (2014).

269. Schuh, T. Magnetic excitations of rare earth atoms and clusters on metallic surfaces. *Nano Lett.* **12,** 4805–9 (2012).

270. Nistor, C. Structure and magnetism of Tm atoms and monolayers on W(110). *Phys. Rev. B* **90,** 064423 (2014).

271. Jensen, J. & Mackintosh, M. *Rare Earth Magnetism: Structures and Excitations* (Clarendon Press, 1991).

272. Johansson, B., Nordström, L., Eriksson, O. & Brooks, M. Magnetism in rare-earth metals and rare-earth intermetallic compounds. *Phys. Scr.* **T39,** 100–109 (1991).

273. Franse, J. J. M. & Radwanski, R. J. *Magnetic Properties Of Binary Rare Earth 3d Transition Metal Intermetallic Compounds* (ed Buschow, K. H. J.) 307–501 (Elsevier, 1996).

274. Campbell, I. A. Indirect exchange for rare earths in metals. *J. Phys. F: Met. Phy.* **2,** L47–L50 (1972).

275. Brooks, M., Eriksson, O. & Johansson, B. 3d-5d band magnetism in rare earth transition metal intermetallics: LuFe2. *J. Phys.: Condens. Matter* **1,** 5861–5874 (1989).

276. Burzo, E., Chioncel, L., Tetean, R. & Isnard, O. On the R 5d band polarization in rare-earth-transition metal compounds. *J. Phys.: Condens. Matter* **23,** 026001 (2011).

277. Nadj-Perge, S. *et al.* Observation of Majorana fermions in ferromagnetic atomic chains on a superconductor. *Science* **346,** 602–607 (2014).